To the Graduate Council:

I am submitting herewith a dissertation written by Jianguo Zhou entitled "Development Of A Mathematical Model For The Solution Dry Spinning Process of Hollow Filaments." I have examined the final copy of this dissertation for form and content and recommend that it be accepted in partial fulfillment of the requirements for the degree of Doctor of Philosophy, with a major in Polymer Engineering.

Joseph E. Spruiell, Major Professor

We have read this dissertation
and recommend its acceptance:

Accepted for the Council:

Associate Vice Chancellor
and Dean of The Graduate School

DEVELOPMENT OF A MATHEMATICAL MODEL FOR THE SOLUTION DRY SPINNING PROCESS OF HOLLOW FILAMENTS

A Dissertation

Presented for the

Doctor of Philosophy

Degree

The University of Tennessee, Knoxville

Jianguo Zhou

May 1996

ACKNOWLEDGMENTS

The author wishes to express his sincere appreciation to Professor Joseph E. Spruiell, the author's advisor for guidance, support, and patient encouragement throughout this work.

Appreciation is also extended to Professors Roberto S. Benson, Donald C. Bogue and Marion G. Hansen for their interest in this research and serving on the author's committee.

The author wishes to thank all the other faculty members, graduate students and other service groups in the Department of Materials Science and Engineering for all kinds of help during his graduate study.

The author is indebted to the Ketema, Inc., Special Filament Division for supporting the author to carry out dry spinning experiments and collect some experimental data for this study.

The author also wishes to thank his current employer, Ethicon, Inc., a Johnson & Johnson Company for supporting the author to complete his dissertation.

Finally, the author expresses his deepest appreciation to his parents, his wife and two children. Without their continuous support this work would not have been completed.

ABSTRACT

Hollow fibers are widely used in many chemical operation of exchange and separation, and medical application such as hemodialysis and blood oxygenation. However, little information is available in the literature regard to understanding of the spinning process of hollow filaments.

This research was to establish a mathematical model for the solution dry-spinning process of hollow filaments, using polyacrylonitrile (PAN)-dimethylformamide (DMF) solution as an example material; and to further utilize the model to predict the behavior of the spinline and the properties of spun hollow filaments under a variety of processing conditions.

The investigation included a theoretical modeling part and an experimental part needed to obtain appropriate input data for modeling and for comparison of the model prediction with actual experiment results. The model is based on the fundamental equations of fluid mechanics, heat and mass transfer and spinning dynamics. It includes the equations of continuity, force balance, energy balance as well as mass transfer.

A "thick walled" model was developed, which treats hollow filament as a thick walled cylinder under the

triaxial stress state during spinning. A "thin walled" model was also developed on the assumption that the variation in the hoop stress with radial position in the filament could be neglected.

The apparent viscosity of PAN-DMF spinning dope was experimentally obtained at different shear rates. A viscosity equation for PAN-DMF spinning dope was developed based on Modified Cross Model and experimental data. The viscosity equation includes variables such as temperature, shear rate and polymer concentration in the spinning dope.

The experiments of the dry spinning of hollow filaments were conducted to collect data from on-line measurements and the properties of spun hollow fibers. The experiments were designed to vary several important processing parameters such as polymer concentration in the spinning dope, take-up velocity, mass throughput and internal pressure.

Computer modeling under the same processing conditions as the experiments was carried out. A comparison between model predictions and experimental data was made in terms of velocity profiles, spinline tension at the take-up, wall thickness, outer and inner diameters of spun hollow filament, and solvent residue in spun hollow filament. It was demonstrated that the mathematical model for hollow fiber spinning was able to predict the basic effects of

processing conditions and material properties on the spinline behavior and properties of spun hollow filaments.

Material and processing variables in dry spinning of hollow filament include polymer concentration in the spinning dope, spinning temperature, mass throughput, internal pressure, quench air temperature and its flow velocity, etc. The complex interaction among these variables requires a lot of experimental trials to investigate the process. In many cases, it is even very difficulty to collect a complete set of experimental data due to the limitation of measurement techniques or other problems. This mathematical model allows us to study the detailed effect of material and processing variables on dry spinning process of hollow fiber and the properties of spun hollow filament. The effects of changing individual processing parameters on the spinline behavior and the properties of as-spun hollow filaments, such as outer and inner diameters, ratio of ID/OD, wall thickness and solvent residue were investigated in detail by modeling.

A comparison between thick-walled and thin-walled models was discussed. It showed that the thick-walled model is able to transform to the thin-walled model when wall thickness of hollow filament becomes small compared to filament radius. The effect of the wall thickness on hoop stress predictions by the two models was also examined. The

difference in hoop stress predictions between the two models increased withe increasing wall thickness (or decreasing Ri/Ro ratio). The comparison of the spinline predictions by the two models was conducted. The difference between the predictions of the two models was small enough to be neglected, for most practical cases, when Ri/Ro > 0.75.

TABLE OF CONTENTS

CHAPTER		PAGE
I.	INTRODUCTION	1
II.	LITERATURE REVIEW	4
	2.1 General Background	4
	2.2 Structures and Properties of PAN Fibers	6
	2.3 Rheological Properties of Concentrated Polymer Solution	12
	2.4 Dynamics of Solution Spinning	18
	2.5 Structure Formation During Solution Spinning	33
	2.6 Hollow Fiber	41
	2.7 Modeling of the Solution Spinning Process	42
III.	MATERIALS AND EXPERIMENTAL PROCEDURES	45
	3.1 Materials	45
	3.2 Material Characterization	46
	3.3 Experimental Procedures for Dry Spinning Process	50
	3.4 On-line Measurements	53
	3.5 Characterization of As-spun Hollow Filaments	55
IV.	EXPERIMENTAL RESULTS	58
	4.1 Non-Newtonian Viscosity of Spinning Dope	58
	4.2 Experiments of Dry Spinning of Hollow Filaments	71

IV. (Continued)

4.3 Results of On-line Measurements 74

4.4 Results of Off-line Measurements 79

V. DEVELOPMENT OF THE MATHEMATICAL MODEL FOR DRY SPINNING OF HOLLOW FILAMENT.....85

5.1 Hollow Filament as A Thick-Walled Cylinder.86

5.2 Hollow Filament as A Thin-Walled Cylinder .92

5.3 The Overall Force Balance Along Spinline ..96

5.4 Mathematical Models of Circumferential and Axial Force Balances for Hollow Filament Spinning 98

5.5 Energy Balance 99

5.6 Mass Transfer 101

5.7 Continuity Equation 105

5.8 Models and Parameters of Material Properties 106

5.9 Numerical Methods for Modeling 112

VI. COMPARISON OF MODELING PREDICTIONS WITH EXPERIMENTS 118

6.1 Processing and Property Variables 118

6.2 Comparison of Simulation Prediction with Experiment 120

VII. FURTHER STUDY OF DRY SPINNING OF HOLLOW FILAMENT BY MODELING 128

7.1 Effect of Mass Throughput 129

7.2 Effect of PAN Concentration in the Spinning Dope 137

VII. (Continued)

7.3 Effect of Inner Pressure 156

7.4 Effect of Spin Column Temperature 156

7.5 Effect of Exhaustion Air Flow Speed 161

7.6 Interactive Effects of Processing Parameters 166

VIII. COMPARISON AMONG THICK-WALLED, THIN WALLED AND NON-HOLLOW FILAMENT MODELS 181

8.1 Thick-walled Model Vs. Thin-walled Model .181

8.2 Comparison of Spinline Predictions by the Two Models 189

8.3 Comparison between Dry Spinning Models for Hollow Filament and Non-Hollow Filament ..199

IX. SUMMARY AND CONCLUSIONS 206

LIST OF REFERENCES 212

APPENDIXES 220

VITA 226

LIST OF FIGURES

FIGURE		PAGE
2.1.1	Chemical structure of PAN molecules of homopolymer and copolymer	5
2.2.1	The irregular helix structure of PAN molecular chain (Oliver and Oliver (12))	8
2.2.2	Wide angle x-ray diffraction pattern of oriented PAN fiber	10
2.2.3	Morphological model of PAN fiber (Warner et al. (18))	11
2.3.1	Non-Newtonian viscosity of concentrated PAN solution (Han and Segal (26))	16
2.3.2	Normal stress in PAN spinning dope as a function of shear rate (Han and Segal (26))	17
2.4.1	Distribution of elongation viscosity, stress and velocity across the radius of the filament (29)	24
3.3.1	Schematic showing the dry spinning process	51
4.1.1	Viscosity of 20% PAN dope at temperature of 30, 50 and 100°C vs. Power law model	62
4.1.2	Viscosity of 25% PAN dope at temperature of 30, 50 and 100°C vs. Power law model	63
4.1.3	Viscosity of 30% PAN dope at temperature of 30, 50 and 100°C vs. Power law model	64
4.1.4	Viscosity of 20% PAN dope at temperature of 30, 50 and 100°C vs. Modified Cross model	66
4.1.5	Viscosity of 25% PAN dope at temperature of 30, 50 and 100°C vs. Modified Cross model	67
4.1.6	Viscosity of 30% PAN dope at temperature of 30, 50 and 100°C vs. Modified Cross model	68

FIGURE PAGE

4.1.7 Log-log plot of coefficient A vs. polymer concentration C 72

4.3.1 On-line measured velocity profiles (D-H-1: 30% PAN, 0.5 g/min; D-H-3: 35% PAN, 0.5 g/min; D-H-5: 30% PAN, 1.0 g/min) varying polymer concentration and mass throughput, but fixed take-up speed of 90 m/min 75

4.3.2 On-line measured velocity profiles (D-H-1: 30% PAN, 0.5 g/min; D-H-3: 35% PAN, 0.5 g/min; D-H-5: 30% PAN, 1.0 g/min) varying polymer concentration and mass throughput, but fixed take-up speed of 120 m/min 77

4.4.1 Light microscopic photograph of PAN hollow filament 80

4.4.2 SEM photograph of a PAN hollow filament 81

5.1.1 Cylindrical coordinate system for hollow filament extrusion 88

5.8.1 Heat and mass transfer, flow past single cylinder (108) 109

5.9.1 Summary of the working relation in the model for the dry spinning of hollow filament 113

5.9.2 Computation mesh for partial differential equation of mass transfer 114

6.2.1 Comparison of on-line measured and model predicted velocity profiles (D-H-1: 30% PAN, 0.5 g/min, 90 m/min; D-H-2: 30% PAN, 0.5 g/min, 120 m/min; ΔP=500 dynes/cm^2) 121

6.2.2 Comparison of on-line measured and model predicted velocity profiles (D-H-3: 35% PAN, 0.5 g/min, 90 m/min; D-H-4: 35% PAN, 0.5 g/min, 120 m/min; ΔP=500 dynes/cm^2) 122

6.2.3 Comparison of on-line measured and model predicted velocity profiles (D-H-5: 30% PAN, 1.0 g/min, 90 m/min; D-H-6: 30% PAN, 1.0 g/min, 120 m/min; ΔP=500 dynes/cm^2) 123

FIGURE PAGE

7.1.1 Influence of mass throughput (0.5, 0.75 and 1.0 g/min) on predicted spinline velocity profiles 131

7.1.2 Influence of mass throughput (0.5, 0.75 and 1.0 g/min) on predicted spinline velocity gradient profiles 132

7.1.3 Influence of mass throughput (0.5, 0.75 and 1.0 g/min) on predicted spinline tension profiles 133

7.1.4 Influence of mass throughput (0.5, 0.75 and 1.0 g/min) on predicted outer diameter profiles along spinline 134

7.1.5 Influence of mass throughput (0.5, 0.75 and 1.0 g/min) on predicted inner diameter profiles along spinline 135

7.1.6 Influence of mass throughput (0.5, 0.75 and 1.0 g/min) on predicted ID/OD ratio profiles along spinline 136

7.1.7 Influence of mass throughput (0.5, 0.75 and 1.0 g/min) on predicted wall thickness profiles along spinline 138

7.1.8 Influence of mass throughput (0.5, 0.75 and 1.0 g/min) on predicted temperature profiles along spinline 139

7.1.9 Influence of take-up speed (90, 120 and 150 m/min) on predicted temperature profiles along spinline 140

7.1.10 Radial distribution of predicted solvent concentration in hollow filament along spinline (mass throughput 0.5 g/min) 141

7.1.11 Radial distribution of predicted solvent concentration in hollow filament along spinline (mass throughput 0.75 g/min) 142

7.1.12 Radial distribution of predicted solvent concentration in hollow filament along spinline (mass throughput 1.0 g/min) 143

FIGURE PAGE

7.1.13 Predicted average solvent concentration in hollow filament along spinline (mass throughput 0.5, 0.75 and 1.0 g/min) 144

7.2.1 Influence of PAN concentration (25%, 30% and 35%) on predicted spinline velocity profiles 146

7.2.2 Influence of PAN concentration (25%, 30% and 35%) on predicted spinline velocity gradient profiles 147

7.2.3 Influence of PAN concentration (25%, 30% and 35%) on predicted inner diameter profiles along spinline.....148

7.2.4 Influence of PAN concentration (25%, 30% and 35%) on predicted outer diameter profiles along spinline.....149

7.2.5 Influence of PAN concentration (25%, 30% and 35%) on predicted wall thickness profiles along spinline.....150

7.2.6 Influence of PAN concentration (25%, 30% and 35%) on predicted tension profiles along spinline.....152

7.2.7 Influence of PAN concentration (25%, 30% and 35%) on predicted ID/OD ratio profiles along spinline.....153

7.2.8 Predicted average solvent in hollow filament along spinline (25%, 30% and 35% PAN in the dope) 154

7.2.9 Influence of PAN concentration (25%, 30% and 35%) on predicted temperature profiles along spinline.....155

7.3.1 Influence of internal pressure (250, 500 and 750 dynes/cm^2) on predicted spinline velocity profiles 157

7.3.2 Influence of internal pressure (250, 500 and 750 dynes/cm^2) on predicted wall thickness profiles along spinline 158

FIGURE PAGE

7.3.3 Influence of internal pressure (250, 500 and 750 dynes/cm^2) on predicted ID/OD ratio profiles along spinline 159

7.4.1 Influence of spin column temperature (180 and 250°C) on predicted temperature profiles along spinline 160

7.4.2 Influence of spin column temperature (180 and 250°C) on predicted solvent residue profiles along spinline 162

7.5.1 Influence of quench air flow speed (10, 20 and 30 cm/s) on predicted spinline velocity profiles 163

7.5.2 Influence of quench air flow speed (10, 20 and 30 cm/s) on predicted temperature profiles along spinline 164

7.5.3 Influence of quench air flow speed (10, 20 and 30 cm/s) on predicted solvent residue profiles along spinline 165

7.6.1 Key processing parameters which affect the diameter and wall thickness of hollow filament 168

7.6.2 Effect of take-up ratio and internal pressure on inner diameter of hollow filament 169

7.6.3 The relation among inner diameter, take-up ratio and internal pressure 170

7.6.4 Effect of take-up ratio and internal pressure on inner diameter reduction ratio of hollow filament 172

7.6.5 The relation among inner diameter reduction ratio, take-up ratio and internal pressure .. 173

7.6.6 Effect of take-up ratio and internal pressure on wall thickness of hollow filament 174

7.6.7 The relation among wall thickness, take-up ratio and internal pressure 175

FIGURE PAGE

7.6.8 Effect of take-up ratio and internal pressure on wall thickness reduction ratio of hollow filament 176

7.6.9 The relation among wall thickness reduction ratio, take-up ratio and internal pressure .. 177

7.6.10 Effect of spin column temperature and mass throughput on solvent residue of as-spun hollow filament 178

7.6.11 The relation among solvent residue, spin column temperature and mass throughput 179

8.2.1 Comparison of spinline velocity profiles predicted by thick-walled and thin-walled models (spinneret parameter ID/OD = 0.75) ... 190

8.2.2 Comparison of spinline velocity profiles predicted by thick-walled and thin-walled models (spinneret parameter ID/OD = 0.50) ... 191

8.2.3 Comparison of spinline velocity profiles predicted by thick-walled and thin-walled models (spinneret parameter ID/OD = 0.25) ... 192

8.2.4 Comparison of velocity gradient profiles predicted by thick-walled and thin-walled models (spinneret parameter ID/OD = 0.75) ... 193

8.2.5 Comparison of velocity gradient profiles predicted by thick-walled and thin-walled models (spinneret parameter ID/OD = 0.50) ... 194

8.2.6 Comparison of velocity gradient profiles predicted by thick-walled and thin-walled models (spinneret parameter ID/OD = 0.25) ... 195

8.2.7 Comparison of wall thickness profiles predicted by thick-walled and thin-walled models (spinneret parameter ID/OD = 0.75) ... 196

8.2.8 Comparison of wall thickness profiles predicted by thick-walled and thin-walled models (spinneret parameter ID/OD = 0.50) ... 197

FIGURE PAGE

8.2.9 Comparison of wall thickness profiles predicted by thick-walled and thin-walled models (spinneret parameter ID/OD = 0.25) ... 198

LIST OF TABLES

TABLE		PAGE
2.4.1	Experimental diffusion constants for wet spinning (29)	30
2.5.1	The relationship between molecular weight and tenacity of PAN fibers (61)	36
3.2.1	Intrinsic viscosity and viscosity-average molecular weight of PAN polymer	48
4.1.1	The complete fitting results by using Modified Cross model	70
4.2.1	Process conditions for dry spinning of hollow filaments	73
4.3.1	Measured take-up tension for dry spinning of hollow filament	78
4.4.1	Properties of as-spun hollow filaments from dry spinning experiments	82
6.1.1	Key input and output variables	119
6.2.1	Comparison of predicted take-up force with experimental values	124
6.2.2	Comparison of predicted diameters with experimental values	126
6.2.3	Comparison of predicted solvent residue with experimental values	127
7.1.1	Dry spinning conditions simulated with varying mass throughput	130
8.1.1	Comparison of hoop stress predictions between thickness-walled and thin-walled models	185
8.1.2	Hoop stress variation across the wall thickness	188

TABLE PAGE

8.2.1 Comparison of predicted diameters and wall thickness of hollow filament by thick-walled and thin-walled models (spinneret parameter ID/OD = 0.75) 200

8.2.2 Comparison of predicted diameters and wall thickness of hollow filament by thick-walled and thin-walled models (spinneret parameter ID/OD = 0.5) 201

8.2.3 Comparison of predicted diameters and wall thickness of hollow filament by thick-walled and thin-walled models (spinneret parameter ID/OD = 0.25) 202

CHAPTER I

INTRODUCTION

Production of synthetic fibers started during 1930's. W. Carothers, in the U.S, first produced nylon-66 fiber in his laboratory in 1935. The pilot plant production of nylon-66 fiber was beginning in 1938 and the industrial-scale production of nylon-66 fiber began in 1940. The first nylon-6 fiber was invented in Germany in 1938 and industrial production of nylon-6 fibers was initiated in 1941. Based on Carothers' early work, British chemists Whinfield and Dickson used terephthalic acid and ethylene glycol to produce high melting point poly(ethylene terephathalate) and made PET fiber in 1944. Large-scale production of PET fiber started in Britain in 1949 and in the U.S. in 1953.

In 1942, Rein in Germany and R. Houtz in the U.S. found a good solvent dimethylformamide (DMF) for polyacrylonitrile (PAN) and made possible the solution spinning of PAN fibers. In 1948, Du Pont marketed polyacrylonitrile fiber under the trade name "Orlon". Later the production of PAN spread to German, Britain, France and Japan.

The industrial production of man-made fibers involves three methods of spinning: melt spinning, wet spinning and dry spinning. In melt spinning, the polymer is melted and mixed in an extruder; and the molten polymer is pumped through a spinneret by a metering pump. The extruded polymer melt is solidified by cooling air and wound up by a take-up device. Wet spinning involves conversion of polymer raw material into a solution, and extrusion of this solution through a spinneret into a coagulation bath, where additional chemical reactions convert the material back into the desired fibrous form. In dry spinning, the polymer is dissolved in a volatile solvent to form a spinning dope. The dope is forced through a spinneret into a column circulated with hot gas. In the column, the hot gas causes the solvent to evaporate and the solidified polymer forms fibers.

New spinning techniques have been introduced by modifying these spinning methods. Some examples are dry-jet spinning, which takes the features of both wet and dry spinning; non-circular fibers, triangular, trilobal and etc., which use exotic shaped dies(1-5); and hollow fibers (6).

Hollow fiber technology has been progressing significantly in recent years. Hollow fibers are used in many chemical operations of exchange and separation, which

includes sea water desalination, ion exchange, ultrafiltration, osmosis and gas permeation. Medical applications use hollow fibers in the artificial kidney dialyzer, gas-gas exchange and gas-liquid exchange in the artificial lung. Hollow fibers also provide a good material for thermal barrier used in textile apparel and comforter.

Polyacylonitrile has been commonly used to produce acrylic filaments through either the dry-spinning or wet-spinning process. Polyacrylonitrile fibers are widely used in textiles, medical applications, and as carbon fiber precursor. It was disclosed that hollow fibers of polyacrylonitrile polymers were prepared through solution spinning techniques in U.S. Patents (7,8) dating back to 1975.

Little information is available in the literature concerning process optimization of the extrusion of hollow filaments. The present proposed research is focused on establishing a mathematical model for the solution dry-spinning process for producing hollow filaments using polyacrylonitrile (PAN). The formulation in the model will include the equations of continuity, force balance, heat transfer, and mass transfer as well as models of material behavior, boundary conditions and assumptions. The model is expected to provide predictions to evaluate the process and design ideas.

CHAPTER II

LITERATURE REVIEW

2.1 General Background

Polyacrylonitrile (PAN) is an atactic, linear macromolecule consisting of a carbon-hydrogen backbone with polar nitrile pendant groups attached. The chemical structure of a homopolymer PAN molecule is presented in Figure 2.1.1 (a).

The physical properties of PAN are significantly influenced by its polar nitrile groups. The glass transition temperature of PAN is on the order of 120°C because of strong intermolecular bonding forces resulting from the polarity of the nitrile groups. The fiber-grade of PAN is often copolymerized with other monomers, such as methyl acrylate (e.g. 94% PAN-6% methyl acrylate) (9) or vinyl acetate, see Figure 2.1.1 (b). The addition of co-monomers lowers the glass transition temperature sufficiently to allow textile manufacturers to stretch the as-spun filaments in boiling water (9,10). The strong intermolecular bonding attributed primarily by the polarity of the nitrile groups is also important to the thermal characteristics of PAN fibers. The fibers made from PAN or its copolymers will tend to decompose before they melt.

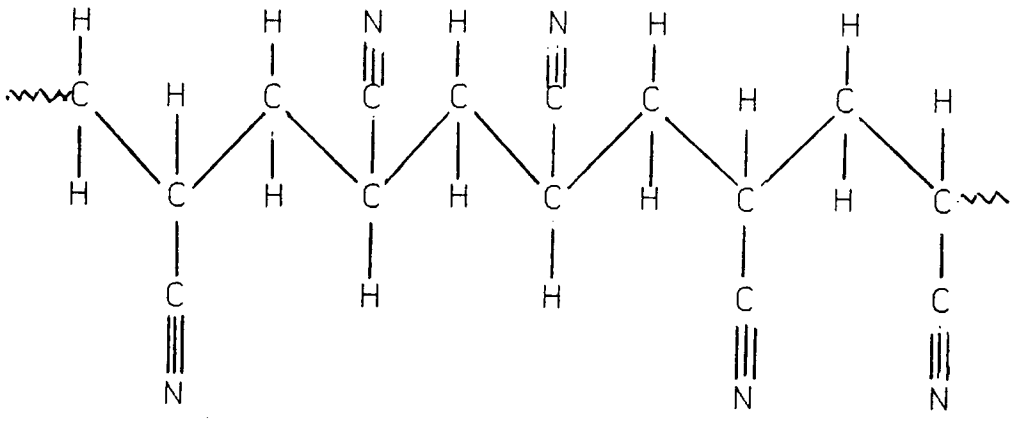

(a) PAN homopolymer

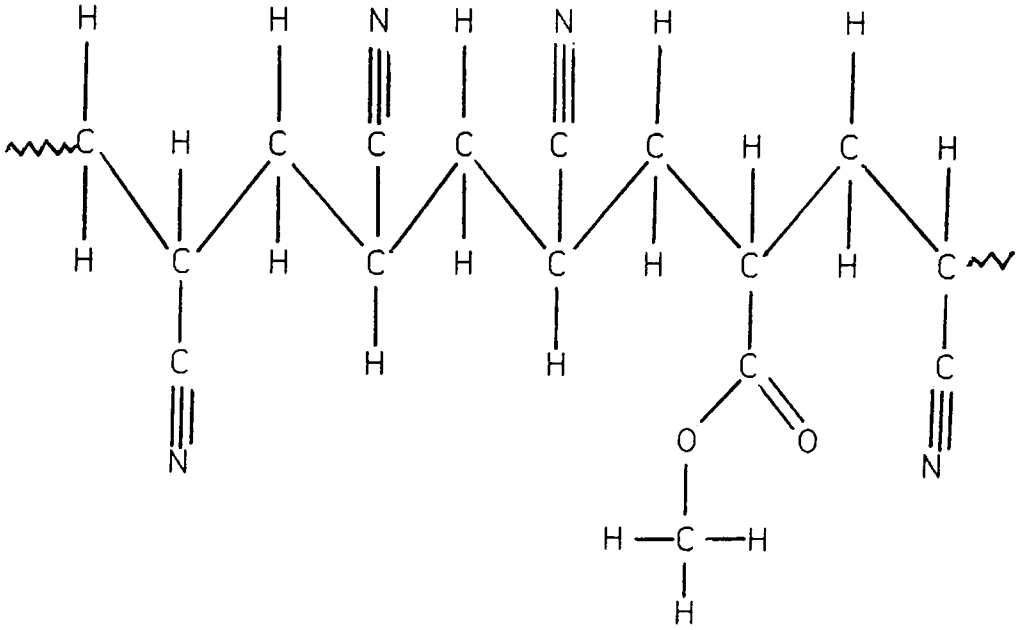

(b) Acrylonitrile-methylacrylate copolymer

Figure 2.1.1 Chemical structure of PAN molecules of homopolymer and copolymer.

This is a very important property when producing carbon fibers from PAN based precursor.

The polarity of the nitrile group of PAN also significantly affects its solution characteristics. This is indicated by the high value of the solubility parameter ($15.4\ (cal/cc)^{1/2}$) (11), which is a measure of the cohesive energy density of the polymer. Only highly polar solvents can be used to dissolve PAN, such as dimethylformamide (DMF) and dimethylacetamide (DMAc).

PAN fibers can be produced by the wet spinning process in which a solution (dope) of the polymer and an appropriate solvent are spun into a coagulating bath and then the fibers are washed, stretched, and dried. PAN fibers can also be made by means of a dry spinning process. In this processing, the polymer solution (dope) is extruded through the spinneret vertically downward into a pipe with a current of hot air, which evaporates most of the solvent before the the tow of fibers is collected. Wet spinning usually results in fibers that have a round shape cross section. But dry spinning results in fibers with a dog-bone cross section.

2.2 Structures and Properties of PAN Fibers

The characteristic of the PAN molecule is the presence of the strongly polar nitrile groups, at an intramolecular

distance of only a few tenths of a nm. The large dipole moment of the nitrile groups (3.9 Debye), together with their close proximity in space, leads to very large intramolecular dipolar and steric repulsions which compel the individual macromolecules into a somewhat helical conformation. The irregular helix structure of PAN chains was proposed by Oliver and Oliver (Figure 2.2.1) (12). Each macromolecule may be thought of as a more or less rigid structure, fitting within a cylinder of about 0.6 nm diameter. Some of the CN groups will extend beyond the confines of the cylinder. These groups are potentially available for intermolecular dipole-dipole interaction. The CN groups present different angles with regard to the helical axis, determined by intramolecular repulsion and intermolecular attraction. The irregularity of the helical conformation is most likely due to the atacticity of the PAN molecules (13,14). Two adjacent macromolecules will tend to lower their energy by bringing together a maximum of groups that can interact favorably. PAN has relatively high molecular stiffness caused by the repulsion of neighboring CN groups in the same molecule. The high molecular stiffness is responsible for the high melting point (>300 °C). The explanation is that the entropy of fusion is low because few degrees of freedom are gained if PAN passes from the crystalline to the molten state.

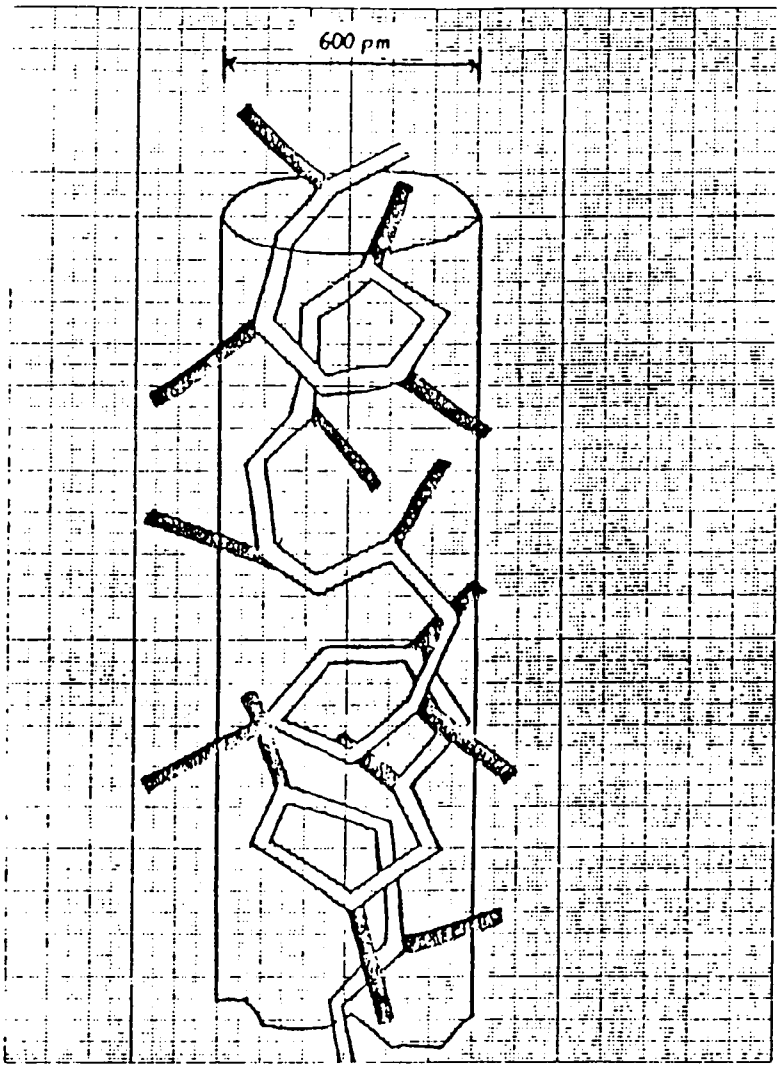

Figure 2.2.1 The irregular helix structure of PAN molecular chain (Oliver and Oliver (12)).

PAN usually is not stable up to its melting point. In the temperature range of 180-380 °C, a number of reactions take place, including autocatalytic cyclization involving the CN groups, and decomposition leading to the production of gaseous products such as NH_3, HCN, nitrile, etc. Extremely high heating rates were necessary to determine the melting point of PAN by differential thermal analysis (15,16).

Wide-angle X-ray diffraction patterns obtained from oriented PAN fiber show only two equatorial reflections (Figure 2.2.2). The diffractogram indicates that these reflections are at Bragg angles $2\theta=17°$(d=0.52nm) and $2\theta=30°$(d=0.3nm), arising from planes more or less parallel to the fiber axis (17,18). Off-equatorial reflections are usually absent, which imply the presence of only lateral order.

Warner et al. (18) proposed a morphological model of PAN fiber (Figure 2.2.3), showing the ordered and disordered regions are connected along the fiber axis. The parallel rods constitute the major part of the ordered phase in a fibril. The rod diameter is approximately 0.6 nm based on WAXD data and molecular model studies (12,18). The rods are not in perfect alignment with respect to the rod ends, but rather exhibit some misalignment. The disordered regions connecting the rods consist of loops, folds,

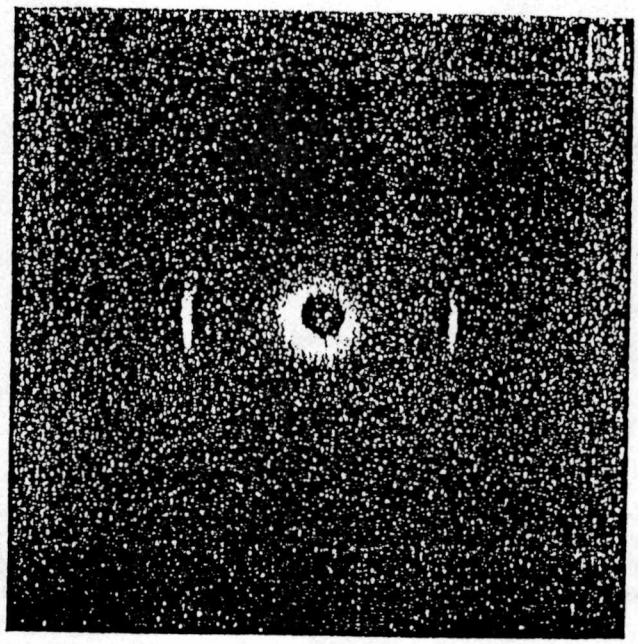

Figure 2.2.2 Wide angle x-ray diffraction pattern of oriented PAN fiber.

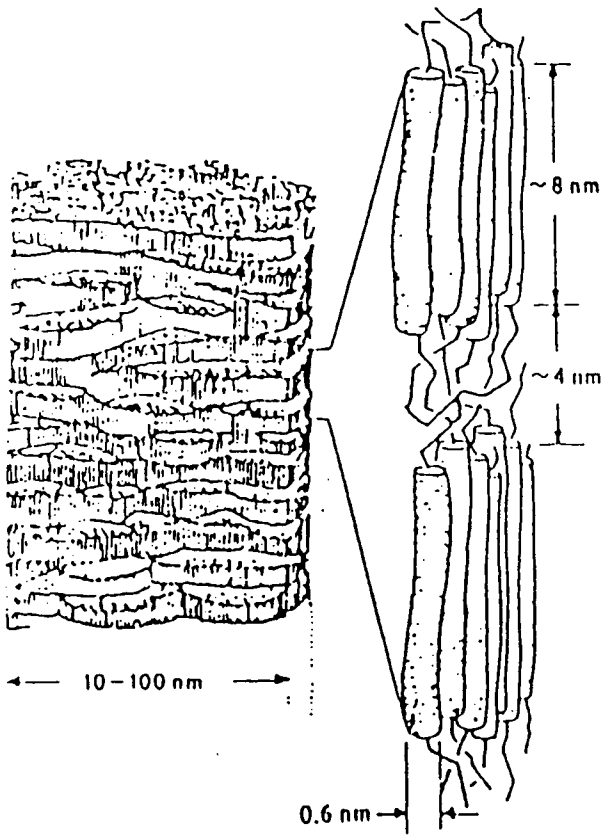

Figure 2.2.3 Morphological model of PAN fiber (Warner et al. (18)).

entangled chains, defects, comonomer sequences, tie chains etc. The lateral dimensions of the ordered regions estimated from WAXD data are in the range of 10-100nm, depending on the processing history of the fibers (19). Small-angle X-ray scattering studies (20) revealed the presence of elongated microvoids in PAN fibers. The fibrils and the microvoids are aligned parallel to the fiber axis.

2.3 Rheological Properties of Concentrated Polymer Solution

The presence of polymer molecules in a solvent can increase the viscosity of solution dramatically, compared to equivalent concentrations of low molecular weight solutes because of the long molecular chain structure of polymers. Staudinger proposed the following equation in the early 1930s:

$$\eta_{sp} = KcM \qquad (2.3.1)$$

and

$$[\eta] = KM \qquad (2.3.2)$$

as a relation between intrinsic viscosity and molecular weight; where K is a constant for a given polymer-solvent-temperature, c is the concentration, M is the molecular weight, η_{sp} is the specific viscosity, and $[\eta]$ is the intrinsic viscosity. It has been found that η_{sp}/c is not

independent of concentration. Huggins (21) has shown empirically that

$$\frac{\eta_{sp}}{c} = [\eta] + k'[\eta]^2 c \qquad (2.3.3)$$

where k' is a constant for a given polymer type, solvent and temperature. It has been empirically found that

$$[\eta] = KM_v^{a} \qquad (2.3.4)$$

known as the Mark-Houwink equation. K and a are constants. The exponent a varies from 0.5 in a theta solvent to about 0.8.

The viscosity η of concentrated polymer solutions is generally represented as (22)

$$\eta = \eta_0\{1 + [\eta]c + k_1[\eta]^2c^2 + \ldots\} \qquad (2.3.5)$$

where η_0 is the solvent viscosity. The zero shear viscosity η depends strongly on the concentration and molecular weight at higher polymer concentration. An approximate equation has been proposed as (23)

$$\eta = KM^{3.4}c^5 \qquad (2.3.6)$$

Oyanangi and Matsumoto obtained an empirical equation for zero shear viscosity for PVA-water solution at 30°C as (24)

$$\log\eta = \log\eta_0 + 5\log c + 3.4\log M_w - 9.43 \qquad (2.3.7)$$

where c is the concentration of PVA in solution (g/cm^3), η_0 is solvent (water) viscosity and M_w is weight-average molecular weight.

In the relatively high temperature range, it was reported (25) that the temperature dependence of zero shear viscosity of concentrated polymer solution can be described by the Arrhenius relation:

$$\eta(T) = \text{const} \times \exp(\frac{E\eta}{RT}) \qquad (2.3.8)$$

where $E\eta$ is activation energy, R is gas constant and T is absolute temperature.

The viscosity of concentrated polymer solution shows non-Newtonian behavior, which has a constant η at low shear rate and decreases with increasing shear rate. Non-Newtonian viscosity of the spin dope of polyacrylonitrile solution has been reported by Han and Segal (26). Their experimental results indicated that concentrated PAN solution was highly non-Newtonian at the shear rate above

10^3 sec^{-1} (Figure 2.3.1). Shear-thinning behavior of polymeric solutions is commonly modeled by the power law:

$$\mu = K\dot{\gamma}^{n-1} \qquad (2.3.9)$$

where μ is apparent viscosity, K is a constant, $\dot{\gamma}$ is shear rate and the exponent n is less than one. The apparent viscosity decreases with increasing shear rate. Fitzgerald and Graig obtained n=0.3 from their experimental data on a polyacrylonitrile spinning dope (10). Philipp and Wulf found n=0.238 ~ 0.364 for rayon spinning solution (27).

Concentrated polymeric solutions will also exhibit viscoelastic behavior. Normal stress in polyacylonitrile spinning dope as a function of shear rate was obtained by Han and Segal (26) as in Figure 2.3.2. They also measured die swell ratio as a function of shear rate in wet spinning of polyacrylonitrile spin dope into a NaSCN (sodium thiocyanate)/water bath. They found that die swell ratio increased with increasing shear rate at fixed bath concentration (weight percentage of NaSCN in water). They also observed that die swell ratio increased with bath concentration at a fixed shear rate, between 0 and 20% bath concentration, which was explained as caused by the decrease in coagulation rate (solidification).

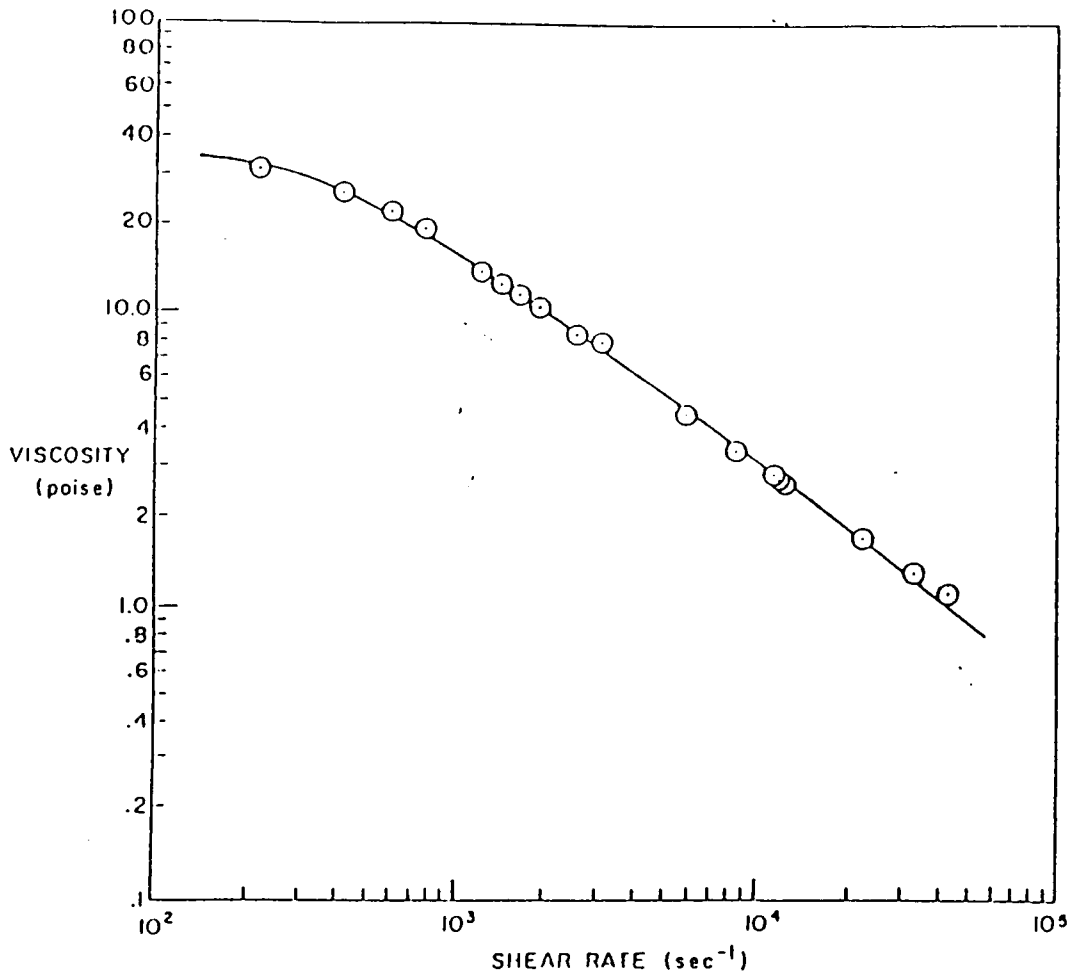

Figure 2.3.1 Non-Newtonian viscosity of concentrated PAN solution (Han and Segal (26)).

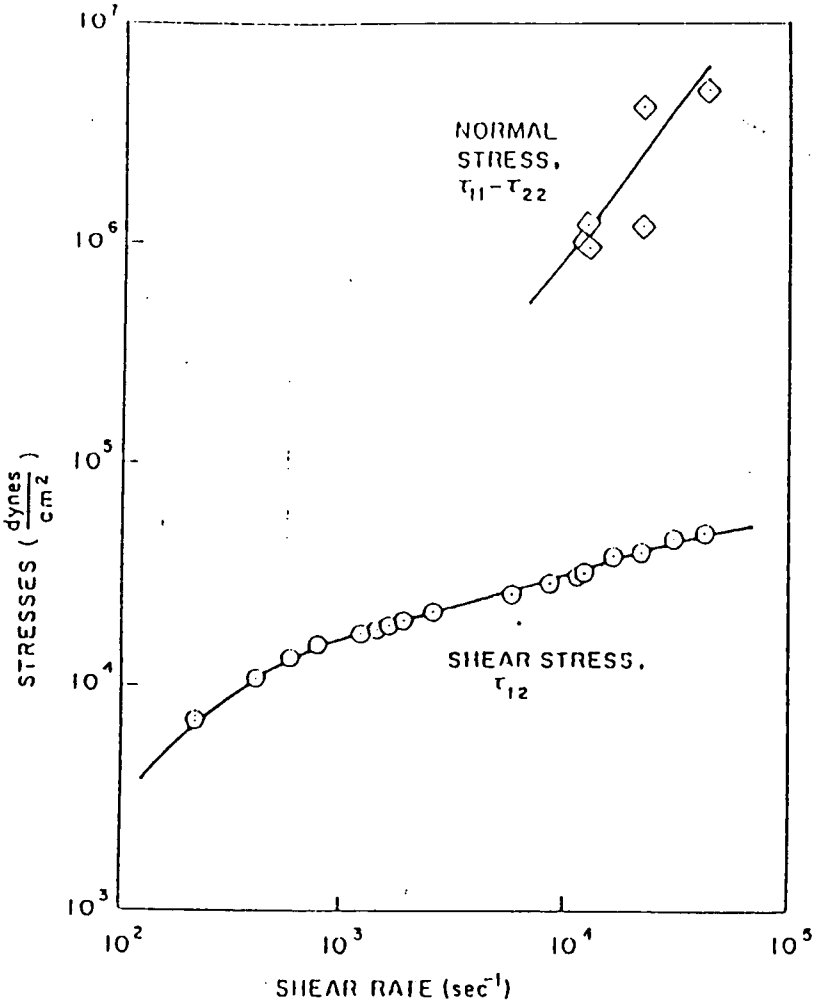

Figure 2.3.2 Normal stress in PAN spinning dope as a function of shear rate (Han and Segal (26)).

More detailed research on die-swell of polyacrylonitrile dope under different coagulation rate was provided by Paul and Armstrong (28). They found that decreasing the coagulation rate in the coagulation bath could decrease die swell ratio and increase spinnability.

2.4 Dynamics of Solution Spinning

The study of dynamics of the solution spinning process basically involves the following equations: force balance, energy balance (heat transfer equation), mass balance (mass transfer equation).

2.4.1 Force Balance in Spinline

Force Balance along Fiber Axis

The macroscopic balance of forces along the fiber axis in solution spinning is very similar to that for melt spinning. The force balance along the spinline was first presented by Ziabicki (29,30). More detailed derivation of equations of force balance can been found in recent literature (31,32). At arbitrary distance z from the spinneret, the force balance along spinline (fiber axis) is described by the following equation:

$$F_L - F_{rheo} - F_{drag} - F_{inert} + F_{grav} - F_s = 0 \qquad (2.4.1)$$

where F_L is the take-up force at the end of the spinline exerted by the take-up device, F_{rheo} is rheological force, F_{drag} is the drag force caused by friction between the filament and quenching medium (such as air, solution), F_{inert} is the inertia force, F_{grav} is the gravity force and F_s is the force due to surface tension of the filament/medium interface.

The drag force F_{drag} may be expressed as:

$$F_{drag} = \int_0^z \pi D \sigma_f dz \qquad (2.4.2)$$

where D is the diameter of the filament at position z, σ_f is the frictional stress between the surface of the filament and surrounding medium. The frictional stress σ_f may be expressed through a friction factor C_f:

$$\sigma_f = C_f \frac{\rho V^2}{2} \qquad (2.4.3)$$

where ρ is the density, and V is the filament velocity. C_f is a function of Reynolds number R_e which is defined as:

$$R_e = \frac{DV\rho_a}{\eta_a} \qquad (2.4.4)$$

where ρ_a is the density of fluid medium, η_a is the viscosity of fluid medium, and the other terms have already been defined.

Evaluation of C_f is not easy. For many years both theoretical and experimental investigation have been done (33-39). Sakiadis (33) used the laminar boundary layer correlations to derive C_f for a constant diameter cylinder passing through a stationary fluid at constant velocity. The form of C_f is expressed as follows:

$$C_f = \frac{4}{\beta} Re \tag{2.4.5}$$

$$\zeta^2 = 8 \int_0^{\beta} \frac{(z-1)\exp(2z)+z+1}{z^2} dz \tag{2.4.6}$$

and

$$\zeta^2 = 64 \frac{z}{d} Re \tag{2.4.7}$$

Glicksman (34) used the turbulent boundary layer theory to obtain C_f on a stationary cylinder surrounded by moving fluid:

$$C_f = 0.65 Re^{-0.7} \tag{2.4.8}$$

Matsui (35) has formulated an expression for C_f by using turbulent theory:

$$C_f = 0.37Re^{-0.61}$$

Sano and Orii (36) measured tension at various points along the spinline and obtained

$$C_f = 0.68Re^{-0.61} \qquad (2.4.9)$$

Gould (37) carried out an experiment on a stationary filament under tension in an air stream at speeds of up to 6,000 m/min and derived

$$C_f = 0.41Re^{-0.61} \qquad (2.4.10)$$

Shimizu et al (38) measured tensile forces along spinline at take-up speeds of up 6,000 m/min and obtained the formula

$$C_f = KRe^{-0.61} \qquad (2.4.11)$$

They found that the K value lies between 0.23 and 0.49 for filaments spun into still air and 0.77 for filaments spun

into an axisymmetric air stream. The K value strongly depends on the filament vibration and for the multifilament case on the filament spacing in the spinline.

Kwon and Prevosek (39) made experimental measurement of air drag during spinning. They found that the experimental values of the air drag were larger than the values based on the existing correlation and explained that it was due to the swaying of filament which makes the effective filament diameter larger than the actual diameter.

Although the numerical constants in the air drag coefficient vary with different authors, the general form of the equation is the same:

$$C_f = KRe^{-n} \qquad (2.4.12)$$

where n is usually found to lie in the range of 0.6 - 0.8.

Vadudevan and Middleman (40) indicated that friction factor in solution spinning was different from that in melt spinning because of mass transfer of solvent between the outer layer of filament and the medium, which causes a change in the thickness of the boundary layer.

Force Distribution along Radial Axis

The radial variation in filament properties spun from melt spinning is mainly caused by temperature gradient along the radial direction during processing. In solution spinning, the variation of physical properties of filaments is caused by not only temperature gradient, but also solvent gradient along the radial direction due to the mass transfer. Severe skin-core structure can be formed, especially during wet spinning.

Ziabicki (29,41) proposed two simplified models for property variation along the radial direction as shown in Figure 2.4.1, considering the filament as cylindrical. Elongational viscosity varies with radial position (continuous), which is higher on the skin of the filament and lower in the core of the filament. The model assumed either a flat stress to get a varied velocity distribution, or a flat velocity to obtain variation of stress distribution on the filament cross section. A model with discontinuous elongational viscosity has been proposed (29) to explain skin-core structure of filament by wet spinning. The mathematical expression of discontinuous viscosity is given as:

$$\eta(r,z) = \begin{cases} \eta_s & \xi < r \le R \\ \eta_c & 0 \le r \le \xi \end{cases} \qquad (2.4.13)$$

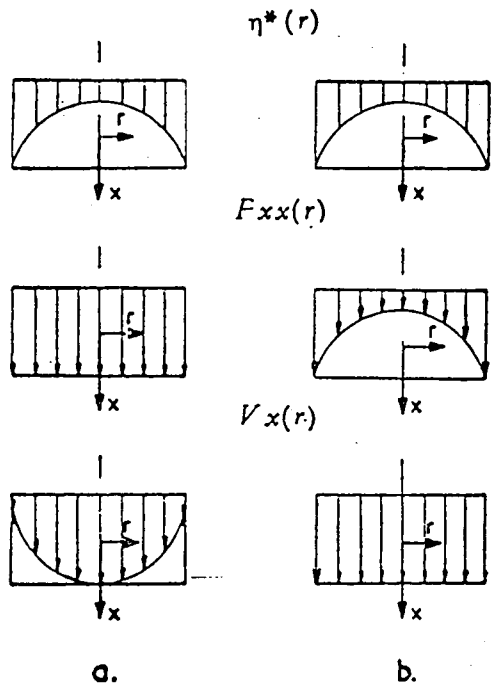

Figure 2.4.1 Distribution of elongation viscosity, stress and velocity across the radius of the filament (29).

where η_S and η_C are elongational viscosity in skin and core of filament, respectively, ξ is the selected boundary position between skin and core.

In general, the rheological force along the spinline can be expressed as:

$$F_{rheo}(z) = \int_0^{R(z)} 2\pi r \, \sigma_{zz}(r,z) dr \qquad (2.4.14)$$

where $\sigma_{zz}(r,z)$ is normal stress distribution at radial position r at a spinline distance z.

2.4.2 Transport Processes During Solution Spinning

Energy Balance

Ziabicki (29) wrote down the following equation for the heat transfer in melt spinning with neglect of radiation and temperature variation in the radial direction:

$$\rho C_p V \frac{dT}{dz}\left(\frac{\pi d^2}{4}\right) = -h(T-T_{air})(\pi d) \qquad (2.4.15)$$

where dT/dz is the cooling rate along spinline, C_p is specific heat capacity of the fiber, T is the temperature

on the surface of the fiber, h is heat transfer coefficient from the fiber to the air, V is the velocity of the filament, d is the diameter of the fiber.

If the release of heat by crystallization is considered (31), the equation becomes

$$\frac{dT}{dz} = -\frac{\pi dh(T-T_{air})}{WC_p} + \frac{\Delta H d\theta}{C_p dz} \qquad (2.4.16)$$

where ΔH is the heat of fusion and θ is the fractional crystallinity.

Heat transfer coefficient h can be given in terms of Nusselt ($Nu=hd/K_{air}$) and Reynolds numbers.

$$Nu = 0.32+0.155Re^{0.5} \quad \text{(Sano and Nishikawa (42))} \qquad (2.4.17)$$

$$Nu = 0.25+0.155Re^{0.36} \quad \text{(Sano (43))} \qquad (2.4.18)$$

$$Nu = 0.118Re^{0.544} \quad \text{(Shimizu et al (44))} \qquad (2.4.19)$$

In case of transverse air flow imposed on the spinline the heat transfer coefficient can be modified by (45)

$$h = h_0[1+8(V_a/V_f)^2]^{0.667} \qquad (2.4.20)$$

where h_0 is heat transfer coefficient in the absence of transverse air flow, V_a and V_f are the air and fiber velocities,respectively.

Ohzawa, Nagano and Matsue (32) proposed the following equation for energy balance of dry spinning, considering heat loss due to evaporation of the solvent across the filament surface.

$$\rho C_p V \frac{d\langle T\rangle}{dz}\left(\frac{\pi d^2}{4}\right) = \pi d[-h(T_0 - T_{air}) - L_s N_{s,0}] \qquad (2.4.21)$$

where Ns,o is the molar flux for the transfer rate of the solvent at the interface, Ls is the heat of vaporization of the solvent at its boiling temperature, To is the temperature of filament surface and <T> is the average temperature of filament cross section and given by:

$$\langle T\rangle = \frac{1}{A}\int_0^R 2\pi r T dr \qquad (2.4.22)$$

where A is the cross sectional area of the filament.

Mass Transfer

In solution spinning, a viscous polymer dope is extruded through the spinneret surrounded either by a

liquid bath (wet spinning) or a hot dry gas (dry spinning). In the wet spinning process, inter-diffusion between the filaments and the liquid bath causes the filaments to solidify, which is commonly called "coagulation". During the coagulation process the solvent originally added to the spin dope diffuses out of the filaments, while non-solvent components diffuse into the filaments. A counter-diffusion mechanism with at least two components (solvent and nonsolvent) should be considered. In the dry spinning process, the solvent in the filaments diffuses to the surface of the filaments and evaporates. The mass transfer of the solvent in dry spinning consists of two steps. The transport of the solvent within the filament can be considered as a molecular diffusion process, while evaporation of the solvent on the surface of filament to gas phase can be treated as interface mass transfer.

A. Wet Spinning

In the wet spinning of acrylic fiber, the fine streams of dope emerging from the spinneret have a higher concentration of solvent than that in the coagulation bath. The concentration gradient is the driving force for the diffusion process. Fick's first law of diffusion (46) states that the mass diffusion rate through a plane is proportional to its area and the concentration gradient as:

$$\frac{dm}{dt} = - DA\frac{dc}{dx} \qquad (2.4.23)$$

or

$$J = - D\frac{dc}{dx} \qquad (2.4.24)$$

where J is the diffusional flux, D is the diffusion constant and dc/dx is concentration gradient in the x direction. If using Fick's first law to describe the counter-diffusion in wet spinning, then

$$J_s = - D_s\frac{dc_s}{dx} \qquad (2.4.25)$$

$$J_n = - D_n\frac{dc_n}{dx} \qquad (2.4.26)$$

where D_s, D_n are the diffusion constants of solvent and non-solvent, respectively; J_s, J_n are the diffusional fluxes of solvent and non-solvent, respectively.

Diffusion constants are basic parameters for diffusion processes in wet spinning. Experimental estimated diffusion constants for wet spinning in published literature are summarized in Table 2.4.1 (29).

B. Dry-Spinning

The mass balance equation for the solvent component during the dry-spinning process is as follows:

Table 2.4.1 Experimental diffusion constants for wet spinning (29).

Polymer	Solvent	Coagulation Bath	Temp. (°C)	$Dx10^6$ (cm^2/sec)
PAN	DMF	60% DMF in water	10	4.2 (DMF) 1.2 (water)
PAN	DMF	0-70% DMF in water	30	2.9-6.2 (DMF) 2.4-5.2 (water)
PAN	DMF	water	30	5.95 (DMF) 5.2 (water)
PAN	DMF	Methanol	30	5.2 (DMF) 1.86 (MeOH)
PAN	DMF	Eethanol	30	4.13 (DMF) 0.87 (EtOH)
PAN	DMF	2-Butanol	30	1.29 (DMF) 0.27 (BuOH)

$$W_{s1} + W_{s2} = 0 \qquad (2.4.27)$$

where W_{s1} is the mass of the solvent which diffuses out from the filament, W_{s2} is the mass of the solvent which evaporates during interphase mass transfer.

The distribution of the concentration of the solvent within the filament is given as (47,48).

$$\frac{C(r,t) - C_s^*}{C_0 - C_s^*} = f(Sh, Fo, \frac{r}{R}) \qquad (2.4.28)$$

where $C_s(r,t)$ is the distribution of the concentration of the solvent within the filament at time t, C_s^* is the concentration of the solvent in the gas phase, C_0 is the initial concentration of the solvent in the filament, R is the radius of the filament, Sh is the Sherwood number and F_o is the Fourier number.

$$Sh = k_m \frac{d}{D_s} \qquad (2.4.29)$$

$$F_o = \frac{D_s t}{R^2} \qquad (2.4.30)$$

where k_m is the mass transfer coefficient, d and R are the diameter and radius of the filament, respectively, D_s is the diffusivity and t is the characteristic time.

Since the differential equations for the heat transfer systems and the mass transfer system are analogous (110), this permits us to derive mass transfer correlations from heat transfer correlations for equivalent boundary conditions by substituting Sherwood number for Nusselt number and Schmidt number for Prandtl number.

Overall rate of mass transfer is determined by both the rate of the diffusion of the solvent within the filament and the rate of the convection of the solvent nearby the surface of the filament (47).

When $100 > Sh < 0.1$, the mass transfer is controlled by the diffusion and convection of the solvent.

When $Sh > 100$, the mass transfer is largely controlled by the diffusion of the solvent within the filament, since the rate of the convection of the solvent on the surface of the filament is very fast.

When $Sh < 0.1$, the mass transfer is largely controlled by the convection of the solvent, since the mass transfer nearby the surface of the filament is a slower process.

Sano and Nishikawa (49-51) and other authors (52-53) studied the mechanism of the diffusion and the convection of the solvent along spinline for the dry-spinning. It was

found that both diffusion and convection controlled the overall mass transfer during the initial stage of the evaporation, and only the diffusion controlled the overall mass transfer during the later stage of the evaporation.

2.5 Structure Formation During Solution Spinning

The structure of PAN fibers can be varied appreciably by solution spinning processing. The structure of PAN fibers can be described on two levels: molecular structure and morphology. The molecular structure is controlled by the unique conformation and intermolecular bonding of the polyacrylonitrile chains regardless of the spinning process. The model of molecular conformation and packing of PAN was proposed by Oliver and Oliver (12) and Warner et al.(18). The individual molecular chain is extended in an irregular conformation because of the strong dipolar repulsion forces between like atoms on adjacent nitrile groups. Each chain tends to remain within a cylinder of about 6 å diameter. The cylinders pack into cystallites containing six polymer chains. Lateral bonding forces are provided by dipole-dipole attraction between differently charged atoms in nitrile groups on adjacent chains. These lateral bonds are randomly spaced with no regular repeat distance along the fiber axis. This structure concept is supported by x-ray patterns which show that crystalline

order is present only in the two directions perpendicular to the fiber axis, with no order along the fiber axis (54).

The morphological structure of PAN fibers is largely determined in the fiber formation step and can be modified substantially by changes in processing variables within each spinning process. In wet spinning, the structure of PAN fiber is described (55) as an oriented, fibrillar network with fibril diameters in the range 60-2000 å separated by micropores of larger diameter. This network is oriented in subsequent stretching and collapses during drawing to form a compact fibrillar network. The occurrence of large radial macrovoids which distort the basic fibrillar network has received much attention (55-60). In dry spun fibers, a homogeneous fine structure with limited orientation is obtained. During stretching, the dry spun fibers develop a fully oriented fibrillar structure.

2.5.1 Effects of PAN molecular properties on spun fibers

Molecular weight of a polymer is a parameter that affects chemical, physical and mechanical properties of the resultant fibers. Most commercial acrylic fibers are produced from PAN polymers with intrinsic viscosities between 1.3 and 1.7. This corresponds to a weight average molecular weight of 99,000 to 142,000. Lower molecular weight polymer would be preferred from consideration of end

group dyesites. But fiber mechanical properties decline with lower molecular weight polymer. It is another advantage of use of lower molecular weight PAN that higher solid percentage of PAN can be utilized to form a dope with relatively lower viscosity and ease of processing. For consideration of high tenacity/high modulus fibers, higher molecular weight polymers up to intrinsic viscosity 2.3 are sometimes used. The improvement in tensile strength can be attributed to reducing the defect regions with increase in molecular weight (61). The relationship between molecular weight and tenacity of PAN fibers is shown in Table 2.5.1 (61).

Fibers from PAN homopolymers suffer from poor processibility and low dye uptake because of the high degree of ordering and lack of segmental mobility. To overcome these problems, copolymerization of acrylonitrile with a number of comonomers has been adopted (62-66). Most commercial acrylic fibers are now made from PAN copolymers to improve processibility, fiber physical properties and dyeability. Comonomers employed include methyl acrylate, methyl methacrylate and vinyl acetate. Most commercial acrylic fibers incorporate about 5 to 8% of one of these comonomers. The effect of this comonomer is to disrupt the PAN sequence and increase the amorphous fraction. The fraction of the amorphous regions is related to neutral

Table 2.5.1 The relationship between molecular weight and tenacity of PAN fibers (61).

Molecular Weight M_w	Tenacity (cN/tex)
2,280,000	222.0
1,350,000	166.0
530,000	151.9
320,000	126.3
120,000	75.9
70,000	33.0

comonomer content, since the neutral comonomers are located in the amorphous regions. The greater the fraction of comonomer, the larger the amorphous regions will be. Many physical properties of PAN are affected by incorporating the comonomers. Paul (67) reported that the gel melting point of PAN in DMAc was reduced from 130°C to 60°C by incorporation of 9 wt% vinyl acetate. The introduction of comonomer in PAN also improves the solubility, by reducing the molecular order, and hence increasing solvent diffusion (12). In consideration of mechanical properties of PAN fibers, the addition of small amounts of a comonomer greatly enhances the internal mobility of polymer segments, reducing the sequence of acrylonitrile molecules capable of interacting with neighboring sequences (12). The dye diffusion is substantially improved, and the low temperature brittleness is decreased.

2.5.2 Structure formation of PAN fibers during processing

In the wet spinning process, the PAN dope is extruded through spinneret holes into a liquid coagulation bath. The coagulation bath usually consists of the solvent diluted with water as a non-solvent. Fiber formation occurs rapidly as the the polymer dope is extruded into the bath and the filaments are drawn onto the first godet. A diffusional interaction between the fluid filaments and coagulation

bath causes the PAN fibers to solidify. The solvent originally added to the spin dope is diffused out from the filaments into the coagulation bath, while water diffuses into the filaments. The PAN precipitates or solidifies as a consequence of this exchange. The phase transformation or solidification rate depends on the diffusion rate which can be varied by changes in coagulation bath temperature and composition. Paul proposed the "moving boundary" concept of solidification based on the experimental evidence (68). The concept is described as: A solidified layer forms around the filament separated from the fluid core by a sharp phase boundary. As coagulation proceeds, the boundary moves inward until it reaches the center. Paul (68) studied the rate of movement of a boundary associated with coagulation which was varied by the bath composition and temperature. Coagulation rates generally increase as the bath temperature decreases or as solvent content in the bath decreases. Rapid coagulation rates increase skin rigidity. Deformable surface layer allows forming of the round filament cross-section, while tough layer leads to non-circular shapes (69).

The morphology of fiber formed is also influenced by the diffusion rate. Wet spun fibers leaving the coagulation bath have a fibrillar network structure. Characterizations of the network structure have been reported by Craig et al.

(55), by Knudsen (56), and other workers (13,14,70). It was shown that the length of the fibrils between network junctions was markedly affected by coagulation temperature. The fibrils became shorter and more densely packed as the coagulation temperature decreased (56). The fibrillar structure formed during coagulation was carried through the post processing, although the fibrils became oriented and most of the voids were removed after hot drawing and drying (13,56). A reduction in the number of large voids was observed with decreasing coagulation bath temperature (56).

In dry spinning, the PAN dope is extruded through the spinneret holes into a tower containing an inert gas heated above the boiling point of the solvent. Fiber formation occurs as the filaments are drawn through the column and the solvent gradually vaporizes. Fiber formation in dry spinning is attributed to gelation which occurs gradually as the solvent diffuses out and the concentration of polymer in the fiber increases. Most dry spun acrylic fibers have a dogbone shape even though they are spun from a round spinneret hole. It is explained that a tough skin is formed around the periphery of the filament while the core is still swollen with solvent. As the solvent diffuses out through the outer skin, the core structure shrinks and the fiber shape is deformed.

Ziabicki (29) proposed three mechanisms of solvent removal from the filaments as (a) flash vaporization near the spinneret, (b) diffusion of the solvent out of the filaments and (c) convective transfer from the filament surface to the surrounding gas. Experimental studies (71,72) indicated that solvent diffusion within the fiber was the rate controlling factor for solvent removal. The production rate is controlled by filament size, gas temperature, spinning length, mass throughput, take-up speed and permissible residual solvent in the fiber.

Dry spun fibers leaving the column have a homogeneous structure with very little orientation except in the thin skin (55,73). Fiber structure contains solvent not removed in the column. Depending on the processing conditions, the residual solvent is in the range of 1-20%. The dry spun fibers showed a marked change in structure during stretching (55). Craig and et. al. reported (55) that fiber structure after orientation was related to the residual solvent content in the spun fiber. The fiber with 1% residual solvent developed to a fibrillar structure without micropores after stretching. The sample containing 10% residual solvent showed an oriented network with fibrillar structure and micropores similar to that obtained in wet spinning after the stretching process.

2.6 Hollow Fiber

The most often quoted early patent was U.S. Patent 3,422,009, issued to Mclain of Dow Chemical Company in 1969, which described the use of hollow monofilaments in connection with reverse osmosis (74).

Polyethylene hollow fibers having microporosity were produced by Mahoney and Schneider of Dow Chemical Company (75,76). They extruded a heated solution of polyethylene and an ester from an annular spinneret, drew the gelled fiber and then removed the ester. The fibers have particular utility as separatory membranes in artificial lungs.

A hollow fiber of polyacronitrile was produced through the wet spinning process by Hashino et al (77,78). The hollow fiber had water permeability greater than 0.2 ml/cm2-min-atm, which was claimed to be useful as an inexpensive superior ultrafilter.

Boland and Henkel studied nylon 6 hollow filament (79). They found that the hollow filament had higher tenacity, higher molecular orientation and lower elongation at break, compared to the round filament with the same denier which were formed under similar processing conditions.

Hoechst Celanese Corporation recently introduced Trevira Loftguard HV polyester fiberfill, which is the

highest void fraction U.S. made hollow fiber (22% void) manufactured for upholstered furniture (80). Hoechst Celanese states that the new generation hollow fiber offers great loft, resiliency, comfort and durability.

The hollow carbon fiber is particularly of interest to the aircraft industry, because of its light weight and improved impact toughness in fiber reinforced composites. Research on the hollow carbon fiber is currently in progress (81,82). The fiber is melt spun from anisotropic mesophase pitch with a specially designed spinneret. Two types of spinnerets are used: one with a C shaped orifice and another with a tiny jet nozzle situated on the center of the orifice opening. In both cases, the wall thickness of the hollow filament can be varied by changing the filament draw ratio and take-up speed during melt spinning. The tensile strength increases with decreasing wall thickness.

It is anticipated (82) that hollow fiber could be also used as a high temperature filtration medium in the design of nuclear reactors.

2.7 Modeling of the Solution Spinning Process

Vasudevan and Middleman (40) studied momentum, heat and mass transfer to a continuous cylindrical surface in axial motion. The study included the effect of high mass

transfer on drag and heat transfer due to rapid vaporization of the jet. The study was restricted to the laminar boundary layer on a jet of constant velocity, temperature, and concentration along the surface conditions which are not valid for most fiber spinning operations.

Han and Segal (83) carried out mathematical modeling of solution wet-spinning of polyacrylonitrile dope into NaSCN coagulation bath. They assumed that elongational viscosity was only a function of concentration of solvent in the filament. The model predicted velocity and concentration profiles of the wet spinning of acrylic fiber well, although the analysis neglected the effect of the frictional drag of the coagulating medium on the moving filament.

Fok and Griskey (52) investigated mass transfer during dry spinning of poly(methyl methacrylate)-benzene solution by numerical analysis to predict the behavior of average solvent concentration in the fiber. The study considered the radial distribution of solvent in the filament. But the study considered only mass transport, not combined with heat transfer and momentum balance.

Paul (68) did extensive studies on the coagulation of wet-spinning. He proposed several moving boundary models for diffusion during coagulation of wet-spinning process,

such as equal-flux model, constant-flux model and variable-flux ratio model.

The most comprehensive modeling of dry-spinning process of several polymer-solvent systems was published by Ohzawa (32,83) etc. Mass-transfer coefficients for the polymer-solvent systems were derived by the experiment of measuring wet and dry-bulb temperature. The research by Ohzawa etc. was focused on theoretical studies rather than practical prediction of the variation of spinline behaviors and filament properties due to change of processing conditions in the dry spinning process.

CHAPTER III

MATERIALS AND EXPERIMENTAL PROCEDURES

The research is focused on establishing a mathematical model for the dry-spinning process of hollow fiber using polyacrylonitrile (PAN)-dimethylformamide (DMF) solution. The research consists of a theoretical modeling part and an experimental part needed to obtain appropriate input data for the modeling and for comparison of the model predictions with actual experimental results. The PAN-DMF solution was selected as an example material in the modeling, because of its availability and well characterized solution system.

3.1 Materials

The polyacrylonitrile (PAN) for the dry spinning process and the other experiments was provided by Courtald Fiber, which was composed of 94% acrylonitrile and 6% methyl acrylate. The average molecular weight would be determined by measuring its intrinsic viscosity. Polyacrylonitrile has a specific gravity of 1.186.

N,N-dimethylformamide (DMF) was the solvent chosen for dissolving PAN, which was supplied by Aldrich Chemical Co.

DMF has a specific gravity of 0.944 and vapor pressure of 2.7 mm at 20°C.

3.2 Material Characterization

3.2.1 Dilute Solution Viscosity

The limiting viscosity number $[\eta]$ of a solution which is often called the "intrinsic viscosity" is defined as

$$[\eta] = \text{Lim} \frac{\eta - \eta_0}{\eta_0 c} \qquad (3.2.1)$$

in terms of the solvent viscosity η_0, the solution viscosity η, and the solute concentration c. The concentration c is expressed in grams of solute per milliliter of solution. The quantity $[\eta]$ of a polymer solution is a measure of the capacity of a polymer molecule to enhance the viscosity, which depends on the size and the shape of the polymer molecule. Within a given series of polymer homologs, $[\eta]$ increases with the molecular weight M, therefore, it is a measure of M. The well established relation for linear, flexible polymers is the Mark-Houwink equation.

$$[\eta] = KM^a \qquad (3.2.2)$$

where K and a are constants for a given polymer-solvent-temperature system. The value of a varies from 0.5 to 0.8 and becomes 0.5 in a theta solvent. M is the viscosity-average molecular weight. Typically the value of viscosity-average molecular weight is found between the value of weight-average and number-average molecular weight.

The solution viscosity of polyacrylonitrile is determined by viscometer. In the present case Ubbelodhe viscometer was used. The design in the Ubbelodhe is such that the measurement is unaffected by the total volume of the solution over a considerable range. It is therefore useful as a dilute solution viscometer, in which solution having several different concentrations can be prepared and measured in situ.

The measurement of the solution viscosity was carried out using dimethylformamide as the solvent at a temperature of 25°C. The values of the constants K and a are 69.8×10^{-3} (ml/g) and 0.65, respectively (88,89). The inherent viscosity at a specified concentration of 0.5 g/dl was used as an approximation to $[\eta]$. The measured intrinsic viscosity and viscosity-average molecular weight of PAN polymer are given in Table 3.2.1.

Table 3.2.1 Intrinsic viscosity and viscosity-average molecular weight of PAN polymer.

t_o (s)	t (s)	c (g/dl)	t/t_o	$[\eta]$	M_v
84	163.5	0.5	1.95	1.33	111,211

3.2.2 Shear Viscosity

A Kayeness capillary rheometer was used to measure the shear viscosity at different temperatures and solvent concentrations. In the measurement, the polymer fluid was forced from a reservoir through a capillary die, in which temperature, plunger speed, applied force, output rate, and barrel and die dimensions can be controlled and measured accurately. The principle of the measurement, Bagley and Rabinowitsch correction are described in Appendixes A and B.

Concentrated PAN-DMF solution generally shows non-Newtonian shear-thinning behavior of its viscosity. By measuring the viscosity at different shear rates, the shear-thinning viscosity can be characterized over the range of shear rate in the spinning process. The generalized Newtonian fluid models will be used to correlate the experimental results of PAN dope viscosity. Most frequently used rheological models (generalized Newtonian fluid) are the power law, Cross and Carreau models of the viscosity as a function of shear rate (111).

The viscosity of the spinning solution decreases with an increase in temperature. By measuring viscosity at several different temperatures, it is possible to predict a flow curve representing the temperature dependence of the viscosity of the spinning solution using the regression

method. The model of temperature dependence of viscosity is represented by

$$\eta(T) = A\exp(\frac{E}{RT}) \qquad (3.2.3)$$

where A is a coefficient depending on the nature of the fluid, E is the energy of activation for flow, R is the gas constant.

The composition of a material is a determining factor of its viscosity. When this composition is altered, a change in viscosity is quite likely. The addition of solvent to the spinning solution reduces its viscosity. The viscosity of the spinning solution with different amount of solvent was also measured.

The least squares minimization methods were used to determine the best parameters for each viscosity model. Linear function is fit using matrix inversion methods (94). Nonlinear function is fit using the Marquardt method (95).

3.3 Experimental Procedures for Dry Spinning Process

A schematic drawing of the equipment used for the dry spinning process is shown in Figure 3.3.1. The spinning solution was prepared by dissolving PAN polymer in the solvent DMF for two hours to yield a slurry. The slurry was

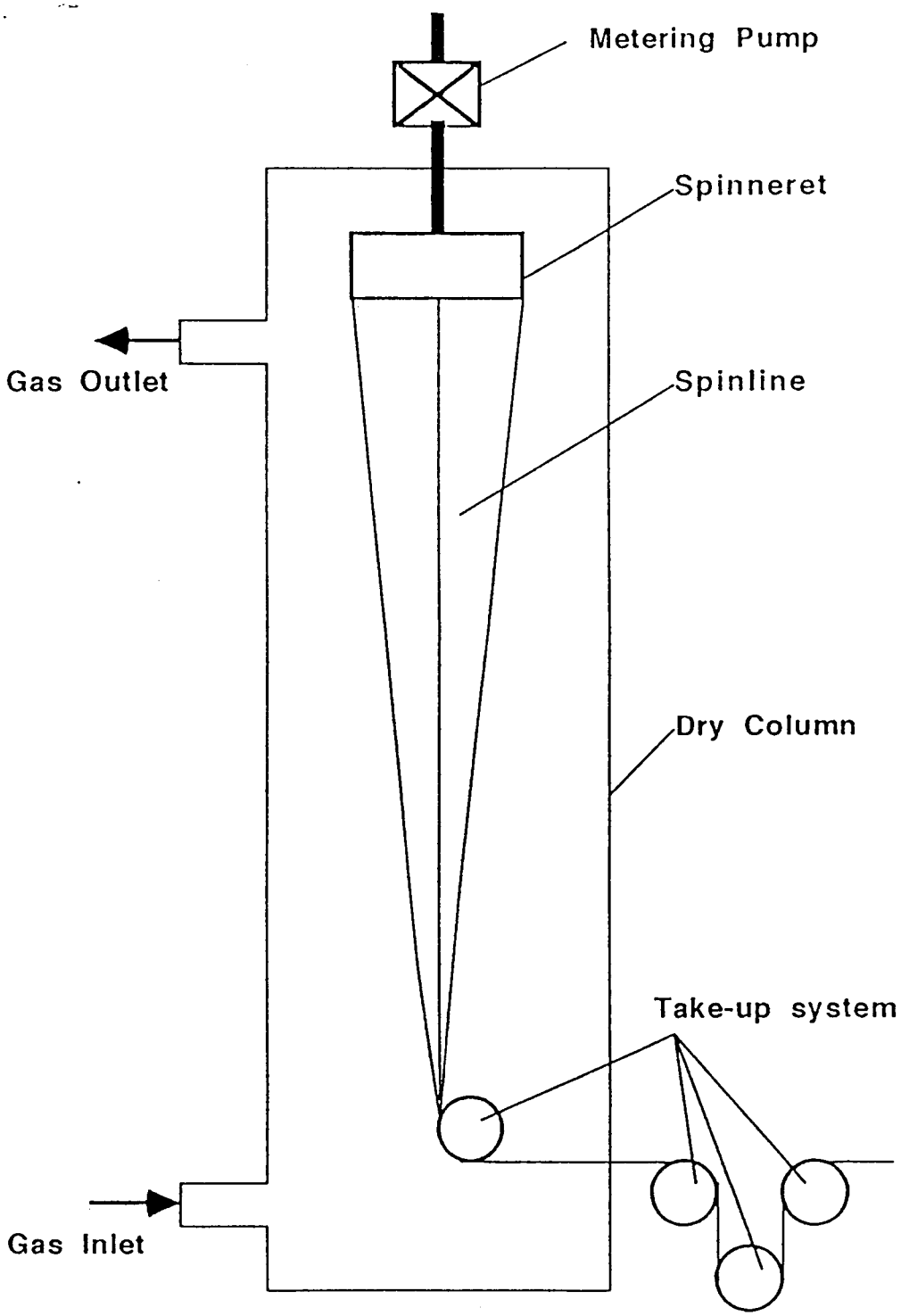

Figure 3.3.1 Schematic showing the dry spinning process.

heated to 95°C over a period of 90 minutes where it was mixed with agitation for two hours. The spinning solution was filtered with an appropriate filtration medium prior to dry spinning in order to remove any residual solid matter which could possibly obstruct the die orifice during the spinning operation. Suitable solution for extrusion should contain 20 to 35 percent PAN polymer by weight. The shear viscosity of the resulting spinning solution was measured by a rheometer. The spinning solution then passed a degassing device, which removed air from the solution. The resulting spinning dope was provided at a temperature of 95°C in a holding tank while under an atmosphere of nitrogen. The solution was fed from the holding tank to the spinneret provided at the top of the dry spinning column using a gear spinning pump.

The extrusion spinneret had one hole with 1600 um in outer diameter and a mandrel of 1200 um. The spinning solution was extruded through annular orifices into an evaporative atmosphere to form dry spun PAN filaments. The extrusion temperature of the spinning solution should be within the range of about 90°C to 150°C, and was generally maintained at about 100°C during the present experiments.

The dry spinning column had a length of about 400 cm. Suitable evaporative atmosphere for the dry spinning zone includes nitrogen, argon, helium, etc. The selected

evaporative gas in this experiment was nitrogen. The evaporative atmosphere was provided at a temperature sufficient to cause a substantial volatilization of the spinning solvent as the spinning solution was extruded. A preheated stream of nitrogen was continuously introduced into the bottom of the dry spinning column and was withdrawn from the top of the dry spinning column together with volatilized solvent. The nitrogen temperature at the jet face was 195°C. The temperature of the nitrogen evaporative atmosphere throughout the dry spinning column ranges from 170°C to 190°C. Wall heaters were provided within the spinning column which aid in maintaining a nearly constant temperature profile along the spinning column.

The resulting as-spun PAN filament was continuously withdrawn from the bottom of the dry spinning column at a speed of 50 to 200 meters per minute. The as-spun filaments contained about 5 to 20 percent residual solvent by weight.

3.4 On-line Measurements

3.4.1 On-line Velocity Measurement

Limited on-line velocity measurements were conducted by using a TSI LaserSpeed system, which employs a technique called Laser Doppler Velocimetry. This technique is a

noncontact method for measuring the speed of a surface as it moves through two laser beams that intersect at an angle. A fringe pattern is formed where the beams intersect due to constructive and destructive interference of the wave fronts of the light. The region where the beams cross is called as the measurement region. When the filament moves through this region, light is scattered. The scattered light is Doppler shifted in an amount proportional to the velocity of the filament.

3.4.2 Take-up Tension Measurement

The tension in the spinline was determined using Digital Fiber Tension Sensor Model 9000 made by American Sahm. The sensor was connected to an 386 PC through a RS232 port. Before on-line measurement, the instrument was calibrated using 100 mg, 200 mg, 500 mg, 1 g, 2 g and 5 g dead weights attached to a PAN filament, respectively. The filament was pulled slowly through the tensiometer head by a variable speed electric motor. A calibration profile was made before on-line measurement.

The tension at the bottom of spinline was measured by carefully inserting the measuring head into the spinline at a position just above the take-up device. 2000 readings were collected by the computer at the measurement position.

The average value of tension was calculated using a statistical program.

3.5 Characterization of As-spun Hollow Filaments

3.5.1 Optical Microscopy

A Nikon Microflex PFX microscope was used to measure the diameter of the spun filament, and hollow area percentage which is the result of void area divided by total cross-section area of the filament. The filament sample for optical microscope examination was prepared by using a microtome according to the method recommended by AATCC Technical Manual (96).

3.5.2 Scanning Electron Microscopy

A Amray-1000 Scanning Electron Microscope (SEM) was used to examine the cross section of the filament and the structure of filaments. The filament sample was cut in liquid nitrogen (cryofracture). The sample was coated with 10 nm of AuPd alloy (60%:40%) using a Anatech Hummer VII at 50% power. The detailed principles and operation of SEM are discussed in reference (97).

3.5.3 Solvent Residue Content in As-spun Hollow Filament

The solvent residue content in as-spun hollow filament was measured by using a gravimetrical method. The detailed procedure is described as follows:

Place about 5-10 grams of the hollow filament to be tested in a previous tared weight bottle and immediately replace the cover. Weight to the 0.1 mg using a Mettler analytical balance and record the weight. Place the uncovered weight bottle containing the specimen in the vacuum oven maintained at 105 to 110°C for about 4 hours. At the end of the time period, remove the bottle from the oven, immediately replace the cover and put it in the desiccator. When the bottle and contents have cooled to room temperature, remove them from the desiccator and reweigh. Repeat the heating and reweighing process for periods of 30 minutes until the weight is constant to within +/- 0.001 g and record the constant weight.

Calculate the solvent residue content of the specimen as follows:

$$S(\%) = \frac{A - B}{A - TA} x100 \qquad (3.5.1)$$

where S(%) is solvent residue content, A is the weight of sample before drying and bottle, B is the weight of sample

after drying and bottle, TA is tare weight of weighting bottle.

CHAPTER IV

EXPERIMENTAL RESULTS

4.1 Non-Newtonian Viscosity of Spinning Dope

The power law model (90, 91) was proposed based on the observation that the logarithm of viscosity plotted as a function of the logarithm of shear rate exhibits linear behavior for many polymer melts. Thus

$$\eta = A\dot{\gamma}^{n} \tag{4.1.1}$$

where η is shear viscosity, $\dot{\gamma}$ is shear rate, n is a power law index and A is a constant.

The Cross model (92) is able to predict the zero-shear viscosity of polymer fluid. The Cross model of the viscosity is given as follows:

$$\eta = \frac{\eta_0}{1 + \left(\frac{\eta_0 \dot{\gamma}}{\tau^*}\right)^{1-n}} \tag{4.1.2}$$

where η_0 is zero-shear viscosity, τ^* is critical stress related to the transition between the Newtonian and shear-thinning regimes.

The most widely used expression relating viscosity of a Newtonian fluid to temperature is the Arrhenius equation:

$$\mu = A\exp(E/T) \qquad (4.1.3)$$

where E is the energy of activation for flow and A is a constant depending on the nature of the fluid. The values of E and A can be determined experimentally.

The dependence of the viscosity on concentration of the polymer in the dope can be expressed as:

$$\mu = A'c^{m} \qquad (4.1.4)$$

where c is the concentration of the polymer in the dope, A' and m are constants which are determined by experiment. Combining equations 4.1.3 and 4.1.4, the following equation is obtained.

$$\mu = A'c^{m}\exp(E/T) \qquad (4.1.5)$$

By building both shear rate and temperature variables into the viscosity models, the following equations are obtained:

Power Law Model:

$$\eta = A\gamma^{n}\exp(\frac{E}{RT}) \qquad (4.1.6)$$

Cross Model:

$$\eta = \frac{''_{0}}{1+\left(\frac{\eta_0\gamma}{\tau^*}\right)^{1-n}}$$

$$\eta_0 = A\exp(\frac{E}{RT}) \qquad (4.1.7)$$

where μ_0 is the zero-shear viscosity, γ is the shear rate, τ^* is the critical stress, n is slope index, E is the activation energy for flow, A and B are coefficients.

The parameters in the rheological models can be obtained from the rheological measurements made over a wide range of shear rates and temperatures.

The polyacrylonitrile dopes with three different concentrations were prepared: 20% PAN/80% DMF, 25% PAN/75% DMF and 30% PAN/70% DMF, respectively. The rheological testing of the above PAN dopes were carried out at temperatures of 30°C, 50°C and 100°C by using a Kayness Capillary Rheometer. The range of shear rates were about 8.0 to $8.0\text{x}10^3$ 1/second.

The experimental data of the apparent viscosities at different shear rates were obtained. The Power law model and modified Cross model were used to fit experimental

viscosity as a function of shear rate and temperature at fixed concentration.

Figures 4.1.1, 4.1.2 and 4.1.3 present the fitting results for the viscosities of the PAN dopes at the concentrations of 20%, 25% and 30% by using the Power law model.

The discrepancy between the model and the experimental data is quantified by either Reduced Chi Squared (RCS) or Root Mean Square Deviation (RMS).

$$RCS = \frac{\Sigma\, Wt\,(Y_{fit} - Y_{data})^2}{DOF} \qquad (4.1.8)$$

$$RMS = \sqrt{\frac{\Sigma(\frac{Y_{fit} - Y_{data}}{Y_{data}})^2}{DOF}} \qquad (4.1.9)$$

where Y_{fit} is the fitted viscosity calculated from the current model and its associated coefficients. The temperature and shear rate of the associated Ydata points are used in the calculation. Y_{data} is the actual viscosity

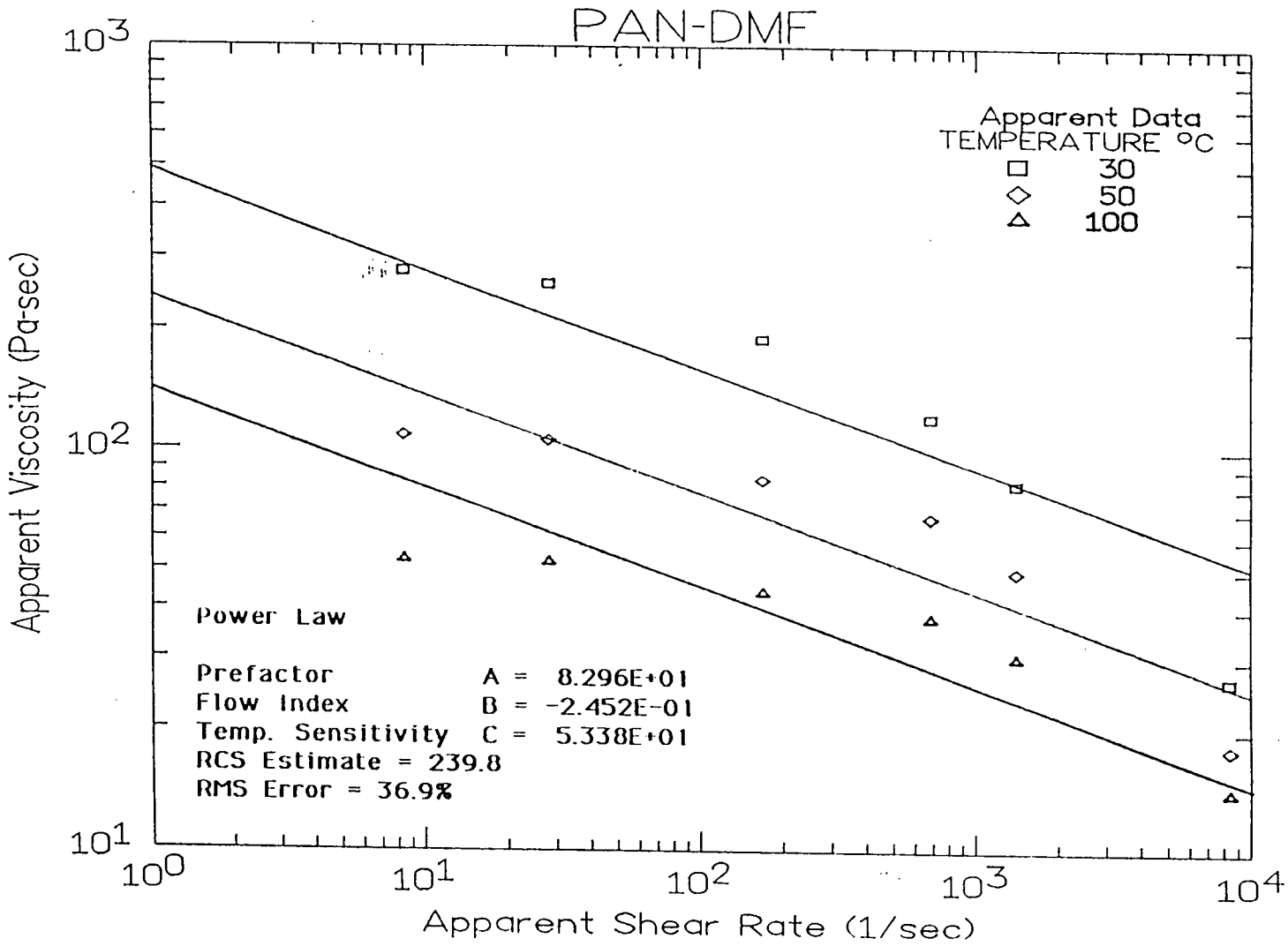

Figure 4.1.1 **Viscosity of 20% PAN dope at temperature of 30, 50 and 100°C vs. Power law model.**

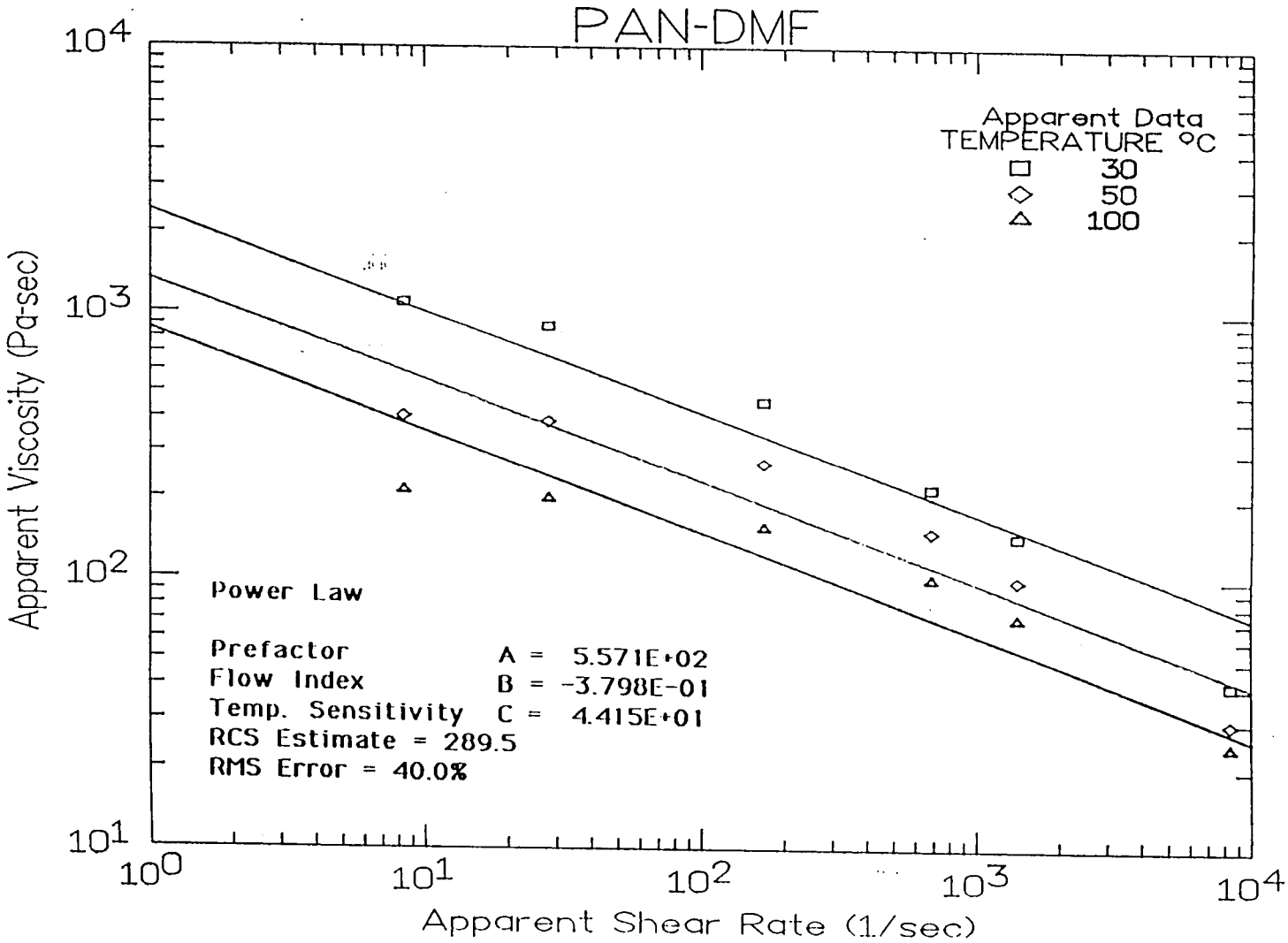

Figure 4.1.2 **Viscosity of 25% PAN dope at temperature of 30, 50 and 100°C vs. Power law model.**

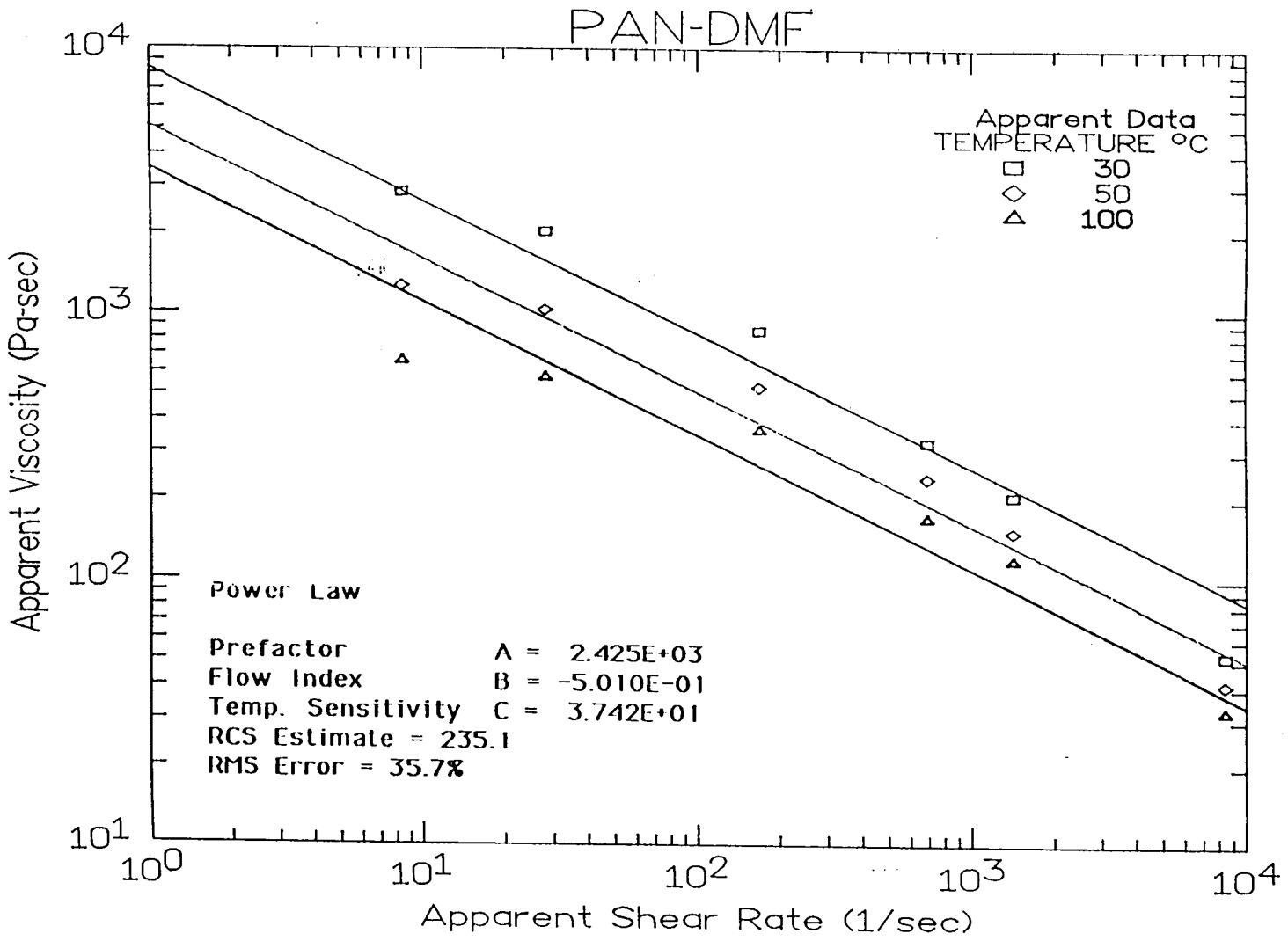

Figure 4.1.3 Viscosity of 30% PAN dope at temperature of 30, 50 and 100°C vs. Power law model.

collected from the rheometer. Wt is the weighting for each Ydata point. DOF is the degree of freedom of the fit (DOF = number of data points - number of fitted parameters).

The total fitted errors result from three sources:

1. The experimental data has random error. Since RCS is a ratio of the total error in the fit to the random error associated with the data, a value of 1.0 indicates the model has fit the experimental data as well as can be expected.

2. The fitting model inadequately represents the experimental data. RCS value close to 1.0 indicates the error contribution resulting from inadequate model is small.

3. If the rheometer is calibrated incorrectly, then no matter how good the fit appears, the estimated parameters for the model will be wrong because they are based on incorrect information.

The RCS values for fitting experimental viscosity data by Power law model are very large, which indicates that Power law model inadequately correlates the experimental viscosity data. The large deviation results from the poor fitting in the range of lower shear rates.

Figures 4.1.4, 4.1.5 and 4.1.6 show the fitting results for the viscosities of the PAN dopes at concentration of 20%, 25% and 30% by using the Modified

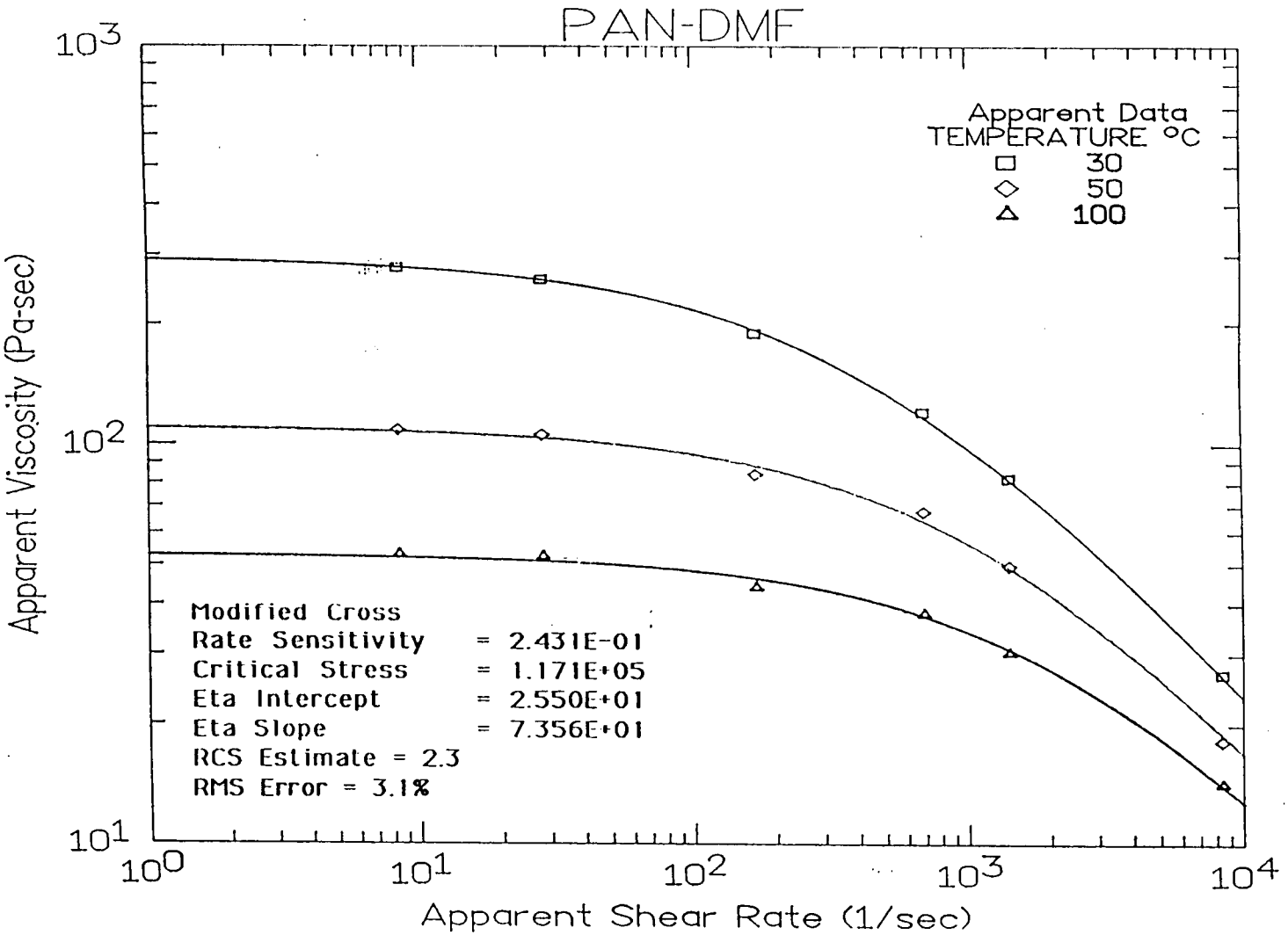

Figure 4.1.4 Viscosity of 20% PAN dope at temperature of 30, 50 and 100°C vs. Modified Cross model.

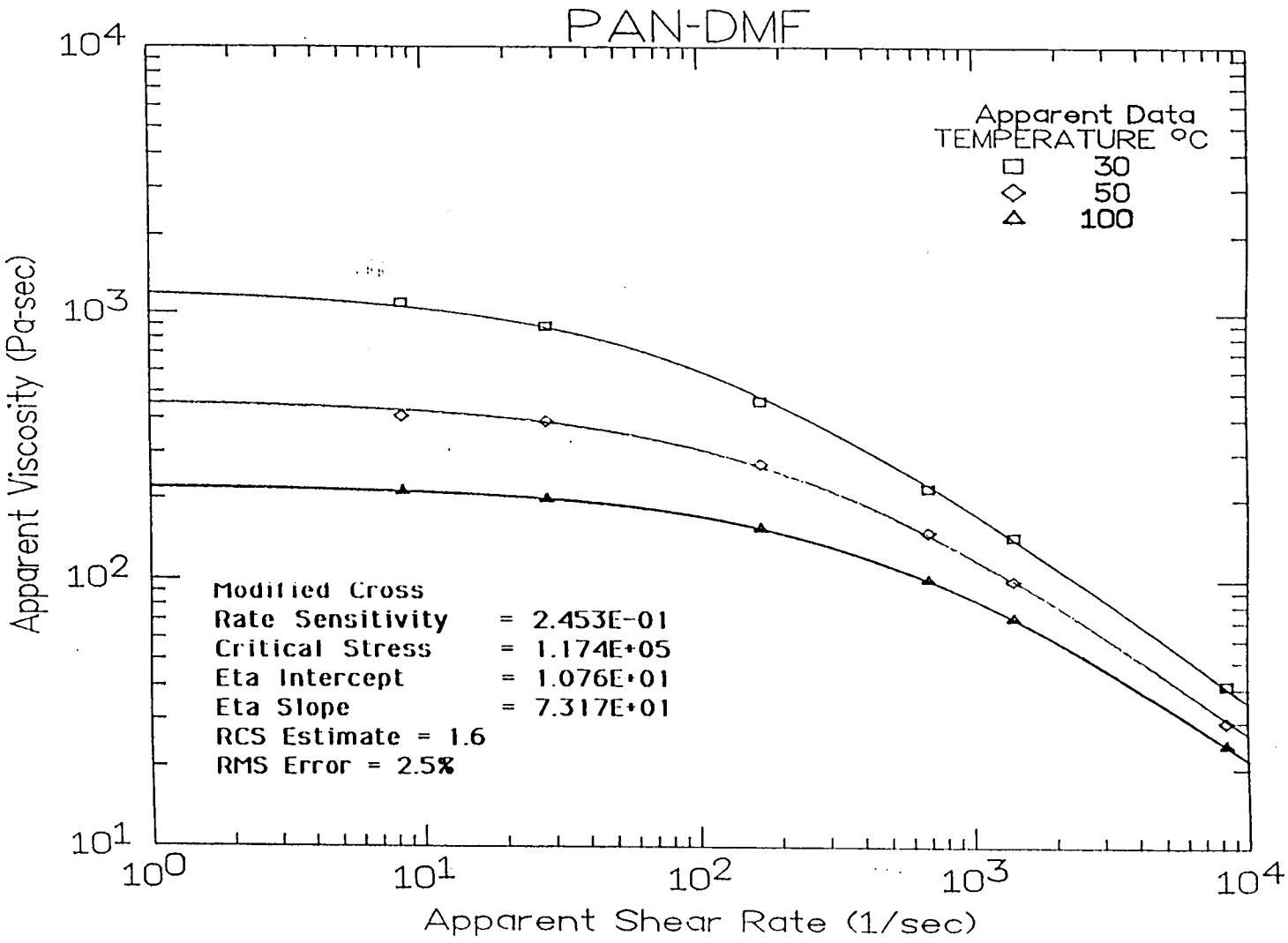

Figure 4.1.5 **Viscosity of 25% PAN dope at temperature of 30, 50 and 100°C vs. Modified Cross model.**

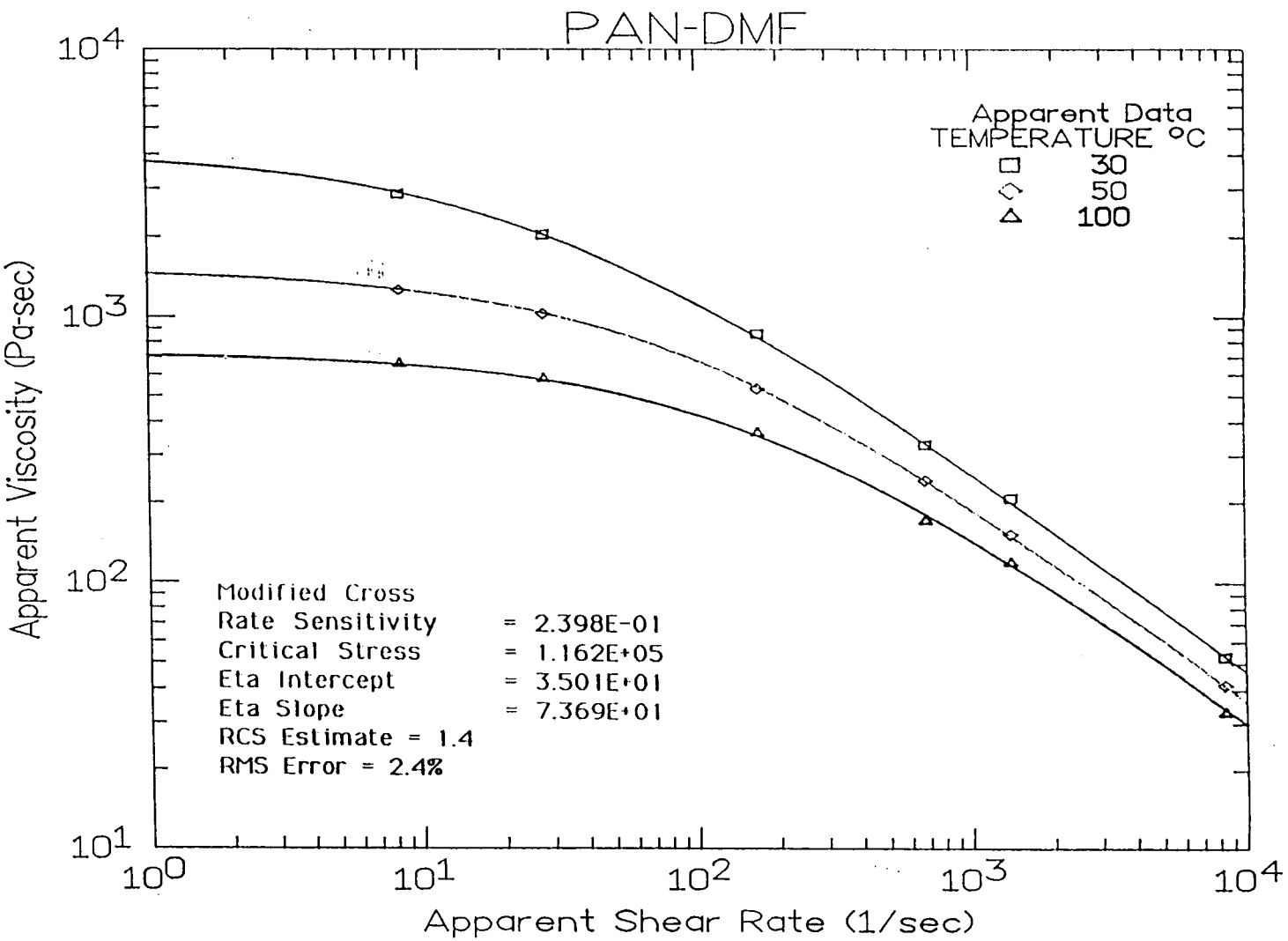

Figure 4.1.6 **Viscosity of 30% PAN dope at temperature of 30, 50 and 100°C vs. Modified Cross model.**

Cross model. The complete fitting results are listed in Table 4.1.1. The RCS values are much smaller compared to that by using the Power law model, which indicates the Modified Cross model describes the viscosity behavior of the PAN dopes very well.

The power law model predicted the viscosity at high shear rates well, but it overestimated the viscosity in the low rate range. The Cross model predicts the viscosity the same as the power law at high shear rates, but also predicts a zero shear viscosity at low shear rate.

The range of values for a fitted model parameter (n, τ^*, A, or E) in Table 4.1.1 indicates the deviation in that parameter necessary to produce an increase in RCS of 1.0 (an increase equal to the random error of the data) while all other parameters are optimized for minimum RCS. This shows the range of values that a parameter can have and still lie within the random error of the data.

The fitted parameters of n (slope index), τ^* (critical stress) and E (activation energy for flow) show their independence on polymer concentration in the dope. As expected, the parameter A varies with polymer concentration in the dope. Thus the following model is proposed:

Table 4.1.1 The complete fitting results by using Modified Cross model.

20% PAN/80% DMF Dope

n = 2.43×10^{-1}	+/- 1.00×10^{-3}	(2.33×10^{-1}, 2.53×10^{-1})
τ^*= 1.17×10^{5}	+/- 3.48×10^{3}	(1.14×10^{5}, 1.20×10^{5})
A = 2.55×10	+/- 4.03×10^{-1}	(2.51×10, 2.59×10)
E = 7.36×10	+/- 6.69×10^{-1}	(7.29×10, 7.43×10)

RCS = 2.35
RMS = 3.06%

25% PAN/75% DMF Dope

n = 2.45×10^{-1}	+/- 6.73×10^{-3}	(2.38×10^{-1}, 2.52×10^{-1})
τ^*= 1.17×10^{5}	+/- 3.40×10^{3}	(1.14×10^{5}, 1.20×10^{5})
A = 1.08×10^{2}	+/- 1.97	(1.06×10^{2}, 1.10×10^{2})
E = 7.32×10	+/- 7.92×10^{-1}	(7.24×10, 7.40×10)

RCS = 1.59
RMS = 2.52%

30% PAN/70% DMF Dope

n = 2.40×10^{-1}	+/- 5.22×10^{-3}	(2.35×10^{-1}, 2.45×10^{-1})
τ^*= 1.16×10^{5}	+/- 3.42×10^{3}	(1.13×10^{5}, 1.19×10^{5})
A = 3.50×10^{2}	+/- 7.62	(3.42×10^{2}, 3.58×10^{2})
E = 7.37×10	+/- 9.38×10^{-1}	(7.28×10, 7.46×10)

RCS = 1.42
RMS = 2.38%

$$\mu = \frac{\mu_0}{1 + (\frac{\mu_0 \dot{\gamma}}{\tau^*})^{1-n}}$$

$$\mu_0 = A \exp(\frac{E}{T})$$

$$A = A' C^m \qquad \text{or } \ln A = \ln A' + m \ln C \qquad (4.1.10)$$

where C is the polymer concentration in the dope, A' and m are the coefficients which can be derived from the experimental data.

Figure 4.1.7 presents log-log plot of A vs. C (polymer concentration), from which the parameters A' and m are obtained.

In summary, the following viscosity equation is derived based on the Modified Cross Model:

$$\mu = \frac{\mu_0}{1 + (\frac{\mu_0 \dot{\gamma}}{1.17 \times 10^5})^{0.758}}$$

$$\mu_0 = A \exp(\frac{73.5}{T})$$

$$A = 8.36 \times 10^5 C^{6.46} \qquad (4.1.11)$$

4.2 Experiments of Dry Spinning of Hollow Filaments

A total eight runs of dry spinning experiments (D-H-1 to D-H-8) were carried out. Table 4.2.1 lists the

$\log A = \log A' + m \log C$, $A' = 8.36 \times 10$, $m = 6.46$

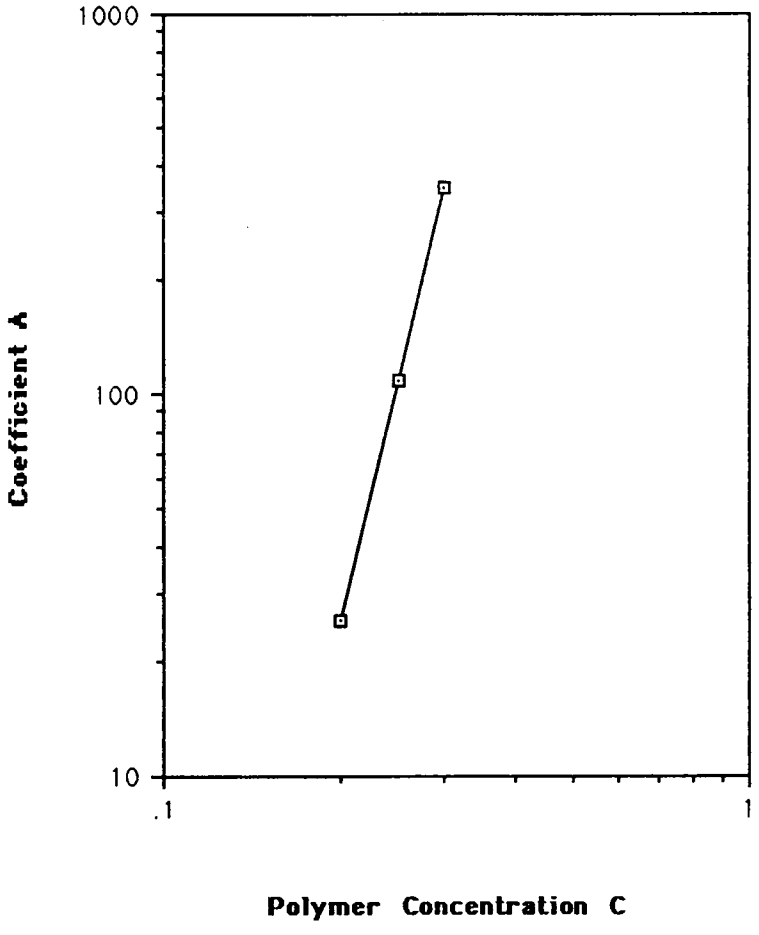

Figure 4.1.7 Log-log plot of coefficient A vs. polymer concentration C.

Table 4.2.1 Process conditions for dry spinning of hollow filaments.

Process Variable	D-H-1	D-H-2	D-H-3	D-H-4	D-H-5	D-H-6	D-H-7	D-H-8
Spinneret Temperature (C)	100	100	100	100	100	100	100	100
Quench Air Temperature (C)	180	180	180	180	180	180	180	180
Quench Air Velocity (cm/s)	10	10	10	10	10	10	10	10
Inner Pressure (dynes/cm2)	500	500	500	500	500	500	250	250
Mass Throughput (g/min)	0.5	0.5	0.5	0.5	1	1	0.5	0.5
Polymer Concentration (%)	30	30	35	35	30	30	30	30
Take-up Speed (m/min)	90	120	90	120	90	120	90	120
Spinline Length (cm)	400	400	400	400	400	400	400	400

processing conditions for the eight runs. The experiments were designed to vary several important processing parameters such as polymer concentration in the dope, take-up velocity, mass throughput and inner pressure. The remaining processing parameters were fixed for all eight runs.

4.3 Results of On-line Measurements

4.3.1 Velocity Profiles

The limited data of velocity at several positions on the spinline were collected by using a TSI LaserSpeed system through the window of the spin column. The velocity of the filament on the spinline was measured at distances of 20 cm, 30 cm and 40 cm from the spinneret.

Figure 4.3.1 presents the measured on-line velocity profiles for D-H-1, D-H-3 and D-H-5. These three dry spinning experiments were carried out at the same take-up speed, 90 meters per minute, but with varying PAN concentration (30% and 35%) in the spinning dope and mass throughput (0.5 g/min and 1.0 g/min).

The velocity profiles show that the velocity acceleration is faster for D-H-1 than D-H-3 when compared at the same take-up speed and mass throughput, but different PAN concentration in the dope. This comparison

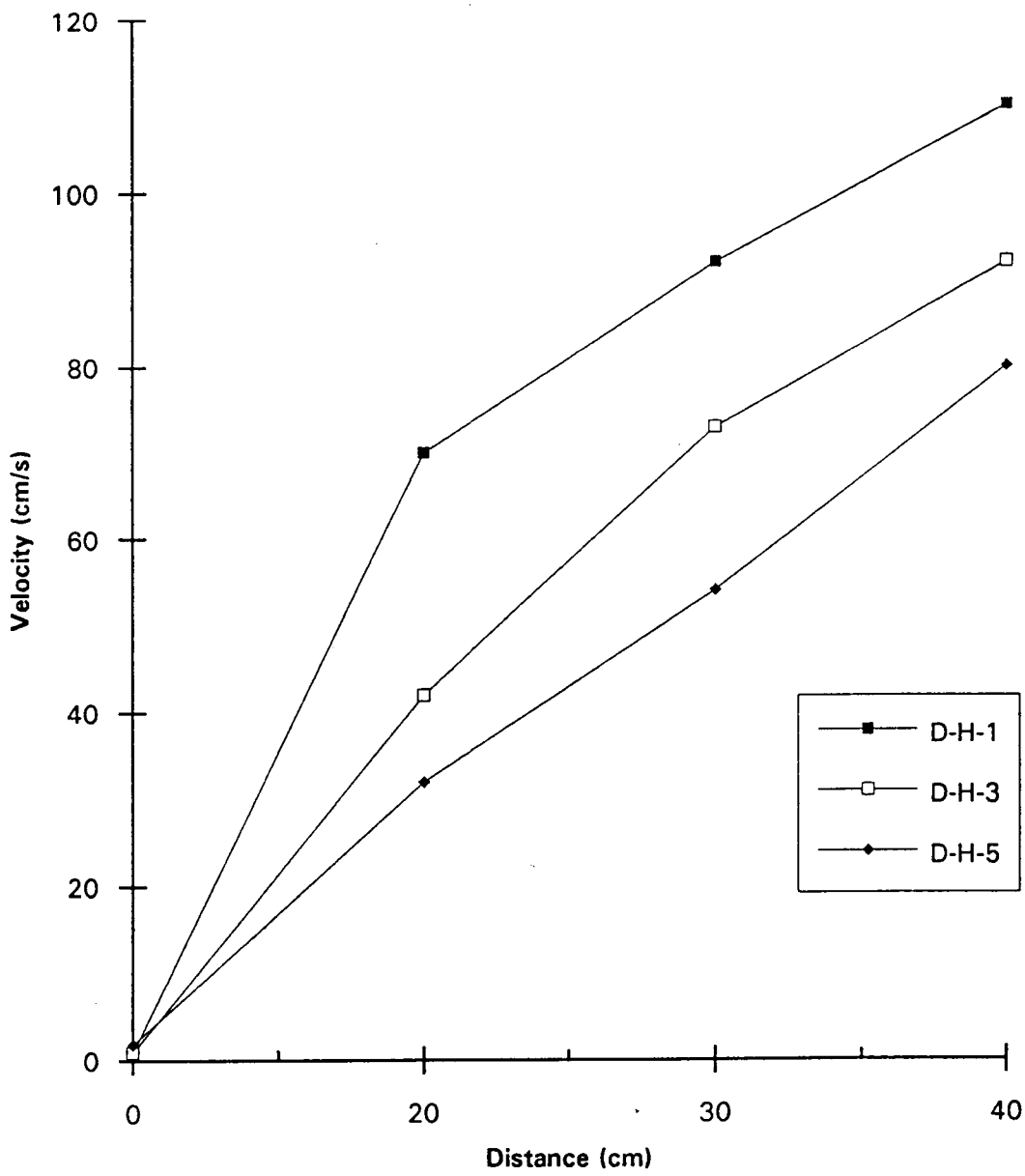

Figure 4.3.1 On-line measured velocity profiles (D-H-1: 30% PAN, 0.5 g/min; D-H-3: 35% PAN, 0.5 g/min; D-H-5: 30% PAN, 1.0 g/min) varying polymer concentration and mass throughput, but fixed take-up speed of 90 m/min.

indicates that the filament on the spinline of 30% PAN dope is more easily deformed due its lower viscosity.

Both D-H-1 and D-H-5 used 30% PAN dope for dry spinning. The velocity acceleration is substantially faster for D-H-1 than for D-H-5 at the same take-up speed, but different mass throughput. Increasing mass throughput slows down the development of velocity on the spinline due to the fact that the ratio of draw down on the spinline decreases with increasing mass throughput, when spun at the same take-up speed.

Figure 4.3.2 presents the measured on-line velocity profiles for D-H-2, D-H-4 and D-H-6, which were spun at the take-up speed of 120 meter per minute, with varying PAN concentration (30% and 35%) and mass throughput (0.5 g/min and 1 g/min). The similar behaviors on the spinline were observed with regard to the effect of PAN concentration and mass throughput on velocity profiles.

4.3.2 Spinline Tension at Take-up

The spinline force was measured at a position close to take-up for each run by using a tensiometer.

Table 4.3.1 shows the measured spinline tensions at the take-up for the six cases. The results indicate that 1) the take-up tension increases with increasing take-up speed; 2) the take-up tension decreases with decreasing PAN

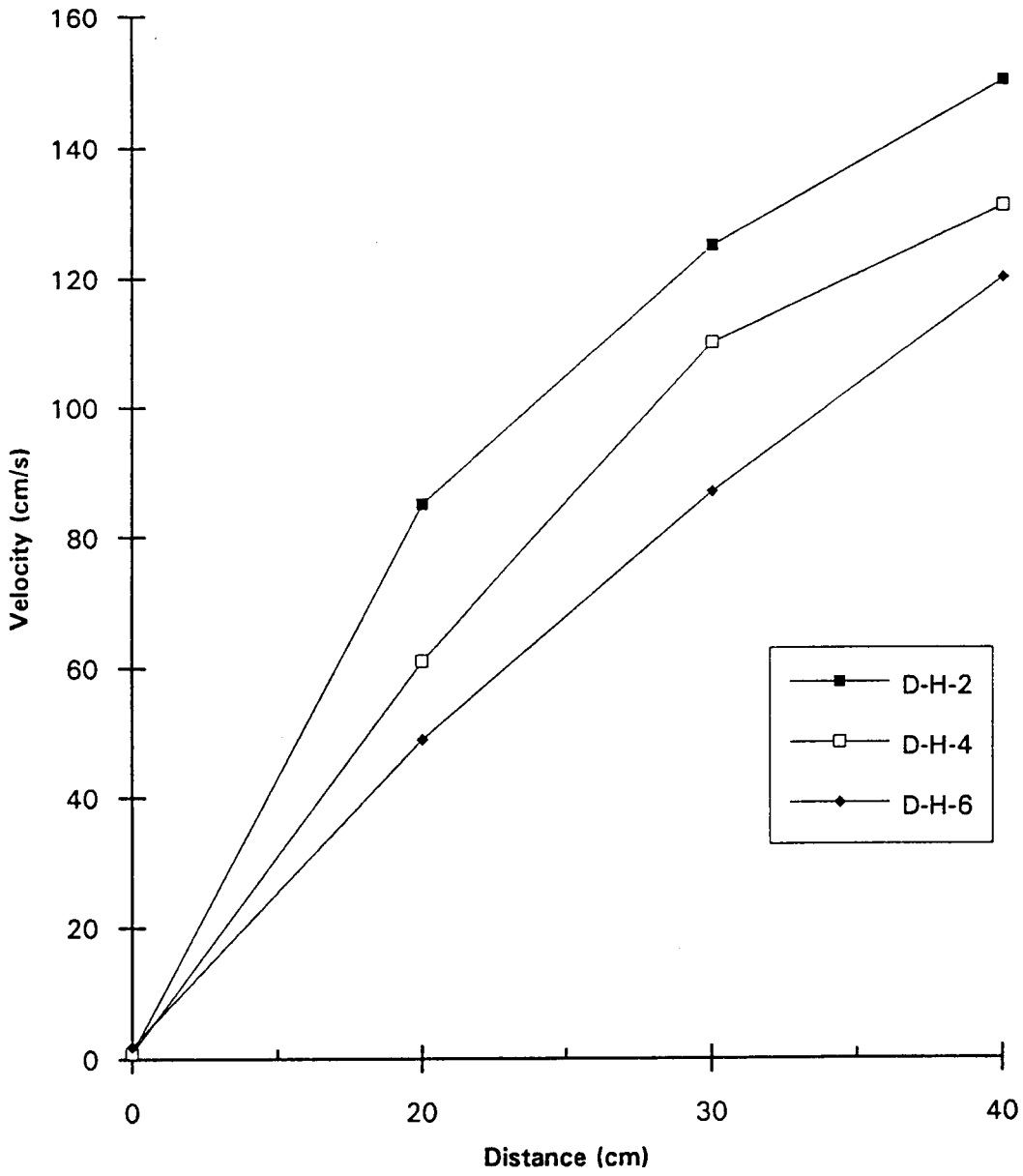

Figure 4.3.2 On-line measured velocity profiles (D-H-1: 30% PAN, 0.5 g/min; D-H-3: 35% PAN, 0.5 g/min; D-H-5: 30% PAN, 1.0 g/min) varying polymer concentration and mass throughput, but fixed take-up speed of 120 m/min.

Table 4.3.1 Measured take-up tension for dry spinning of hollow filaments.

Process Variable	D-H-1	D-H-2	D-H-3	D-H-4	D-H-5	D-H-6	D-H-7	D-H-8
Inner Pressure (dynes/cm2)	500	500	500	500	500	500	250	250
Mass Throughput (g/min)	0.5	0.5	0.5	0.5	1.0	1.0	0.5	0.5
Polymer Concentration (%)	30	30	35	35	30	30	30	30
Take-up Speed (m/min)	90	120	90	120	90	120	90	120
Measured Spinline Tension at Take-up (dynes)	107.2	131.8	270.9	298.3	79.1	110.4	103.7	125.1

concentration because of lowering viscosity of the dope; 3) the take-up tension deceases with increasing mass throughput when spun at the same take-up speed.

4.4 Results of Off-line Measurements

4.4.1 Outer and Inner Diameters of As-spun Hollow Filaments

The outer and inner diameters of as-spun hollow filament were measured by using a Nikon Microflex light microscope. The cross-section of the hollow filament was prepared using a microtome. Some samples were also examined under an Amray-1000 Scanning Electron Microscope (SEM). The detailed methods for preparing the sample are described in Chapter III.

Figure 4.4.1 and Figure 4.4.2 show photographs of the cross section of a hollow filament by light microscope and scanning electron microscope, respectively.

Table 4.4.1 presents measured outer and inner diameters of hollow filaments spun under the conditions described in Table 4.2.1 (page 73). The ratio of inner diameter over outer diameter (ID/OD) is calculated. The hollow area percentage is the result of void area divided by total cross section area of the filament.

The increase of take-up speed decreases both outer and inner diameter of hollow filament, when spun at the same

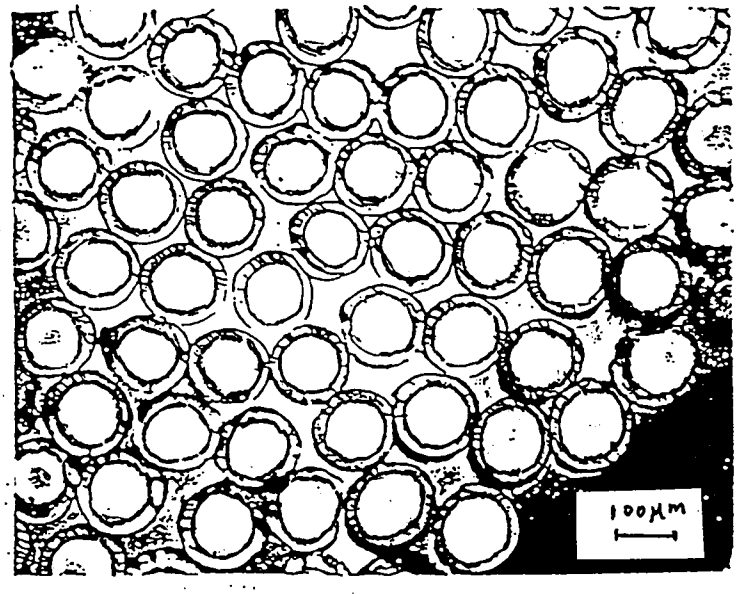

Figure 4.4.1 Light microscopic photograph of PAN hollow filament.

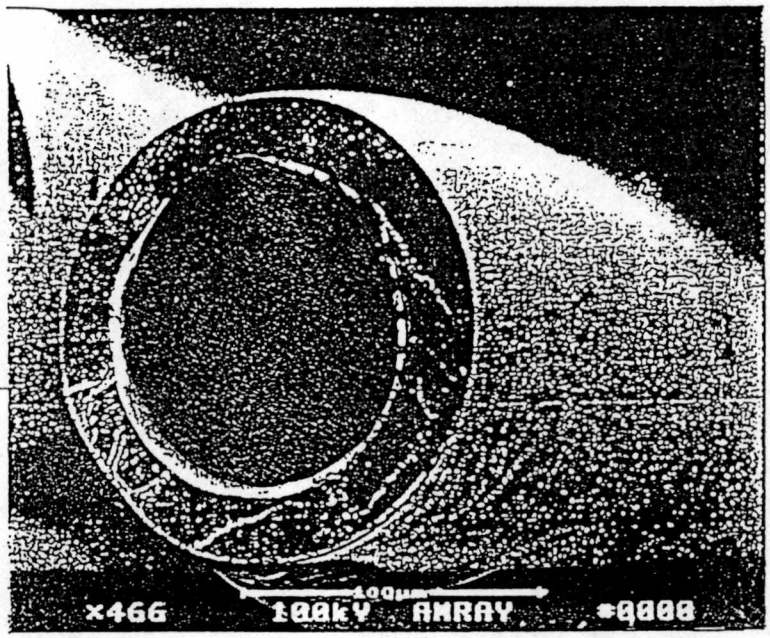

Figure 4.4.2 SEM photograph of a PAN hollow filament.

Table 4.4.1 Properties of as-spun hollow filaments from dry spinning experiments.

Process Variable	D-H-1	D-H-2	D-H-3	D-H-4	D-H-5	D-H-6	D-H-7	D-H-8
Inner Pressure (dynes/cm2)	500	500	500	500	500	500	250	250
Mass Throughput (g/min)	0.5	0.5	0.5	0.5	1.0	1.0	0.5	0.5
Polymer Concentration (%)	30	30	35	35	30	30	30	30
Take-up Speed (m/min)	90	120	90	120	90	120	90	120
Outer Diameter (um)	141.2	121.5	132.3	114.7	199.2	172.4	134.1	115.1
Inner Diameter (um)	110.5	95.2	98.2	84.8	156.3	134.6	100.6	86.4
Wall Thickness (um)	15.4	13.2	17.1	15.0	21.5	18.9	16.8	14.4
ID/OD	0.78	0.78	0.74	0.74	0.78	0.78	0.75	0.75
Hollow Area (%)	61.2	61.3	55.1	54.7	61.2	61.0	56.3	56.3
Solvent Residue (%)	9.1	8.8	8.8	8.6	19.5	19.1	9.1	8.9

process conditions except take-up speed. The ID/OD ratio does not change with increasing take-up speed from 90 meters/minute to 120 meters/minute.

The change of PAN polymer concentration in the spinning dope has a major impact on outer and inner diameters of the hollow filament. Both outer and inner diameters of the hollow filament increase with decreasing PAN polymer concentration in the spinning dope, when the other process conditions were fixed. Furthermore, the ID/OD ratio is higher with 30% PAN than 35% PAN in spinning dope.

The change of mass throughput from 0.5 to 1.0 gram/minute increases the overall outer and inner diameters of the hollow filament significantly, when compared at the same take-up speed.

Reducing inner pressure from 500 to 250 dynes/cm2 decreases both outer and inner diameters, but increases wall thickness of hollow filament. Furthermore, the ratio of ID/OD decreases with reducing inner pressure.

4.4.2 Solvent Residue in As-spun Hollow Filament

The solvent residue in as-spun hollow filament was measured by a gravimetric method as described in Chapter III. The weight percentage of solvent residue in the filament is calculated and given in Table 4.4.1 (page 82).

The solvent residue in as-spun hollow filament decreases slightly with increase of PAN polymer concentration from 30% to 35%. It is also observed that the solvent residue decrease slightly with increasing take-up speed from 90 to 120 meter/minute. This observation further proves the fact that solvent diffusion within the filament is the rate controlling factor for solvent removal during dry spinning, which was also observed by previous investigators (71, 72).

The mass throughput has significant effect on solvent residue in as-spun hollow filament. The solvent residue in the filament rises from 8.5% to 19% with increasing mass throughput from 0.5 to 1 gram/minute.

CHAPTER V

DEVELOPMENT OF THE MATHEMATICAL MODEL FOR DRY SPINNING OF HOLLOW FILAMENT

Compared to the melt spinning process, the modelling of solution spinning processes has been less extensively studied because it is a more complex system with which to deal either experimentally or theoretically. However, a deep understanding of solution spinning processing is important not only practically but also theoretically. A successful model can provide quantitative predictions to evaluate the process, to test design ideas and to reduce the need for experiments.

Formation of the model involves establishing a set of differential equations which represent the process according to physical laws. A set of parameters has to be provided in order to solve these differential equations, which includes rheological, thermal and physical parameters. The formulation of fundamental equations in this study includes the equations of continuity, motion and energy as well as models of material behavior, boundary conditions, assumptions and simplification.

Hollow fiber extrusion using an air injected mandrel spinneret is a more complicated process than conventional

fiber spinning. Several types of mathematical modeling of force balances in hollow fiber spinning are described here. First, the circumferential and axial stress equations are derived by considering hollow filament as a thick walled cylinder through Newtonian fluid mechanics (in traditional solid mechanics, it is called "Thick Wall Theory"; no prior literature was found on modeling of hollow fiber spinning by this concept). Second, the hoop and axial stress equations are derived by considering hollow filament as a thin walled cylinder ("Thin Wall Theory" in solid mechanics and "Membrane Theory" in fluid mechanics, e.g. in Pearson and Petrie's equation for blown film process (101-105)) as an asymptote.

5.1 Hollow Filament as A Thick-Walled Cylinder

A mathematical model is developed in this section, which treats hollow filament as a thick walled cylinder having inner radius R_i, outer radius R_0, internal pressure ΔP and axial stress σ_{zz}.

The force balance equations are derived based on the following assumptions:

1. A Modified Cross model is used to describe the rheological behavior of the fluid. Radial variation is avoided by using the average radial concentration to establish the viscosity.

2. Axial velocity u_z is a function of the spinline distance z only.

3. Axial stress σ_{zz} is a function of the spinline distance z only.

4. Hoop stress $\sigma_{\theta\theta}$ varies across the radius. The maximum hoop stress happens on the inner surface of the hollow fiber, while the minimum hoop stress happens on the outer surface of the hollow fiber.

5.1.1 Kinematics

The cylindrical coordinates system (r,θ,z) used in the analysis is shown in Figure 5.1.1. The deformation rate tensor for describing hollow fiber spinning is present as follows:

$$\Delta = \begin{bmatrix} \Delta_{rr} & 0 & 0 \\ 0 & \Delta_{\theta\theta} & 0 \\ 0 & 0 & \Delta_{zz} \end{bmatrix} \qquad (5.1.1)$$

where

$$\Delta_{rr} = 2\frac{du_r}{dr} \qquad (5.1.2)$$

$$\Delta_{\theta\theta} = 2\frac{u_r}{r} \qquad (5.1.3)$$

$$\Delta_{zz} = 2\frac{du_z}{dz} \qquad (5.1.4)$$

Assuming that the deformation is in cylindrical symmetry, then $\frac{du_\theta}{d\theta} = 0$. From the continuity equation, we have

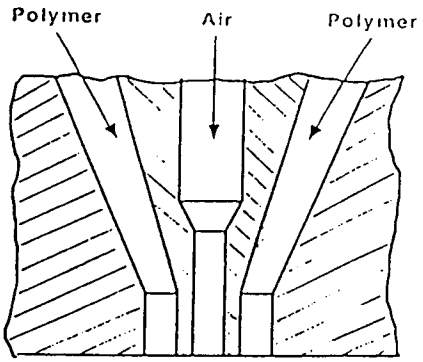

Cross Section of Spinneret for the Production of Hollow Filaments

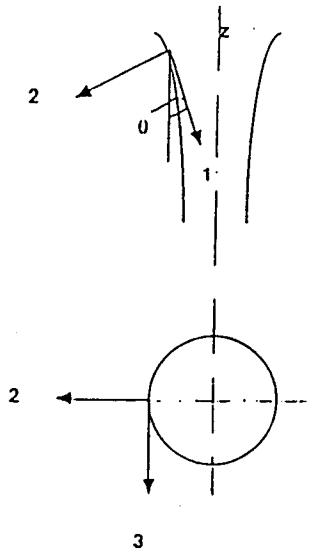

Cylindrical Coordinates

Figure 5.1.1 Cylindrical coordinate system for hollow filament extrusion.

$$\frac{1}{r}\frac{\partial}{\partial r}(ru_r) + \frac{\partial}{\partial z}(u_z) = 0 \qquad (5.1.5)$$

If we further assume $u_z = u_z(z)$ only, then

$$\frac{d}{dr}(ru_r) = -r\frac{d}{dz}(u_z)$$

and

$$u_r = -\frac{1}{2}r\frac{du_z}{dz} + \frac{A}{r} \qquad (5.1.6)$$

where A is a constant which will be determined by the boundary conditions later. Substituting Eq.(5.1.6) into Eqs.(5.1.2) and (5.1.3) , the three components of deformation rate tensor are derived as follows:

$$\Delta_{rr} = -\frac{du_z}{dz} - \frac{2A}{r^2} \qquad (5.1.7)$$

$$\Delta_{\theta\theta} = -\frac{du_z}{dz} + \frac{2A}{r^2} \qquad (5.1.8)$$

$$\Delta_{zz} = 2\frac{du_z}{dz} \qquad (5.1.9)$$

5.1.2 Equations of Circumferential and Axial Stress

Assuming Newtonian fluid in the system, the viscous forces σ_{ij} are related to the deformation rate Δ_{ij} as the following equation:

$$\sigma_{ij} = -p + \mu\Delta_{ij} \qquad (5.1.10)$$

where p is hydrostatic pressure and μ is Newtonian shear viscosity. The following boundary conditions are assumed at the inner and outer surface of the hollow fiber:

$$\sigma_{rr} = -\Delta P, \quad \text{when } r = R_i \text{ (at inner surface)}$$
$$\sigma_{rr} = 0, \quad \text{when } r = R_0 \text{ (at outer surface)} \qquad (5.1.11)$$

where R_i and R_0 are inner and outer radius of hollow filament. ΔP is the internal gas pressure input on the inner wall of the hollow filament during spinning. The three components of the constitutive equation are derived as follows by using equations (5.1.7), (5.1.8), (5.1.9), (5.1.10) and boundary conditions (5.1.11):

$$\sigma_{rr} = \frac{\Delta P R_i^2}{(R_0^2 - R_i^2)}\left[1 - \frac{R_0^2}{r^2}\right] \qquad (5.1.12)$$

$$\sigma_{\theta\theta} = \frac{\Delta P R_i^2}{(R_0^2 - R_i^2)}\left[1 + \frac{R_0^2}{r^2}\right] \qquad (5.1.13)$$

$$\sigma_{zz} = \frac{\Delta P R_i^2}{(R_0^2 - R_i^2)} + 3\mu\frac{du_z}{dz} \qquad (5.1.14)$$

It is worth showing two important constants from the above mathematical derivation here:

$$A = \frac{\Delta P R_i^2 R_0^2}{2\mu(R_0^2 - R_i^2)} \tag{5.1.15}$$

$$-p = \frac{\Delta P R_i^2}{(R_0^2 - R_i^2)} + \mu \frac{du_z}{dz} \tag{5.1.16}$$

5.1.3 Differential Equation Describing Inner and Outer Radius of Hollow Filament Along Spinline

Notice the following transformation:

$$u_r = \frac{dr}{dt} = \frac{dr}{dz}\frac{dz}{dt} = u_z \frac{dr}{dt} \tag{5.1.17}$$

and

$$\Delta\theta\theta = 2\frac{u_r}{r} = \frac{2u_z dr}{r\ dz} \tag{5.1.18}$$

From equations (5.1.10), (5.1.13), (5.1.16) and (5.1.18), we have:

$$\sigma\theta\theta = -p + \mu\Delta\theta\theta = \mu\frac{du_z}{dz} + \frac{\Delta P R_i^2}{R_o^2 - R_i^2} + \frac{2\mu u_z dr}{r\ dz} = \frac{\Delta P R_i^2}{R_o^2 - R_i^2}\left[1 + \frac{R_o^2}{r^2}\right]$$

or

$$\frac{dr}{dz} = \frac{r}{2\mu u_z}\left[\frac{\Delta P R_i^2\ R_o^2}{(R_o^2 - R_i^2)\ r^2} - \mu\frac{du_z}{dz}\right] \tag{5.1.19}$$

From equation (5.1.14), it is transformed to:

$$\mu\frac{du_z}{dz} = \frac{1}{3}\left(\sigma_{zz} - \frac{\Delta P R_i^2}{R_o^2 - R_i^2}\right) \tag{5.1.20}$$

Substitute equation (5.1.20) into equation (5.1.19), a differential equation describing the radius as a function of r and z is derived as:

$$\frac{dr}{dz} = \frac{r}{6\mu u_z}\left[\frac{\Delta P R_i^2}{R_o^2 - R_i^2}\left(1+3\frac{R_o^2}{r^2}\right) - \sigma_{zz}\right] \tag{5.1.21}$$

or

$$\frac{dR_i}{dz} = \frac{R_i}{6\mu u_z}\left[\left(\frac{3R_o^2+R_i^2}{R_o^2+R_i^2}\right)\sigma_{\theta\theta}(R_i) - \sigma_{zz}\right] \tag{5.1.22}$$

$$\frac{dR_o}{dz} = \frac{R_o}{6\mu u_z}\left[2\sigma_{\theta\theta}(R_o) - \sigma_{zz}\right] \tag{5.1.23}$$

where

$$\sigma_{\theta\theta}(R_i) = \frac{\Delta P(R_o^2 + R_i^2)}{(R_o^2 - R_i^2)} \tag{5.1.24}$$

$$\sigma_{\theta\theta}(R_o) = \frac{2\Delta P R_i^2}{(R_o^2 - R_i^2)} \tag{5.1.25}$$

5.2 Hollow Filament as A Thin-Walled Cylinder

A mathematical model is developed in this section, which treats the hollow filament as a thin walled cylinder having a outer radius of R, wall thickness h, internal pressure ΔP and axial stress σ_{zz}. The distinction of "thin wall" from "thick wall" is that the wall thickness is thin enough that the variation of the circumferential (or hoop) stress over the thickness may be neglected.

5.2.1 Kinematics

The deformation rate tensor for describing hollow fiber spinning is present as equation 5.1.1. From equation 5.1.6., we have:

$$u_r|_R = -\frac{1}{2}R\frac{du_z}{dz} + \frac{A}{R} = \frac{dR}{dt} = u_z\frac{dR}{dz} \qquad (5.2.1)$$

$$A = \frac{1}{2}R^2\frac{du_z}{dz} + Ru_z\frac{dR}{dz} \qquad (5.2.2)$$

$$\frac{du_r}{dr}|_R = -\frac{du_z}{dz} - \frac{u_z dR}{R\,dz} \qquad (5.2.3)$$

and

$$\Delta_{rr} = 2\frac{du_r}{dr}|_R = -2\left(\frac{du_z}{dz} + \frac{u_z dR}{R\,dz}\right) \qquad (5.2.4)$$

$$\Delta_{\theta\theta} = 2\frac{u_r}{r}|_R = \frac{2u_z dR}{R\,dz} \qquad (5.2.5)$$

$$\Delta_{zz} = 2\frac{du_z}{dz} \qquad (5.2.6)$$

5.2.2 Equations of Hoop and Axial Stresses

In the thin walled cylindrical model, the stresses $\sigma_{\theta\theta}$ (hoop stress) and σ_{zz} (axial stress) are plane stress elements properly oriented on the outside surface of the cylinder, where σ_{zz} is parallel to the fiber axis and $\sigma_{\theta\theta}$ is perpendicular to fiber axis. The radial stress σ_{rr} equals to zero.

$$\sigma_{rr} = -p - 2\mu\left(\frac{du_z}{dz} + \frac{u_z dR}{R\,dz}\right) = 0 \qquad (5.2.7)$$

$$-p = 2\mu\left(\frac{du_z}{dz} + \frac{u_z dR}{R^2\,dz}\right) \qquad (5.2.8)$$

$$\sigma_{\theta\theta} = -p + \frac{2\mu u_z dR}{R\ dz} = 2\mu\left(\frac{du_z}{dz} + \frac{2u_z dR}{R\ dz}\right) \qquad (5.2.9)$$

$$\sigma_{zz} = -p + 2\mu\frac{du_z}{dz} = 2\mu\left(2\frac{du_z}{dz} + \frac{u_z dR}{R\ dz}\right) \qquad (5.2.10)$$

5.2.3 Differential Equation Describing Radius and Wall Thickness of Hollow Filament Along Spinline

In the thin walled cylindrical model, the hoop stress $\sigma_{\theta\theta}$ due to internal pressure ΔP is expressed as:

$$\sigma_{\theta\theta} = \Delta P\frac{R}{h} \qquad (5.2.11)$$

where R is radius of cylinder and h is wall thickness. Combining equations (5.2.9) and (5.2.11), the following mathematical transformation is carried out:

$$\Delta P\frac{R}{h} = 2\mu\frac{du_z}{dz} + 4\mu\frac{u_z dR}{R\ dz} \qquad (5.2.12)$$

From equation (5.2.10), we have

$$2\mu\frac{du_z}{dz} = \frac{\sigma_{zz}}{2} - \mu\frac{u_z dR}{R\ dz} \qquad (5.2.13)$$

Substituting equation (5.2.13) into (5.2.12), we obtain

$$\Delta P\frac{R}{h} = \frac{\sigma_{zz}}{2} + 3\mu\frac{u_z dR}{R\ dz} \qquad (5.2.14)$$

or

$$\frac{dR}{dz} = \frac{R}{6\mu u_z}[\frac{2R}{h}\Delta P - \sigma_{zz}] \qquad (5.2.15)$$

In this thin walled cylindrical model, the plane stress condition ($\sigma_{\theta\theta}\neq 0$, $\sigma_{zz}\neq 0$ and $\sigma_{rr}=0$) leads to the three components $\Delta_{\theta\theta}$, Δ_{zz} and Δ_{rr} of deformation rate tensor. The deformation rate Δ_{rr} in thickness of the wall is considered in the following derivation, which starts from equation (5.2.4):

$$\Delta_{rr} = 2\frac{du_r}{dr}\Big|_R \approx 2\frac{u_r|_R}{h} = \frac{2u_z dh}{h\ dz} = -2(\frac{du_z}{dz} + \frac{u_z dR}{R\ dz}) \qquad (5.2.16)$$

or

$$\frac{dh}{dz} = -\frac{h}{u_z}(\frac{du_z}{dz} + \frac{u_z dR}{R\ dz}) \qquad (5.2.17)$$

By substituting equations (5.2.13) and (5.2.15) into equation (5.2.17), a differential equation describing the change of wall thickness along the spinline distance z is derived:

$$\frac{dh}{dz} = -\frac{h}{6\mu u_z}[\frac{R}{h}\Delta p + \sigma_{zz}] \qquad (5.2.18)$$

5.3 The Overall Force Balance Along Spinline

It is here attempted to derive "macro" (average) force balance in hollow fiber spinline from continuity and momentum equations.

By assuming a steady state process for the dry spinning of hollow fiber, the equations of continuity and momentum balance in cylindrical coordinates are as follows:

Continuity

$$\frac{1}{r}\frac{\partial}{\partial r}(\rho r u_r) + \frac{\partial}{\partial z}(\rho u_z) = 0 \qquad (5.3.1)$$

Momentum Balance

z-component

$$\rho(u_r\frac{\partial u_z}{\partial r} + u_z\frac{\partial u_z}{\partial z}) = \frac{1}{r}\frac{\partial}{\partial r}(r\sigma_{rz}) + \frac{\partial \sigma_{zz}}{\partial z} + \rho g \qquad (5.3.2)$$

It is assumed that isotropic flow properties exist in the plane perpendicular to the direction of fiber axis. This assumption applies to equation of continuity and momentum by using a plane-averaging.

The continuity equation is averaged as:

$$\int_{R_i}^{R_o}[\frac{1}{r}\frac{\partial}{\partial r}(\rho r u_r)]2\pi r\, dr = 0 \qquad (5.3.3)$$

$$\int_{R_i}^{R_o}[\frac{\partial}{\partial z}(\rho u_z)2\pi r dr = \frac{d}{dz}\int_{R_i}^{R_o}\rho u_z 2\pi r dr = \frac{d}{dz}[\pi(R_o^2-R_i^2)\rho\overline{u_z}] \qquad (5.3.4)$$

Thus, the continuity equation is converted to:

$$\frac{d}{dz}[\pi(R_o^2-R_i^2)\rho\overline{u_z}] = 0$$

or

$$\pi(R_o^2-R_i^2)\rho\overline{u_z} = \text{constant} \qquad (5.3.5)$$

The equation of z-component of momentum balance is averaged as:

$$u_r\frac{\partial u_z}{\partial r} = 0 \qquad (5.3.6)$$

$$\int_{R_i}^{R_o}[\rho u_z\frac{du_z}{dz}]2\pi r dr = \rho\pi(R_o^2-R_i^2)\overline{u_z}]\frac{d\overline{u_z}}{dz} = W\frac{d\overline{u_z}}{dz} \qquad (5.3.7)$$

$$\int_{R_i}^{R_o}[\rho g]2\pi r dr = \pi(R_o^2-R_i^2)\rho g \qquad (5.3.8)$$

$$\int_{R_i}^{R_o}\frac{\partial\sigma_{zz}}{\partial z}2\pi r dr = \pi(R_o^2-R_i^2)\frac{d\overline{\sigma_{zz}}}{dz} \qquad (5.3.9)$$

$$\int_{R_i}^{R_o}[\frac{1}{r}\frac{\partial}{\partial r}(r\sigma_{rz})]2\pi r dr = 2\pi R_o\sigma_{rz}(R_o) - 2\pi R_i\sigma_{rz}(R_i) \qquad (5.3.10)$$

where $\sigma_{rz}(R_i) = 0, \sigma_{rz}(R_o) = \frac{1}{2}C_D\rho_a\overline{u_z}^2$

Thus z-component of momentum balance becomes:

$$W\frac{d\overline{u_z}}{dz} = \pi(R_o^2-R_i^2)\frac{d\overline{\sigma_{zz}}}{dz} - \pi R_o C_D \rho_a \overline{u_z}^2 + \pi(R_o^2-R_i^2)\rho g \qquad (5.3.11)$$

5.4 Mathematical Models of Circumferential and Axial Force Balances for Hollow Filament Spinning

In summary of sections 5.1, 5.2 and 5.3, the following system equations of force balances for hollow filament spinning are proposed:

Thick Walled Cylindrical Model

$$\frac{dR_i}{dz} = \frac{R_i}{6\mu u_z}\left[\left(\frac{3R_o^2+R_i^2}{R_o^2+R_i^2}\right)\sigma_{\theta\theta}(R_i) - \sigma_{zz}\right] \qquad (5.4.1)$$

$$\frac{dR_o}{dz} = \frac{R_o}{6\mu u_z}\left[2\sigma_{\theta\theta}(R_o) - \sigma_{zz}\right] \qquad (5.4.2)$$

$$\sigma_{\theta\theta}(R_i) = \frac{\Delta P(R_o^2 + R_i^2)}{(R_o^2 - R_i^2)} \qquad (5.4.3)$$

$$\sigma_{\theta\theta}(R_o) = \frac{2\Delta P R_i^2}{(R_o^2 - R_i^2)} \qquad (5.4.4)$$

$$\pi(R_2^2-R_1^2)\rho\bar{u}_z = W \tag{5.4.5}$$

$$W\frac{d\bar{u}_z}{dz} = \pi(R_o^2-R_i^2)\frac{d\bar{\sigma}_{zz}}{dz} - \pi R_o C_D \rho_a \bar{u}_z^2 + \pi(R_o^2-R_i^2)\rho g \tag{5.4.6}$$

Thin Walled Cylindrical Model

$$\frac{dR}{dz} = \frac{R}{6\mu u_z}\left[\frac{2R}{h}\Delta p - \sigma_{zz}\right] \tag{5.4.7}$$

$$\frac{dh}{dz} = -\frac{h}{6\mu u_z}\left[\frac{R}{h}\Delta p + \sigma_{zz}\right] \tag{5.4.8}$$

$$2\pi Rh\rho\bar{u}_z = W \tag{5.4.9}$$

$$W\frac{d\bar{u}_z}{dz} = 2\pi Rh\frac{d\bar{\sigma}_{zz}}{dz} - \pi R C_D \rho_a \bar{u}_z^2 + 2\pi Rh\rho g \tag{5.4.10}$$

5.5 Energy Balance

The heat transfer equation is derived based on the following assumptions:

1. Steady state process.

2. The viscous heat dissipation is negligible.

3. Heat conduction in the z direction within the fiber is negligible in comparison to that in the r direction.

4. The heat flux in the radial direction at the fiber surface is due to the convection and heat loss from the evaporation of the solvent.

5. The radiation contribution is negligible.

6. Radial temperature gradient with the filament is negligible.

Based on the above assumptions, the equation of energy becomes:

$$\rho C_p(u_r\frac{\partial T}{\partial r} + u_z\frac{\partial T}{\partial z}) = -\{\frac{1}{r}\frac{\partial}{\partial r}(rq_r)\} \qquad (5.5.1)$$

If the energy transport due to the flow u_r in the r direction is negligible, compared to that in the z direction, then

$$\rho C_p(u_z\frac{\partial T}{\partial z}) = -\{\frac{1}{r}\frac{\partial}{\partial r}(rq_r)\} \qquad (5.5.2)$$

The heat flux in the radial direction at the fiber surface is accomplished by convection, radiation and heat loss due to evaporation of the solvent as

$$q_r = h(T - T_a) + \lambda\varepsilon(T^4 - T_a^4) + \Delta H_v J_r(r=R_o) \qquad (5.5.3)$$

where h is the heat transfer coefficient, λ is the Stephen-Boltzman constant, ε is the emissivity, T is the surface temperature of the fiber, T_a is the temperature of air flow, ΔH_v is the heat of vaporization of the solvent and

$J_r(r=R_o)$ is the mass flux of the solvent at the interface. If we assume that heat conduction in the z direction is negligible, the energy balance at the fiber surface becomes

$$\rho C_p(u_z\frac{\partial T}{\partial z}) = -\{\frac{1}{R_o}[h(T - T_a) + \lambda\varepsilon(T^4 - T_a^4) + \Delta H_v J_r(r=R_o)]\} \qquad (5.5.4)$$

By further assuming that the radiation contribution is negligible, the energy balance at the fiber surface is

$$\rho C_p(u_z\frac{\partial T}{\partial z}) = -\{\frac{1}{R_o}[h(T - T_a) + \Delta H_v J_r(r=R_o)]\} \qquad (5.5.5)$$

5.6 Mass Transfer

The mass transfer equation is derived based on the following assumptions:

1. Steady state process.

2. The diffusion flux in the z direction is negligible.

3. The diffusion flux on the outer surface of hollow fiber can be described as interface mass transfer, which is one of boundary conditions describing mass transfer at interface boundary.

4. The diffusion flux on the inner surface of hollow fiber is assumed to be zero because the gas inside the hollow filament is almost static, and mass transfer on the

inner face is close to zero. furthermore, the internal gas is sealed inside of the hollow filament in a normal stable process such that no solvent should be carried away by internal gas.

The concentration distribution of solvent within the filament is given by

$$u_r\frac{\partial c}{\partial r} + u_z\frac{\partial c}{\partial z} = -\{\frac{1}{r}\frac{\partial}{\partial r}(rJ_r) + \frac{\partial J_z}{\partial z}\} \qquad (5.6.1)$$

If flow u_r is neglected, compared to u_z, then

$$u_z\frac{\partial c}{\partial z} = -\{\frac{1}{r}\frac{\partial}{\partial r}(rJ_r) + \frac{\partial J_z}{\partial z}\} \qquad (5.6.2)$$

Further, the diffusional flux in the z direction is negligible, therefore

$$u_z\frac{\partial c}{\partial z} = -\frac{1}{r}\frac{\partial}{\partial r}(rJ_r) \qquad (5.6.3)$$

where J_r is the diffusional flux in the r direction, given by:

$$J_r = -D\frac{\partial c}{\partial r} \qquad (5.6.4)$$

Thus the concentration distribution within the filament becomes

$$u_z \frac{\partial c}{\partial z} = \frac{1}{r} \frac{\partial}{\partial r}(rD \frac{\partial c}{\partial r}) \qquad (5.6.5)$$

The diffusional flux of interface boundary on the outer surface of the fiber can be described as:

$$J_r(r=R_o) = - k_x(\frac{x_{sg} - x_{so}}{1 - x_{sg}}) \qquad (5.6.6)$$

where k_x is mass transfer coefficient, x_{sg} is the concentration of solvent in the gas medium (in the main stream), x_{so} is the concentration of the solvent on the interface boundary of fiber surface. Substituting $J_r(r=R_o)$ into equation (5.6.3), then the solvent distribution in the interface is:

$$u_z \frac{\partial c}{\partial z} = \frac{1}{r} \frac{\partial}{\partial r}[rk_x(\frac{x_{sg} - x_{so}}{1 - x_{sg}})] \qquad (5.6.7)$$

In the interface boundary, the solvent is under going a phase change, from liquid phase to gas phase. The equilibrium relation of the solvent between the liquid phase and gas phase can be represented by Flory-Huggins theory (98-100) as

$$\ln(\frac{P_s}{P_s^o}) = \ln c + (1-c)(1-\zeta) + \chi_{12}(1-c)^2 \qquad (5.6.8)$$

where P_s is vapor pressure of the solvent, P_s^c is vapor pressure of pure solvent, c is the volume fraction of the solvent, ζ is the ratio of molar volume of the solvent to polymer and χ_{12} is Flory-Huggins interaction parameter. The vapor pressure of pure solvent is a function of temperature, which can be expressed using the following experimental equation as:

$$P_s^o = A\exp(-\frac{B}{T+T_a}) \qquad (5.6.9)$$

Dalton's law states that the pressure of a gas mixture will be the sum of partial pressure and the pressure of a gas is in proportion to the numbers of molecules present, then:

$$P_s = x_{so}P \qquad (5.6.10)$$

where P_s is the vapor pressure due to solvent component in gas phase, x_{so} is the molar fraction of the solvent and P is total pressure of the gas. If we assume that the total

pressure of the gas is equal to 1 atm, the concentration of the solvent on the interphase boundary will be

$$x_{so} = \frac{P_s}{P} = P_s^{o} c \exp[(1-c)(1-\zeta) + \chi_{12}(1-c)^2] \qquad (5.6.11)$$

In Flory-Huggins theory of polymer solution (98), the interaction parameter is defined as:

$$\chi_{12} = \frac{\Delta H}{RTn_1 v_2} \qquad (5.6.12)$$

where ΔH is the heat of mixing, R is gas constant, T is temperature, n_1 is mole number of solvent and v_2 is volume fraction of polymer. Although χ_{12} has both temperature and concentration dependence, it was assumed to be a constant value of χ_{12}=0.5 for the purpose of the modeling study.

5.7 Continuity Equation

The steady state equation of conservation of mass for polymer component is:

$$\frac{dW_p}{dz} = 0 \qquad (5.7.1)$$

where W_p is the mass flow rate of the polymer component. The steady state equation of mass balance for the solvent component is:

$$\frac{dW_s}{dz} = - 2\pi R_o J_r(r=R_o) \qquad (5.7.2)$$

where W_S is the mass flow rate of the solvent component, M_S is molecular weight of solvent and $J_r(r=R_O)$ is the mass flux at the interface. Since the total mass flow rate W is the sum of the two components, the total mass balance of the system in steady state is

$$\frac{dW}{dz} = - 2\pi R_o J_r(r=R_o) \qquad (5.7.3)$$

5.8 Models and Parameters of Material Properties

Heat Transfer Coefficient

Heat transfer from the hot gas medium to the spinline involves two mechanisms: radiation and convection. Because the temperature of the extrusion is generally less than 400 °C, the radiation contribution is less than 1% (106,107). Heat transfer by convection flow is considered in this model. Thus the key parameter in calculating the temperature profile of the spinline is the heat transfer coefficient h. There have been many attempts to establish theoretical and empirical relationships between h and the spinning conditions. These approaches use a Nusselt number as a function of the Reynolds, Prandtl (forced convection)

and/or Grashof (natural convection) numbers (29). The correlation function by Kase and Matsuo (45) was selected to use in the simulation.

$$Nu = 0.42(Re)_p^{1/3} \quad \text{for parallel air flow} \qquad (5.8.1)$$

$$Nu = 0.84(Re)_c^{1/3} \quad \text{for cross air flow} \qquad (5.8.2)$$

Mass Transfer Coefficient

The mass transfer coefficient for the case of low mass transfer rates can be obtained by analogy with corresponding correlations in heat transfer (110). This important analogy permits us to derive mass transfer correlations from heat transfer correlations for equivalent boundary conditions by substituting Sherwood number Sh for Nusselt number Nu and Schmidt number Sc for Prandtl number Pr.

$$Nu = \frac{hd}{k} = \text{const} \cdot Re^m Pr^n \quad \text{heat transfer} \qquad (5.8.3)$$

$$Sh = \frac{k_x d}{cD} = \text{const} \cdot Re^m Sc^n \quad \text{mass transfer} \qquad (5.8.4)$$

where h is the heat transfer coefficient, k_x is the mass transfer coefficient, d is the fiber diameter, k is the thermal conductivity, D is the diffusivity of the air-gas

system, c is the molar concentration of the air-gas system. Thus

$$\frac{k_x}{h} = \frac{cD}{k}\left(\frac{Sc}{Pr}\right)^n \qquad (5.8.5)$$

The equation 5.8.5 states that the ratio of k_x/h is not a function of Reynolds number regarding flow state. Figure 5.8.1 shows the comparison between heat and mass transfer when the flow passes over a single cylinder (108). Experiments by Ohzawa and Nagano (83) on several solvents commonly used in dry spinning have proved the constancy of the k_x/h ratio. They also obtained h/k_x = 7.5 cal/mol°C for DMF solvent by the experiment of measuring wet and dry bulb temperature.

Diffusivity of Solvent

Because diffusion of solvent in polymer involves an activated process, it depends on temperature. The Arrhenius relation is normally used (109) to describe this dependence:

$$D = D_0 \exp\left(\frac{-E_a}{RT}\right) \qquad (5.8.6)$$

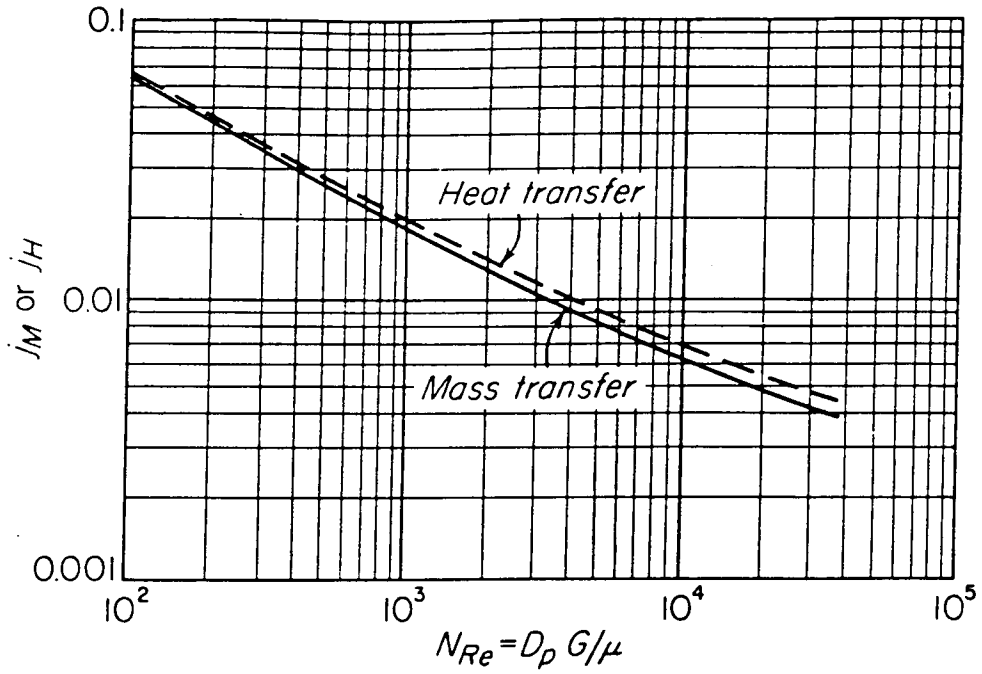

Figure 5.8.1 Heat and mass transfer, flow past single cylinder (108).

where D_0 is a constant, E_a is the activation energy, R is gas constant and T is the temperature. For DMF-polyacrylonitrile system, D_0 is 6.25 cm^2/sec, E_a is 3.37 kcal/mol (29).

Physical Parameters of Solvent

The vapor pressure of the solvent varies with temperature. The simple model for describing its temperature-dependence is to use the Arrenhius equation (109). For DMF pure solvent, its vapor pressure is $3.55x10^{-3}$ atm at 20°C and 1.0 atm at its boiling temperature of 153°C. Based on these physical data, the following equation for vapor pressure of DMF solvent is derived:

$$P_s^0 = 2.69x10^5 \exp(-\frac{4.42x10^4}{RT}) \qquad (5.8.7)$$

where P_s^0 is the vapor pressure (atm) of DMF solvent, R is the gas constant and T is the temperature in kelvin.

The heat of vaporization ΔH_v is 116 (cal/gram) for DMF solvent.

Drag Coefficient

Drag coefficient is normally expressed as a function of Reynolds number. The following equation is adopted for the simulation of dry spinning (38):

$$C_f = 0.77 Re^{-0.61} \qquad (5.8.8)$$

Viscosity Equation

The viscosity equation based on experimental data was derived by using Modified Cross Model in Chapter IV "EXPERIMENTAL RESULTS". The viscosity equation used in the model as follows:

$$\mu = \frac{\mu_0}{1 + \left(\frac{\mu_0 \dot{\gamma}}{1.17 \times 10^5}\right)^{0.758}}$$

$$\mu_0 = A \exp\left(\frac{73.5}{T}\right)$$

$$A = 8.36 \times 10^5 C^{6.46} \qquad (5.8.9)$$

The viscosity depends on shear rate γ, temperature T and PAN concentration C in the spinning dope.

5.9 Numerical Methods for Modeling

The differential equations in the model for the solution dry spinning process of hollow filament are summarized in Figure 5.9.1. Numerical methods have been adopted to solve those equations simultaneously (112, 113).

5.9.1 Numerical Solution for the Partial Differential Equation of Mass Transfer

Consider the mesh shown in Figure 5.9.2. The indices j,k represent the nodal locations in radial r direction and spinline distance z direction, respectively. The value of a variable f at location (j,k) is indicated by $f_{j,k}$.

The following equation is a partial differential equation for the diffusion of solvent during dry spinning of hollow fiber:

$$u_z \frac{\partial c}{\partial z} = \frac{1}{r}\frac{\partial}{\partial r}\left(rD\frac{\partial c}{\partial r}\right) \qquad (5.9.1)$$

The initial condition is:

$$z = 0,\ c = co,\ Ri \le r \le Ro \qquad (5.9.2)$$

The boundary conditions are:

$$-D\frac{\partial c}{\partial r} = J_r(r=R_o) \qquad z > 0,\ r = R_O \qquad (5.9.3)$$

1. CONTINUITY

$$W = W_P + W_S$$

$$\frac{dW}{dz} = -2\pi R_o J_r(r=R_o)$$

2. MOMENTUM BALANCE

$$\frac{dF_{rheo}}{dz} = W\frac{du_z}{dz} + \pi R_o^2 C_D \rho_a u_z^2 - \pi(R_o^2 - R_i^2)\rho g$$

$$\sigma_{\theta\theta}(R_o) = \frac{2\Delta P R_i^2}{(R_o^2 - R_i^2)} \qquad \sigma_{\theta\theta}(R_i) = \frac{\Delta P(R_o^2 + R_i^2)}{(R_o^2 - R_i^2)}$$

$$\frac{dR_o}{dz} = \frac{R_o}{6\mu u_z}[2\sigma_{\theta\theta}(R_o) - \sigma_{zz}]$$

$$\frac{dR_i}{dz} = \frac{R_i}{6\mu u_z}[(\frac{3R_o^2+R_i^2}{R_o^2+R_i^2})\sigma_{\theta\theta}(R_i) - \sigma_{zz}]$$

$$\sigma_{zz} = \frac{F_{rheo}}{\pi(R_o^2 - R_i^2)}$$

3. ENERGY BALANCE

$$\rho C_p u_z \frac{dT}{dz} = -\{\frac{1}{R_o}[h(T-T_a) + \Delta H_v J_x]\}$$

$T = T_O$, when $z = 0$

4. MASS BALANCE

$$u_z\frac{\partial c}{\partial z} = \frac{1}{r}\frac{\partial}{\partial r}(rD\frac{\partial c}{\partial r}) \qquad R_O > r > R_i; \quad c = c_O, \text{ when } z = 0$$

$$-D\frac{\partial c}{\partial r} = J_r(r=R_o) \qquad r = R_O$$

$$-D\frac{\partial c}{\partial r} = J_r(r=R_i) \qquad r = R_i$$

$$J_r(r=R_i) = 0$$

$$J_r(r=R_o) = -k_x(\frac{x_{sg} - x_{so}}{1 - x_{sg}})$$

$$x_{so} = P_s^o c \exp[(1-c)(1-\zeta) + \chi_{12}(1-c)^2]$$

5. RHEOLOGICAL CONSTITUTIVE EQUATION

$$\frac{du_z}{dz} = \frac{1}{3\mu}[\sigma_{zz} - \frac{\Delta P R_i^2}{(R_o^2 - R_i^2)}]$$

$$\mu = \frac{\mu_o}{1 + (\frac{\mu_o \bar{\gamma}}{\tau^*})^{1-n}} \qquad \mu_o = A\exp(\frac{E}{RT}) \qquad A = A'(1-c)^m$$

Figure 5.9.1 Summary of the working relation in the model for the dry spinning of hollow filament.

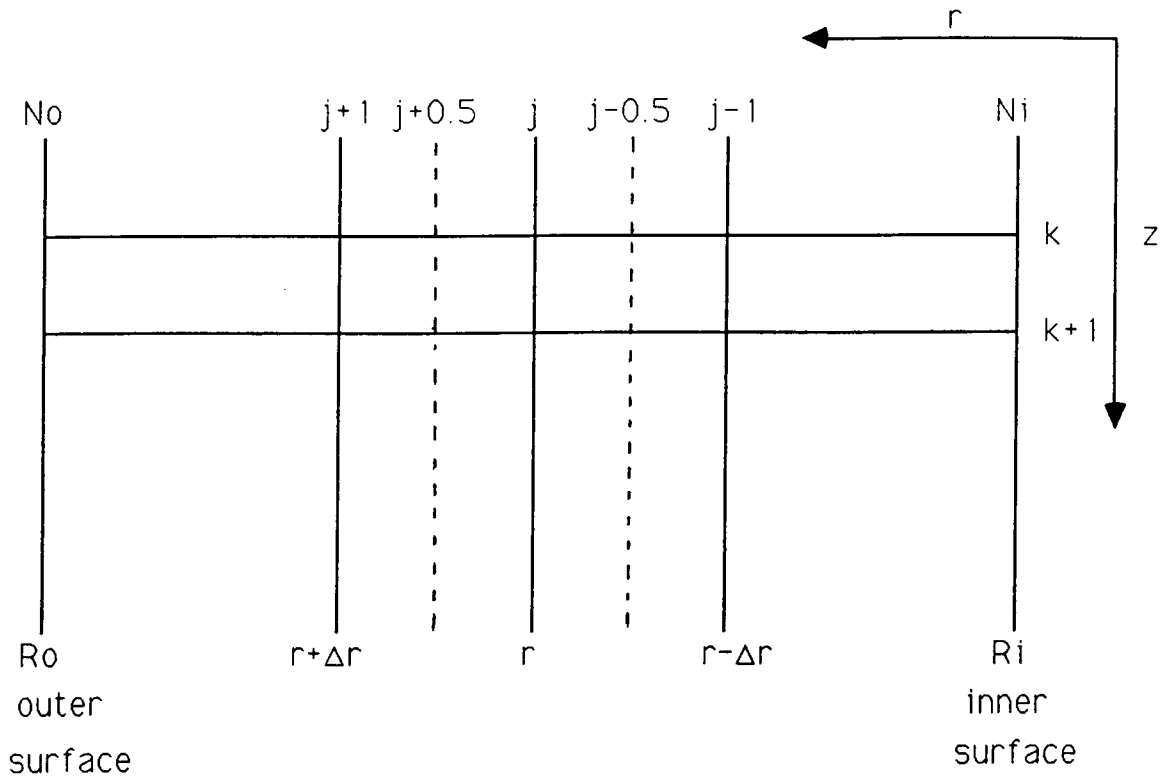

Figure 5.9.2 Computation mesh for partial differential equation of mass trnasfer.

$$J_r(r=R_o) = -k_x\left(\frac{X_{sg}-X_{so}}{1-X_{sg}}\right) \qquad r = Ro \qquad (5.9.4)$$

$$J_r(r=R_i) = 0 \qquad r = Ri \qquad (5.9.5)$$

In the hollow cylinder, we have

$$R_i \leq r \leq R_O$$

$$N_i \leq j \leq N_O$$

$R_i = N_i\Delta r$ inner radius of hollow fiber

$R_O = N_O\Delta r$ outer radius of hollow fiber

$$r_{j,k} = j\Delta r \qquad (5.9.6)$$

By using finite difference method, the equation (5.9.1) can be transformed to the following form:

$$u_z(k)2\pi r\Delta r\Delta c = \Delta[2\pi rD\frac{\partial c}{\partial r}]\Delta z \qquad (5.9.7)$$

$$\Delta c = c_{j,k+1} - c_{j,k} \qquad (5.9.8)$$

$$(\frac{\partial c}{\partial r})_{j-\frac{1}{2}} = \frac{c_{j-1}-c_j}{\Delta r} \qquad (5.9.9)$$

$$(\frac{\partial c}{\partial r})_{j+\frac{1}{2}} = \frac{c_j-c_{j+1}}{\Delta r} \qquad (5.9.10)$$

Substitute Equations (5.9.6), (5.9.8), (5.9.9) and (5.9.10) into Equation (5.10.7), the following equation is obtained:

$$c_{j,k+1}=c_{j,k}+\frac{\Delta z}{j(\Delta r)^2 u_z(k)}[I_{j-\frac{1}{2}}-I_{j+\frac{1}{2}}] \qquad (5.9.11)$$

where
$$I_{j-\frac{1}{2}}=(j-\frac{1}{2})D(c_{j-1,k}-c_{j,k})$$
$$I_{j+\frac{1}{2}}=(j+\frac{1}{2})D(c_{j,k}-c_{j+1,k})$$

The $c_{j-1,k}$, $c_{j,k}$, $c_{j+1,k}$ and $c_{j,k+1}$ are the solvent concentration at the nodal locations of j-1,k, j,k, j+1,k and j,k+1, respectively. $u_z(k)$ is the spinline velocity at the distance $k\Delta z$ from the spinneret.

At the surface of the hollow filament, we have:

$$-D(\frac{\partial c}{\partial r}) = J_r(r=R_o) = -k_x(\frac{x_{sg}-x_{so}}{1-x_{sg}}) \qquad (5.9.12)$$

Use the same finite difference method as discussed, we are able to obtain the following equation, which is suitable for calculating the mass transfer at the interface boundary on the outer surface of the hollow filament:

$$c_{No,k+1} = c_{No,k}+\frac{2\Delta z}{(No-\frac{1}{4})(\Delta r)^2 u_z(k)}[J_r(r=R_o,k)No\Delta r - I_{No-\frac{1}{2}}] \qquad (5.9.13)$$

where
$$I_{No-\frac{1}{2}} = (No-\frac{1}{2})D(c_{No-1,k}-c_{No,k})$$

$J_r(r=R_o,k)$ is the mass flux on the outer surface of the hollow filament at the spinline distance of $k\Delta z$.

5.9.2 Numerical Solution for Ordinary Differential Equation

The ordinary differential equations in the mathematical model for the dry spinning of hollow filament are solved by using Fourth-Order Runge-Kutta Method. The following is called the classical fourth-order RK method:

$$y_{k+1} = y_k + [\frac{1}{6}(k_1+2k_2+2k_3+k_4)]h \qquad (5.9.14)$$

where

$$k_1 = f(z_k, y_k)$$

$$k_2 = f(z_k+\frac{1}{2}h,\ y_k+\frac{1}{2}hk_1)$$

$$k_3 = f(z_k+\frac{1}{2}h,\ y_k+\frac{1}{2}hk_2)$$

$$k_4 = f(z_k+h,\ y_k+hk_3)$$

$f(z_k,y_k)$ is an ordinary differential equation; y_k is a dependent variable and z_k is the independent variable - spinline distance.

CHAPTER VI

COMPARISON OF MODELING PREDICTIONS WITH EXPERIMENTS

In previous chapter, a mathematical model for the solution dry spinning of hollow filament was developed based on the theory of the thick-walled cylinder as well as heat and mass transfers. In order to check the validity of this model, a validation must be performed to test the model predictions against experiments.

6.1 Processing and Property Variables

Dry spinning of hollow filament is a complex process, which involves numerous variables of input parameters and outcome quantities. In order to facilitate validation, the key input and output variables are listed in Table 6.1.1. The input variables include spinneret temperature, mass throughput, take-up speed, polymer dope concentration and etc., which are key process parameters or material parameters. The output variables are outcome quantities, such as velocity profile, filament outer and inner diameter and etc. measured by either on-line or off-line methods.

Table 6.1.1 Key input and output variables.

Variables	Type	Comments
Spinneret Temperature (°C)	Input	Process parameter
Spin Column Temperature (°C)	Input	Process parameter
Mass Throughput (g/min)	Input	Process parameter
Take-up Speed (m/min), (cm/s)	Input	Process parameter
Inner Pressure (dynes/cm^2)	Input	Process parameter
Polymer Dope Concentration (%)	Input	Material parameter
Quench Air Velocity (cm/s)	Input	Process parameter
Velocity Profile (cm/s)	Output	On-line measured
Spinline Tension at Take-up (Dynes)	Output	On-line measured
Outer Diameter of Hollow Filament (um)	Output	Off-line measured
Inner Diameter of Hollow Filament (um)	Output	Off-line measured
Solvent Residue in Hollow Filament (%)	Output	Off-line measured

6.2 Comparison of Simulation Prediction with Experiment

A set of experiments of hollow filament spinning was conducted under controlled processing conditions as presented in Chapter IV. Computer modeling under the same processing conditions as the experiments was carried out. A comparison of model predictions and experimental data was made in terms of velocity profiles, spinline tension at the take-up, outer and inner diameters of as-spun hollow filament, and solvent residue in as-spun hollow filament. This comparison tested the validity of the model under varied processing conditions and material parameters.

6.2.1 Comparison of Velocity Profiles in the Spinline

The predicted velocity profiles were compared with experimental on-line data in Figure 6.2.1 to 6.2.3. From these comparisons it is clear that velocity profiles predicted by the model are qualitatively consistent with experimental results regarding the effects of take-up speeds, PAN polymer concentration in the spinning dope, and mass throughput.

6.2.2 Comparison of Spinline Tension at Take-up

Table 6.2.1 presents the comparison of take-up tensions predicted by the model and measured by

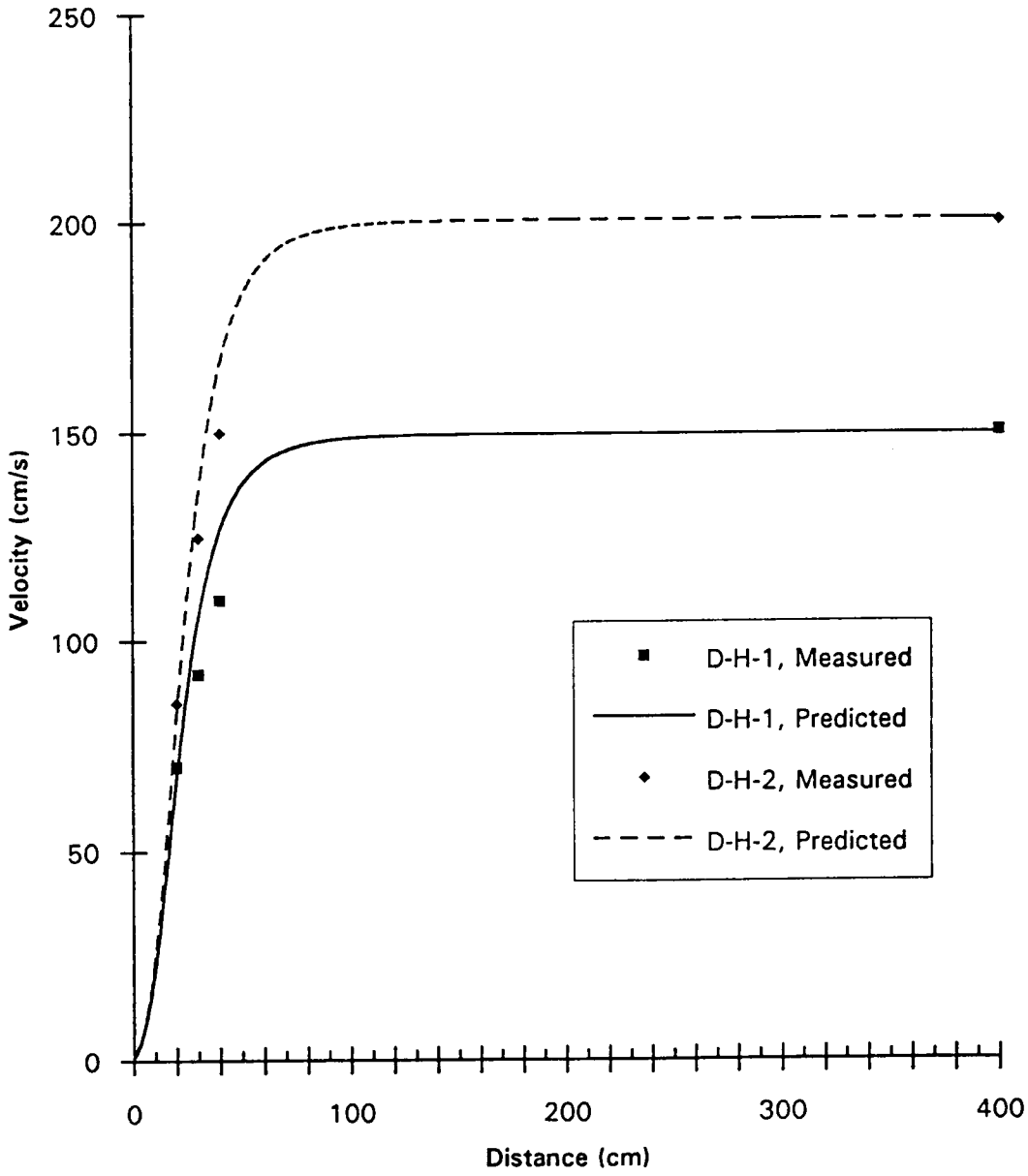

Figure 6.2.1 Comparison of on-line measured and model predicted velocity profiles (D-H-1: 30% PAN, 0.5 g/min, 90 m/min; D-H-2: 30% PAN, 0.5 g/min, 120 m/min; ΔP=500 dynes/cm^2).

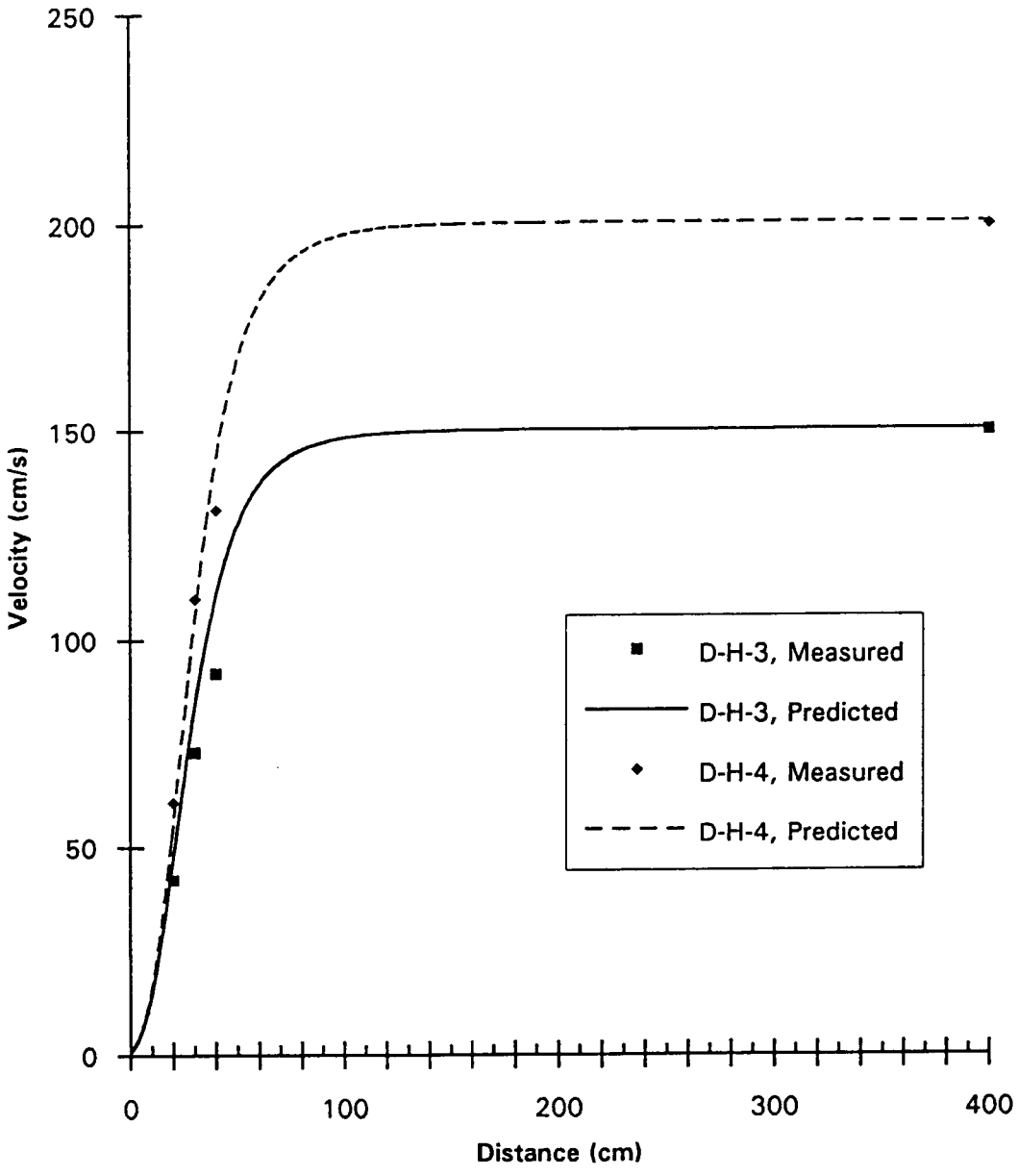

Figure 6.2.2 Comparison of on-line measured and model predicted velocity profiles (D-H-3: 35% PAN, 0.5 g/min, 90 m/min; D-H-4: 35% PAN, 0.5 g/min, 120 m/min; ΔP=500 dynes/cm^2).

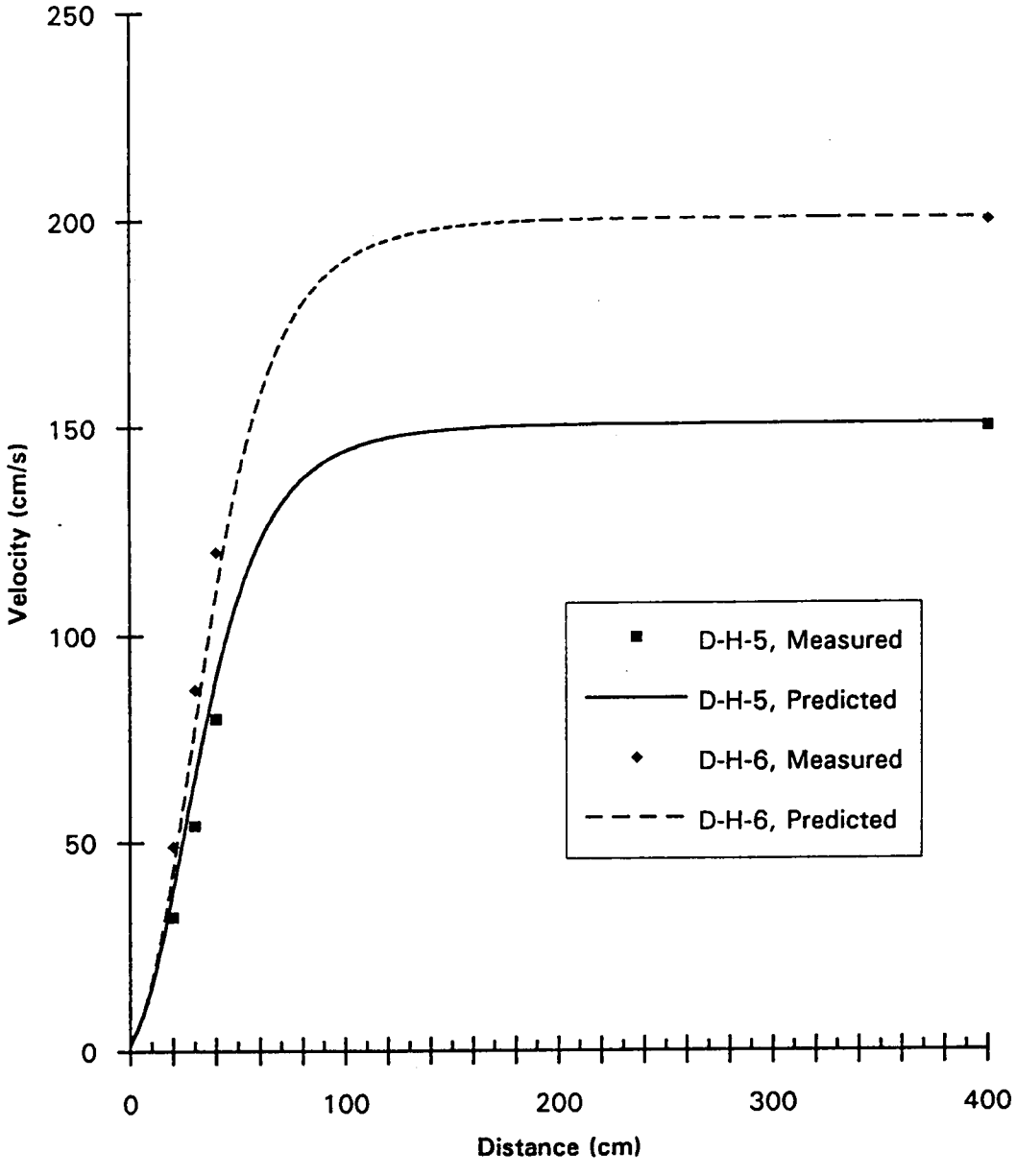

Figure 6.2.3 Comparison of on-line measured and model predicted velocity profiles (D-H-5: 30% PAN, 1.0 g/min, 90 m/min; D-H-6: 30% PAN, 1.0 g/min, 120 m/min; ΔP=500 dynes/cm^2).

Table 6.2.1 Comparison of predicted take-up force with experimental values.

Batch No.	Take-up Force (dynes)	
	Experimental	Predicted
D-H-1	107.2	105.66
D-H-2	131.8	128.92
D-H-3	270.9	267.9
D-H-4	298.3	294.23
D-H-5	79.1	74.68
D-H-6	110.4	105.03
D-H-7	103.7	99.72
D-H-8	125.1	122.94

experiments. The model predictions are in good agreement with experimental data.

6.2.3 Comparison of Outer and Inner Diameters of Hollow Filaments

The comparison of experimental outer and inner diameters of hollow filaments with the model predictions is shown in Table 6.2.2. It is clear that the model is able to predict the outer and inner diameters of as-spun hollow filament with changing process conditions and material parameters.

6.2.4 Comparison of Solvent Residue in Hollow Filament

The solvent residue in hollow filament measured by gravimetric methods is compared with the value predicted by the model in Table 6.2.3. The trend of variation of solvent residue in hollow filament with spinning conditions is generally predicted by this model.

Table 6.2.2 Comparison of predicted diameters with experimental values.

Batch No.	Outer Diameter (um)		Inner Diameter (um)	
	Experimental	Predicted	Experimental	Predicted
D-H-1	141.2	139.6	110.5	111.6
D-H-2	121.5	120.3	95.2	96.1
D-H-3	132.3	130.3	98.2	100.1
D-H-4	114.7	112.7	84.8	86.6
D-H-5	199.2	197.6	156.3	158.1
D-H-6	172.4	170.9	134.6	136.6
D-H-7	134.1	132.7	100.6	102.9
D-H-8	115.1	114.3	86.4	88.5

Table 6.2.3 Comparison of predicted solvent residue with experimental values.

Batch No.	Solvent Residue (%)	
	Experimental	Predicted
D-H-1	9.1	8.79
D-H-2	8.8	8.56
D-H-3	8.8	8.63
D-H-4	8.6	8.43
D-H-5	19.5	19.02
D-H-6	19.1	18.61
D-H-7	9.1	9.05
D-H-8	8.9	8.78

CHAPTER VII

FURTHER STUDY OF DRY SPINNING OF HOLLOW FILAMENT BY MODELING

The previous chapter has demonstrated that the present model (thick-walled) is able to predict some important features of dry spinning of hollow filaments, such as spinline velocity profile, outer and inner diameter of as-spun hollow filament and solvent residue in the filament with varying spinning process conditions. In this chapter, an attempt is made to use this model to further study the process of dry spinning of hollow filament.

Material and processing variables in dry spinning of hollow filament include polymer concentration in the spinning dope, spinning temperature, mass throughput, inner pressure, quench air temperature and its flow velocity, spinneret hole and mandrel sizes, etc. The complex interaction among these variables requires a lot of experimental trials to investigate the process. In many cases, it is even very difficulty to collect a complete set of experimental data due to the limitation of measurement techniques or other problems. This mathematical modeling will allow us to study the detailed effect of material and processing variables on the spinline behaviors for dry

spinning of hollow filaments, and the inner diameter and wall thickness of as-spun hollow filament.

7.1 Effect of Mass Throughput

Table 7.1.1 shows the dry spinning conditions simulated with varying mass throughput of 0.5, 0.75 and 1.0 grams/minute.

Figure 7.1.1 and Figure 7.1.2 present simulated velocity and velocity gradient profiles. These profiles clearly indicate that the velocity gradient profile is broadened, and the peak value of the velocity gradient is decreased with increasing mass throughput at constant take-up speed. The spinline tension decreases with increasing mass throughput at fixed take-up speed as shown in Figure 7.1.3. The decrease of spinline tension is caused by the reduction of draw down ratio (take-up speed over initial jet speed out of spinneret) with increasing mass throughput.

At constant take-up, both outer and inner diameters of the hollow filament increases with mass throughput as predicted in Figures 7.1.4 and 7.1.5. However, the ratio of inner diameter divided by outer diameter of hollow filament (ID/OD) is little affected by changing mass throughput, which is shown in Figure 7.1.6.

Table 7.1.1 Dry spinning conditions simulated with varying mass throughput.

Process Variable	Parameter Value
Spinneret Temperature (°C)	100
Quench Air Temperature (°C)	180
Quench Air Velocity (cm/s)	10
Inner Pressure (dynes/cm^2)	500
Mass Throughput (g/min)	0.5, 0.75, 1.0
Polymer Concentration (%)	30
Take-up Speed (m/min)	120
Spinline Length (cm)	400

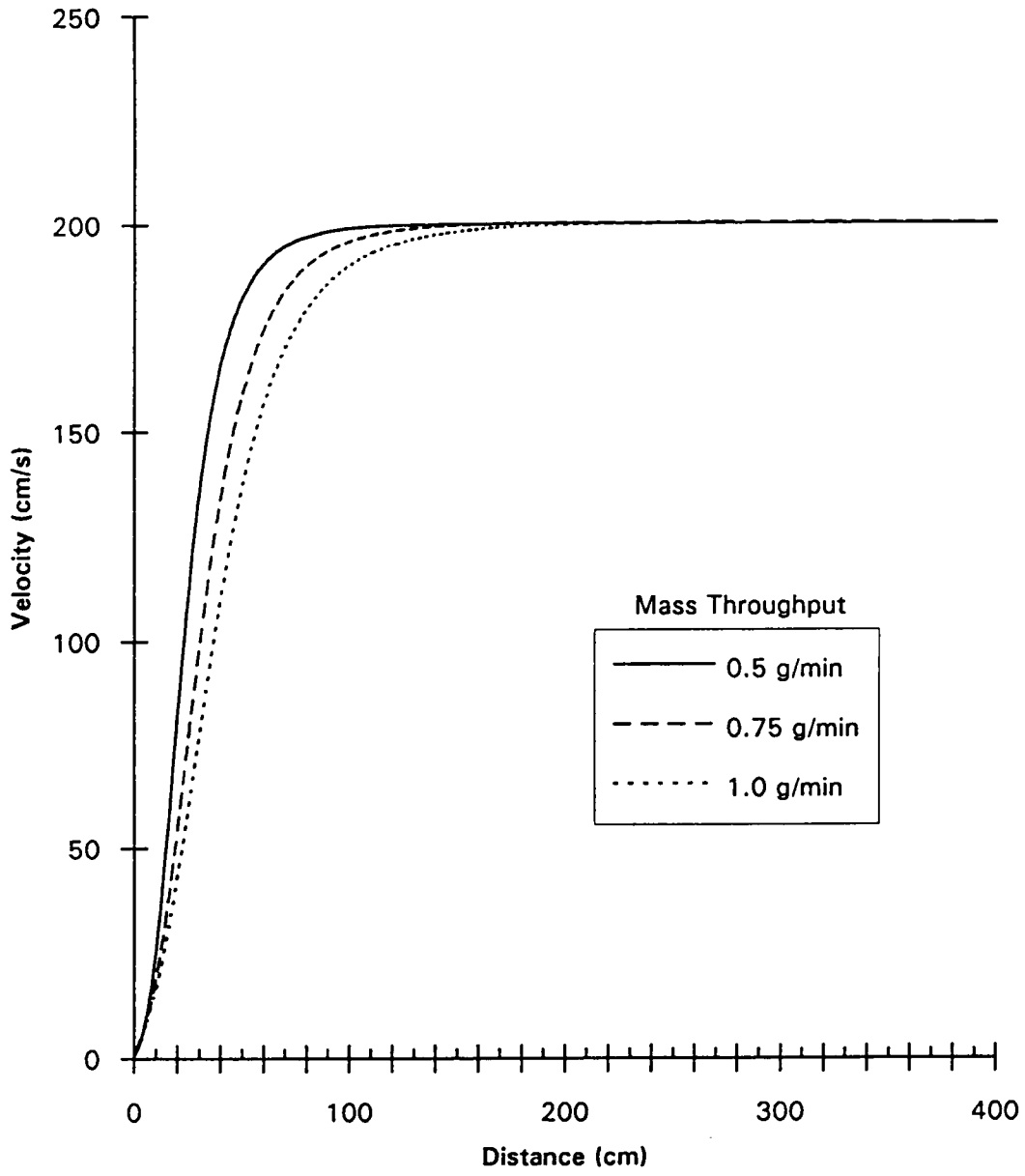

Figure 7.1.1 Influence of mass throughput (0.5, 0.75 and 1.0 g/min) on predicted spinline velocity profiles.

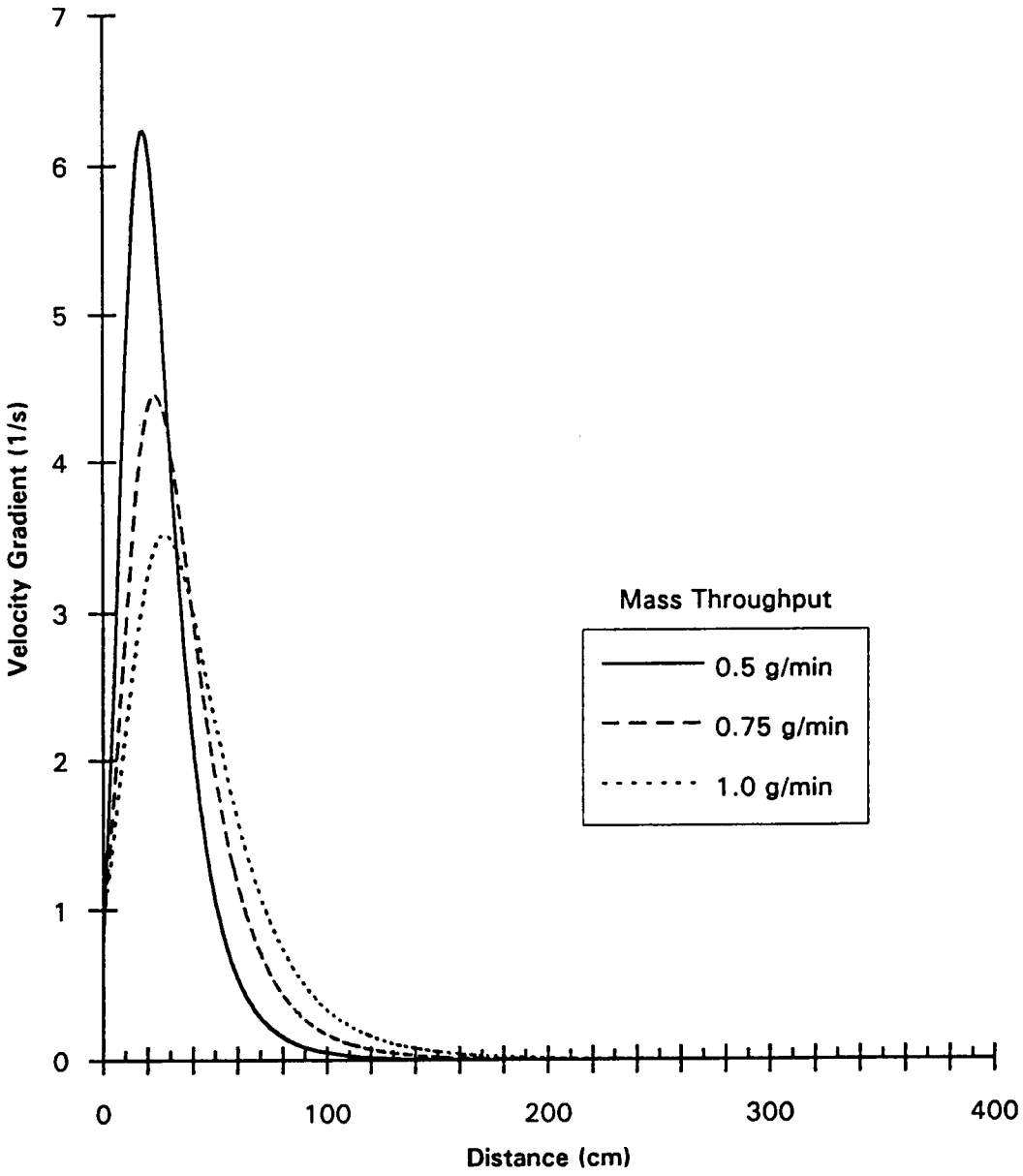

Figure 7.1.2 Influence of mass throughput (0.5, 0.75 and 1.0 g/min) on predicted spinline velocity gradient profiles.

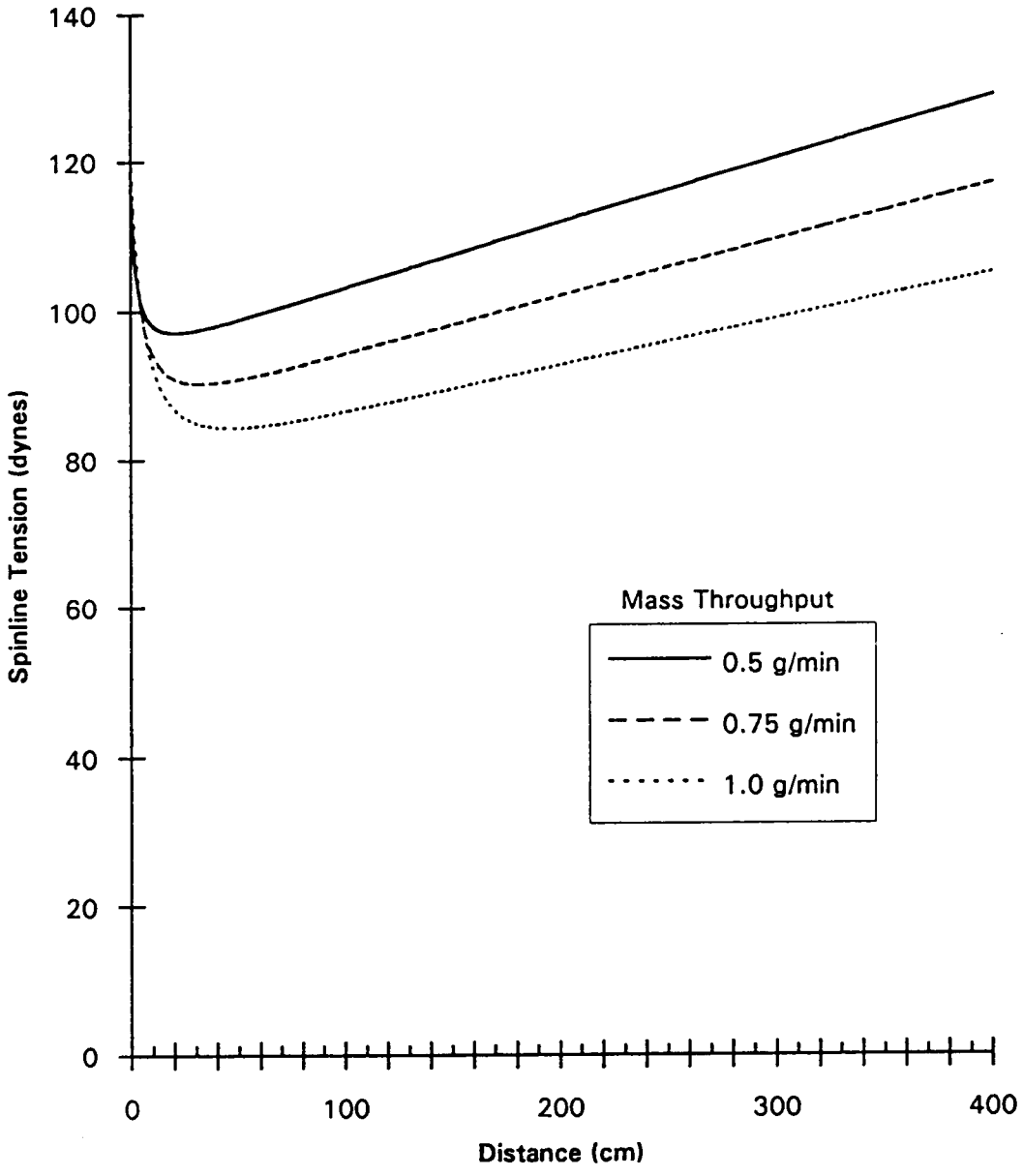

Figure 7.1.3 Influence of mass throughput (0.5, 0.75 and 1.0 g/min) on predicted spinline tension profiles.

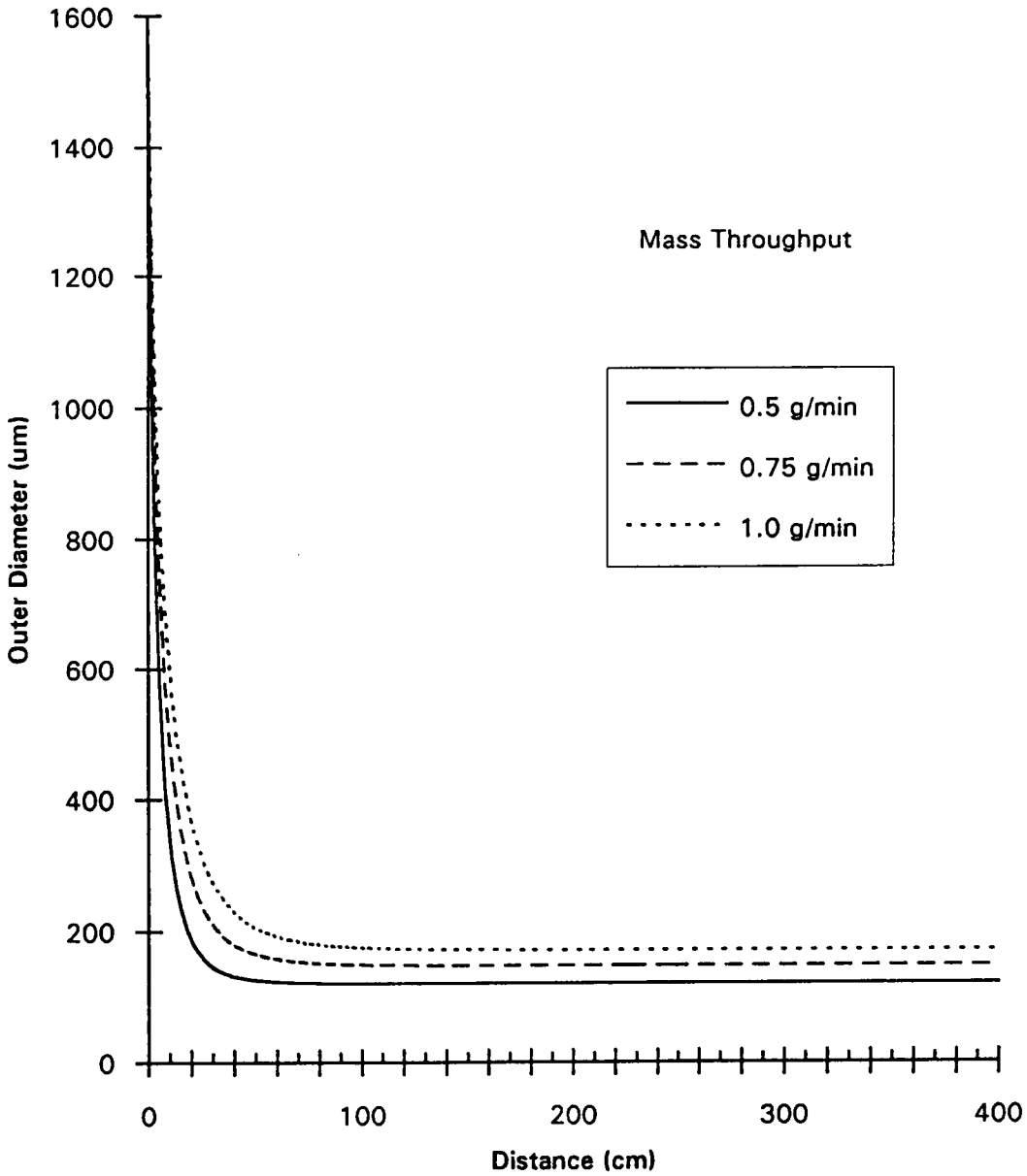

Figure 7.1.4 Influence of mass throughput (0.5, 0.75 and 1.0 g/min) on predicted outer diameter profiles along spinline.

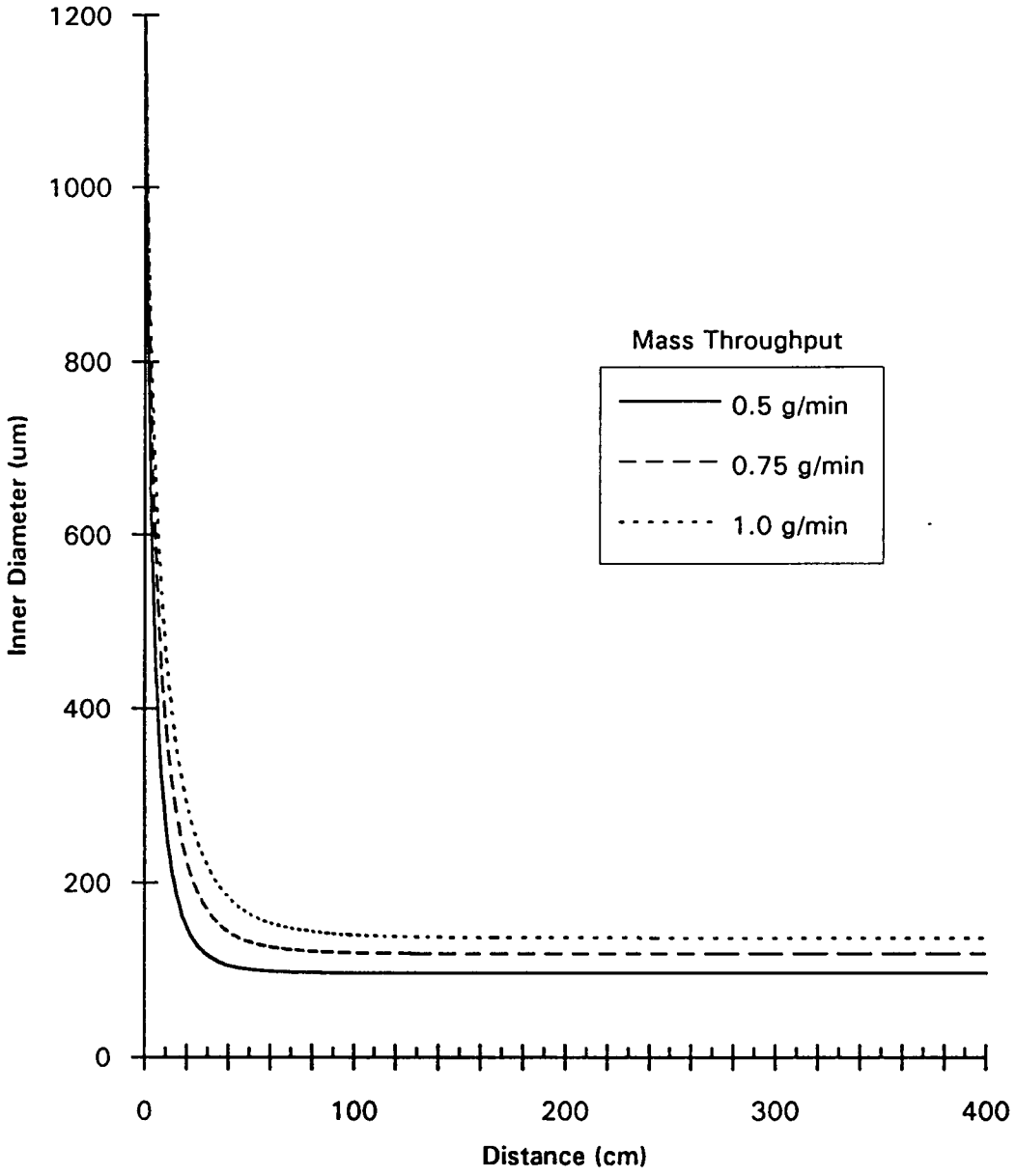

Figure 7.1.5 Influence of mass throughput (0.5, 0.75 and 1.0 g/min) on predicted inner diameter profiles along spinline.

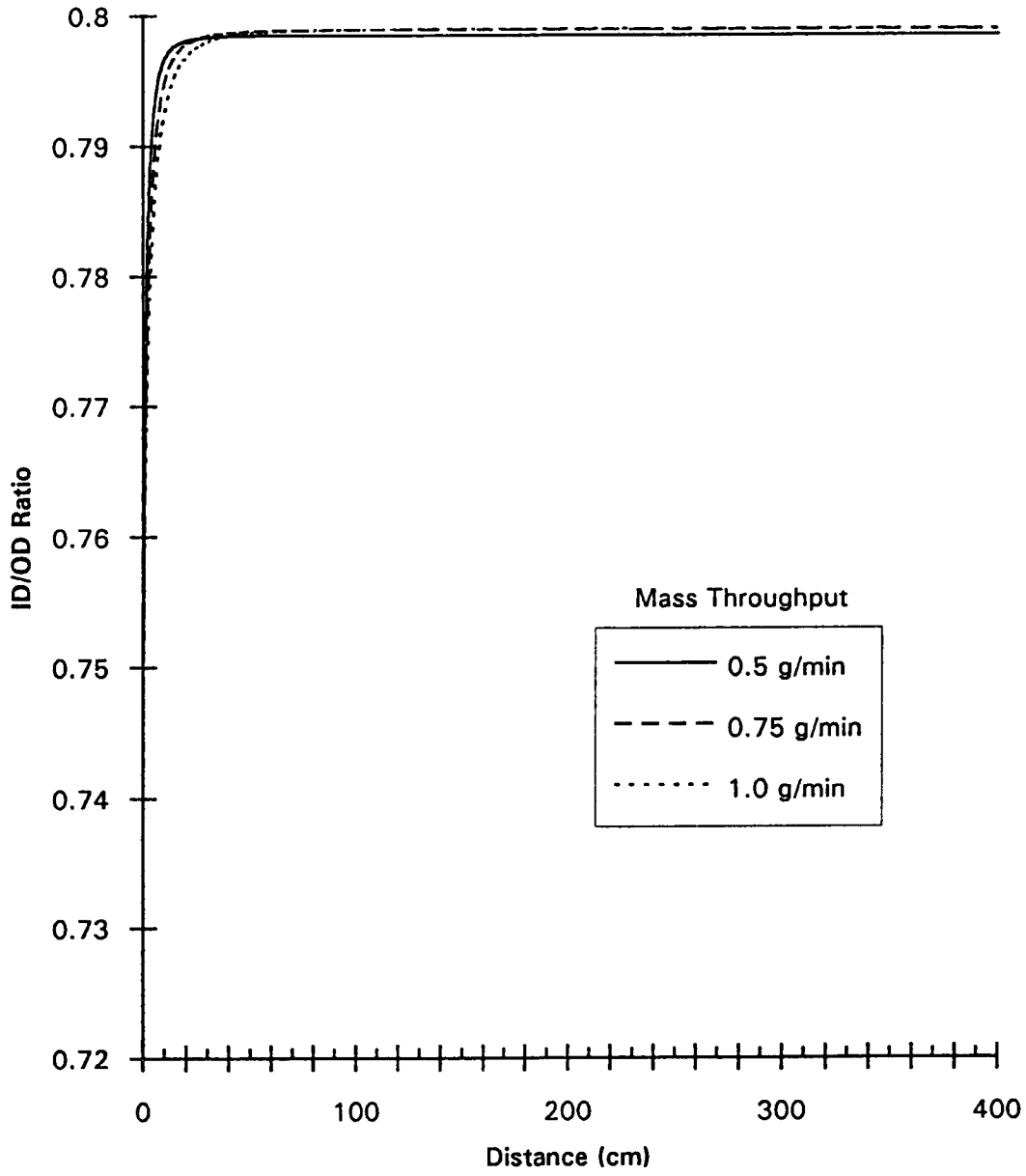

Figure 7.1.6 Influence of mass throughput (0.5, 0.75 and 1.0 g/min) on predicted ID/OD ratio profiles along spinline.

Another important parameter of hollow filament is its wall thickness. With constant take-up speed, the wall thickness of hollow filament increases with increasing mass throughput as presented in Figure 7.1.7.

The spinline temperature profile is greatly affected by mass throughput as demonstrated in Figure 7.1.8. The depression of temperature of the filament near the spinneret is caused by the heat loss due to rapid vaporization of the solvent. In Contrast, the spinline temperature profile is only slightly varied by changing take-up speed, under constant mass throughput shown in Figure 7.1.9.

The profiles of solvent concentration in the hollow filament are shown in Figures 7.1.10 to 7.1.12 for varying mass throughput. Figure 7.1.13 shows the profiles of the average solvent concentration in the filament along the spinline. The solvent concentration profile is significantly influenced by mass throughput. The solvent concentration decreases much faster along the spinline under lower mass throughput conditions than higher mass throughput.

7.2 Effect of PAN Concentration in the Spinning Dope

PAN concentration in the spinning dope determines its viscosity, which further influences the dynamics of the

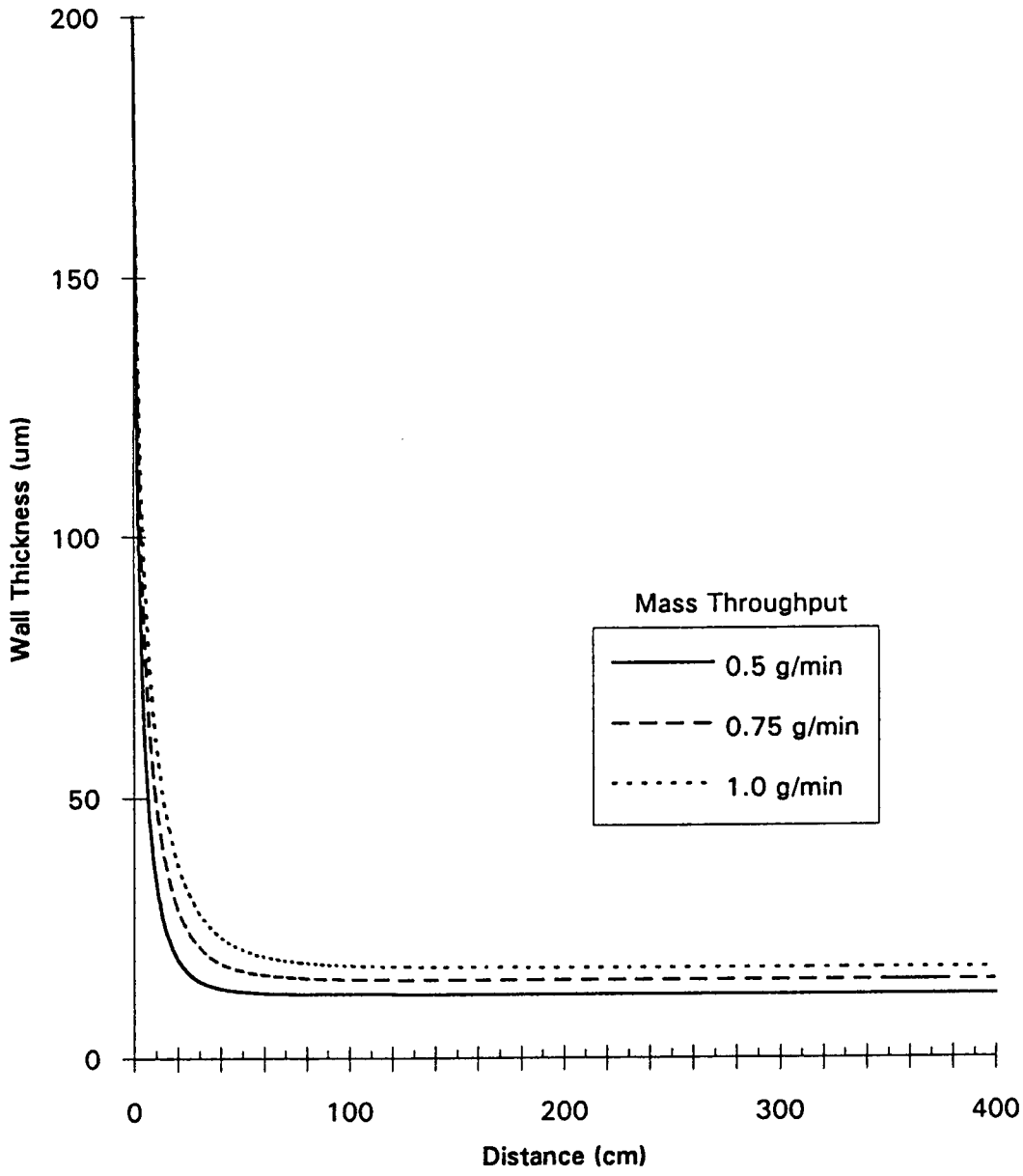

Figure 7.1.7 Influence of mass throughput (0.5, 0.75 and 1.0 g/min) on predicted wall thickness profiles along spinline.

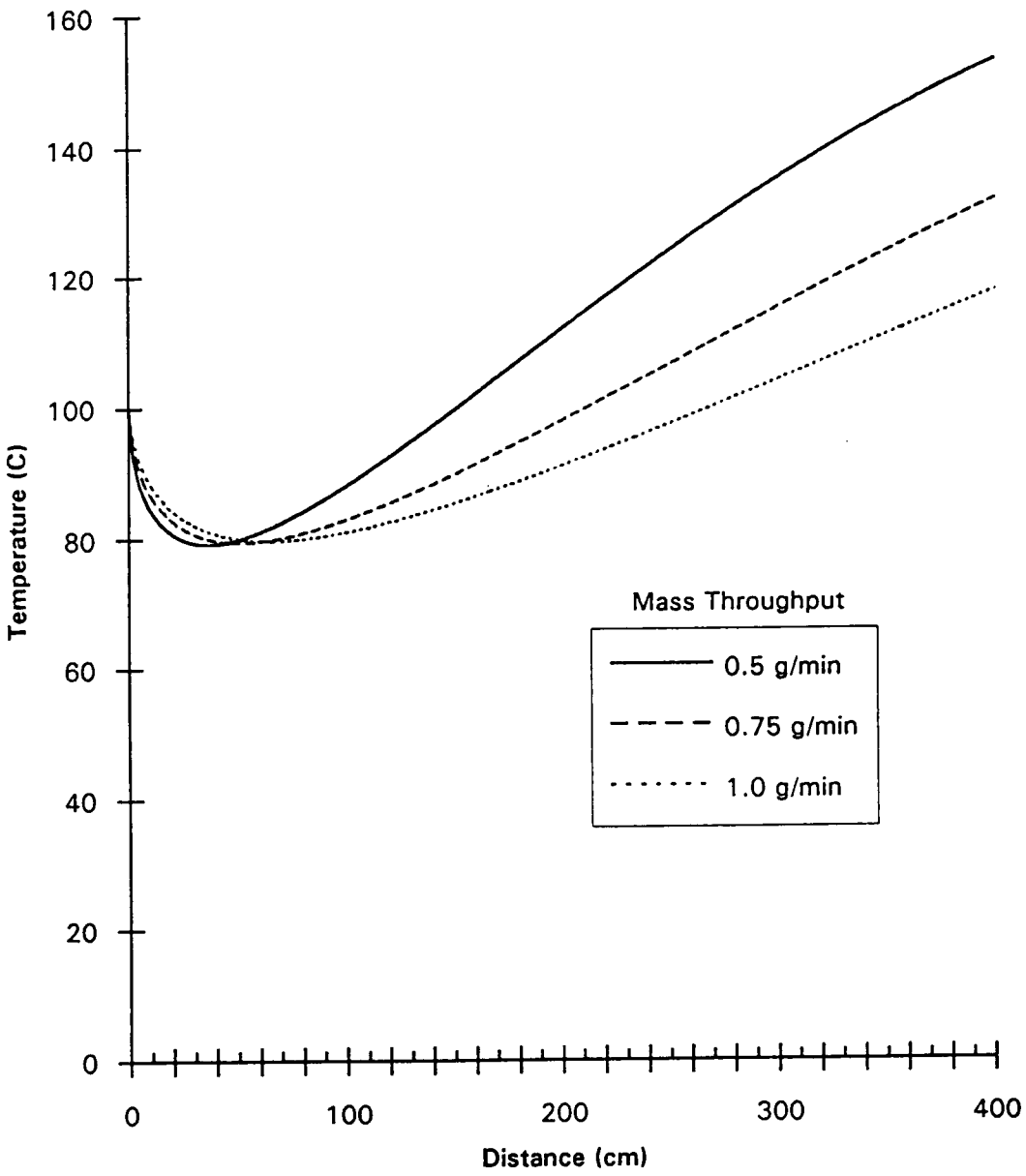

Figure 7.1.8 Influence of mass throughput (0.5, 0.75 and 1.0 g/min) on predicted temperature profiles along spinline.

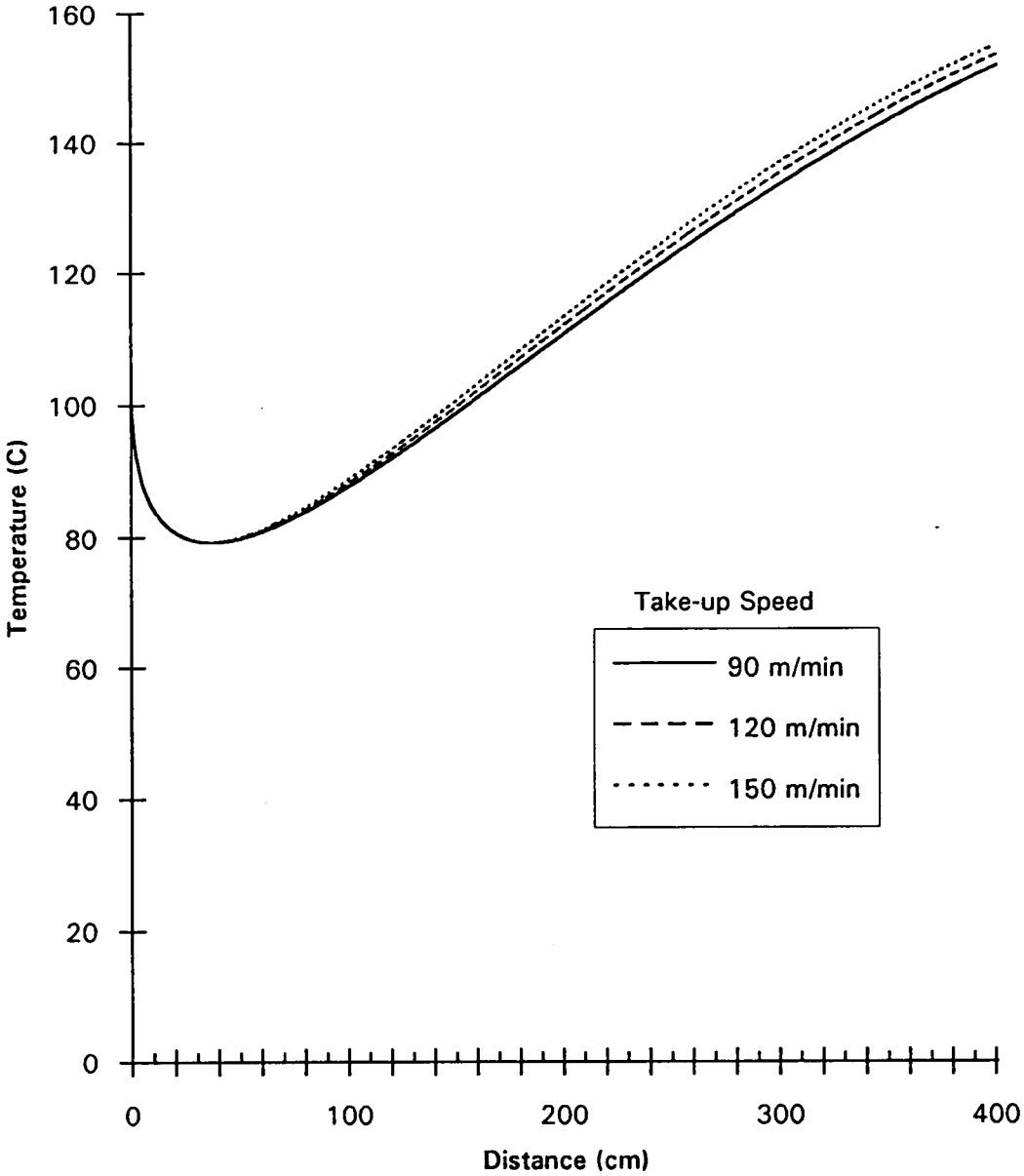

Figure 7.1.9 Influence of take-up speed (90, 120 and 150 m/min) on predicted temperature profiles along spinline.

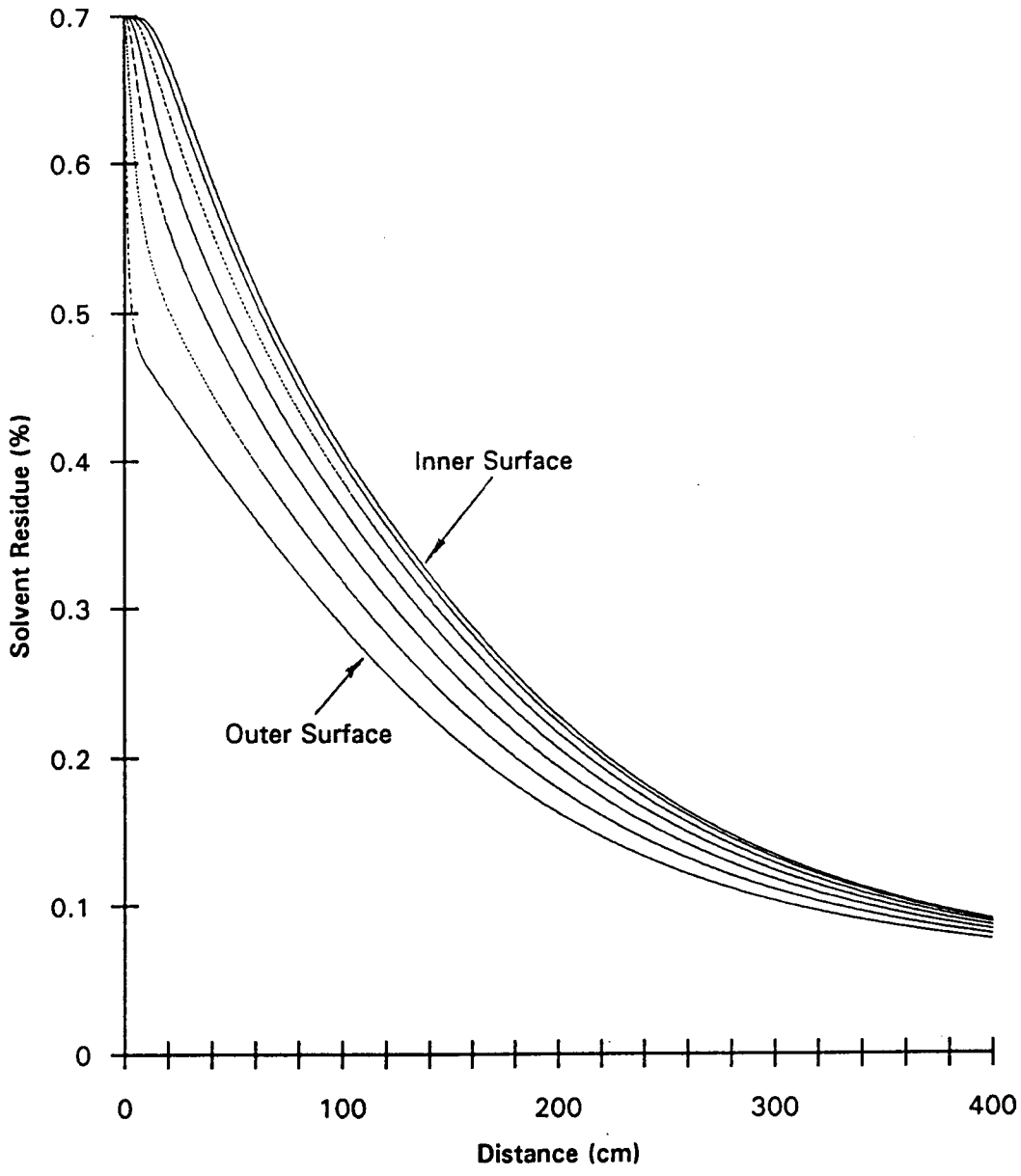

Figure 7.1.10 Radial distribution of predicted solvent concentration in hollow filament along spinline (mass throughput 0.5 g/min).

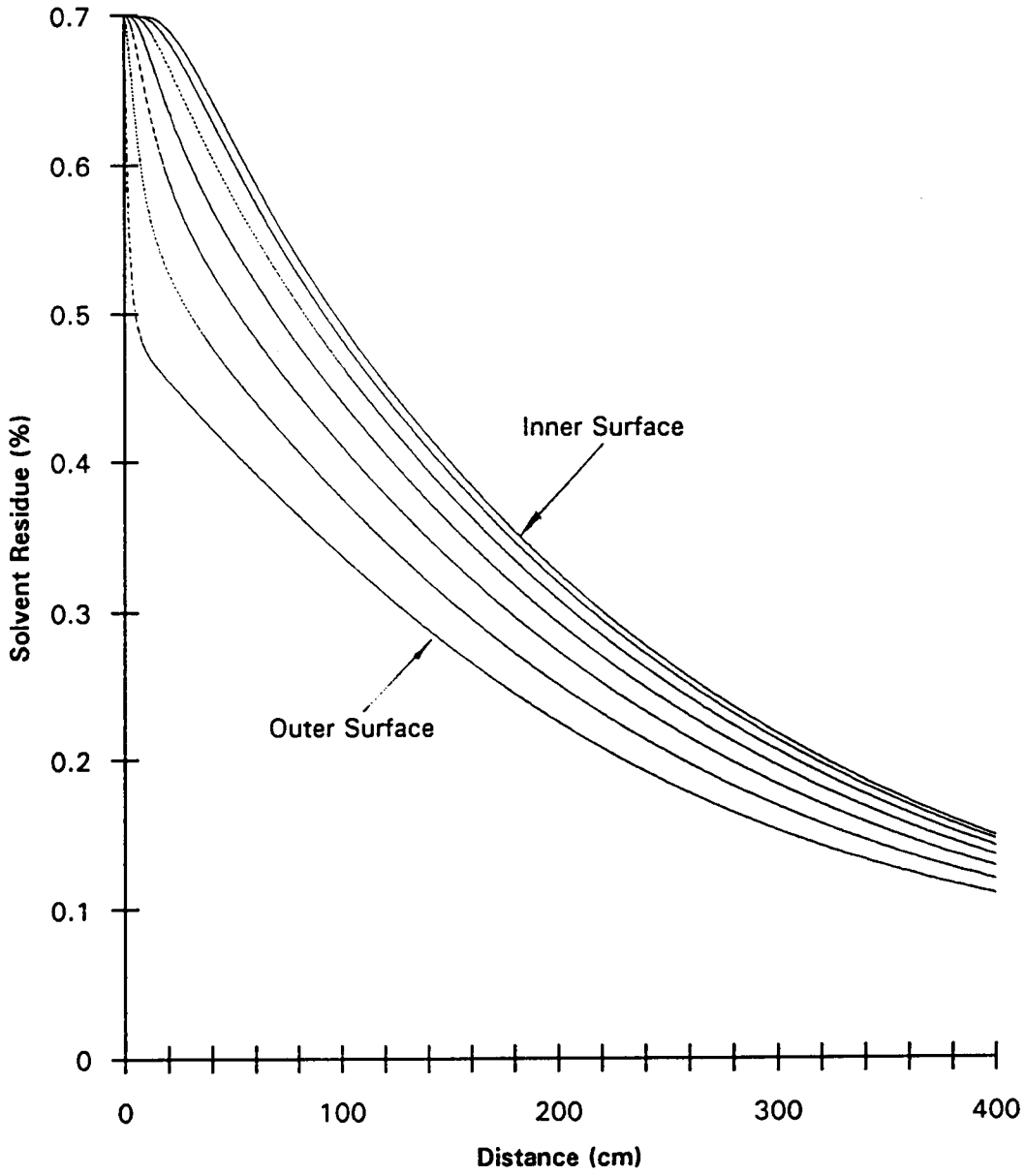

Figure 7.1.11 Radial distribution of predicted solvent concentration in hollow filament along spinline (mass throughput 0.75 g/min).

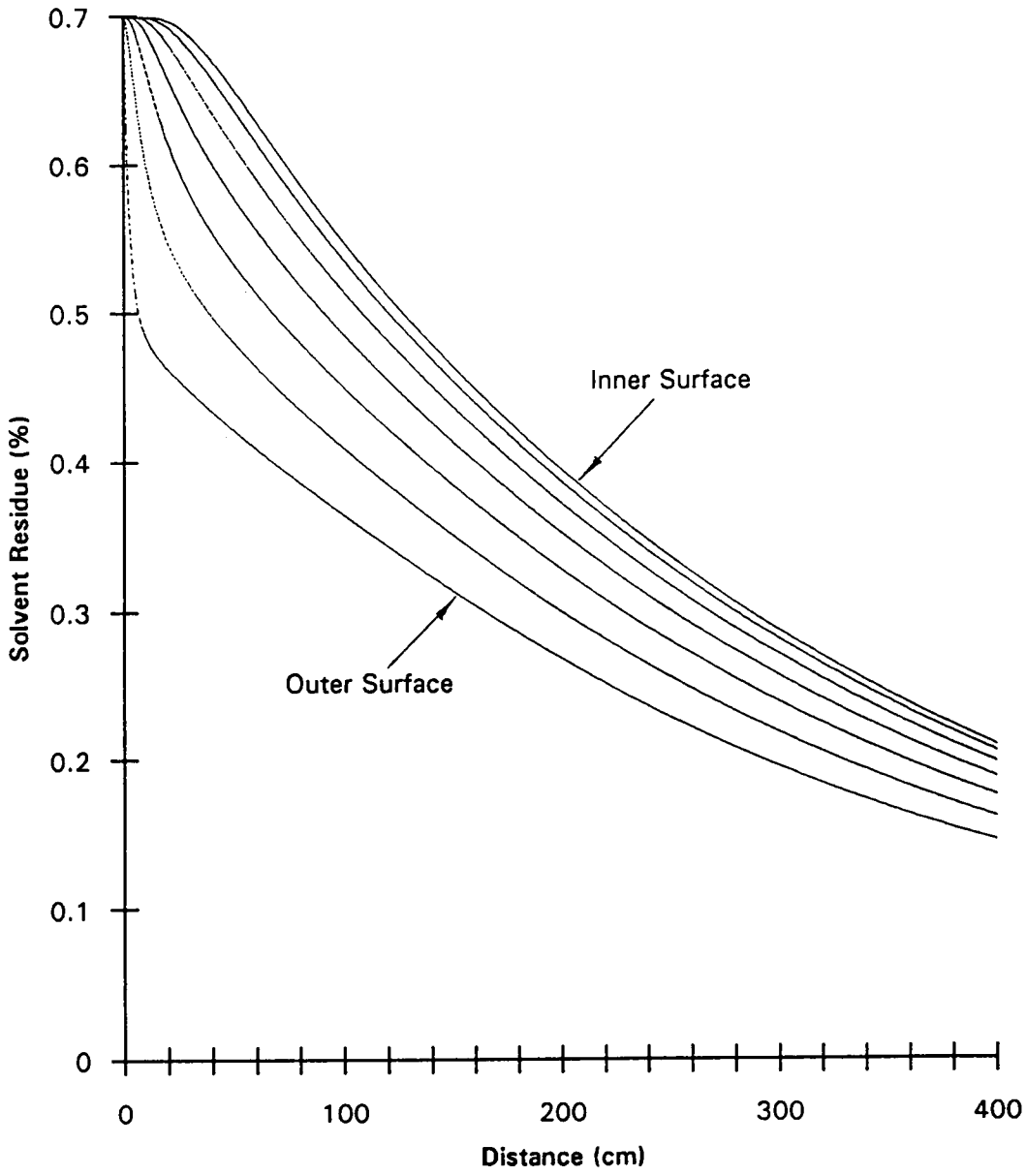

Figure 7.1.12 Radial distribution of predicted solvent concentration in hollow filament along spinline (mass throughput 1.0 g/min).

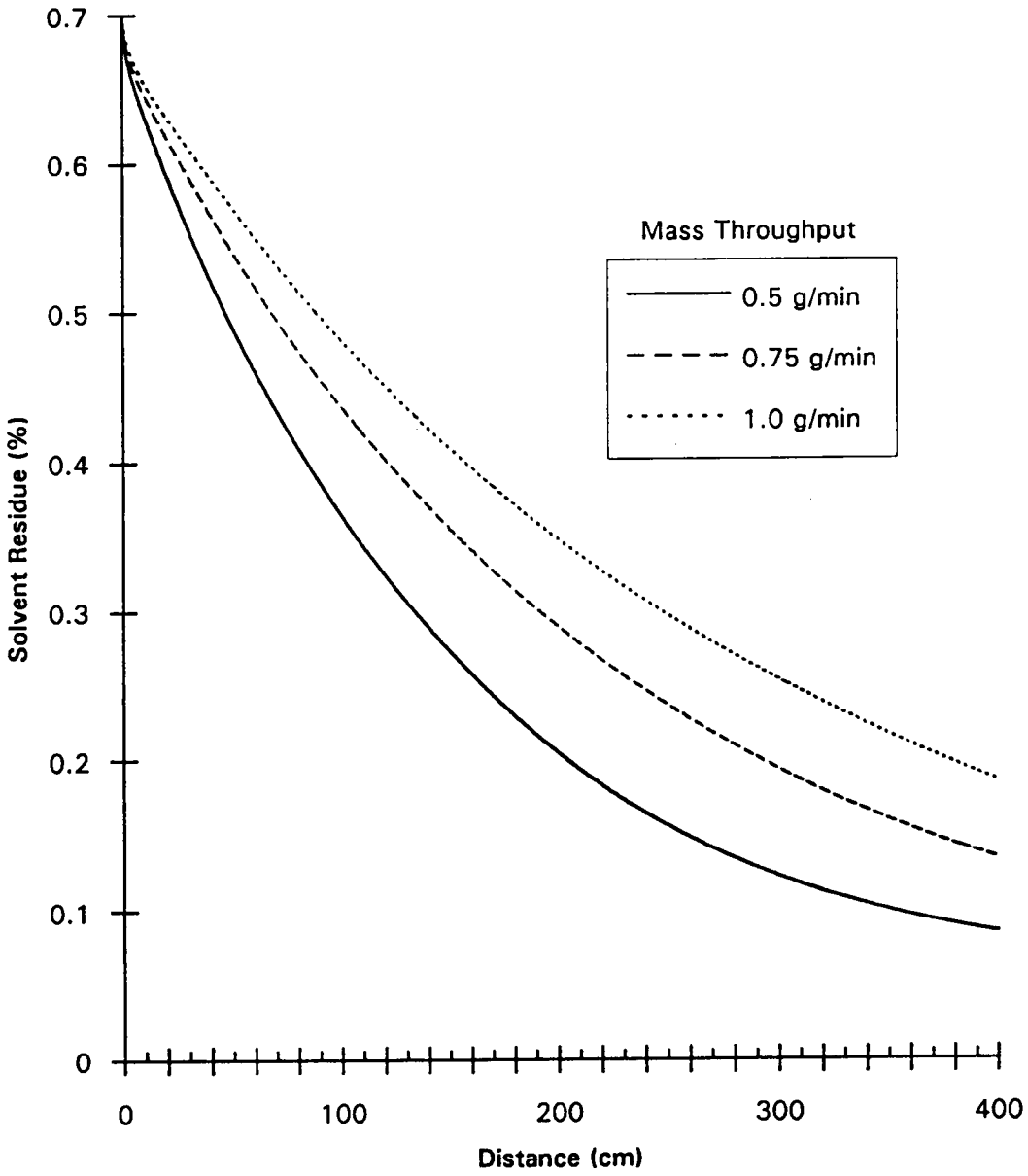

Figure 7.1.13 Predicted average solvent concentration in hollow filament along spinline (mass throughput 0.5, 0.75 and 1.0 g/min).

spinline and characteristics of the resulting hollow filament.

Figures 7.2.1 and 7.2.2 show velocity and velocity gradient profiles along the spinline predicted by modeling for three different levels of PAN concentration in the spinning dope. The velocity gradient (deformation rate) is broadened, and the maximum value of velocity gradient is reduced with increasing PAN concentration in the spinning dope. This phenomenon indicates that the deformation along the spinline is more rapid and more localized with lower viscosity dope (25% PAN) than higher viscosity dope (35% PAN).

Both inner and outer diameters of hollow filament increase with decreasing PAN concentration in the spinning dope (Figures 7.2.3 and 7.2.4). The wall thickness of hollow filament decreases with decreasing PAN concentration in the spinning dope as shown in Figure 7.2.5. These effects result from the interaction of axial stress (caused by the take-up device) and the hoop stress (caused by internal pressure). The axial stress tends to draw down the filament in the spinline and reduces hollow filament diameter, while the hoop stress tends to sustain or expand the diameter of the hollow filament. Since the internal pressure is maintained at a constant level of 500 dynes/cm^2 in this case, the hoop stress is relatively constant.

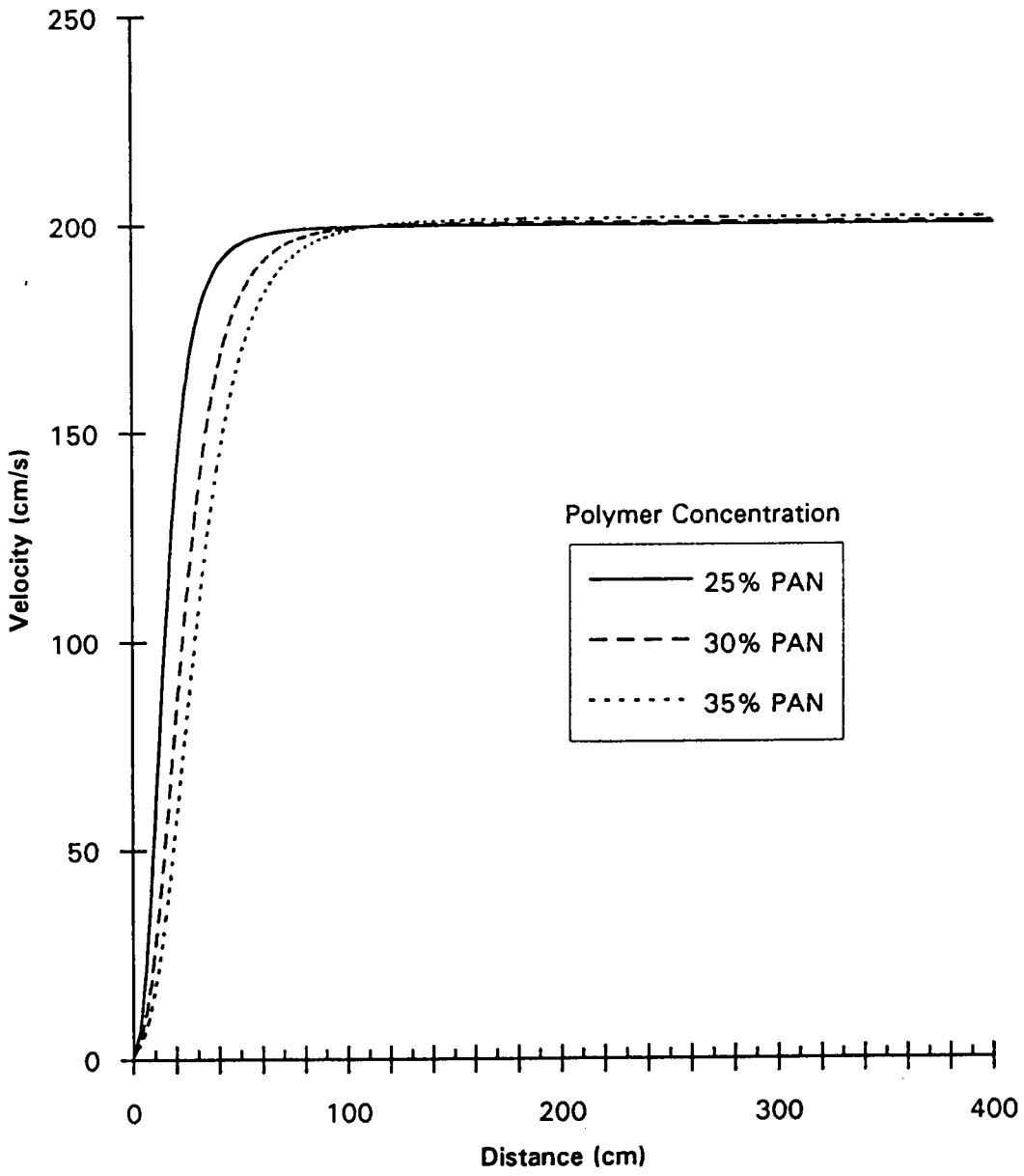

Figure 7.2.1 Influence of PAN concentration (25%, 30% and 35%) on predicted spinline velocity profiles.

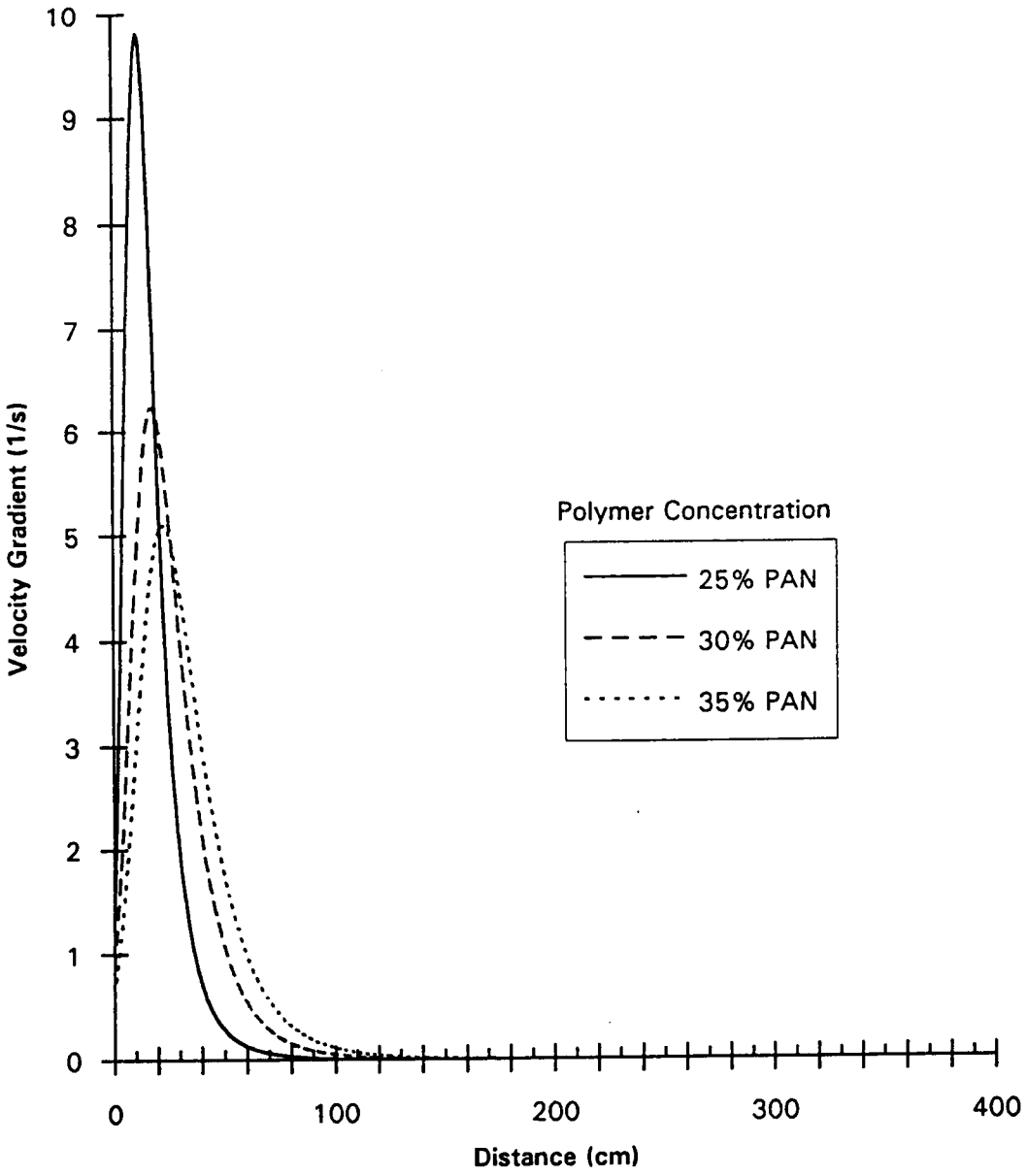

Figure 7.2.2 Influence of PAN concentration (25%, 30% and 35%) on predicted spinline velocity gradient profiles.

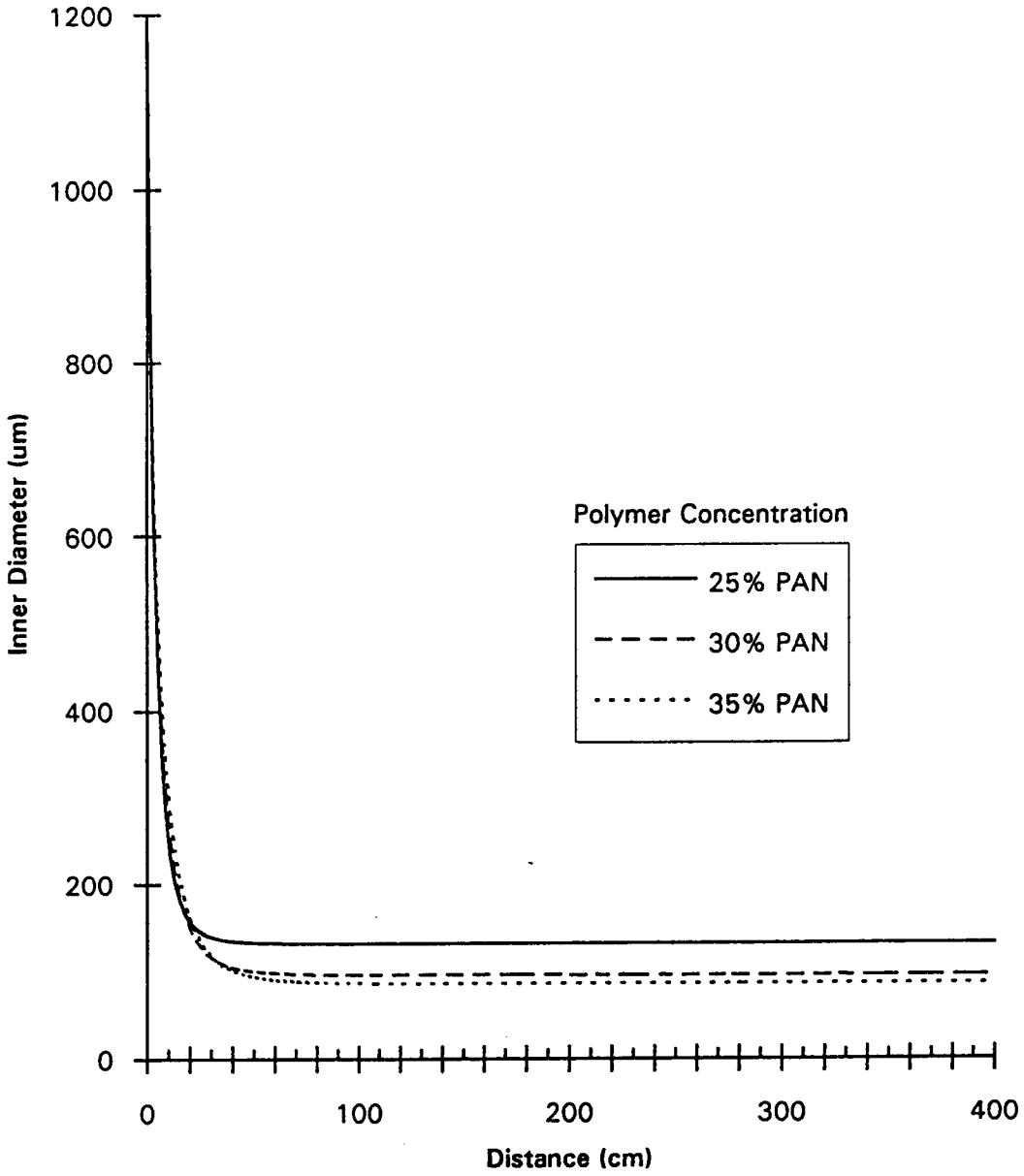

Figure 7.2.3 Influence of PAN concentration (25%, 30% and 35%) on predicted inner diameter profiles along spinline.

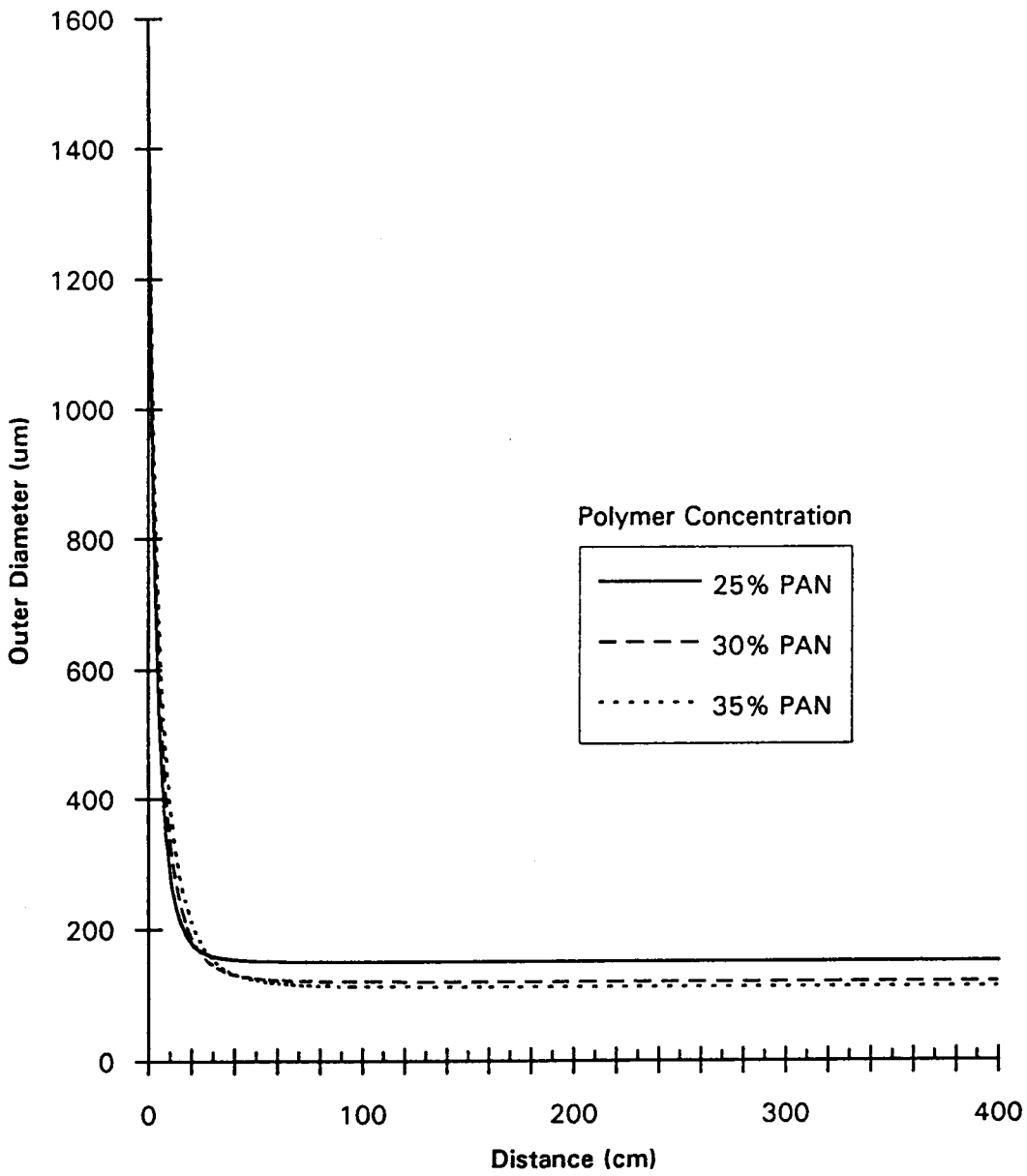

Figure 7.2.4 Influence of PAN concentration (25%, 30% and 35%) on predicted outer diameter profiles along spinline.

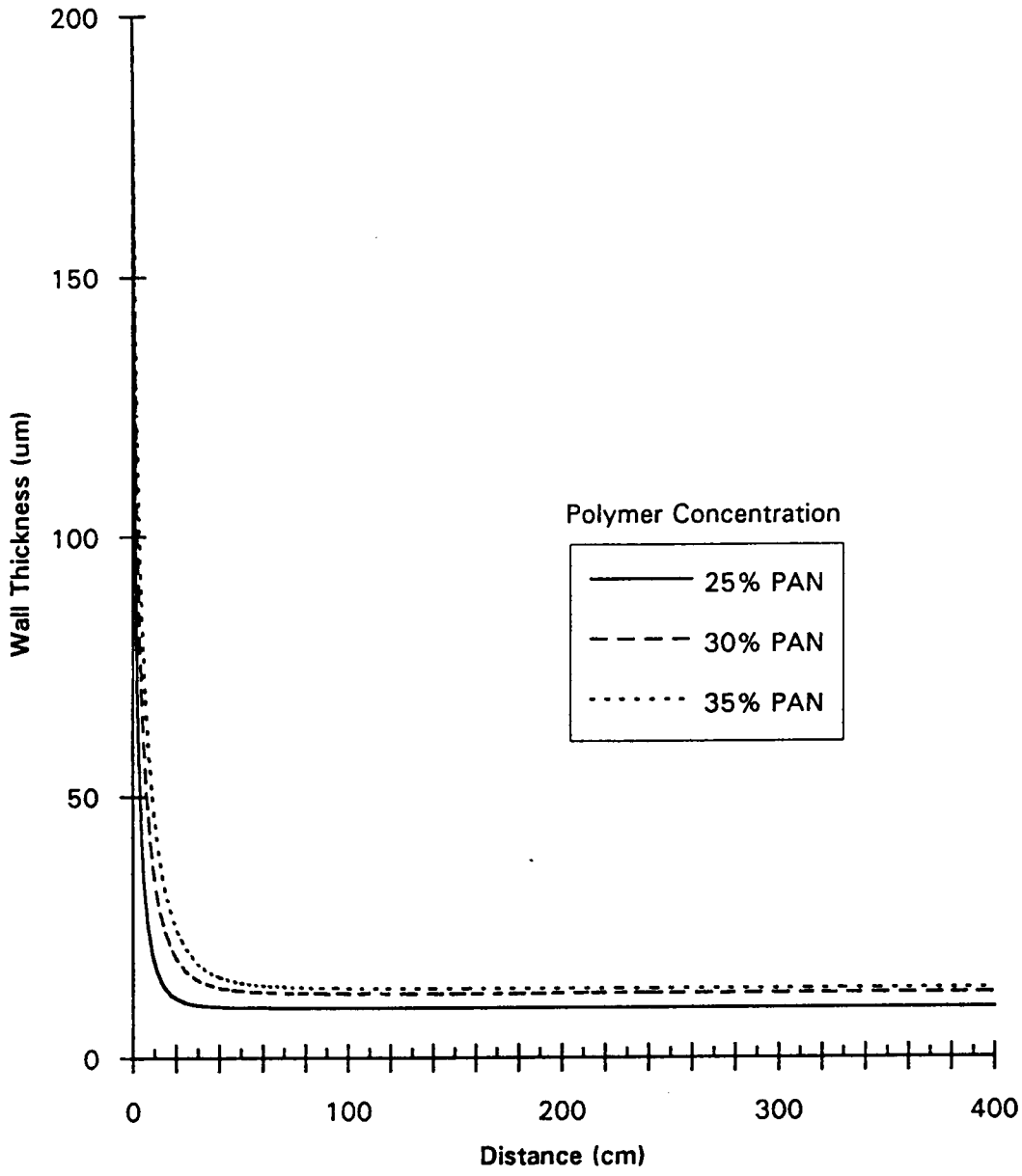

Figure 7.2.5 Influence of PAN concentration (25%, 30% and 35%) on predicted wall thickness profiles along spinline.

Because the spinning dope with lower PAN concentration has a lower viscosity, the axial stress in the spinline decreases with reducing PAN concentration in the spinning dope while other conditions remain constant (Figure 7.2.6). The decrease of axial stress by reducing PAN concentration causes the increase of diameter of hollow filament. Furthermore, the ratio of inner diameter over outer diameter (ID/OD) is significantly higher for lower PAN concentration dope than higher PAN concentration dope as demonstrated in Figure 7.2.7.

The solvent concentration profiles in Figure 7.2.8 show more rapid evaporation of solvent (compare slopes of solvent concentration profiles) at the beginning part of the spinline for lower PAN percentage dope than higher PAN percentage dope. The physical reason is that higher contents of solvent in the spinning dope has a higher potential for solvent diffusion, which results in higher diffusion rate in the spinline near the spinneret. However, PAN percentage in the spinning dope has little effect on final solvent residues in as-spun hollow filament.

The spinline temperature profiles are also affected by PAN concentration in the spinning dope. Figure 7.2.9 shows temperature profiles predicted by the model for 25%, 30% and 35% PAN in the spinning dope. Lower PAN concentration in the dope (higher solvent concentration) results a lower

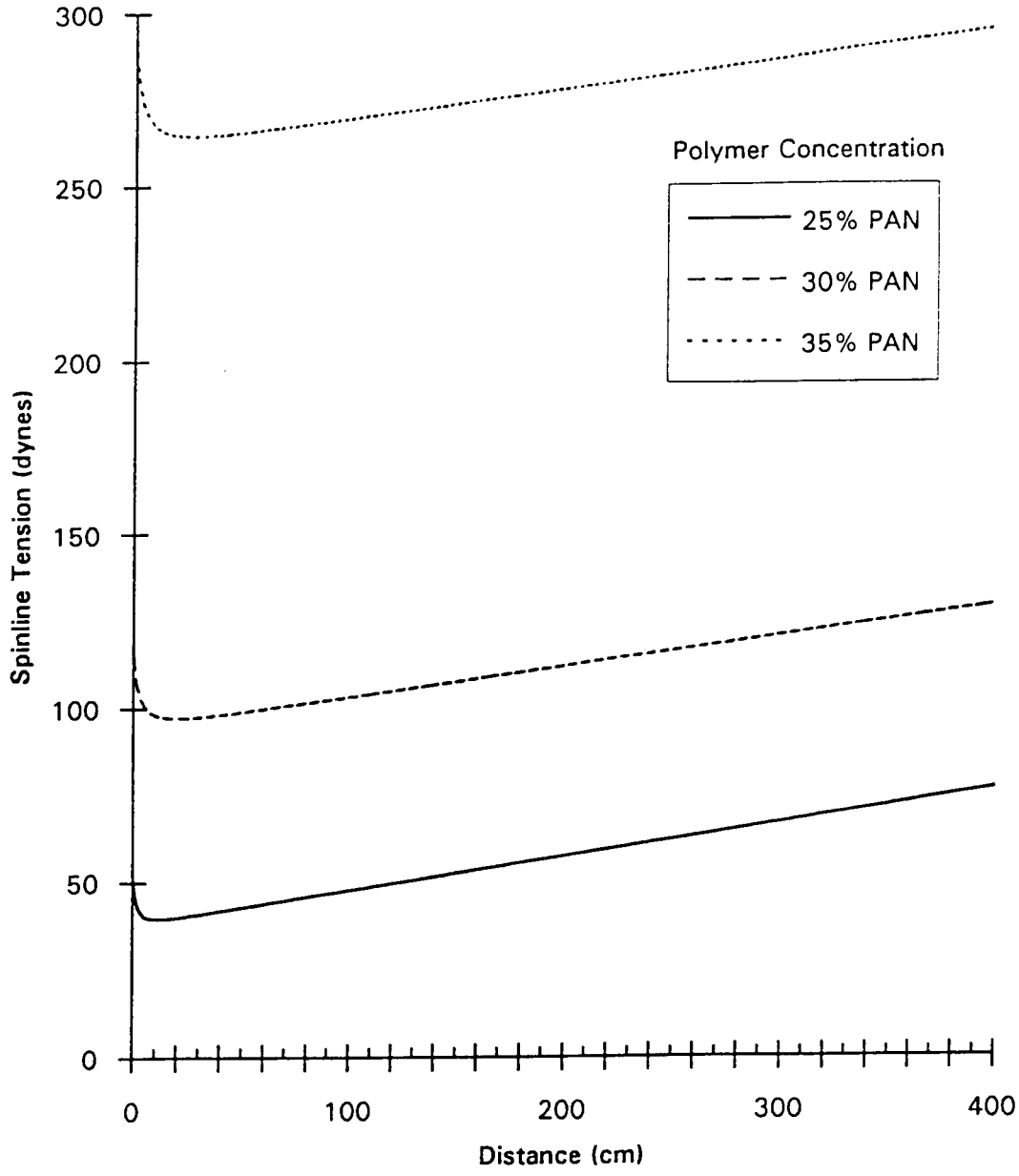

Figure 7.2.6 Influence of PAN concentration (25%, 30% and 35%) on predicted tension profiles along spinline.

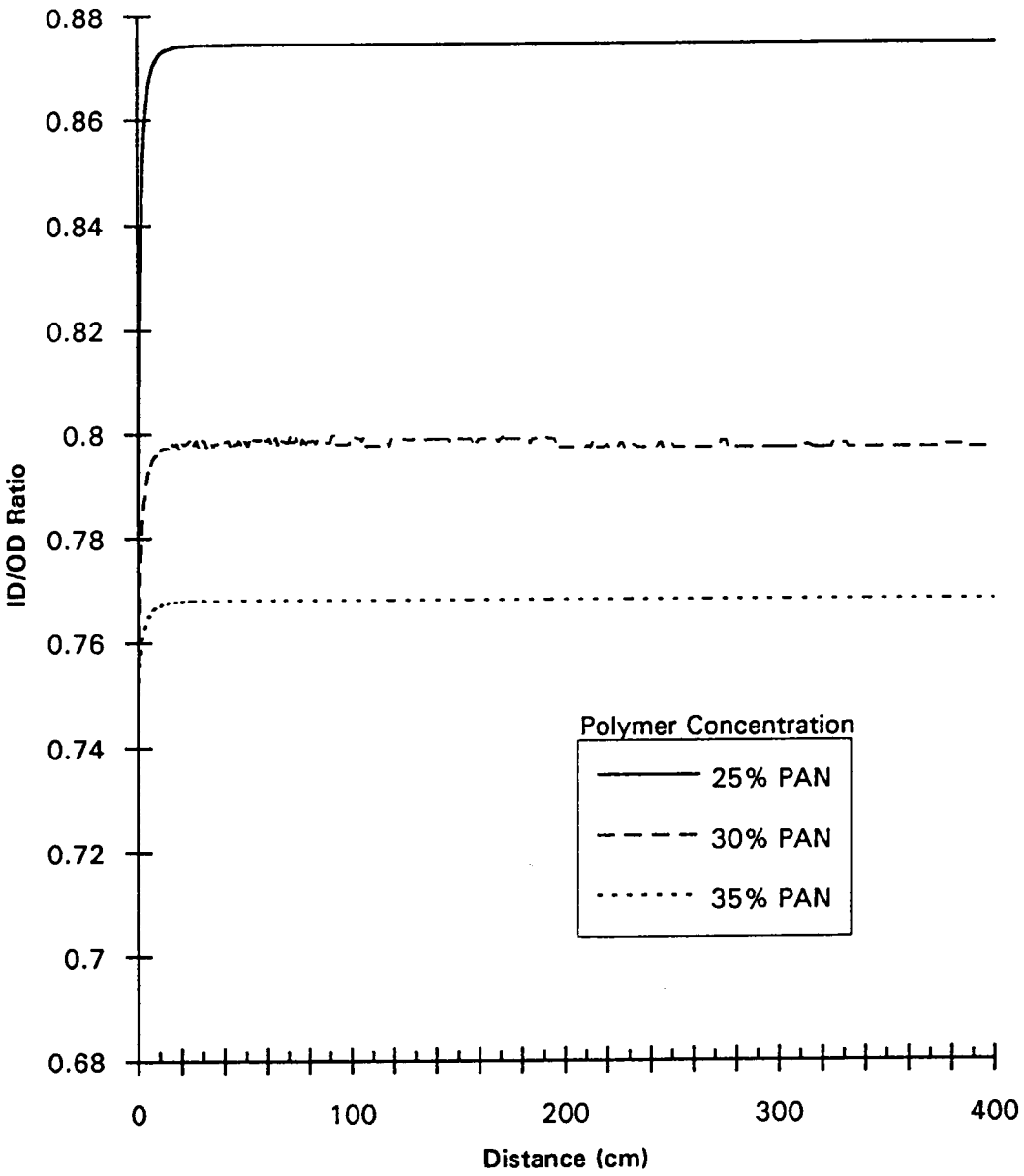

Figure 7.2.7 Influence of PAN concentration (25%, 30% and 35%) on predicted ID/OD ratio profiles along spinline.

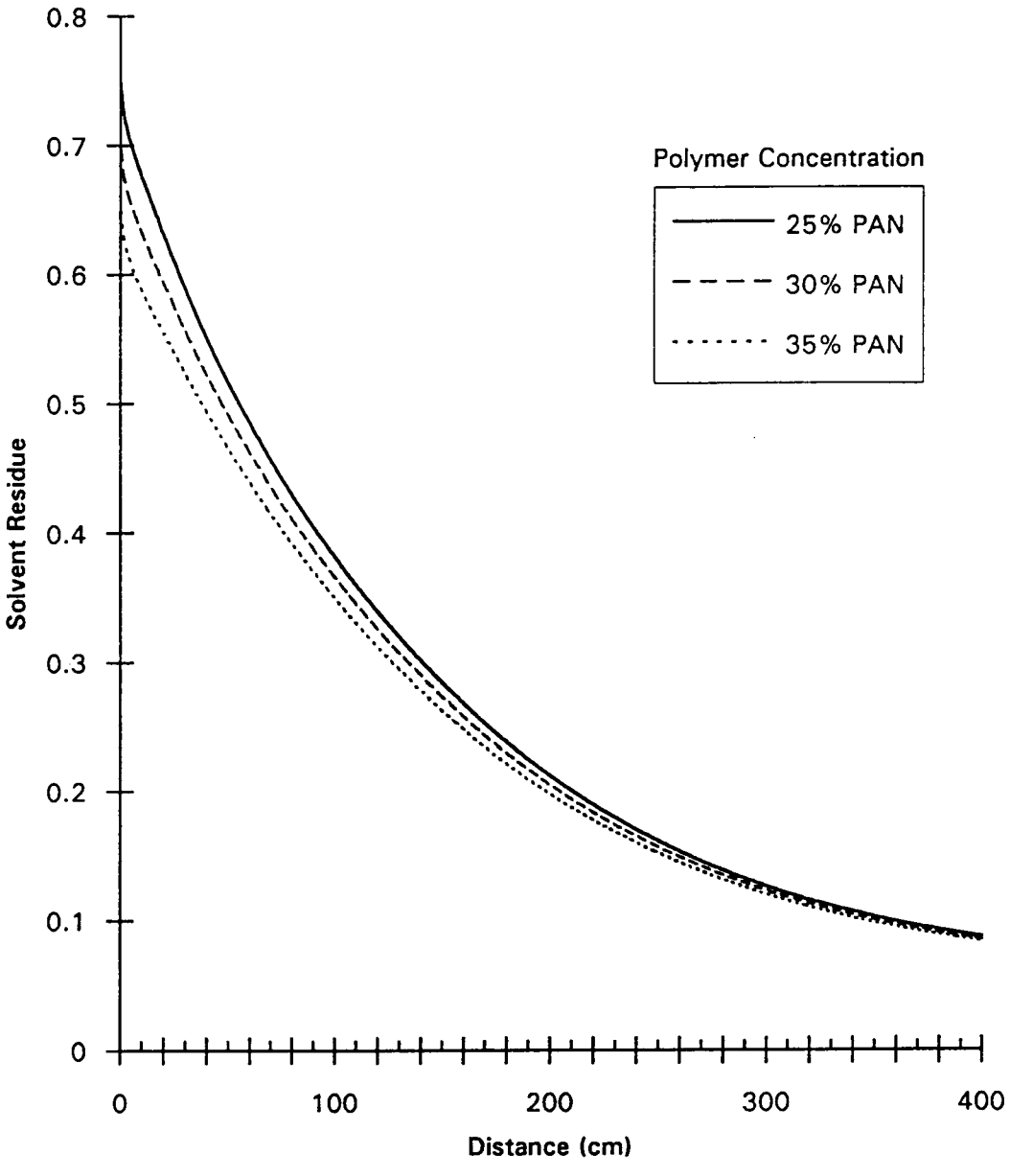

Figure 7.2.8 Predicted average solvent residue in hollow filament along spinline (25%, 30% and 35% PAN in the dope).

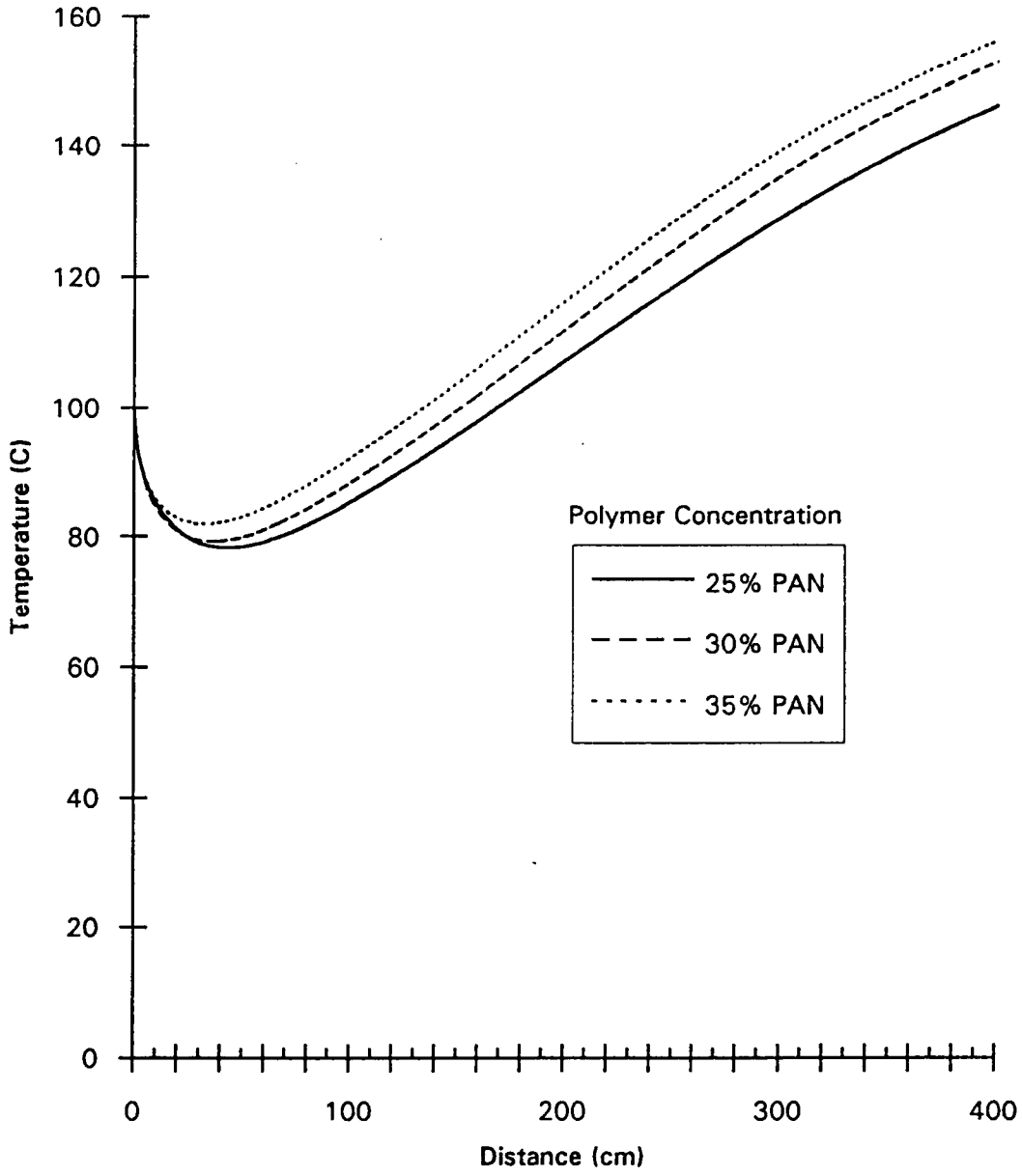

Figure 7.2.9 Influence of PAN concentration (25%, 30% and 35%) on predicted temperature profiles along spinline.

level of temperature profile along the spinline due to the fact that energy loss is proportional to the amount of solvent evaporated.

7.3 Effect of Inner Pressure

Internal pressure provides the hoop stress to sustain or expand the internal hole in the hollow filament.

Figures 7.3.1 and 7.3.2 present spinline velocity and thickness profiles predicted by the model, with three levels of internal pressure - 250, 500 and 750 dynes/cm^2. Both velocity and thickness profiles are only slightly affected by changing internal pressure. However, the ratio of inner diameter over outer diameter (ID/OD) is greatly impacted by varying internal pressure. The ratio of ID/OD increases significantly with increasing internal pressure as shown in Figure 7.3.3.

7.4 Effect of Spin Column Temperature

The heated air in the spin column provides a means to evaporate and carry away the solvent component from hollow filament along the spinline. The air temperature in the spin column has some effect on spinline behavior, especially as regards heat transfer and mass transfer.

Figure 7.4.1 presents predicted temperature profiles of hollow filament along the spinline, spun under spin

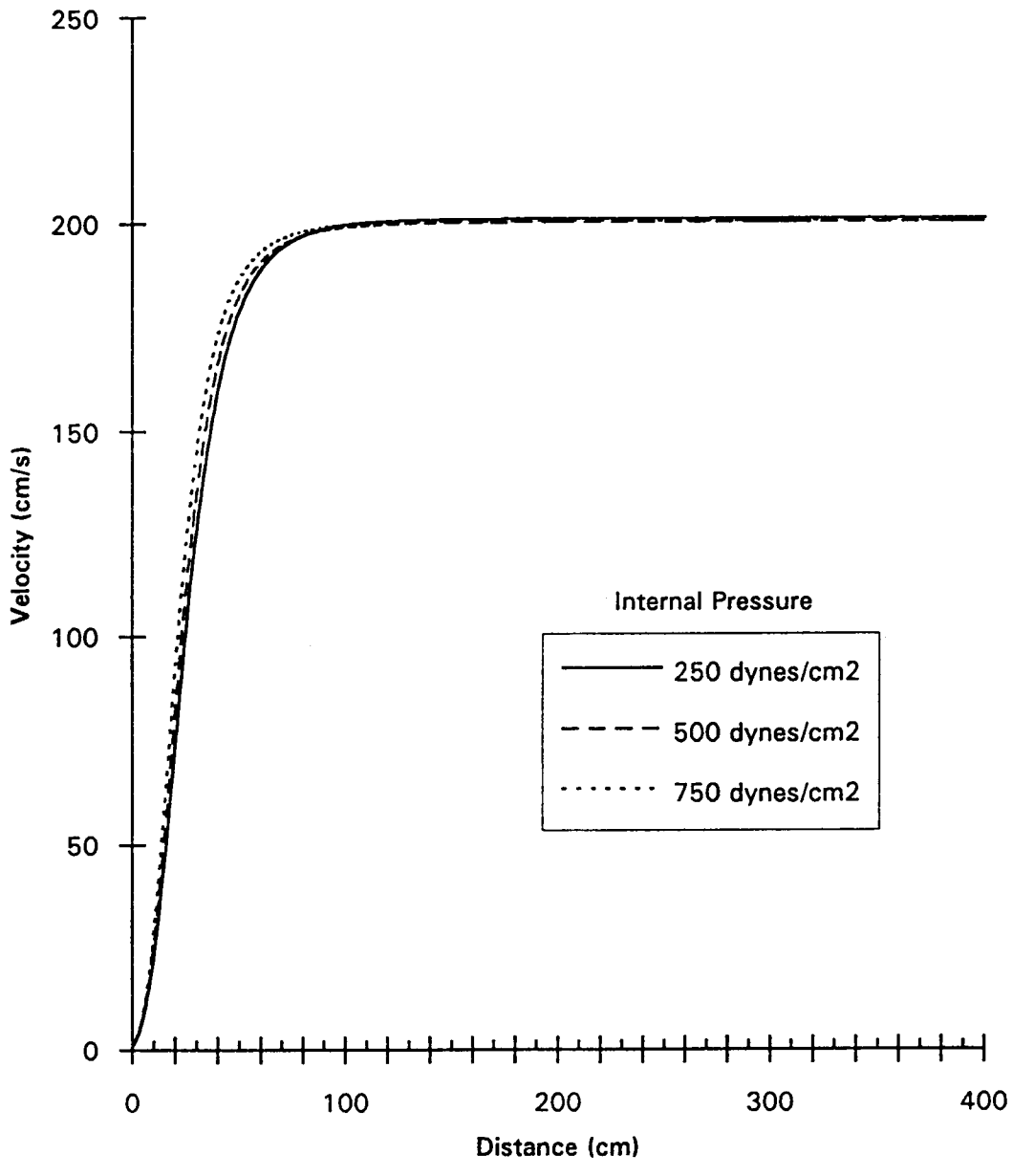

Figure 7.3.1 Influence of internal pressure (250, 500 and 750 dynes/cm^2) on predicted spinline velocity profiles.

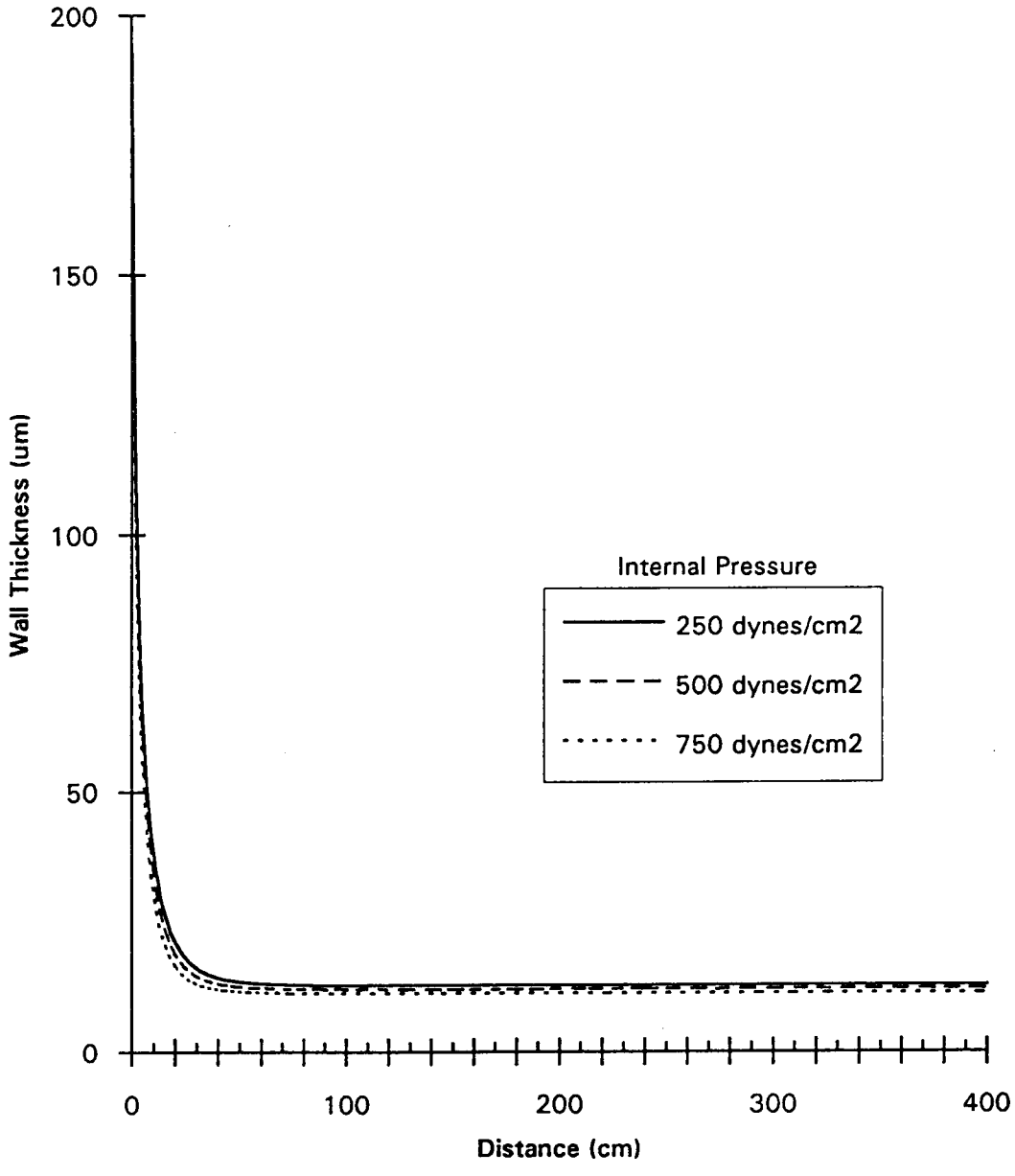

Figure 7.3.2 Influence of internal pressure (250, 500 and 750 dynes/cm^2) on predicted wall thickness profiles along spinline.

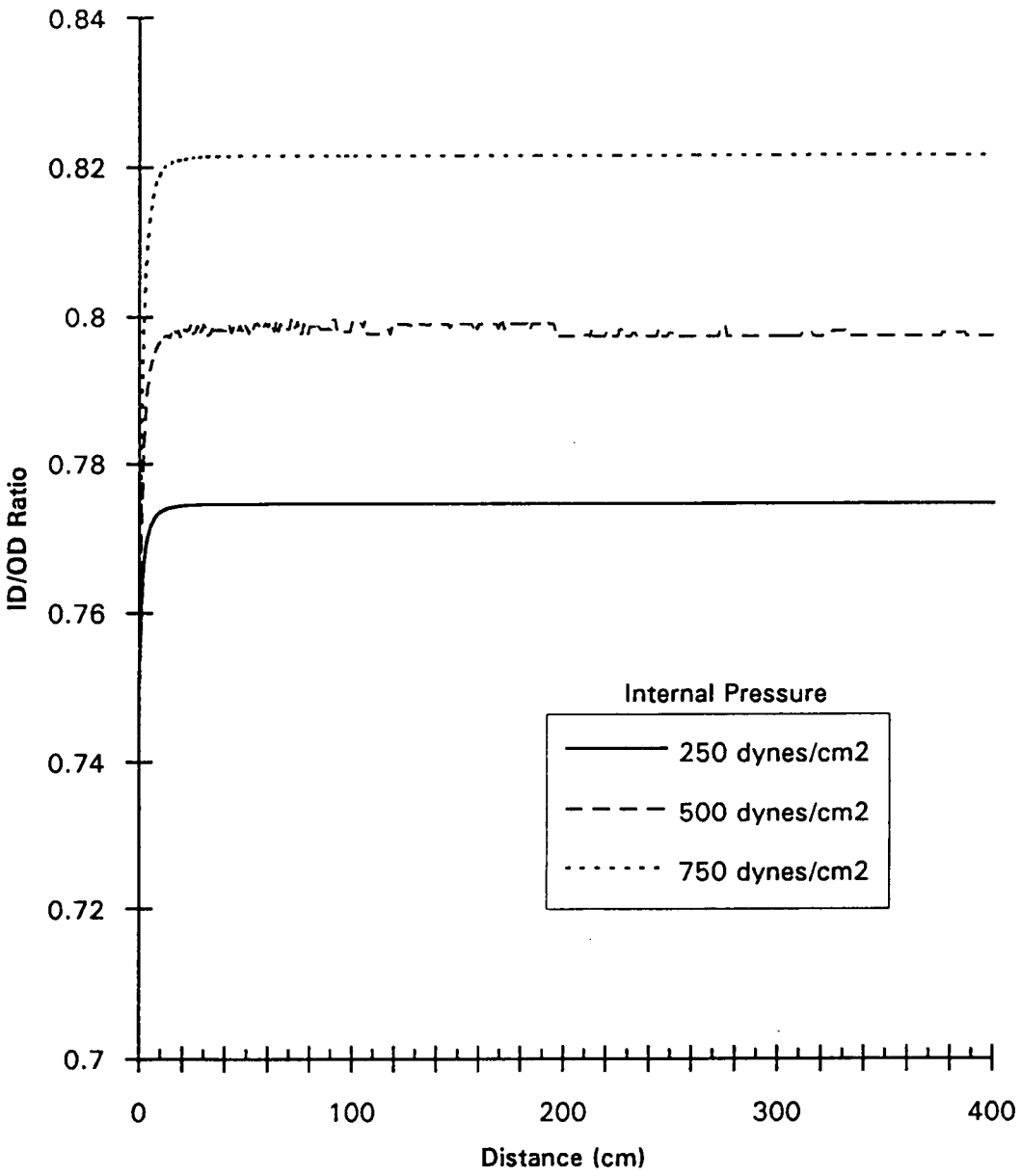

Figure 7.3.3 Influence of internal pressure (250, 500 and 750 dynes/cm^2) on predicted ID/OD ratio profiles along spinline.

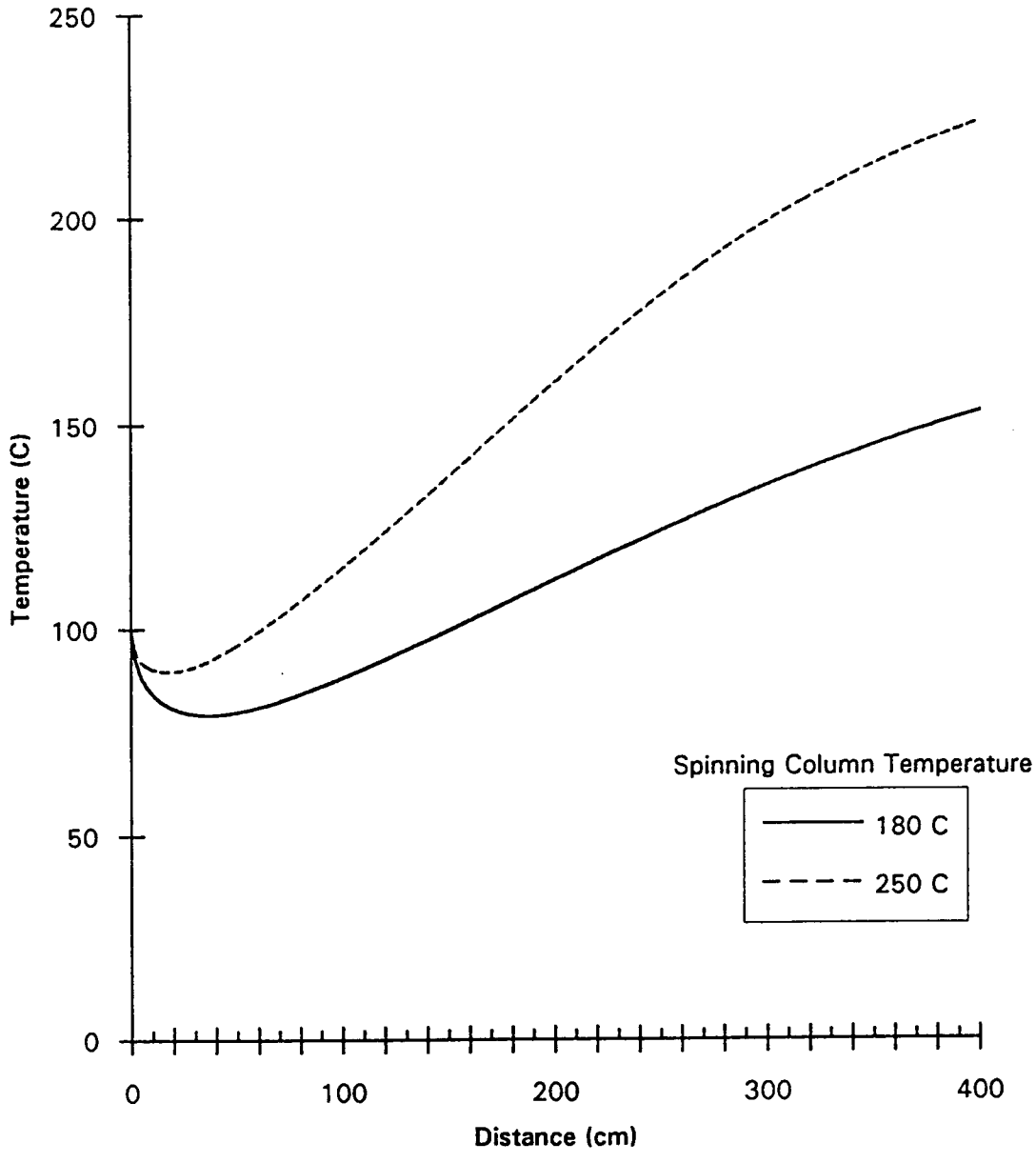

Figure 7.4.1 Influence of spin column temperature (180 and 250°C) on predicted temperature profiles along spinline.

column temperatures of 180 C and 250 C, respectively. As expected, the rise of filament temperature along spinline is much fast under the temperature of 250 C than 180 C.

The greatest benefit of using higher spin column temperature is to be able to evaporate solvent from hollow filament faster along the spinline as show in Figure 7.4.2. The higher spin column temperature results in lower solvent residue in as-spun hollow filament with the rest of the processing conditions fixed. In practice, the spin column length is always limited; therefore, in order to achieve low solvent residue in hollow filament, it is necessary to use high spin column temperature to speed up the evaporation of the solvent from hollow filament, especially when spinning with high mass throughput.

7.5 Effect of Exhaustion Air Flow Speed

The effect of quench air flow speed on the profiles of velocity, temperature and solvent residue along the spinline is present in Figures 7.5.1 to 7.5.3. The velocity profile in the spinline is only slightly affected by quench air flow speed. The filament temperature along the spinline is increased by using higher air flow speed because of higher heat transfer coefficient. The rate of solvent evaporation along the spinline is slightly increased with increasing quench air speed as shown in Figure 7.5.3. But

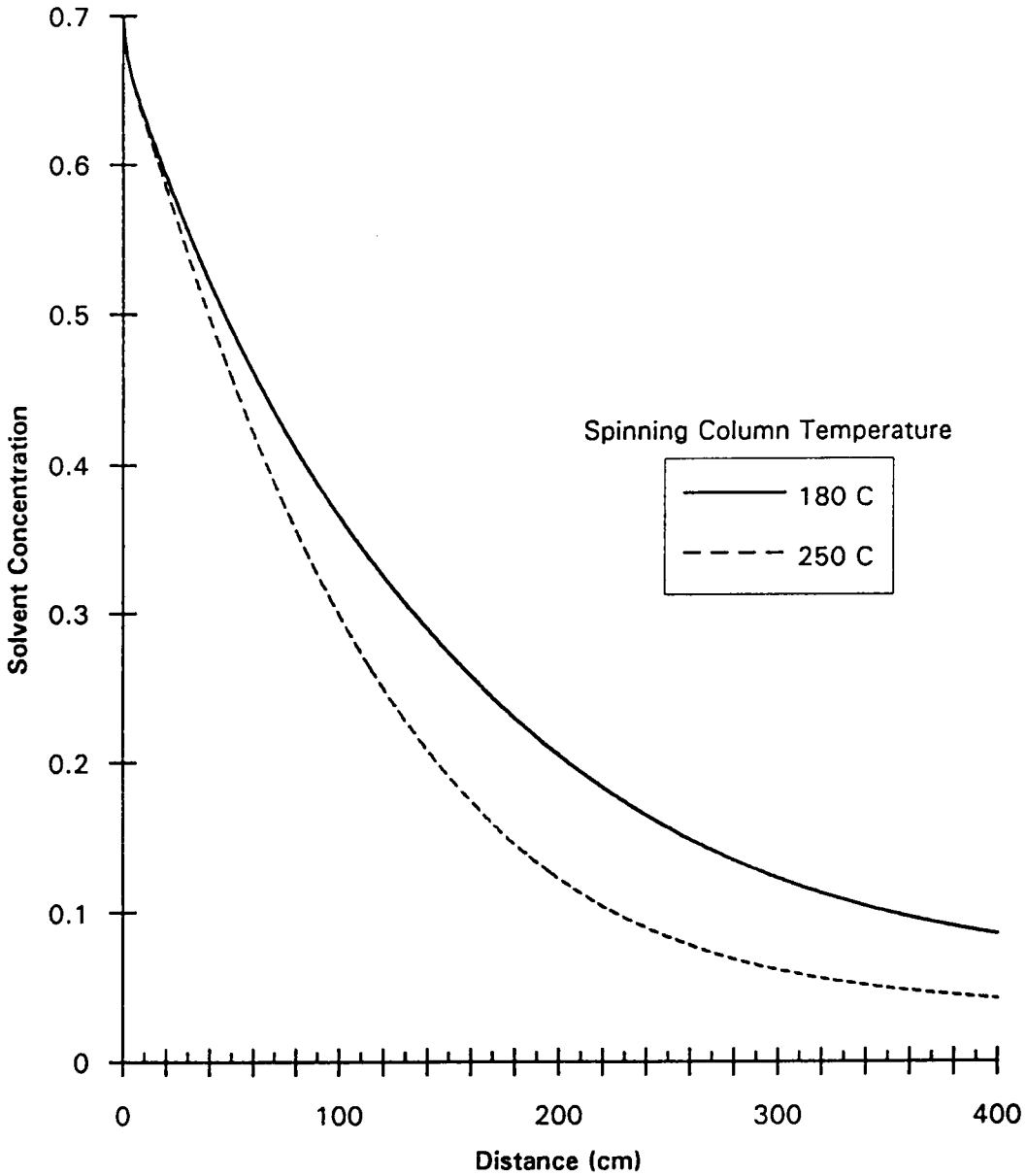

Figure 7.4.2 Influence of spin column temperature (180 and 250°C) on predicted solvent residue profiles along spinline.

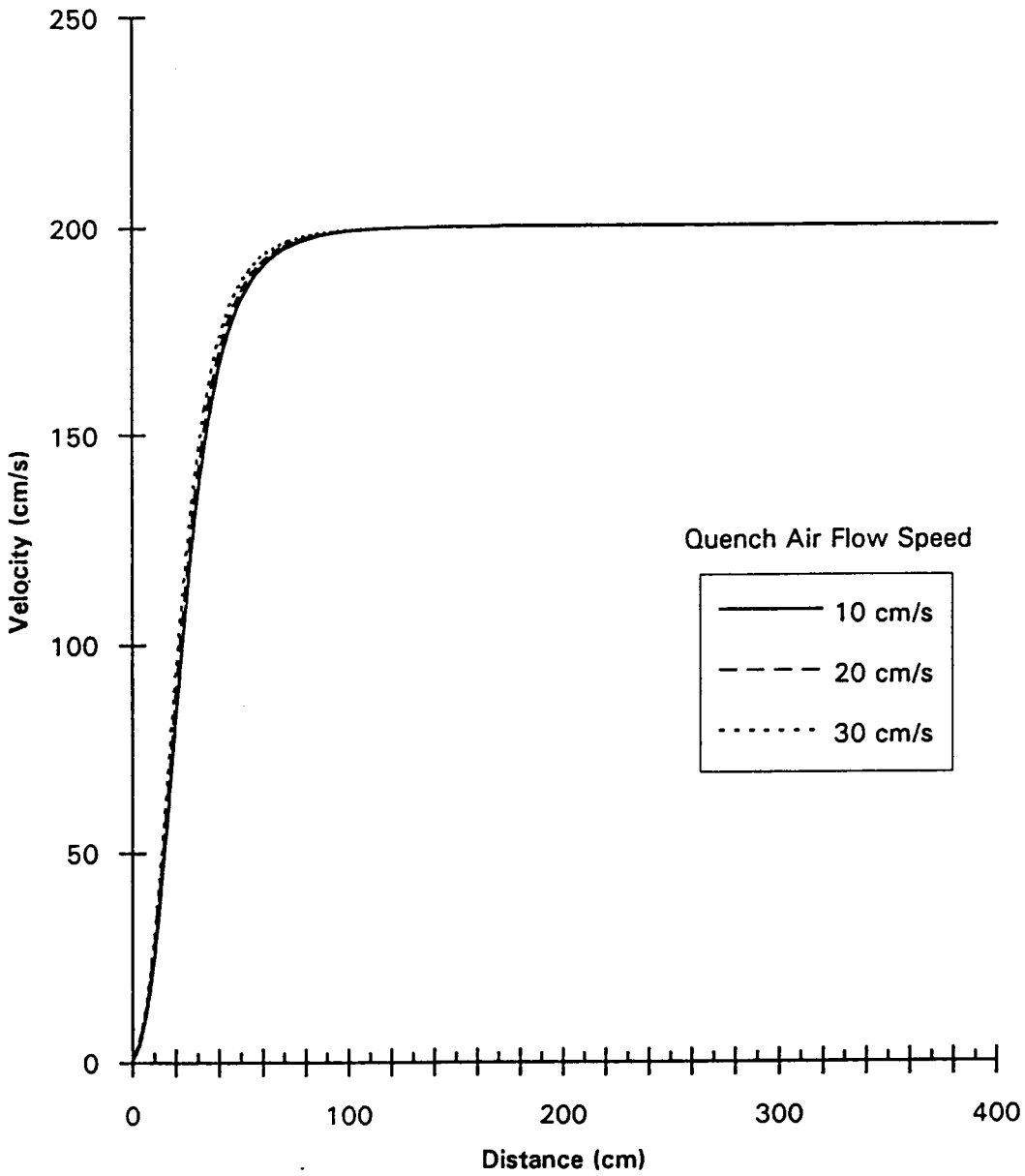

Figure 7.5.1 Influence of quench air flow speed (10, 20 and 30 cm/s) on predicted spinline velocity profiles.

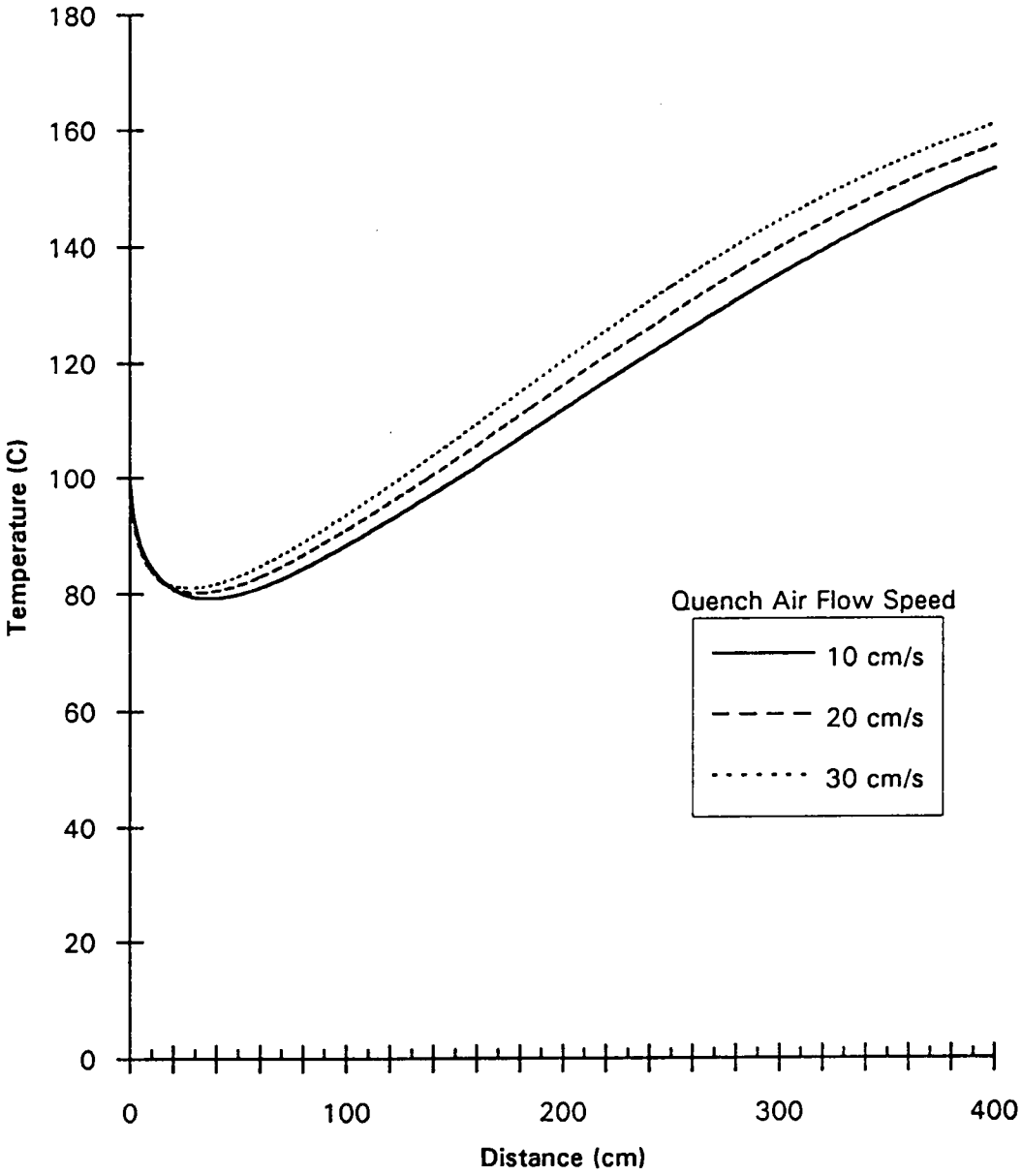

Figure 7.5.2 Influence of quench air flow speed (10, 20 and 30 cm/s) on predicted temperature profiles along spinline.

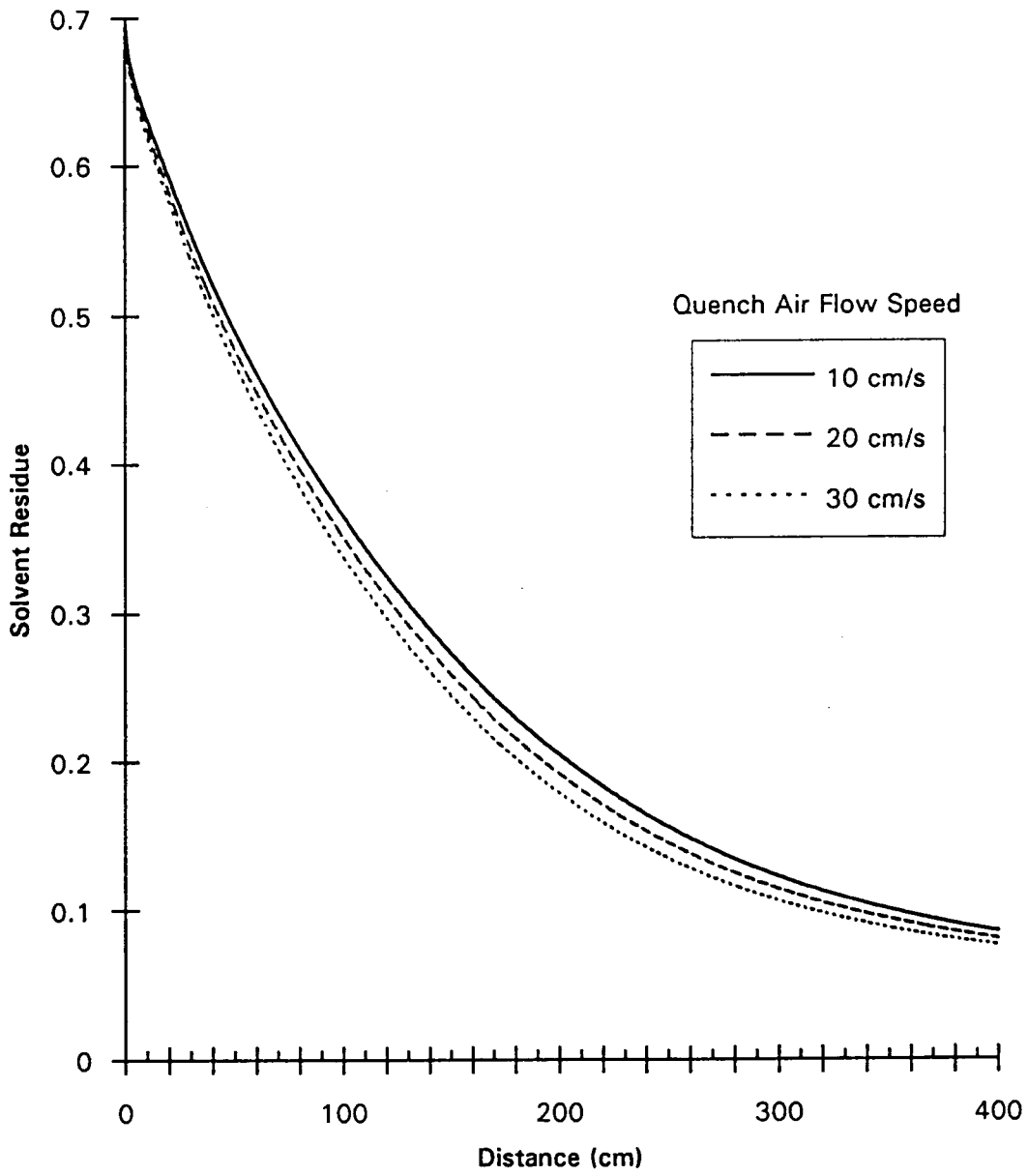

Figure 7.5.3 Influence of quench air flow speed (10, 20 and 30 cm/s) on predicted solvent residue profiles along spinline.

the solvent residue in the as-spun filament (at a distances of 400 cm from the spinneret) is little affected by quench air flow speed because the spin column is long enough to let solvent residue profile along spinline reach a plateau. It is clearly demonstrated here that the solvent residue in the filament is much more sensitive to the length of the spin column than quench air flow speed. This further proves that the rate of solvent evaporation along the spinline is very much controlled by the rate of solvent diffusion in the filament.

7.6 Interactive Effects of Processing Parameters

In previous sections, the effect of each individual processing parameter on spinline behavior and the properties of hollow filament has been discussed. It was found that quench air temperature and mass throughput have a great influence on the solvent residue in the as-spun hollow fiber. In addition, the inner diameter and wall thickness of hollow fiber are profoundly affected by take-up velocity, mass throughput and inner pressure. In this section, it is intended to further use this model to study interactive effects of key processing parameters on properties of hollow filament such as inner diameter, wall thickness and solvent residue.

Two approaches are used in the following discussion. One is to use dimensional variables such as take-up velocity, mass throughput, inner diameter, etc., which is intuitive. The other method is to use some dimensionless variables such as take-up ratio, inner diameter reduction ratio, wall thickness reduction ratio, etc. Although the second method is less intuitive, the number of variables to be studied is reduced. Furthermore, the outcoming results from dimensionless analysis are much more useful for future design and scale-up application.

Figure 7.6.1 lists the key processing parameters which affect the inner diameter and wall thickness of as-spun hollow filament. Both dimensional and dimensionless variables are defined. The equivalence of the two methods is graphically illustrated.

Figure 7.6.2 presents the predicted relationship among inner diameter (ID) of spun hollow fiber, take-up ratio (TUR) and inner pressure(IP). The inner diameter of hollow fiber decreases with either increase of take-up ratio or decrease of inner pressure. The 3-D surface plot for this relation is shown in Figure 7.6.3. Each gray shaded area represents the range of processing conditions which will resulted in nearly equivalent inner diameter of the hollow fiber. The larger the gray area, the wider the processing range will be to produce a targeted diameter range of

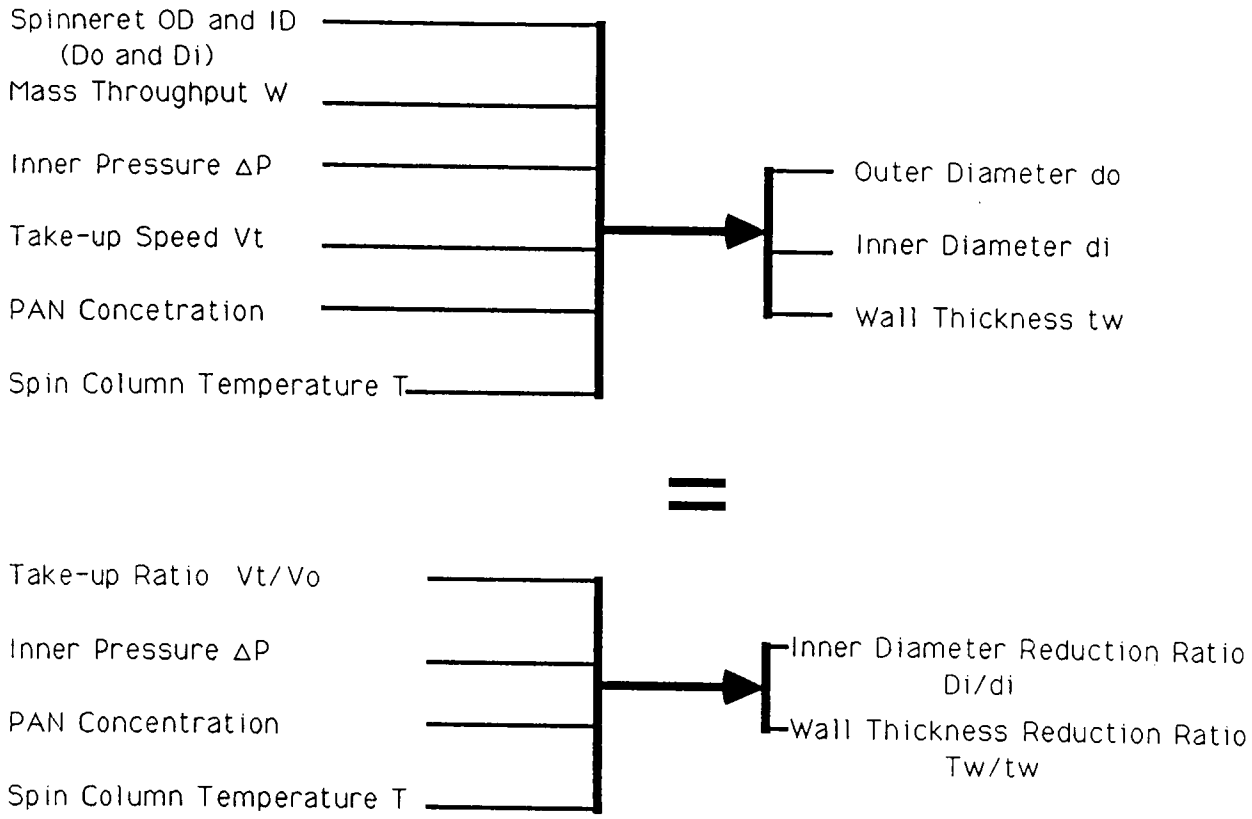

Figure 7.6.1 Key processing parameters which affect the diameter and wall thickness of hollow filament.

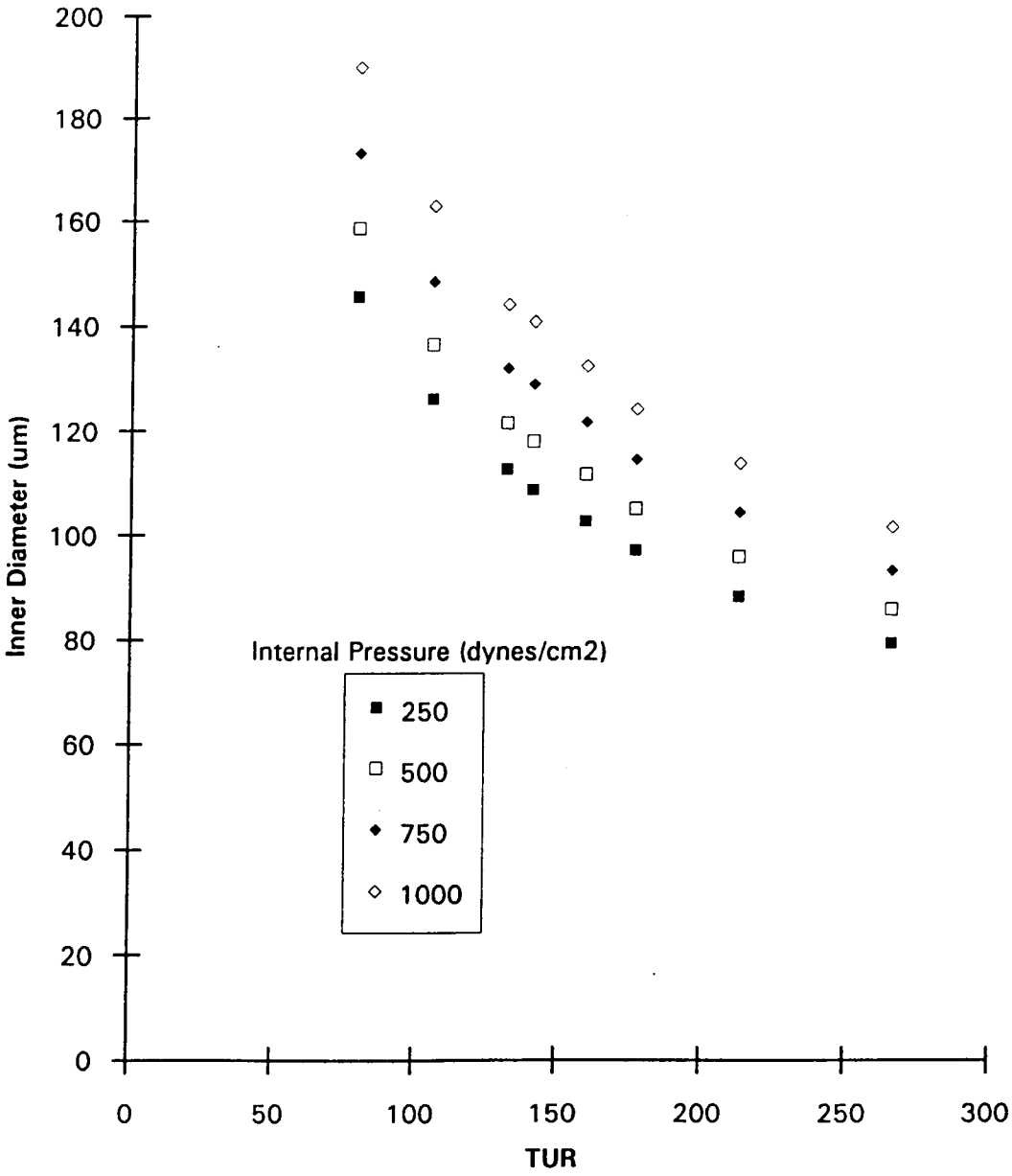

Figure 7.6.2 Effect of take-up ratio and internal pressure on inner diameter of hollow filament.

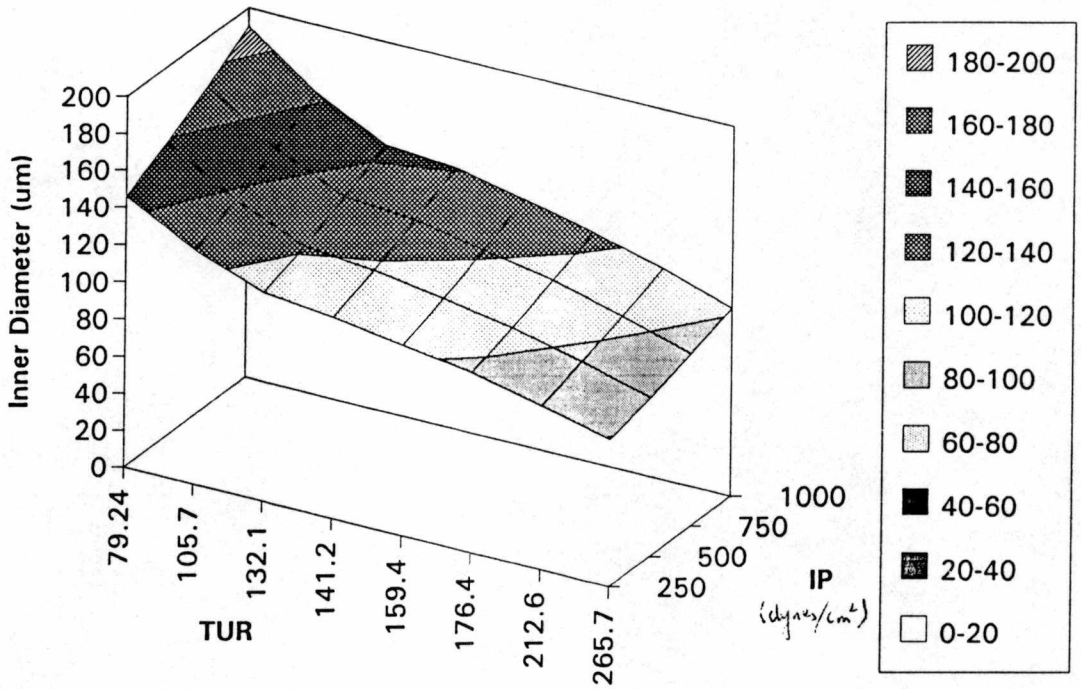

Figure 7.6.3 The relation among inner diameter, take-up ratio and internal pressure.

hollow fiber. The diameter range of 180-200 um has the smallest processing window, while the rest of the diameter ranges have very reasonable processing windows.

The dimensionless variable, Inner Diameter Reduction Ratio (IDRR), incorporates spinneret mandrel size. Figures 7.6.4 and 7.6.5 present the relationship among IDRR, TUR and IP as line and surface plots, respectively. The IDRR ranges of 10-12 and 8-10 have larger processing window than the rest of IDRR ranges.

Figures 7.6.6 and 7.6.7 show the effect of take-up ratio (TUR) and inner pressure (IP) on the wall thickness of as-spun hollow filament. The wall thickness decreases with either increasing take-up ratio or inner pressure. The processing window for producing hollow fiber with the thickness ranges of 20 - 22 um and 8 - 10 um is very narrow, as shown in Figure 7.6.7.

The effect of take-up ratio and inner pressure on wall thickness reduction ratio (TRR) is shown in Figures 7.6.8 and 7.6.9, which is in consideration of the size of annular gap in the spinneret.

As indicated before, spinning column temperature and mass throughput have significant influence on the solvent residual content in as-spun hollow filament. Figures 7.6.10 and 7.6.11 show the effect of spinning column temperature and mass throughput on the solvent residue in the hollow

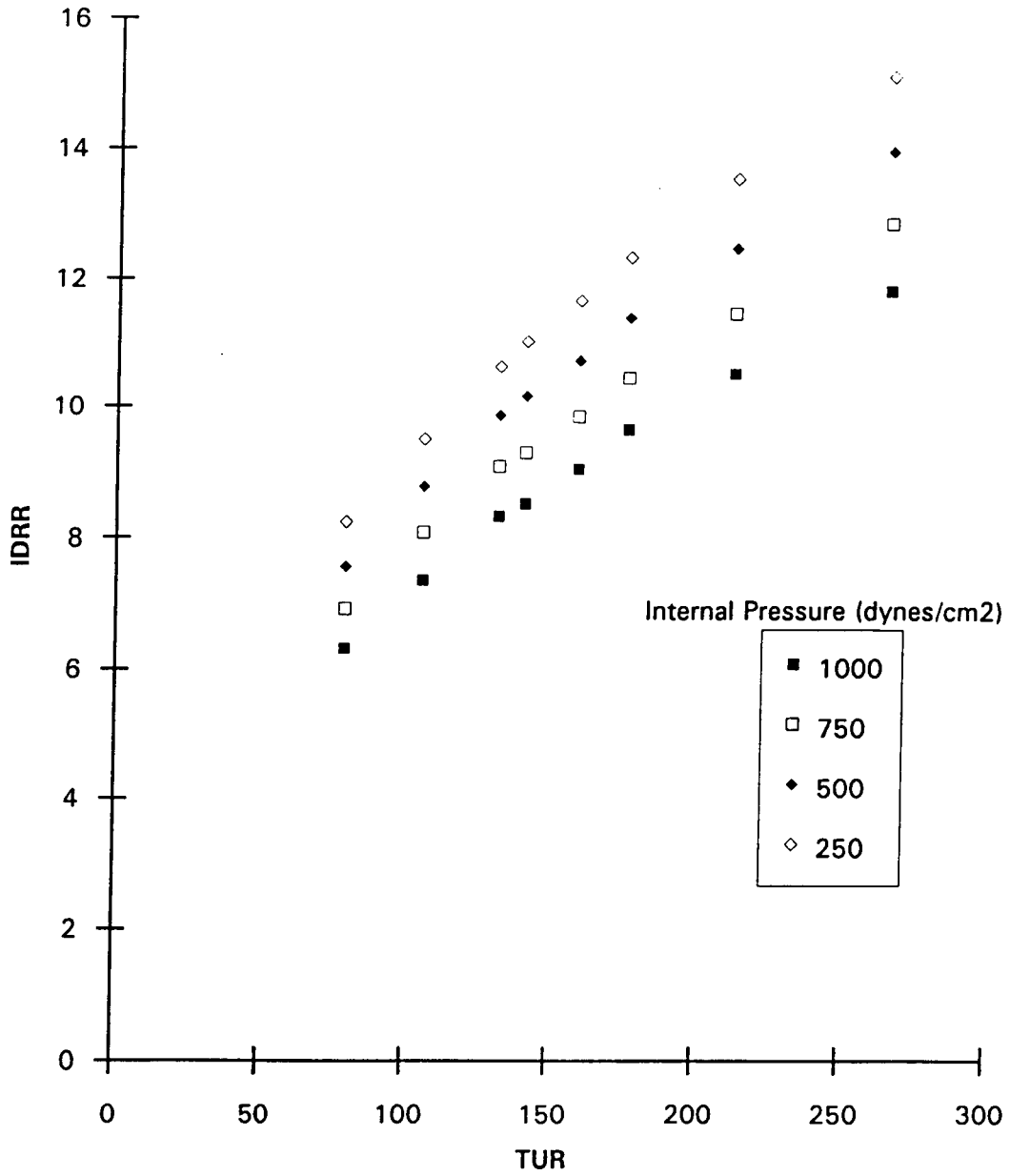

Figure 7.6.4 Effect of take-up ratio and internal pressure on inner diameter reduction ratio of hollow filament.

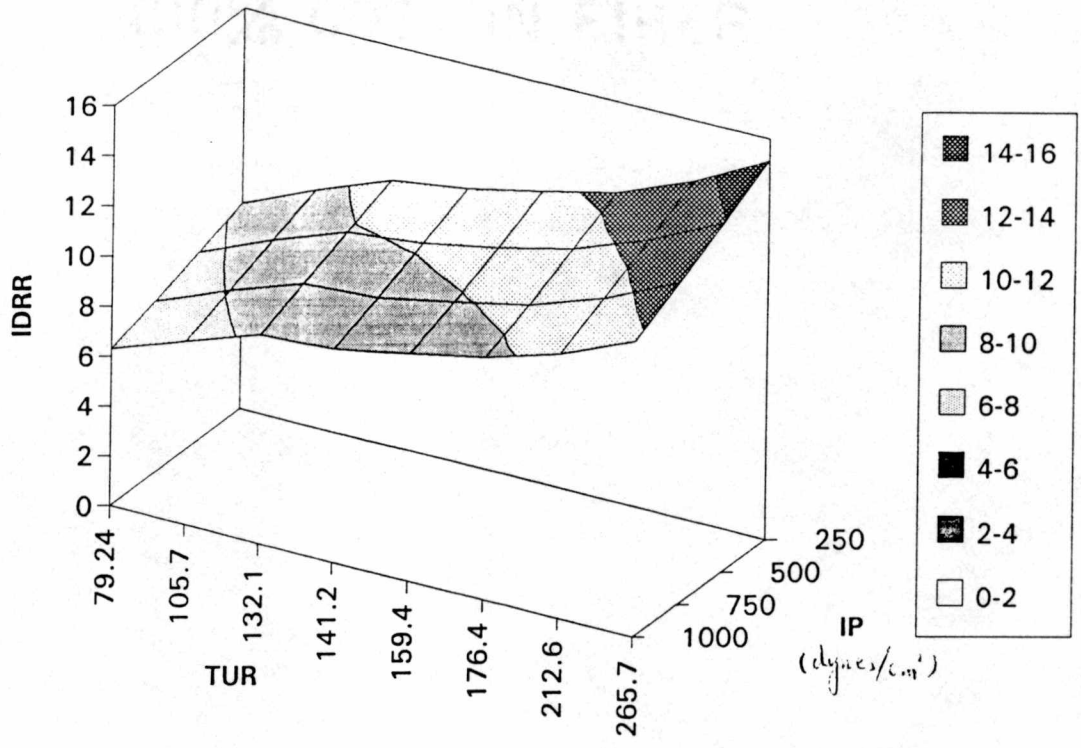

Figure 7.6.5 The relation among inner diameter reduction ratio, take-up ratio and internal pressure.

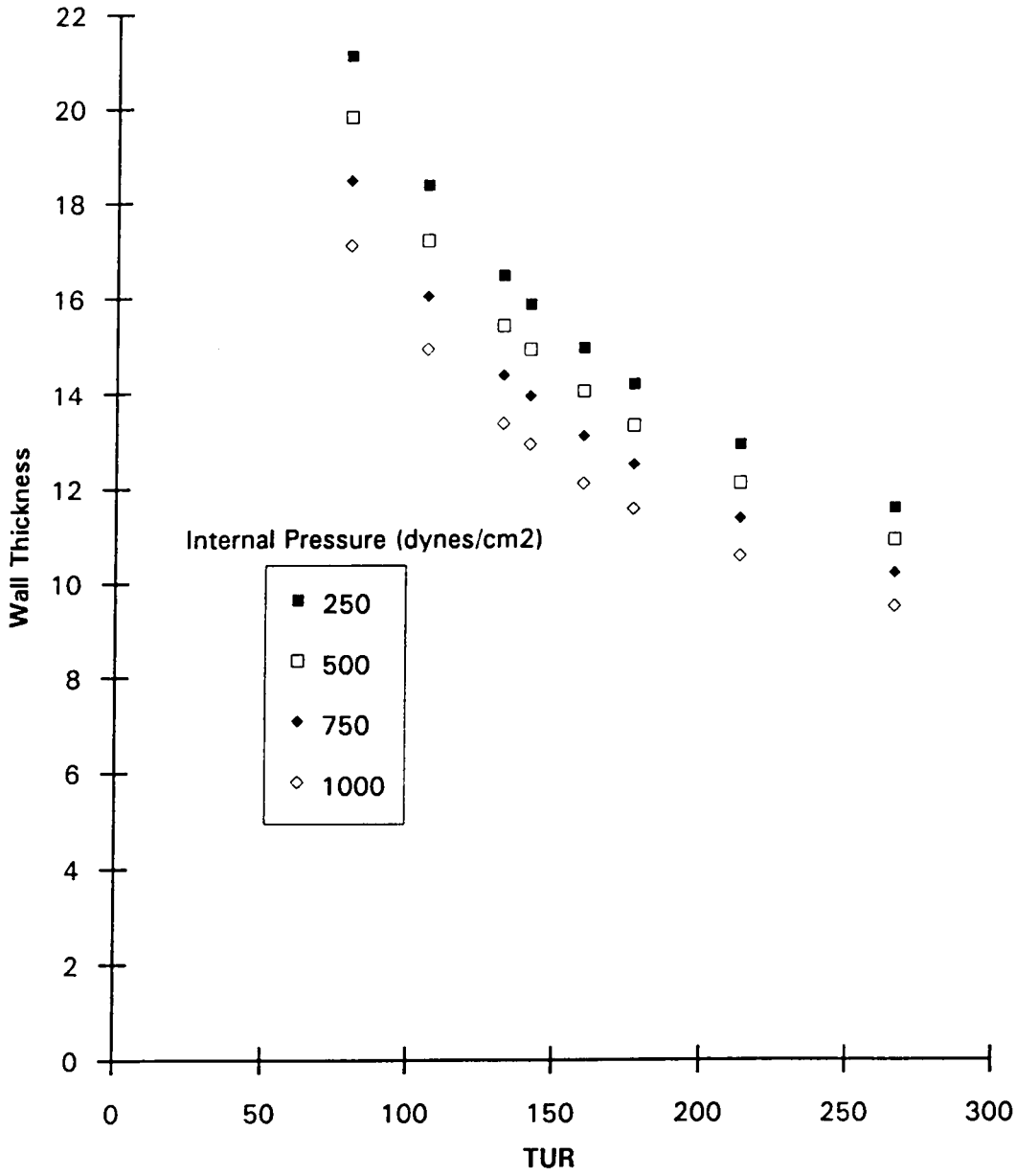

Figure 7.6.6 Effect of take-up ratio and internal pressure on wall thickness of hollow filament.

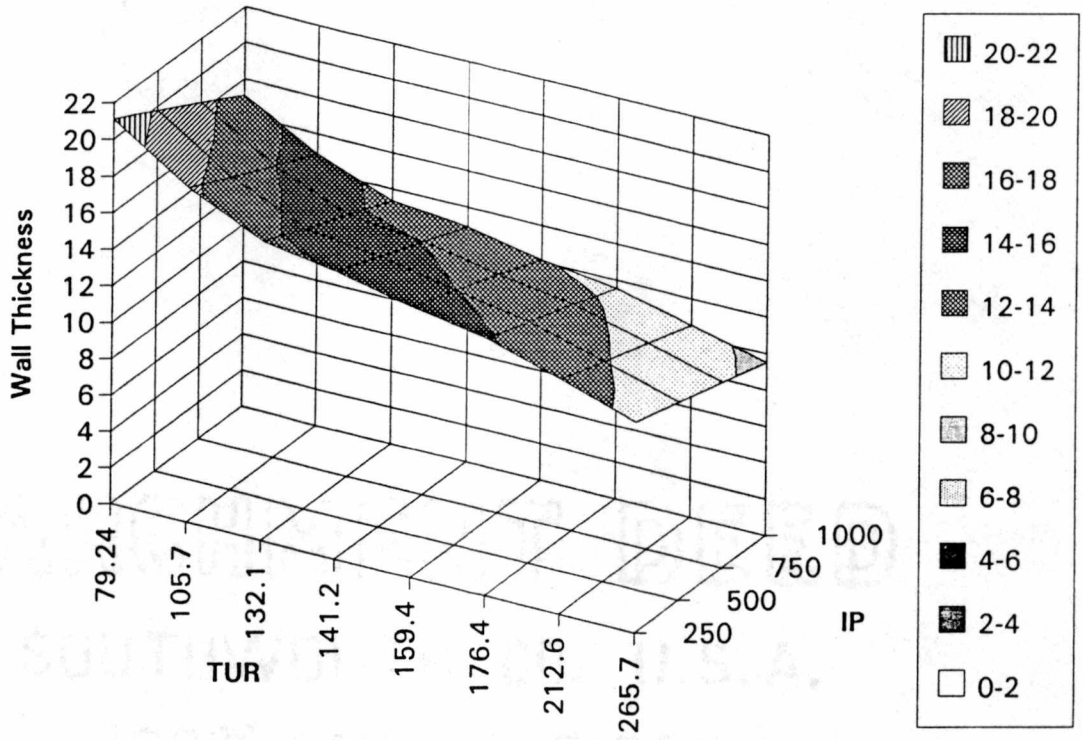

Figure 7.6.7 The relation among wall thickness, take-up ratio and internal pressure.

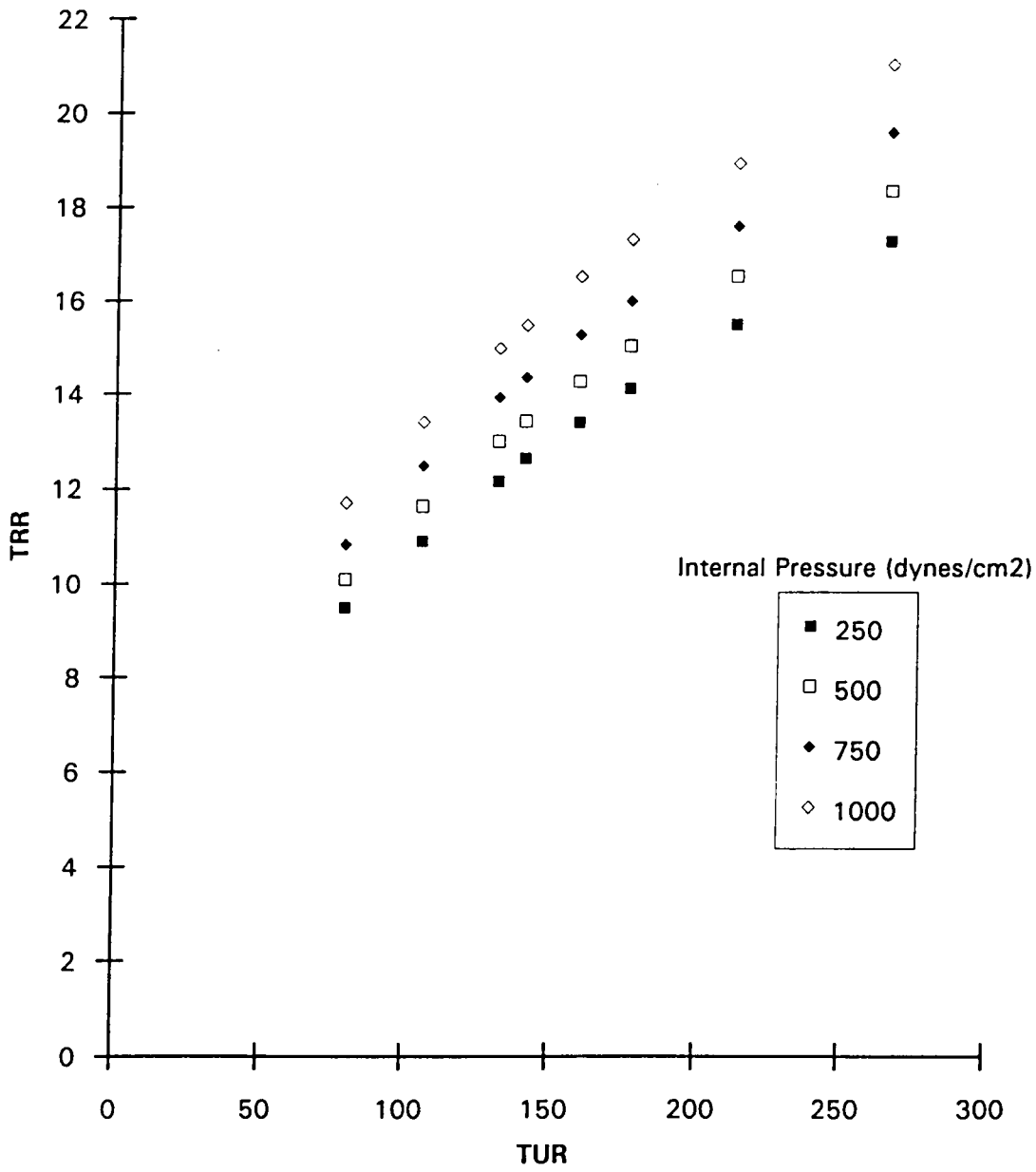

Figure 7.6.8 Effect of take-up ratio and internal pressure on wall thickness reduction ratio of hollow filament.

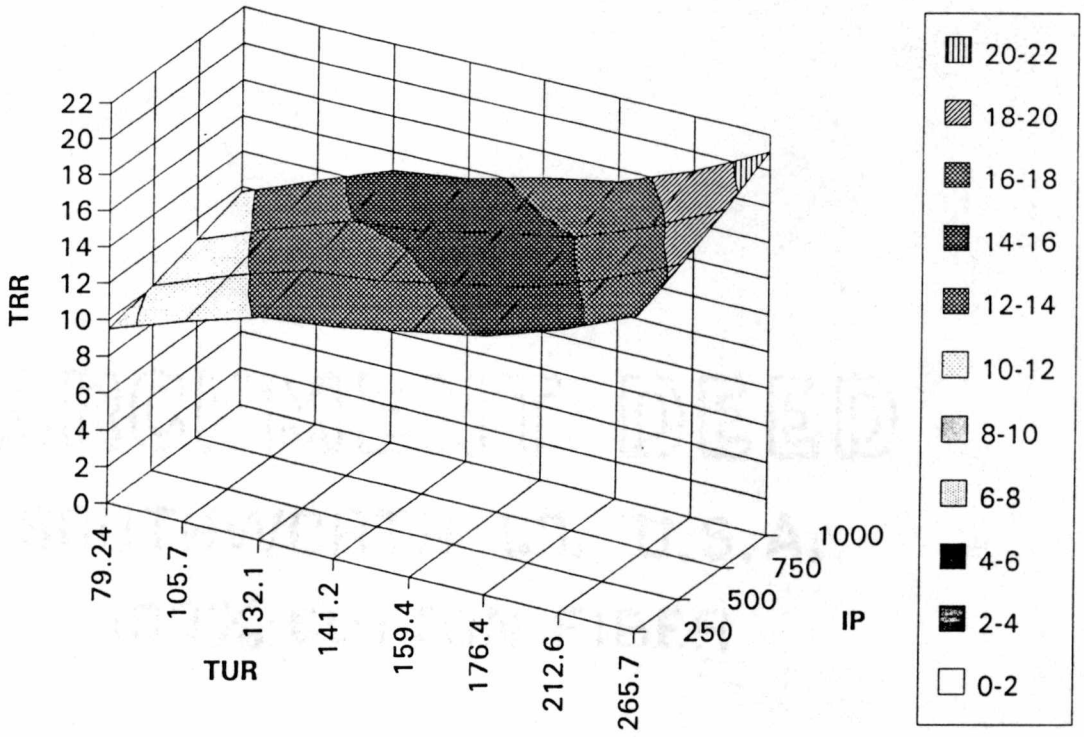

Figure 7.6.9 The relation among wall thickness reduction ratio, take-up ratio and internal pressure.

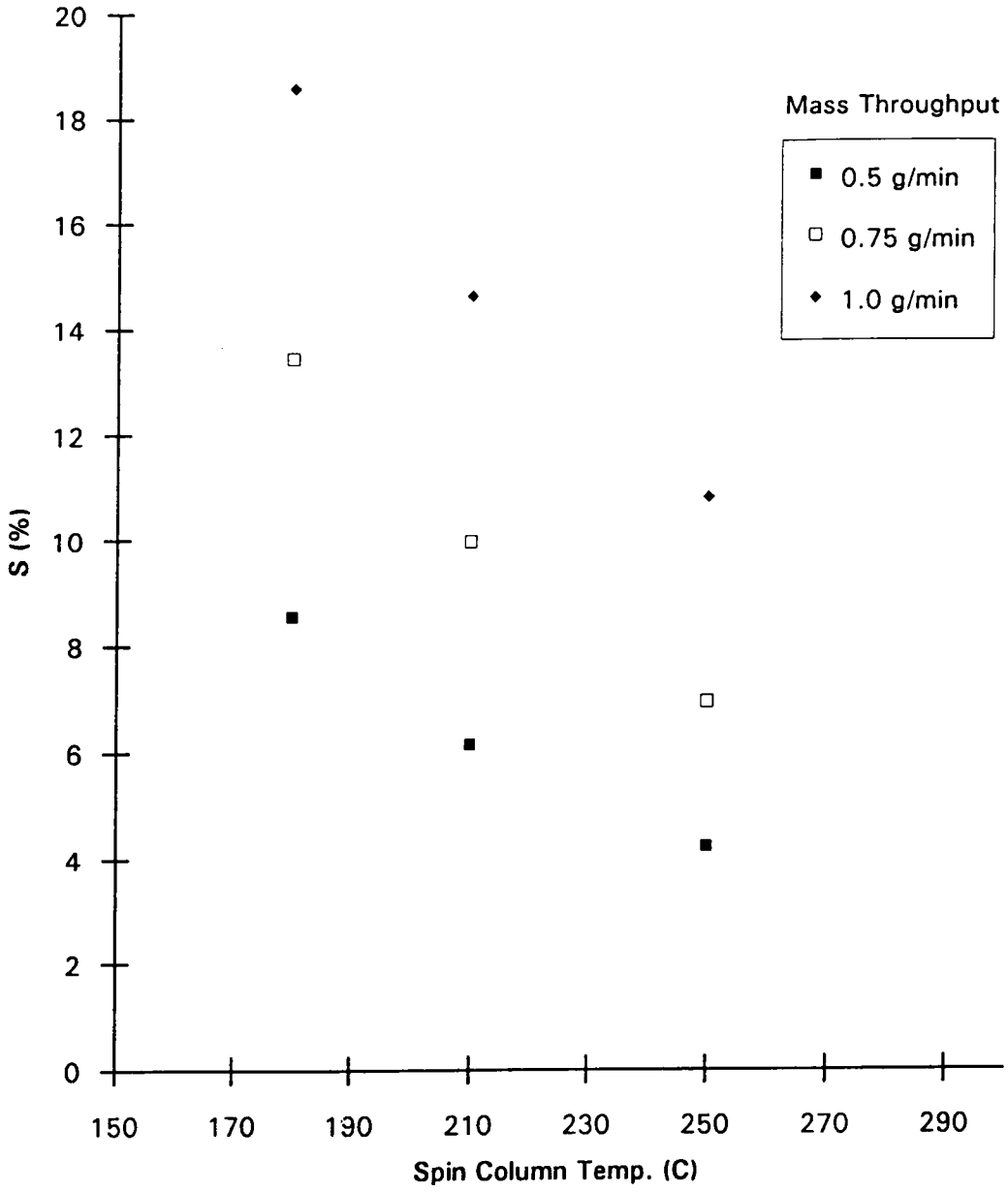

Figure 7.6.10 Effect of spin column temperature and mass throughput on solvent residue of as-spun hollow filament.

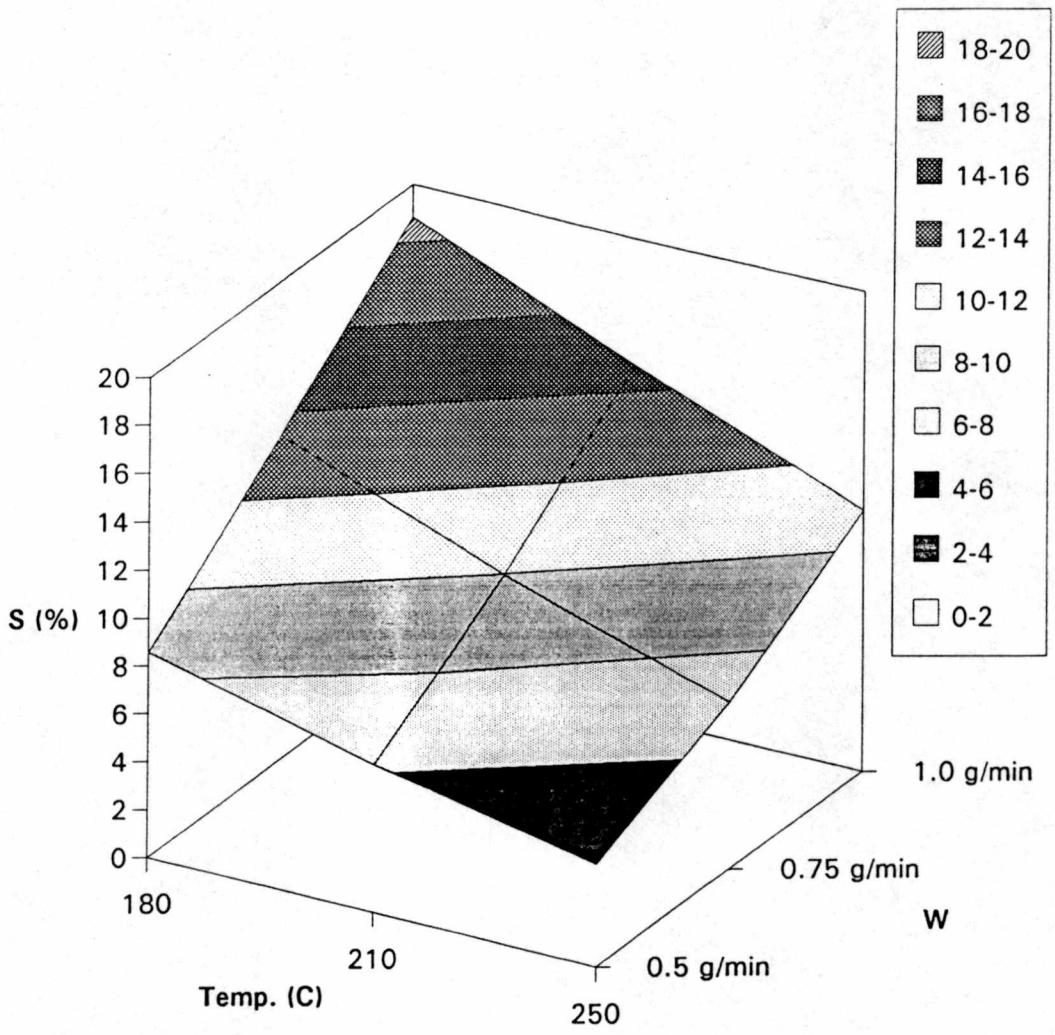

Figure 7.6.11 The relation among solvent residue, spin column temperature and mass throughput.

fiber. Either increasing column temperature or decreasing mass throughput will result in reducing the solvent residue in as-spun hollow filament. Higher spinning column temperature increases the rate of vaporization, and lower mass throughput reduces the amount of the solvent to be vaporized per unit time.

CHAPTER VIII

COMPARISON AMONG THICK-WALLED, THIN WALLED AND NON-HOLLOW FILAMENT MODELS

8.1 Thick-walled Model Vs. Thin-walled Model

A thick-walled model for hollow fiber spinning was developed in Chapter V. The model considers the triaxial stress state within the filament in cylindrical coordinate. A thin-walled model for hollow fiber spinning was also derived, which considers only plane stress elements, properly oriented on the outside surface of the cylinder (σ_{zz} is axial stress and $\sigma_{\theta\theta}$ is hoop stress). The radial stress equals to zero in the thin-walled model.

Although the two models were derived independently, we are able to demonstrate that the thin-walled model is a special case of the thick-walled model when the wall thickness of the hollow filament approaches "thin". We start with the triaxial stress equations in the thick-walled model:

$$\sigma_{rr} = \frac{\Delta P R_i^2}{(R_0^2 - R_i^2)}\left[1 - \frac{R_0^2}{r^2}\right] \qquad (8.1.1)$$

$$\sigma_{\theta\theta} = \frac{\Delta P R_i^2}{(R_0^2 - R_i^2)}\left[1 + \frac{R_0^2}{r^2}\right] \qquad (8.1.2)$$

$$\sigma_{zz} = \frac{\Delta P R_i^2}{(R_0^2 - R_i^2)} + 3\mu \frac{du_z}{dz} \qquad (8.1.3)$$

When the wall thickness of hollow the filament becomes small, notice the following transformation:

$$\pi(R_0^2 - R_i^2) \approx 2\pi Rh$$

or

$$(R_0^2 - R_i^2) \approx 2Rh \qquad (8.1.4)$$

$$R_0 \approx R_i \approx R \approx r \qquad (8.1.5)$$

Substitute Equations (8.1.4) and (8.1.5) into Equations (8.1.1) to (8.1.3), then the following results are obtained:

$$\sigma_{rr} = 0 \qquad (8.1.6)$$

$$\sigma_{\theta\theta} = \frac{\Delta P R^2}{2Rh} \cdot 2 = \Delta P \frac{R}{h} \qquad (8.1.7)$$

$$\sigma_{zz} = \Delta P \frac{R}{h} + 3\mu \frac{du_z}{dz} \qquad (8.1.8)$$

Equations (8.1.6) to (8.1.8) are the plane stress equations for the thin-walled model.

The thick walled model is a general model, while the thin walled model is a simplified model for the special case that the wall thickness becomes small compared to the filament radius. Since the key difference between the two models is the assumption of "wall thickness", it is interesting to see the effect of the wall thickness on hoop stress $\sigma_{\theta\theta}$ predictions by the two models. The hoop stress $\sigma_{\theta\theta}$ by thick-walled model (equation 8.1.2) depends on radial distance r, meanwhile the thin-walled model predicts an average hoop stress (equation 8.1.7). In order to compare hoop stress predictions by the two models, the hoop stress by the thick-walled model, by equation 8.1.2, must be converted to an average hoop stress across the radial direction as follows:

$$\sigma_{\theta\theta} = \frac{1}{\pi(R_0^2 - R_i^2)} \int_{R_i}^{R_0} \sigma_{\theta\theta} 2\pi r \, dr \qquad (8.1.9)$$

The integration brings about the following results:

$$\sigma_{\theta\theta} = \frac{\Delta P a^2}{(1-a^2)}\left[(1-a^2) + 2\ln\frac{1}{a}\right]$$

or

$$\frac{\overline{\sigma_{\theta\theta}}}{\Delta P} = \frac{a^2}{(1-a^2)}\left[(1-a^2) + 2\ln\frac{1}{a}\right] \qquad (8.1.10)$$

where $a = R_i/R_o$.

The thin walled model predicts an average hoop stress as follows:

$$\sigma_{\theta\theta} = \Delta P \frac{R}{h} = \Delta P \frac{R_i}{R_0 - R_i} = \Delta P \frac{a}{1 - a}$$

or

$$\frac{\overline{\sigma_{\theta\theta}}}{\Delta P} = \frac{a}{1 - a} \qquad (8.1.11)$$

where $a = R_i/R_o$.

Table 8.1.1 shows the comparison of $\frac{\overline{\sigma_{\theta\theta}}}{\Delta P}$ prediction between thick-walled model and thin-walled model. The deviation (%) is calculated based on:

$$\text{Deviation } (\%) = \frac{V_{thick} - V_{thin}}{V_{thick}} \times 100 \qquad (8.1.12)$$

where V_{thick} is the value predicted by the thick-walled model, and V_{thin} is the value predicted by the thin-walled model.

The calculation results in Table 8.1.1 indicate that the thin-walled model overpredicts the hoop stress compared to the hoop stress predicted by the thick-walled model. Moreover, the deviation increases with increasing wall thickness or decreasing ratio of Ri/Ro. These results further confirm that the thin-walled model is a special case of thick-wall model when Ri/Ro approaches to unity.

Table 8.1.1 Comparison of hoop stress predictions between thick-walled and thin-walled models.

Ri/Ro (ID/OD)	$\sigma_{\theta\theta}/\Delta P$ Thick-Walled Model	$\sigma_{\theta\theta}/\Delta P$ Thin-Walled Model	Deviation (%)
0.9	8.991	9.000	0.10
0.8	3.982	4.000	0.45
0.7	2.305	2.333	1.21
0.6	1.460	1.500	2.74
0.5	0.949	1.000	5.37
0.4	0.606	0.667	10.07
0.3	0.361	0.429	18.84
0.2	0.181	0.250	38.12
0.1	0.057	0.111	94.74

From equation (5.1.13) in Chapter V, we know that the hoop stress is a function of radius r:

$$\sigma_{\theta\theta} = \frac{\Delta P R_i^2}{(R_o^2 - R_i^2)}\left[1+\frac{R_o^2}{r}\right] \qquad (8.1.13)$$

where Ri≤r≤Ro.

At r=Ri, the hoop stress is maximum:

$$\sigma_{\theta\theta(R_i)} = \frac{\Delta P(R_o^2+R_i^2)}{(R_o^2-R_i^2)}$$

or

$$\sigma_{\theta\theta(max)} = \frac{1+a^2}{1-a^2}\Delta P \qquad (8.1.14)$$

At r=Ro, the hoop stress is minimum:

$$\sigma_{\theta\theta(R_o)} = \frac{2\Delta P R_i^2}{(R_o^2-R_i^2)}$$

or

$$\sigma_{\theta\theta(min)} = \frac{2a^2}{1-a^2}\Delta P \qquad (8.1.15)$$

where a=Ri/Ro. The maximum of hoop stress happens on the inner surface of the hollow filament, while the minimum of hoop stress happens on the outer surface of the hollow filament.

The ratio of maximum hoop stress over minimum hoop stress is dependent on the Ri/Ro ratio as indicated as following equation, which is a good indicator of the hoop stress variation across the radius although the hoop stress decreases continuously from the inner to outer radius.

$$\frac{\sigma_{\theta\theta(max)}}{\sigma_{\theta\theta(min)}} = \frac{1+a^2}{2a^2} = \frac{1}{2}[1 + (\frac{R_0}{R_i})^2] \qquad (8.1.16)$$

The Table 8.1.2 lists the results of calculation based on Equation (8.1.16). The ratio of Ro/Ri (or Ri/Ro) for which hollow filament may be considered as "thin wall" depends on the tolerance of stress variation across the wall thickness. If a 10% hoop stress variation is allowed across the wall thickness, that is

$$\frac{\sigma_{\theta\theta(max)}}{\sigma_{\theta\theta(min)}} = 1.10 \qquad (8.1.17)$$

then

$$\frac{R_0}{R_i} = 1.09 \qquad (8.1.18)$$

This means that the wall thickness may be as large as 9% of the inner radius of the hollow filament.

Table 8.1.2 Hoop stress variation across the wall thickness.

Ri/Ro (ID/OD)	Ro/Ri(OD/ID)	$\sigma_{\theta\theta}$(max)/$\sigma_{\theta\theta}$(min)
0.9	1.11	1.12
0.8	1.25	1.28
0.7	1.43	1.52
0.6	1.67	1.89
0.5	2.00	2.50
0.4	2.50	3.63
0.3	3.33	6.06
0.2	5.00	13.00
0.1	10.00	50.50

8.2 Comparison of Spinline Predictions by the Two Models

The spinline predictions by both thick-walled model and thin-walled model were conducted using three different Ri/Ro ratios (0.75, 0.5, and 0.25) of spinnerets, that is the mandrel radius divided by hole radius. Figures 8.2.1 to 8.2.3 present spinline velocity profiles predicted by both thick-walled and thin walled models at three levels of Ri/Ro ratios, which are 0.75, 0.5 and 0.25, respectively. The velocity gradient profiles are also presented in Figures 8.2.4 to 8.2.6. In addition, Figures 8.2.7 to 8.2.9 show wall thickness profiles of hollow filaments along the spinline. In the case of Ri/Ro = 0.75, the difference in predictions between the two models is quite small. This means that for this case the thin-walled model predicts spinline behaviors as well as the thick-walled model. With increase of thickness of annular gap of the spinneret (decrease of Ri/Ro), the difference in spinline predictions between the two models increases. In general, the thin-walled model predicts faster development of velocity and faster reduction of the wall thickness of the hollow filament along the spinline than the predictions by the thick-walled model. This is due to the fact that the thin-walled model overpredicts the hoop stress as shown in Table 8.1.1.

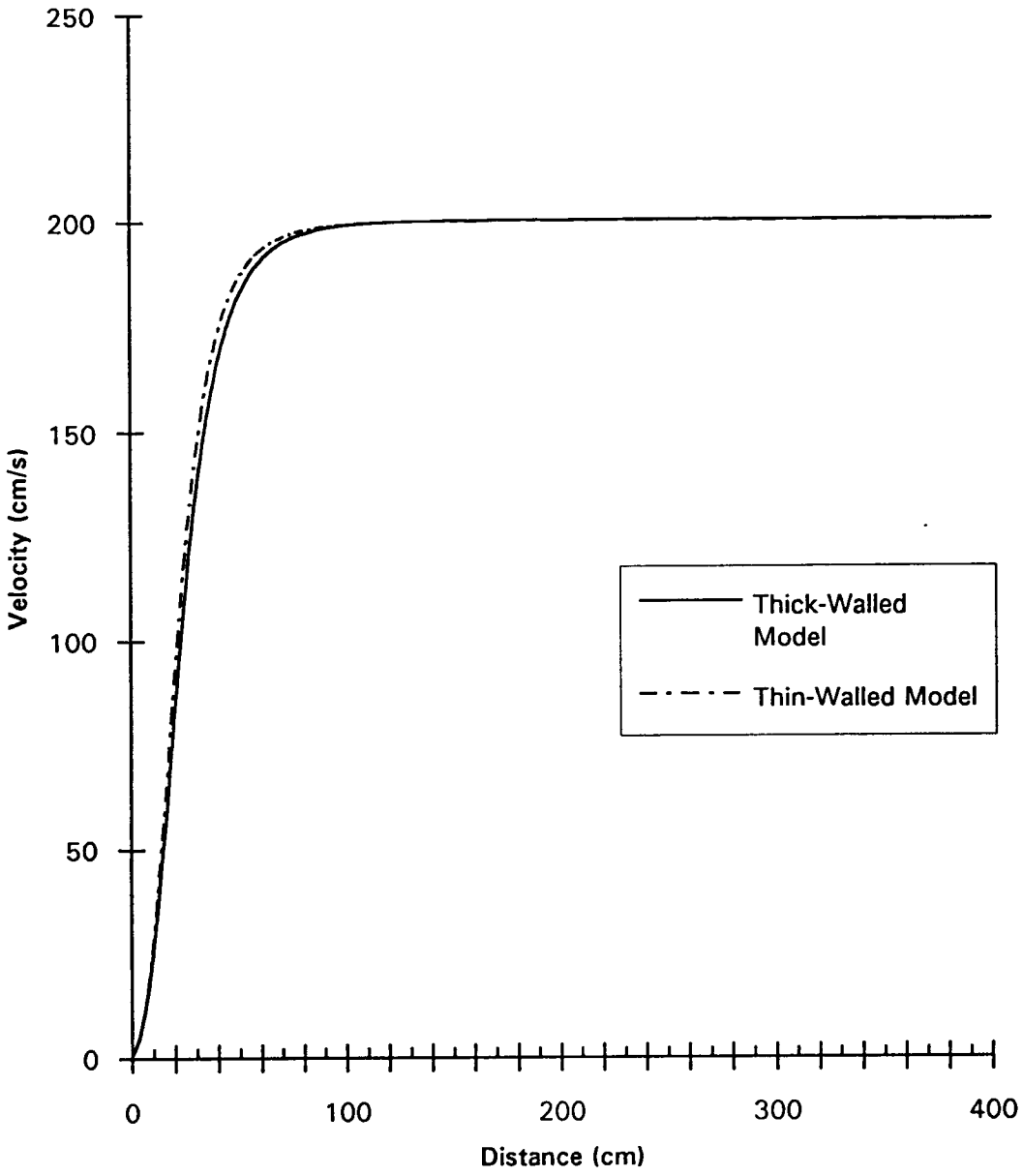

Figure 8.2.1 Comparison of spinline velocity profiles predicted by thick-walled and thin-walled models (spinneret parameter ID/OD = 0.75).

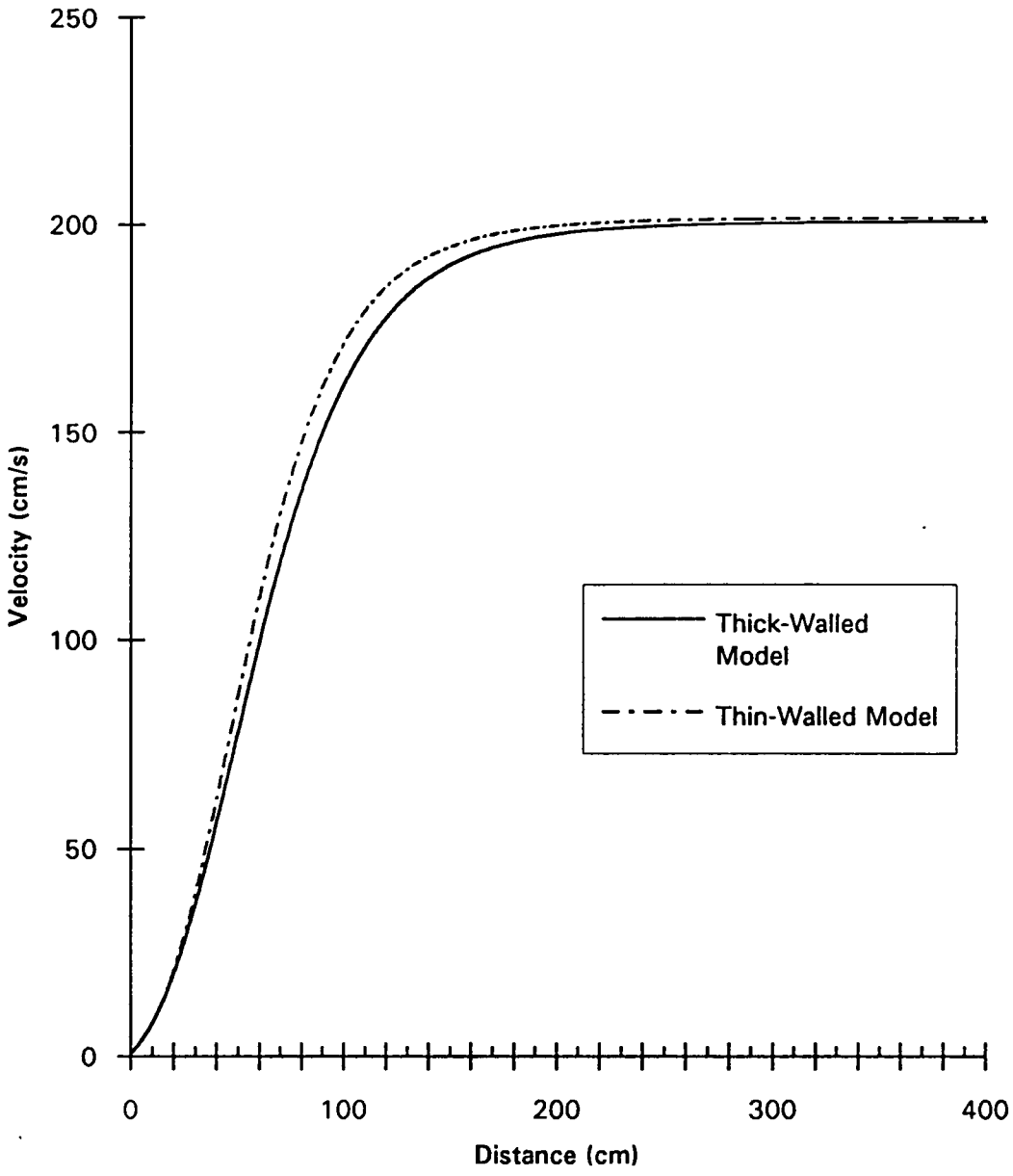

Figure 8.2.2 Comparison of spinline velocity profiles predicted by thick-walled and thin-walled models (spinneret parameter ID/OD = 0.50).

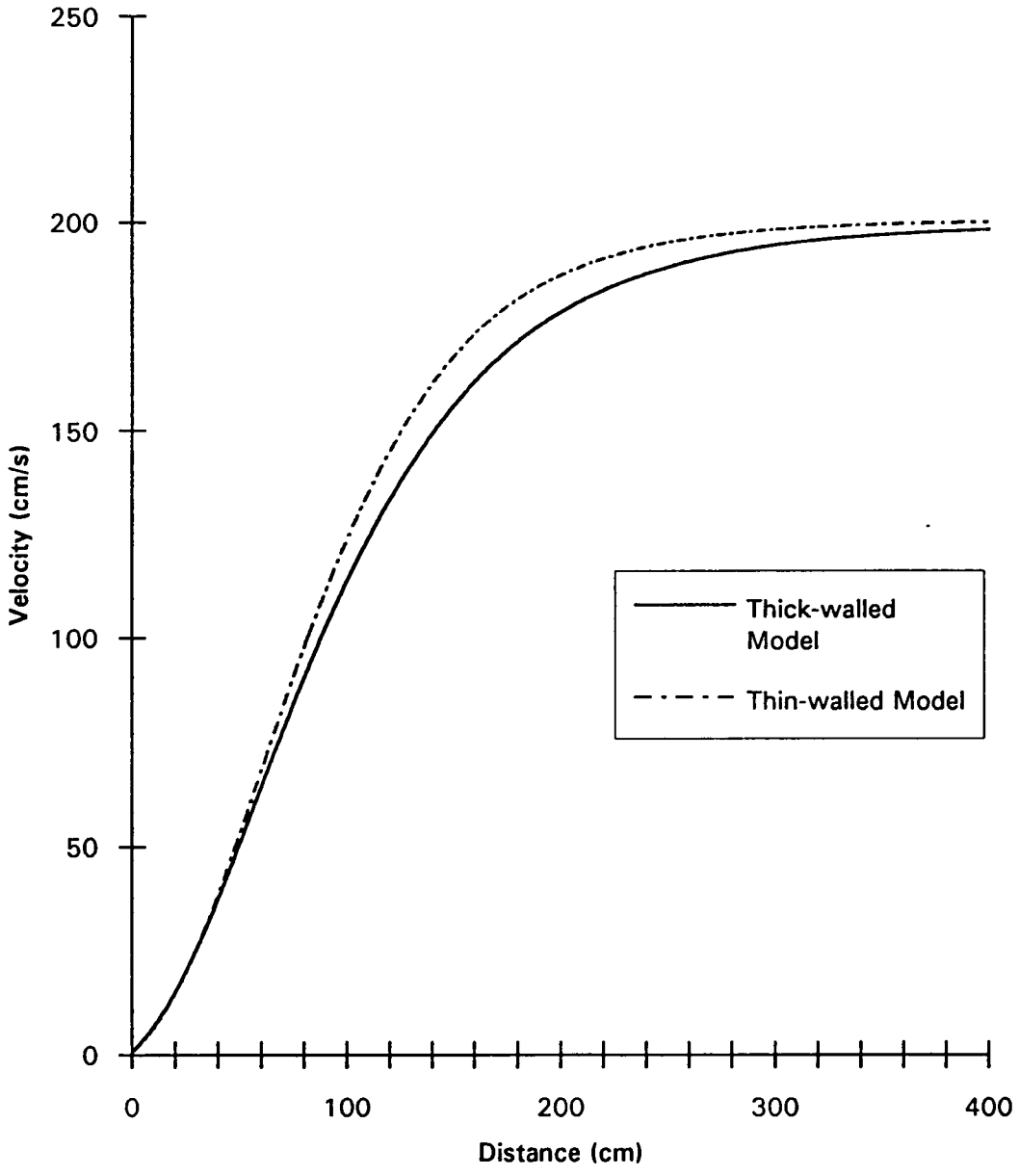

Figure 8.2.3 Comparison of spinline velocity profiles predicted by thick-walled and thin-walled models (spinneret parameter ID/OD = 0.25).

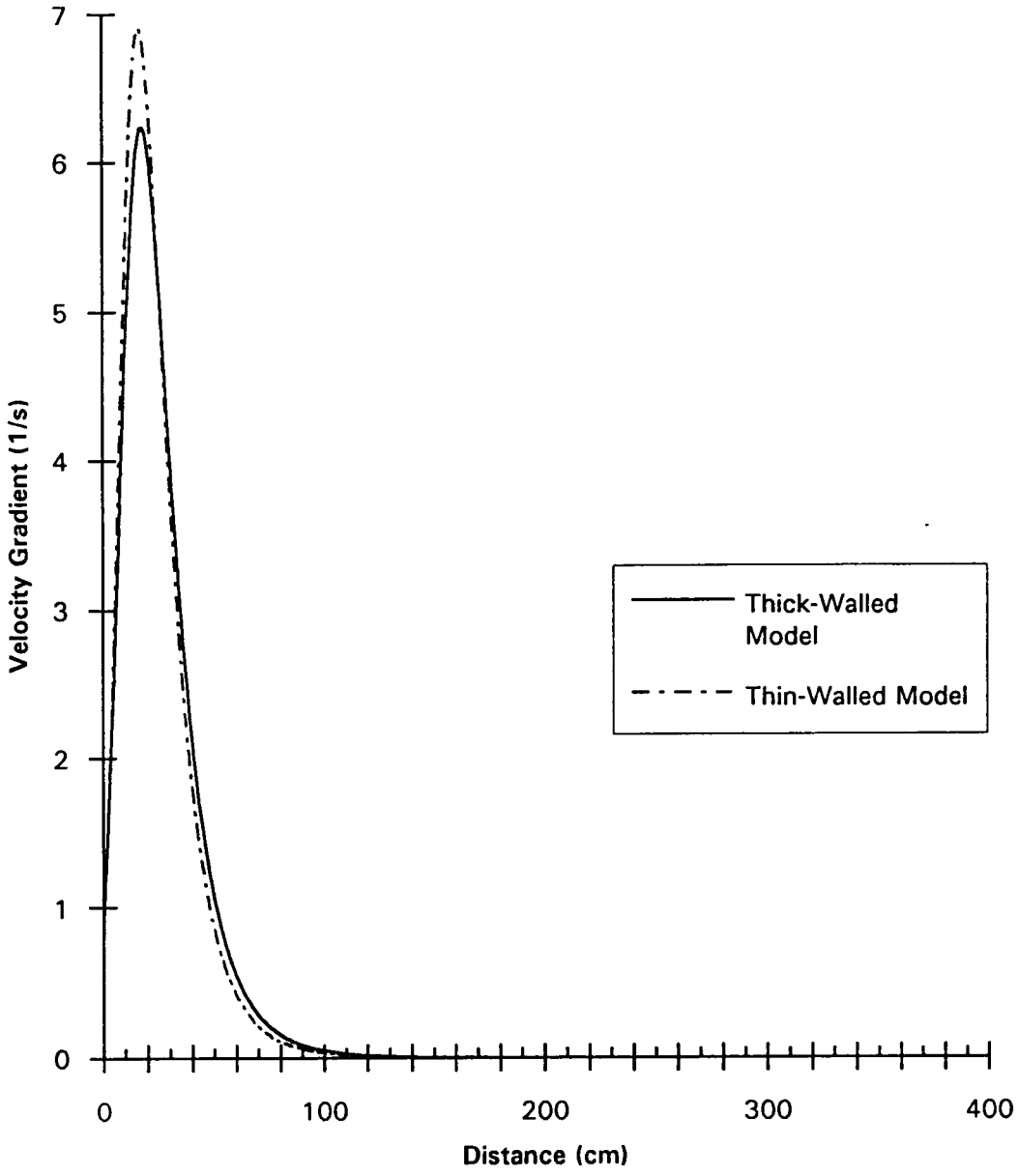

Figure 8.2.4 Comparison of velocity gradient profiles predicted by thick-walled and thin-walled models (spinneret parameter ID/OD = 0.75).

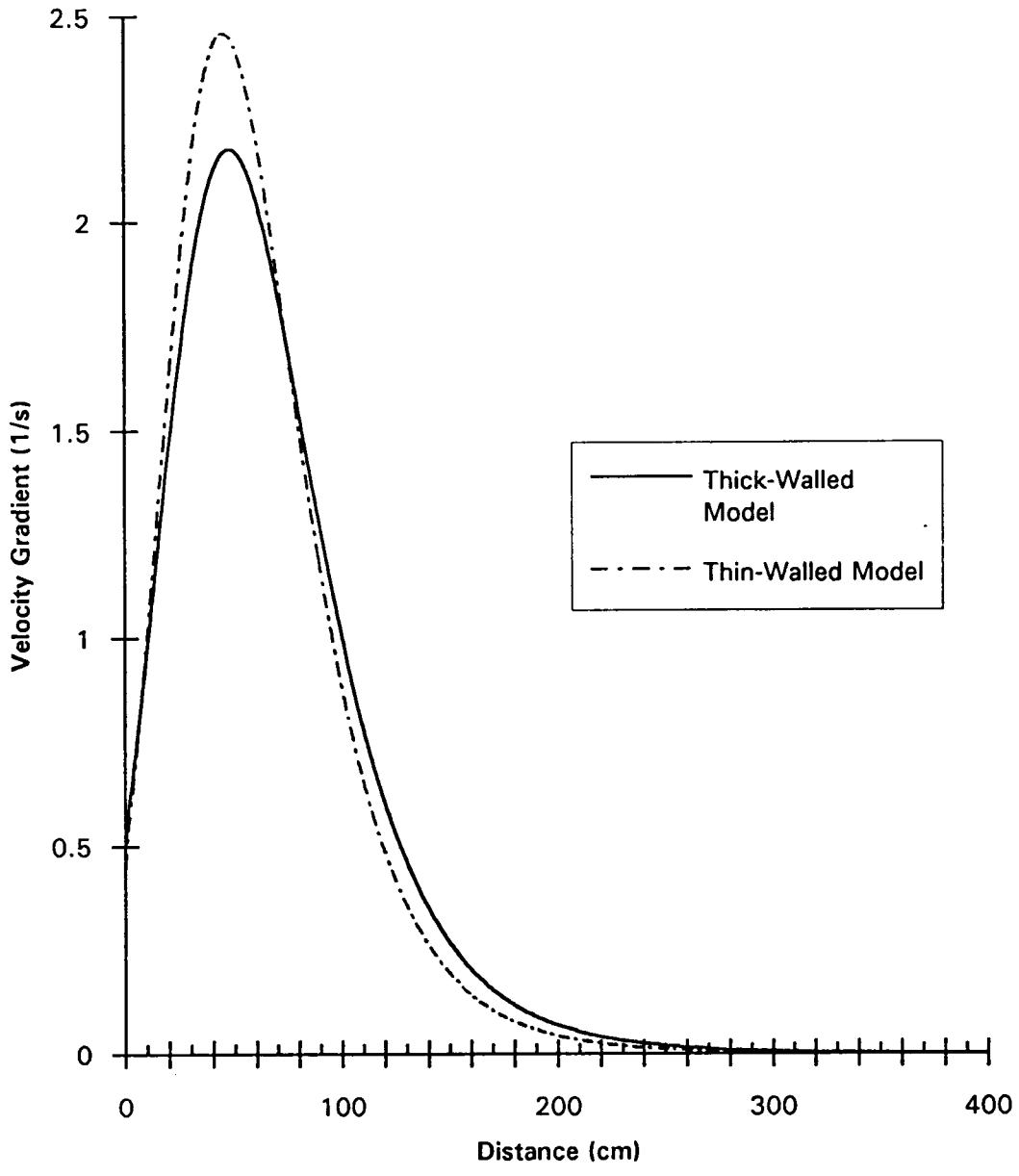

Figure 8.2.5 Comparison of velocity gradient profiles predicted by thick-walled and thin-walled models (spinneret parameter ID/OD = 0.50).

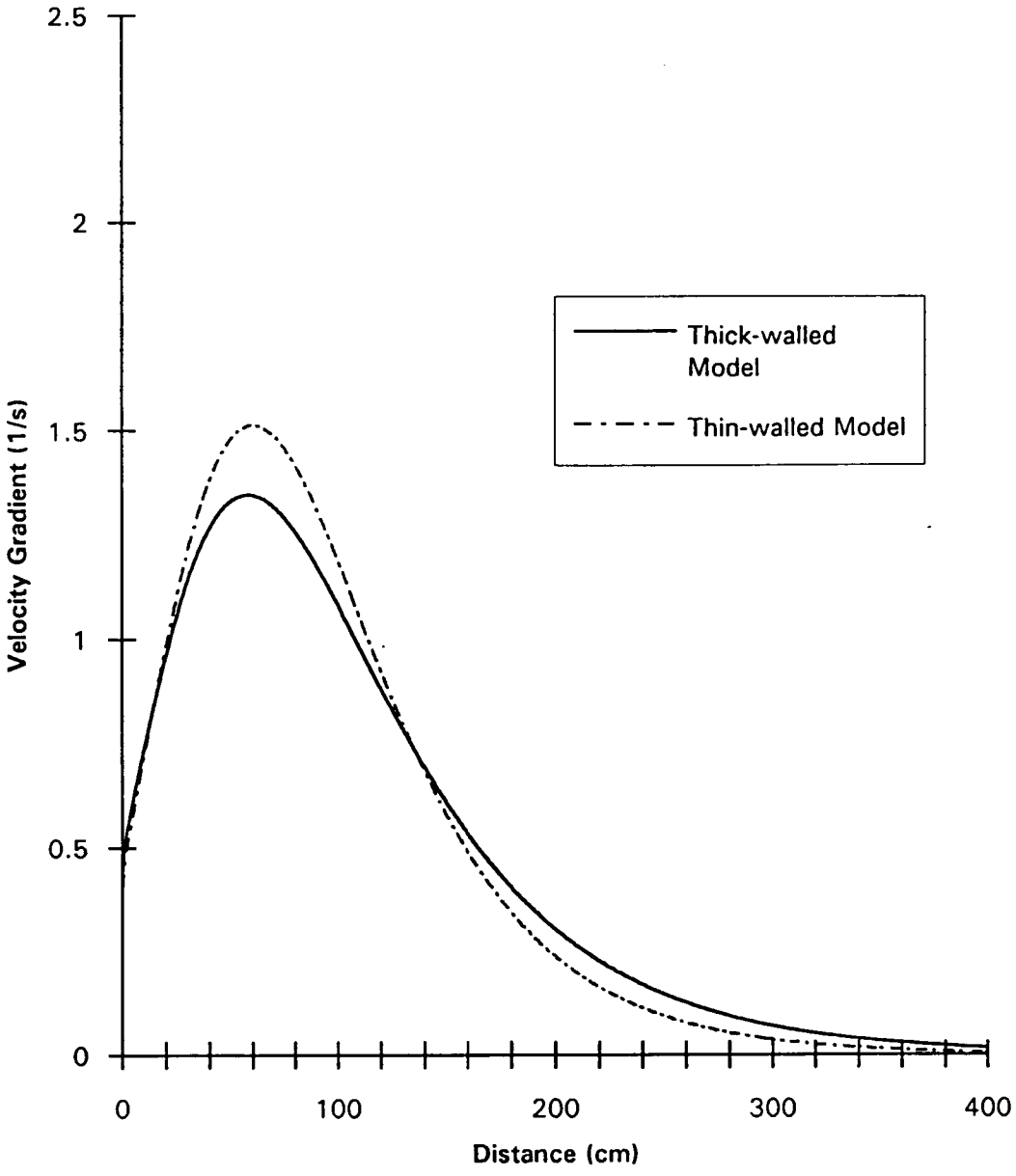

Figure 8.2.6 Comparison of velocity gradient profiles predicted by thick-walled and thin-walled models (spinneret parameter ID/OD = 0.25).

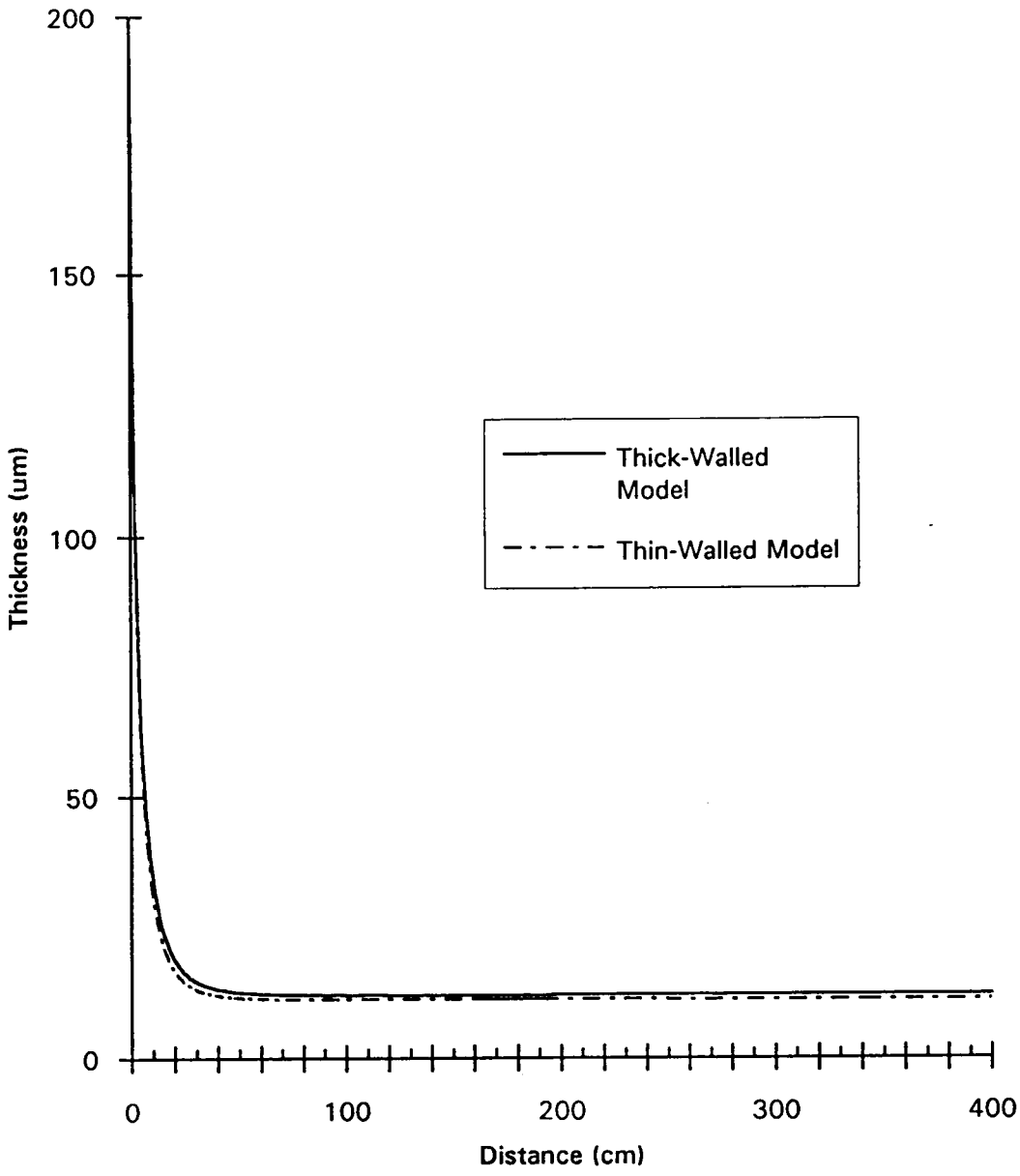

Figure 8.2.7 Comparison of wall thickness profiles predicted by thick-walled and thin-walled models (spinneret parameter ID/OD = 0.75).

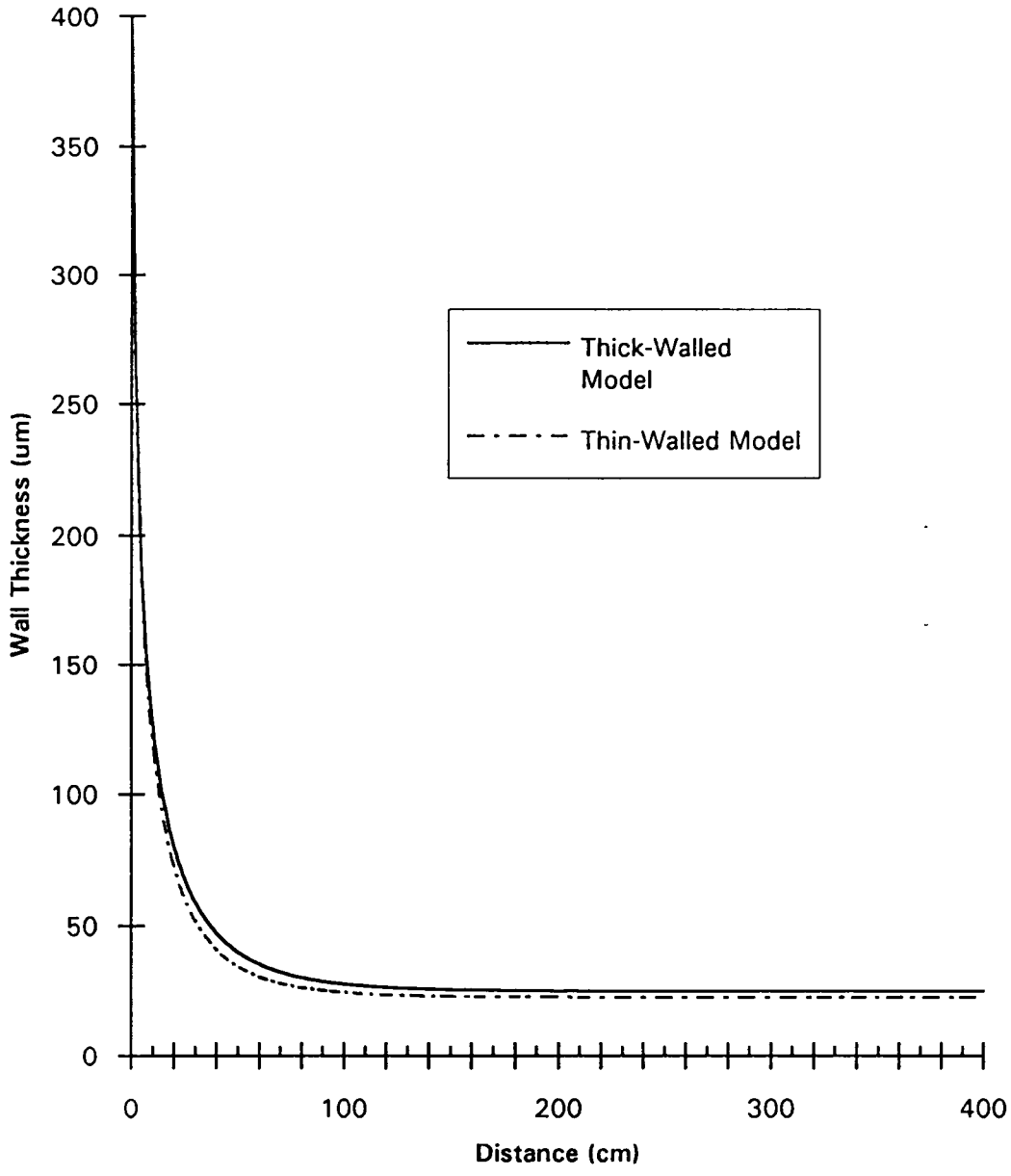

Figure 8.2.8 Comparison of wall thickness profiles predicted by thick-walled and thin-walled models (spinneret parameter ID/OD = 0.50).

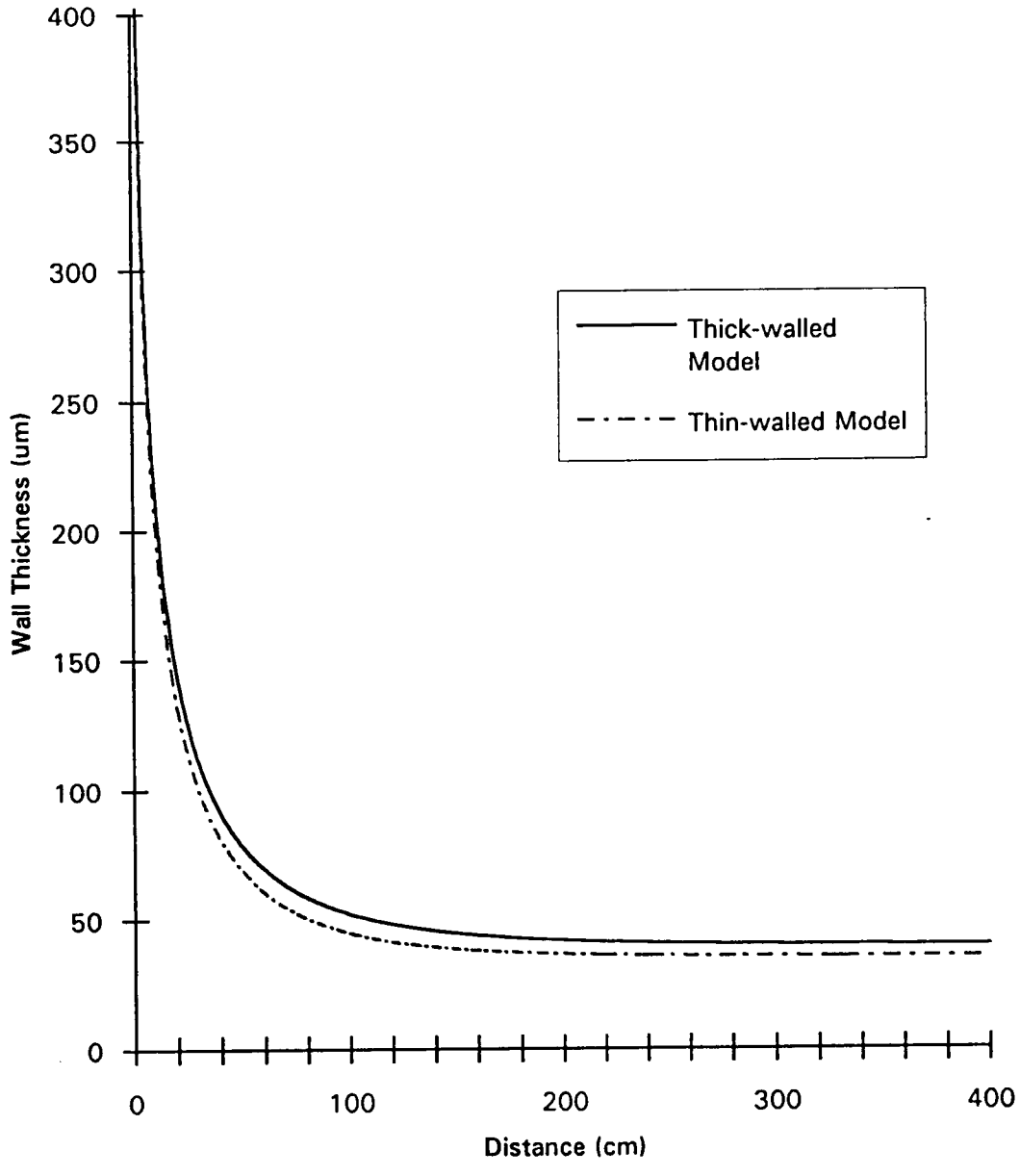

Figure 8.2.9 Comparison of wall thickness profiles predicted by thick-walled and thin-walled models (spinneret parameter ID/OD = 0.25).

Tables 8.2.1 to 8.2.3 show the results of comparison of predicted diameters and wall thicknesses of hollow filaments by both models using three Ri/Ro ratios of spinnerets (0.75, 0.5 and 0.25). In the case of Ri/Ro = 0.75, the predictions by thin-walled and thick-walled models are very close. The thin-walled model generally predicts larger diameters and thinner wall thickness than the thick-walled model, and the difference becomes greater with decreasing Ri/Ro ratio. The smaller is Ri/Ro ratio, the more deviation in predictions between two models.

8.3 Comparison between Dry Spinning Models for Hollow Filament and Non-Hollow Filament

The mathematical model for the solution dry spinning process of hollow fiber proposed in this research can be converted to describe the solution dry spinning process of conventional non-hollow fiber.

8.3.1 Conversion of the Model for Hollow Filament to the Model for Non-Hollow Filament

Continuity Equation

The continuity equation consider only mass flow rate regardless of the geometrical feature of the fiber. The

Table 8.2.1 Comparison of predicted diameters and wall thickness of hollow filament by thick-walled and thin-walled models (spinneret parameter ID/OD = 0.75).

	Diameter (um)	Wall Thickness (um)	ID/OD
Spinneret Parameters	1600 (OD) 1200 (ID)	200	0.75
Hollow Fiber Properties Predicted by Thick-walled Model	120.40 (OD) 96.00 (ID)	12.20	0.80
Hollow Fiber Properties Predicted by Thin-walled Model	120.61 (OD) 97.99 (ID)	11.31	0.81

Table 8.2.2 Comparison of predicted diameters and wall thickness of hollow filament by thick-walled and thin-walled models (spinneret parameter ID/OD = 0.5).

	Diameter (um)	Wall Thickness (um)	ID/OD
Spinneret Parameters	1600 (OD) 800 (ID)	400	0.5
Hollow Fiber Properties Predicted by Thick-walled Model	114.82 (OD) 64.68 (ID)	25.07	0.56
Hollow Fiber Properties Predicted by Thin-walled Model	119.77 (OD) 74.23 (ID)	22.77	0.62

Table 8.2.3 Comparison of predicted diameters and wall thickness of hollow filament by thick-walled and thin-walled models (spinneret parameter ID/OD = 0.25).

	Diameter (um)	Wall Thickness (um)	ID/OD
Spinneret Parameters	1600 (OD) 400 (ID)	600	0.25
Hollow Fiber Properties Predicted by Thick-walled Model	111.79 (OD) 32.59 (ID)	39.60	0.29
Hollow Fiber Properties Predicted by Thin-walled Model	118.56 (OD) 48.02 (ID)	35.27	0.41

continuity equation applies to dry spinning processes for both hollow fiber and non-hollow fiber.

$$W = W_P + W_S$$
$$\frac{dW}{dz} = -2\pi R J_r(r=R)$$
$$J_r(r=R) = -k_x\left(\frac{x_{sg} - x_{so}}{1 - x_{sg}}\right) \qquad (8.3.1)$$

Momentum Balance

The macro force balance equations (5.1.12, 5.1.13, 5.1.14, 5.3.5 and 5.3.11 in Chapter V) of hollow fiber spinning can be simply converted to describe spinning of conventional fiber by assuming Ri = 0 and $\Delta P = 0$. Thus we derive the following equations for the spinning of conventional fiber.

$$\pi R^2 \rho \bar{u}_z = W$$
$$W\frac{d\bar{u}_z}{dz} = \pi R^2 \frac{d\bar{\sigma}_{zz}}{dz} - \pi R C_D \rho_a \bar{u}_z^2 + \pi R^2 \rho g$$
$$\bar{\sigma}_{rr} = \sigma_{\theta\theta} = 0$$
$$\bar{\sigma}_{zz} = 3\mu\frac{d\bar{u}_z}{dz} \qquad (8.3.2)$$

Energy Balance

Since only heat transfer on the surface of the hollow fiber was considered in the model, and furthermore we assumed that there was no radial distribution of

temperature so that the heat transfer equation should also apply to the dry spinning process of conventional fiber.

$$\rho C_p u_z \frac{dT}{dz} = -\{\frac{1}{R}[h(T-T_a) + \Delta H_v J_x]\}$$

$$T = T_O, \text{ when } z = 0 \qquad (8.3.3)$$

Mass Balance

The diffusion equation and boundary conditions are ready to be used for modeling of the solution dry spinning of conventional fiber, when change the range of radius from Ro > r > Ri to R > r > 0 as follows:

$$u_z \frac{\partial c}{\partial z} = \frac{1}{r}\frac{\partial}{\partial r}(rD\frac{\partial c}{\partial r}) \qquad R > r > 0; \qquad c = c_0, \text{ when } z = 0$$

$$-D\frac{\partial c}{\partial r} = J_r(r=R) \qquad r = R$$

$$J_r(r=R) = -k_x(\frac{x_{sg} - x_{so}}{1 - x_{sg}})$$

$$J_r = 0 \qquad r = 0 \qquad (8.3.4)$$

Rheological Constitutive Equation

If we assume Ri=0 and ΔP=0 (no hole), the following constitutive equation is derived for conventional fiber spinning:

$$\frac{du_z}{dz} = \frac{1}{3\mu}\sigma_{zz}$$

$$\mu = \frac{\mu_o}{1 + (\frac{\mu_o \dot{\gamma}}{\tau^*})^{1-n}}$$

$$\mu_o = A\exp(\frac{E}{RT})$$

$$A = A'(1-c)^m \qquad (8.3.5)$$

8.3.2 Comparison to the Model for the Dry Spinning of Non-Hollow filament in the Literature

Ishihara et al. (114) proposed a mathematical model for dry spinning process of non-hollow fiber using polyurethane-urea elastomers (also see Appendix C). The converted equations as discussed above in terms of the dry spinning of non-hollow fiber are basically the same as the equations proposed by Ishihara et al. Thus it further proves that the mathematical model for the dry spinning of hollow fiber can be converted to a model for the dry spinning of non-hollow fiber by assuming that Ri=0 and $\Delta P=0$.

CHAPTER IX

SUMMARY AND CONCLUSIONS

The major objective of this research was to establish a mathematical model for the dry spinning process of hollow fiber using polyacrylonitrile (PAN)-dimethylformamide (DMF) solution; to further use the model to predict spinline behavior and hollow fiber properties under a variety of processing conditions. This objective has been achieved by developing a mathematical model, by checking its validity through comparing model prediction with experimental results, and by utilizing the model to understand the effects of key processing parameters on spinline dynamics and the properties of as-spun hollow filaments. The major conclusions of the present research are listed as follows:

1. A mathematical model was established for the dry spinning process of hollow filaments (Chapter V). The model is based on the fundamental equations of fluid mechanics, heat and mass transfer and spinning dynamics. It includes the equations of continuity, force balance, energy balance as well as mass transfer. The mass transfer model described the diffusion of the solvent phase within the filament and solvent evaporation at the filament-gas interface at which the solvent was under going a phase change from liquid phase to gas phase. The mathematical model was set up in

two dimensions for describing solvent concentration along the axis of the filament as well as along the radial direction of the filament. This model in its complete form is referred to as the "thick-walled" model, and it is presumably valid for describing the spinning of hollow filaments with a wide range of inner to outer diameters.

2. A viscosity equation for PAN-DMF spinning dope was developed based on Modified Cross Model and capillary experimental data (Chapter IV, 4.1). The viscosity equation was successfully used in the mathematical model of hollow filament spinning. The viscosity equation includes variables such as temperature, shear rate and polymer concentration in the spinning dope.

3. A "thin-walled" model was also developed on the assumption that the variation in the hoop stress with radial position in the filament could be neglected (Chapter V, 5.2). It was also shown that the thick-walled model is able to transform to the thin-walled model when wall thickness of hollow filament becomes small compared to filament radius (Chapter VIII, 8.1).

4. Limited on-line measured data was collected for velocity profile and take-up tension. In addition, the outer and inner diameters, wall thickness and solvent residue of as-spun filaments were measured (Chapter IV, 4.2, 4.3 and 4.4). In comparing model predictions with

experimental data, it was demonstrated that the mathematical model for hollow fiber spinning was able to predict the basic effects of processing conditions and material properties on the spinline behavior and properties of spun hollow filaments (Chapter VI, 6.2).

5. The effects of changing individual processing parameters on the spinline behavior and the properties of as-spun hollow filaments, such as outer and inner diameters, the ratio of ID/OD, wall thickness and solvent residue were studied in detail by modeling (Chapter VII). Results are summarized below.

(a) Mass Throughput

At constant take-up speed, the wall thickness and the outer and inner diameters of hollow filament increased with increasing mass throughput. However, the ratio of ID/OD of hollow filament was little affected by changing mass throughput.

The spinline temperature profile was greatly affected by mass throughput. In contrast, the spinline temperature profiles were only slightly influenced by changing take-up speed, under constant mass throughput.

The solvent residue profile was significantly influenced by mass throughput. The solvent concentration decreased much faster along the spinline under lower mass throughput conditions than higher mass throughput.

(b) Polymer Concentration in the Dope

Both inner and outer diameters of hollow filament increased with decreasing PAN concentration in the spinning dope at fixed processing conditions. The ratio of ID/OD of hollow filament was significantly higher for lower PAN concentration dope than higher PAN concentration dope.

Lower PAN concentration in the dope (higher solvent concentration) resulted in a lower level of the temperature profile along the spinline due to the fact that energy loss was proportional to the amount of solvent evaporated.

(c) Internal Pressure

The ratio of ID/OD of hollow filament was greatly impacted by varying internal pressure. The ratio of ID/OD increased significantly with increasing internal pressure.

(d) Spinning Column Temperature

Higher spinning column temperature speeded up the evaporation of the solvent in the spinline with the remaining process conditions fixed, which is especially useful for spinning under high mass throughput when the length of the spinning column is limited.

(e) Quench Air flow Speed

Quench air flow speed had little effect on the solvent residue in as-spun hollow filament due to the fact that solvent evaporation was largely controlled by

diffusion, and the spin column was long enough to let the solvent residue profile along the spinline reach a plateau. It was demonstrated that the solvent residue in the filament was much more sensitive to the length of the spin column than to quench air flow speed.

6. Furthermore, the interactive effects of key processing parameters on hollow filament spinning were also investigated by modeling (Chapter VI, 7.6). The key processing and property variables were summarized into take-up ratio (TUR), internal pressure (IP), inner diameter reduction ratio (IDRR) and wall thickness reduction ratio (TRR). The interactive effects of processing conditions on the properties of hollow filament were graphically presented. The process windows for producing hollow filament with a specified range of inner diameter and wall thickness were examined using modeling results.

7. A detailed comparison between thick-walled and thin-walled models was discussed (Chapter VIII, 8.1). The effect of the wall thickness on hoop stress predictions by the two model were examined. The analysis also indicated that the thin-walled model overpredicted the hoop stress compared to the prediction by the thick-walled model. The difference in hoop stress predictions between the two models increased with increasing wall thickness (or decreasing Ri/Ro ratio). The difference between the

predictions of the two models were small enough to be neglected, for most practical cases, when Ri/Ro > 0.75.

LIST OF REFERENCES

REFERENCES

1. L. Wood and A. A. Hill, Brit. Patent 710,087 (1950).

2. H. Bohringer and F. Bolland, Melliand Textilber., 36, 677 (1955).

3. G. Siemer, H. Laurisch and W. Stockigt, Brit. Patent 843,179 (1956).

4. Eastman Kodak, U.S. Patent 2,825,120

5. Monsanto Co., Brit. Patent 1,212,786 (1968).

6. J. Scott (Edited), Hollow Fibers, Noyes Data Corp., Park Ridge, NJ, U.S.A. (1981).

7. Asahi Kasei Kogyo KK, Japan, U.S. Patent 3,871,950 (1975); and U.S. Paten 4,181,694 (1980).

8. Monsanto Co., U.S. Patent 3,975,478 (1976); U.S. Patent 4,084,036 (1978) and U.S. Patent 4,209,307 (1980).

9. F. Siclari, Man-Made Fibers, Edited by H. F. Mark, S. M. Atlas, and E. Cernia, Vol. 1, Wiley-Interscience,(1967).

10. W. E. Fitzgerald and J. P. Craig, " The Extrusion Process in Solution Spinning," Appl. Polym. Symp. No.6, 67, (1967).

11. D. J. Williams, Polymer Science and Engineering, Prentice-Hall, Englewood Cliffs, New Jersey, (1971).

12. G. H. Oliver and S. Oliver, Adv. Polm. Sci., 32, 123 (1979).

13. S. Okajima et al., J. Polym. Sci. Part A-1, 6, 1925 (1968).

14. W. R. Krigbaum and N. Tokita, J. Polym. Sci., 43, 467 (1968).

15. P. Dunn and B. C. Ennis, J. Appl. Polym Sci., 14, 1795 (1970).

16. G. Hinrichsen, Angew. Makromol. Chem., 20, 121 (1974).

17. R. C. Houtz, Text. Res. J., 786 (1950).

18. S. B. Warner, D. R. Uhlmann and L. H. Peebles Jr., J. Mater. Sci. 14, 1893 (1979).

19. P. Tucher and W. George, Polym. Eng. Sci.12, 364 (1972).

20. W. O. Statton, J. Polym. Sci., 58, 205 (1962).

21. M. L. Huggins, J. Am. Chem. Soc., 64, 2716 (1942).

22. D. C. Bogue and J. L. White, Engineering Analysis of Non-newtonian fluid, NATO AGARDOGRAPH, (1970).

23. R. L. Boles and D. C. Bogue, 27th ANTEC Proceeding, Soc. Plastics Engr., (1968).

24. Y. Oyanagi and M. Matsumoto, J. Colloid. Sci., 17, 426 (1962).

25. A. Ziabicki, O. Elsner, K. Kedzierska and H. Muzyto, IUPAC Symposium on Macromolecules, Prague, (1957).

26. C. D. Han and L. Segal, J. Appl. Polym. Sci., 14, 2973 (1970).

27. B. Philipp and K. Wulf, Rheol. Acta, 5, 93 (1966).

28. D. R. Paul and A. A. Armstrong, J. Appl. Polym. Sci., 17, 1269 (1973).

29. A. Ziabicki, Fundamentals of Fiber Formation, John Wiley and Sons, New York, (1976).

30. A. Ziabicki, SEN-I GAKKAISHI, Vol.38, No.9, P409, (1982).

31. K. F. Zieminsky and J. E. Spruiell, J. Appl. Polm. Sci., 35, 2223 (1988).

32. Y. Ohzawa, Y. Nagano and T. Matsuo, J. Appl. Polym. Sci., 13, 257 (1969).

33. B. C. Sakiadis, AICHE. Journal, Vol.7, No.3, 467 (1961).

34. L. R. Glicksman, Glass Technology, 9, 131 (1968).

35. M. Matsui, Trans. Soc. Rheol., 20, 465 (1976).

36. Y. Sano and K. Orii, Sen-I Gakkaishi, 24, 212 (1968).

37. J. Gould and F. S. Smith, J. Text. Inst., 71, No.1, 38 (1980).

38. J. Shimizu, N. Okui and K. Tamai, Sen-I Gakkaishi, 39, No.10, 62 (1983).

39. Y. D. Kwon and P. C. Prevorsek, J. Appl. Polym. Sci., 23, 3105 (1979).

40. G. Vasudevan and S. Middleman, AIChE Journal, 16, 614 (1970).

41. A. Ziabicki, Kolloid Z., 175, 14 (1961).

42. Sano, Y. and Nishikawa, S., Kagaku Kogaku, 2, 100 (1964).

43. Sano, Y., in Formation of Fibers and Development of Their Structure (in Japanese), edited by The Society of Fiber Science and Technology, Japan, Kagaku Dojin, Kyoto (1969).

44. J. Shimizu, K. Shimazaki, K. Toriumi and T. Mitsui, J. Text. Mach. Soc., Japan, 18,125 (1972).

45. S. Kase and T. Matsuo, J. Polym. Sci., A3, 2541 (1965).

46. J. H. Noggle, Physical Chemistry, Little, Brown & Company Limited, (1985).

47. J. Crank, The mathematics of Diffusion, Claredon Press, Oxford, (1957).

48. J. Crank and C. S. Park, Diffusion in Polymers, Acad. Press, London, (1968).

49. Y. Sano and S. Nishkawa, Kagaku Kagaku, 29, 294 (1965).

50. Y. Sano and S. Nishkawa, Kagaku Kagaku, 30, 245 (1966).

51. Y. Sano and S. Nishkawa, Kagaku Kagaku, 30, 335 (1966).

52. S. Y. Fok and R. G. Griskey, J. Appl. Polym. Sci., 11, 2417 (1967).

53. S. Y. Fok and R. G. Griskey, Appl. Sci. Res., 16, 141 (1966).

54. C.R. Bohn, J. R. Schaefgen and W. O. Statton, J. Polym. Sci., 55, 540 (1961).

55. J. P. Craig, J. P. Knudsen and V. F. Holland, Textl. Res. J., 32, 435 (1962).

56. J. P. Knudsen, Textile Res. J., 33, 13 (1963).

57. T. Kiyotosukuri and I. Hirasa, Sen-I-Gakkaishi, 28, 15 (1972).

58. T. A. Hancock, J. E. Spruiell and J. L. White, J. Appl. Polym. Sci., 21, 1227 (1977).

59. T. A. Hancock, J. L. White and J. E. Spruiell, Polym. Engr. and Sci., 20, 1126 (1980).

60. R. S. Lenk, J. L. White and J. F. Fellers, J. Appl. Polym. Sci., 21, 1543 (1977).

61. U.S. Patern 4658004 (1987) and U.S. Patern 4659529 (1987).

62. P. Bajaj, A. K. Sengupta and P. C. Jain, Textile Res. J. 50, 218 (1980).

63. P. Bajaj and M. S. Kumari, J. Macromol. Sci. Rev., C-27, 181 (1987).

64. Monsanto Co., Brit. Pat. 1,472645, (1977).

65. D. J. Poyton, Textile Prog., 8, 51 (1976).

66. H. Tanaka, S. Fujii, M. Watanabe and T. Kato (Toray Industries Inc.), Jap. Pat. 7,234,441, (1972); Chem. Abstr. 78, 137, 815z (1973).

67. D. R. Paul, J. Appl. Polym. Sci., 11, 439 (1967).

68. D. R. Paul, J. Appl. Polym. Sci., 12, 383 (1968).

69. H. Porosoff (American Cyanamid), U.S. Pat. 4,163,770, Aug. 7, (1979).

70. P. H. Lindenmeyer and R. Hosemann, J. Appl. Phys. 34, 42 (1963).

71. Y. Sano and S. Nishikawa, Kagaku Kogaku, 30, 245 (1966).

72. Y. Sano and S. Nishikawa, Kagaku Kogaku, 30, 335 (1966).

73. W. O. Statton, in Newer Methods of Polymer Characterization, B. Ke Ed., Interscience, New York, (1964).

74. Dow Chemical Company, U.S. Patent 3,422,009, (1969).

75. Dow Chemical Company, U.S. Patent 4,020,230, (1977).

76. Dow Chemical Company, U.S. Patent 4,115,492, (1978).

77. Asahi Kasei Kogyo KK, Japan, U.S. Patent 3,871,950, (1975).

78. Asahi Kasei Kogyo KK, Japan, U.S. Patent 4,181,694, (1980).

79. F. Bolland and H. Henkel, Mitt. Inst. Textiltechnologie Chemiefasern, Rudolstadt, 3, 173 (1959).

80. Fiber World News, From American's Textile International, FW 10, January, (1993).

81. B. S. Rhee et al., Proceedings of the 20th Biennial Conference on Carbon, 306, June (1991).

82. S. Lin, SAMPE Journal, Vol.28, No.4, 9, August (1992).

83. Y. Ohzawa and Y. Nagano, J. Appl. Polym. Sci., 14, 1879 (1970).

84. K. F. Zieminsky, Ph.D. dissertation, University of Tennessee, Knoxville, (1986).

85. J. H. Bheda, Ph.D. dissertation, University of Tennessee, Knoxville, (1987).

86. J. Zhou, M.S. Thesis, University of Tennessee, Knoxville, (1988).

87. J. L. Lambach, M.S. Thesis, University of Tennessee, Knoxville, (1988).

88. R. F. Onyon, J. Polym. Sci., 22, 13 (1956).

89. J. Brandrup and E. H. Immergut, Polymer Handbook, 2nd Ed., John Wiley, New York, NY (1982).

90. A. de Waele, Oil and Color Chem. Assoc. J., 6, 23 (1923).

91. W. Ostwald, Kolloid-Z, 36, 99 (1925).

92. M. M. Cross, Rheol. Acta, 18, 609 (1979).

93. P. J. Carreau, Ph.D. Thesis, Department of Chemical Engineering, University of Wisconsin, Madison, Wisconsin (1968).

94. D. G. Kleinbaum & L. L. Kupper, Applied Regression Analysis and Other Multivariable Methods, Duxbury Press, Boston, MA (1978).

95. E. P. Box, Statistics for Experimenters, Wiley & Sons, New York (1978).

96. AATCC Technical Manual, Volume 60, 45 (1985).

97. M. T. Postek and et al., Scanning Electron Microscopy, Ladd Research Indstries, Inc. (1980).

98. P. J. Flory, Principles of Polymer Chemistry, Cornell University Press, Ithaca, N.Y. (1953).

99. P. J. Flory, J. Chem. Phys., 10, 51 (1942).

100. M. L. Huggins, J. Phys. Chem., 46, 151 (1942).

101. J. R. Pearson and C. J. S. Petrie, J. Fluid Mech., 40, 1 (1970).

102. J. R. Pearson and C. J. S. Petrie, J. Fluid Mech., 40, 609 (1970).

103. J. R. Pearson and C. J. S. Petrie, Plast. Polym., 38, 85 (1970).

104. C. J. S. Petrie, AlChE J., 21, 275 (1975).

105. C. J. S. Petrie, Rheol. Acta, 12, 92 (1973).

106. V. G. Wilhelm, Kolloid. Z.-Z. Polym., 208, 97 (1966).

107. A. Ziabicki and K. Kedzierska, Chemie Stosowana, 3, 151 (1960).

108. W. L. McCabe & J. C. Smith, Unit Operations of Chemical Engineering, McCraw-Hill, New York, NY (1967).

109. D. Tabor, Gases, Liquids and Solids and Other States of Matter, Third Edt., Cambridge Univ. Press, (1991).

110. R. B. Bird, W. E. Stewart and E. N. Lightfoot, Transport Phenomena, Wiley & Sons, New York (1962).

111. Z. Tadmor and C. G. Gogos, Principles of Polymer Processing, John Wiley & Sons, New York, (1979).

112. J. M. Vergnaud, Lquid Transport Process in Polymer Materials, Prentice-Hall, Englewood Cliffs, NJ (1991).

113. S. C. Chapra and R. P. Canale, Numerical Methods For Engineers, McCraw-Hill, New York, NY (1985).

114. H. Ishihara, K. Tani, S. Hayashi and H. Ikeuchi, J. of Polym. Engineering, 6, 237 (1986).

APPENDIXES

APPENDIX A

BASIC CAPILLARY RHEOLOGICAL EQUATIONS

Viscosity is equal to shear stress over shear rate as:

$$\eta = \frac{\tau}{\dot{\gamma}} \tag{A-1}$$

where η is viscosity, τ the shear stress and $\dot{\gamma}$ the shear rate.

The shear stress is determined by:

$$\tau = \frac{F}{A} = \frac{D_c \Delta P}{4L_c} = \frac{F_p r_c}{2\pi R_b^2 L_c} \tag{A-2}$$

where F is force acting on surface area A. F_p is the force on the plunger and r_c, D_c are the inner radius and diameter of the capillary, R_b is the inner radius of the barrel and L_c is length of the capillary and ΔP is the pressure drop along the capillary.

The shear rate is determined by:

$$\dot{\gamma} = \frac{32Q}{\pi D_c^3} = \frac{4R_b^2 S}{r_c^3} \tag{A-3}$$

where S is the speed of the plunger, Q is the volumetric flow rate.

Combine Eqs. (A-1), (A-2) and (A-3), the viscosity reduces to the following equation:

$$\eta = \frac{Fr_c^4}{8\pi R_b^4 L_c S} \qquad \text{(A-4)}$$

APPENDIX B

BAGLEY AND RABINOWITSCH CORRECTIONS

Bagley Correction (correct pressure drop across the die)

The shear stress is often corrected using Bagley method to account for the effect of any stationary pressure (usually entrance and exit effects) on the true pressure drop across the die.

$$\tau_{wc} = \frac{P_b D_c}{4(L_c + B_a)} \qquad \text{(B-1)}$$

where P_b is the pressure in the barrel, D_c the capillary diameter, L_c the capillary length and B_a is a intercept obtained by plotting pressure in the barrel versus L/D for a given shear rate.

Rabinwitsch Correction (correct shear rate at the capillary wall)

Rabinowitsch and Mooney proposed a equation relating the true shear rate at the wall to the apparent shear rate, $4Q/\pi R^3$, and its derivative with respect to the true shear stress at the wall.

$$-\gamma_{wc} = \frac{4Q}{\pi R^3}\left\{\frac{3}{4} + \frac{1}{4}\left[\frac{d[\log(4Q/\pi R^3)]}{d[\log(\Delta P_b R/2L_c]}\right]\right. \qquad \text{(B-2)}$$

where γ_{wc} is the corrected shear rate at the wall.

APPENDIX C

FUNDAMENTAL EQUATIONS FOR DRY SPINNING OF NON-HOLLOW FIBER (by H. Ishihara et al. (114))

Fundamental Equations for Dry Spinning

Macroscopic Equations

(1) Equation of Continuity

$$\frac{dW}{dx} + 2\pi R M_s N_s = 0$$

(2) Equation of Motion

$$\frac{dF}{dx} = W\left[\frac{dv}{dx} - \frac{g}{v}\right] + 0.23 \times 10^{-3}\left[\frac{W}{\rho}\right]^{0.195} v^{1.195}$$

(3) Equation of Energy

$$\frac{dT}{dx} = \frac{2}{\rho C_p v}\sqrt{\frac{\pi}{A}}\left[h(T^* - T) - L_s N_s\right]$$

(4) Equation of Rheology

$$F = A\beta\frac{dv}{dx}$$

(5) Equation of Deflection

$$\frac{d^2y}{dx^2} = \frac{\rho A g\frac{dy}{dx} - \rho^* v_y^2 R C_D}{F - \rho A v^2}$$

Microscopic Equation

(6) Equation of Continuity for Solvent Component

$$V\frac{d\omega_s}{dx} = \frac{1}{r}\frac{d}{dr}\left[rD\frac{d\omega_s}{dr}\right]$$

VITA

The author, Jianguo Zhou (周建国) was born in Zhejiang Province, China on October 9, 1956. During 1978-1981, he studied Chemical & Textile Engineering at Shanghai Textile Engineering Institute, Shanghai, China. During 1982-1983, he worked for Shanghai Textile Industrial Bureau; and studied Polymer & Textile Materials at East China Institute of Textile Science & Technology, Shanghai, China. He obtained his Bachelor of Science degree in 1983. After graduation he worked as a teaching assistant at East China Institute of Textile Science & Technology.

He came to the United States and entered The University of Tennessee, Knoxville to study Polymer Engineering at Department of Materials Science & Engineering in 1985. He received his Master of Science degree in Polymer Engineering in August, 1988. He continued for a doctorate degree in the same program. He received his Doctor of Philosophy degree in May, 1996. He has been working for plastic and medical industries in the United States since 1990.

The author is married and has two children. He is currently working for Ethicon, Inc., a Johnson & Johnson Company.